Control of spin relaxation and spin precession in diffusive 2DEG channels

DISSERTATION ZUR ERLANGUNG DES DOKTORGRADES DER NATURWISSENSCHAFTEN (DR. RER. NAT.) DER FAKULTÄT PHYSIK DER UNIVERSITÄT REGENSBURG

vorgelegt von

Franz Eberle

aus Regensburg

im Jahr 2022

Promotionsgesuch eingereicht am: 09.06.2022

Die Arbeit wurde angeleitet von: Prof. Dr. Dieter Weiß

Prüfungsausschuss:

Vorsitzender:	Prof. Dr. Jaroslav Fabian
Erstgutachter:	Prof. Dr. Dieter Weiß
Zweitgutachter:	Prof. Dr. Dominique Bougeard
Weiterer Prüfer:	Prof. Dr. John Lupton

Contents

1 Introduction

According to Moore's empirical law [1], the transistor density of electrical integrated circuits doubles roughly every 12 to 24 months [2]. However, it is expected that this trend cannot be sustained in the long term. The increasing miniaturization requires more sophisticated lithographic approaches, but also new concepts regarding heat dissipation [3]. Additionally, for smaller devices the contact resistances and the gate capacitance become comparable to parasitic resistances and capacitances, which poses additional challenges with regard to the circuit design [4]. At the same time, quantum mechanical effects and temperature noise have to be taken into account for feature sizes approaching the atomic scale [3]. These limitations of conventional electric circuits require investigating novel concepts, one of which is spintronics. While in conventional electronic devices charge currents are controlled, spintronics is based on the manipulation of spin currents. One of the first commercial spintronic devices was a hard drive storage, which was introduced by IBM in 1997 [5]. This device is based on the giant magneto-resistance (GMR) effect, which was discovered by the A. Fert et al. [6] and P. Grünberg [7]. Data storage spintronic devices are well established by now and mainly based on metal spintronics. Semiconductor spintronic devices which allow data manipulation, on the other side, have not yet been realized. A well-known example for such a device is the spin field effect transistor (spinFET) proposed in 1989 by S. Datta and B. Das [8]. This conceptual device operates in the 1D ballistic transport limit, and requires efficient electrical spin injection and detection, but also gate control of the spin precession frequency. Electrical injection and detection in semiconductor (SC) structures have already been achieved and profoundly investigated in all-electrical spin injection devices [9–17], and also in fully SC-based device geometries [18, 19], in which ferromagnetic semiconductors are

implemented. Gate manipulation of electrically injected spins, on the other hand, could only be demonstrated by H. Koo et al. [20] in an InAs quantum well (QW) structure in the ballistic transport limit, followed by a number of subsequent publications with similar device setups [21–25]. One of the main restrictions for the realization of a spinFET-like device geometry is the strict prerequisite of ballistic transport, which, in particular, requires the injector-detector distance to be smaller than the electron's mean free path. In such devices a strong spin orbit coupling (SOC) strength is essential, in order to rotate the injected spin on such a small distance, which considerably limits the material choice. Thus, it is highly desirable to investigate spin device geometries, which allow inducing gate controllable spin precession in the diffusive spin transport regime.

Here, we present spintronic devices which allow efficient electrical spin injection and detection into a semiconductor heterostructure with a 2DEG channel. Introducing an enhanced device geometry allows realizing narrow transport channels with a width down to $w_c = 400\,\mathrm{nm}$, thus approaching the 1-dimensional spin transport regime. This considerable spatial confinement gives rise to a significant suppression of spin relaxation, for instance, but also allows identifying spin orbit coupling (SOC) related signatures in non-local spin transport measurements. One of the major findings presented in this thesis is the demonstration of the gate tunability of these SOC related spin signal characteristics. Thus, it is possible to extract gate voltage dependent non-local spin signal oscillations, similar to the expected signal modulation in a spinFET device. Contrary to the spinFET proposal by S. Datta and B. Das [8], however, spin transport is not purely ballistic in the investigated devices, instead it takes place in an intermediate regime between ballistic and diffusive transport. This is a considerable relaxation of the prerequisites required for the realization of a spinFET device, in particular allowing larger device dimensions, for instance, which significantly facilitates investigations of the fundamental physical properties.

The conceptual structure of this thesis is summarized in the following. In the theoretical part (Chapter 2), basic concepts of electrical spin injection and detec-

tion, spin transport, and SOC related phenomena are introduced. Additionally, an extended spin diffusion model is presented that includes SOC. In Chapter 3 the heterostructure system is described and the device geometry is explained, along with the experimental non-local measurement setup. The required microfabrication steps are also shortly summarized. The experimental part of this thesis (Chapter 4) is divided into three main sections. First, a novel sample geometry is introduced in Chapter 4.1, which allows investigating spin transport in narrow channels, approaching the 1-dimensional limit. The spin transport properties in dependence on the channel width are extensively studied in this section. In the following experimental subsection (Chapter 4.2) the new sample design is implemented in order to identify and investigate SOC related signal features in non-local spin transport measurements. This confirms the presence of a finite SOC strength in the investigated devices, and implies a strong anisotropy of SOC with regard to the crystallographic orientation. Additionally, the SOC related signal characteristics can be qualitatively reproduced by finite element simulations, based on the extended spin diffusion model, which is introduced in the theoretical part of this thesis. In the final section (Chapter 4.3), the central experimental findings of this thesis are presented. There, the gate tunability of the SOC related features, described in the previous chapter, is demonstrated and discussed in detail. Additionally, it is possible to extract gate dependent oscillations of the non-local spin signal. A detailed evaluation strongly suggests that these spin signal oscillations can be attributed to the gate tunability of SOC and the accompanying change of the spin precession frequency.

2 Theoretical Framework

2.1 Spin transport

Before discussing electrical spin injection from a ferromagnetic (FM) into a non-magnetic (NM) conductor in Chapter 2.2, basic quantities and fundamental relations describing spin transport are introduced, following the treatment and notation of the comprehensive description by J. Fabian et al. [26] and I. Žutić et al. [27]. In the model described in the following, spin transport is treated as a parallel circuit of two separate transport channels for majority and minority spins. This so-called two current model was introduced by N. Mott [28], and extended by I. Campell et al. [29] and A. Fert et al. [30]. It allows introducing separate quantities for the two spin species, like separate carrier densities for spin-up $n_\uparrow$ and spin-down $n_\downarrow$. Thus, the total carrier density n and the spin density s can be defined in terms of $n_\uparrow$ and $n_\downarrow$:

$$\begin{aligned} n &= n_\uparrow + n_\downarrow \\ s &= n_\uparrow - n_\downarrow. \end{aligned} \tag{2.1}$$

The spatial and temporal evolution of the spin density can be described by the spin drift-diffusion equation, which can be derived from a random walk approach, as presented by J. Fabian et al. [26], yielding:

$$\frac{\partial s}{\partial t} = D\,\frac{\partial^2 s}{\partial x^2} + \mu_e E\,\frac{\partial s}{\partial x} - \frac{s}{\tau_s}, \tag{2.2}$$

with the spin relaxation time τ_s, diffusion coefficient D, electric field E, and electron mobility μ_e. Another important quantity is the spin diffusion length λ_s,

which is related to τ_s and D:

$$\lambda_s = \sqrt{D\tau_s}. \tag{2.3}$$

In a rather simplified picture, spin injection from a ferromagnet ($x < 0$) into a non-magnetic conductor ($x > 0$) can be regarded as a configuration in which a constant spin current $J_s(0) = -D\,\partial s/\partial x|_{x=0}$ enters the non-magnetic channel at $x = 0$ (Fig. 2.1). The corresponding accumulated spin at the interface is thus given by

$$s(0) = J_s(0)\frac{\lambda_s}{D}. \tag{2.4}$$

The steady state solution of the spin diffusion equation without drift ($E = 0$) yields the spatial distribution of the spin density in the NM, which decays exponentially with the distance from the interface, with the decaying behavior being determined by the spin diffusion length λ_s:

$$s(x) = s(0)\exp\left(-\frac{x}{\lambda_s}\right). \tag{2.5}$$

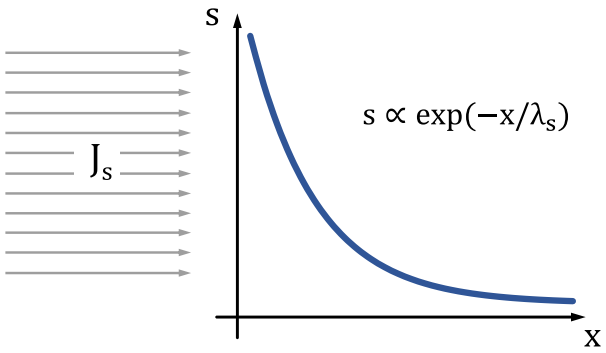

Figure 2.1. Schematic understanding of electrical spin injection from a FM ($x < 0$) into a NM ($x > 0$) with a constant spin current J_s at $x = 0$. The spin density s decays exponentially for $x > 0$. Adapted from [26].

For modeling spin injection across a FM-NM junction in detail, it is beneficial not to directly regard the spin density s, but rather introduce the so-called quasi-chemical potential for two spin species ($\mu_\uparrow$ and $\mu_\downarrow$), which allows defining the total quasi-chemical potential μ and the spin quasi-chemical potential μ_s:

$$\begin{aligned} \mu &= 1/2\,(\mu_\uparrow + \mu_\downarrow) \\ \mu_s &= 1/2\,(\mu_\uparrow - \mu_\downarrow)\,. \end{aligned} \tag{2.6}$$

The spin quasi-chemical potential μ_s is related to the spin density s by the following expression:

$$s = s_0 + 4e\mu_s \frac{g_\uparrow g_\downarrow}{g}, \tag{2.7}$$

where s_0 is the equilibrium spin density and $g_{\uparrow/\downarrow}$ are the corresponding densities of state (DOS) for spin-up and spin-down electrons. A gradient in the quasi-chemical potential gives rise to a current of the corresponding spin component:

$$j_{\uparrow/\downarrow} = \sigma_{\uparrow/\downarrow} \nabla \mu_{\uparrow/\downarrow}, \tag{2.8}$$

with the conductivities $\sigma_{\uparrow/\downarrow}$. An important relation can be derived from Eq. 2.6 and Eq. 2.8, which relates the electric charge current j and the spin current j_s to the quasi-chemical potentials μ and μ_s (spin-charge coupling):

$$\begin{aligned} j &= j_\uparrow + j_\downarrow = \sigma \nabla \mu + \sigma_s \nabla \mu_s \\ j_s &= j_\uparrow - j_\downarrow = \sigma_s \nabla \mu + \sigma \nabla \mu_s, \end{aligned} \tag{2.9}$$

with $\sigma = \sigma_\uparrow + \sigma_\downarrow$ and $\sigma_s = \sigma_\uparrow - \sigma_\downarrow$. These two relations imply, that in a ferromagnetic conductor with $\sigma_s \neq 0$, a gradient in the spin quasi-chemical potential can generate a charge current j. For a non-magnetic conductor, on the other hand, where $\sigma_s = 0$, a spin current can only be due to a gradient of the spin accumulation μ_s, while a charge current can only flow in the presence of a gradient of the quasi-chemical potential μ. This is indeed relevant for both injection and detection of spin polarized electrons, as discussed in the following. Another relevant quantity with regard to spin injection and detection is the current spin polarization P_j, which is given by

$$P_j = \frac{j_s}{j} = P_\sigma + \frac{4}{j} \nabla \mu_s \frac{\sigma_\uparrow \sigma_\downarrow}{\sigma}, \tag{2.10}$$

where $P_\sigma = \sigma_s / \sigma$ denotes the conductivity spin polarization. In particular, this equation implies, that for non-magnetic conductors, in which $P_\sigma = 0$, a large gradient in the spin quasi-chemical potential $\nabla \mu_s$ is necessary in order to obtain a finite spin polarization of the current. Moreover, the spatial profile of μ_s can be

described by the following diffusion equation:

$$\nabla^2 \mu_s = \frac{\mu_s}{L_s}, \tag{2.11}$$

with the generalized spin diffusion length L_s, which is related to the generalized diffusion constant $\overline{D}$:

$$L_s = \sqrt{\overline{D}\tau_s}, \quad \text{with} \quad \overline{D} = \frac{g}{g_\uparrow/D_\downarrow + g_\downarrow/D_\uparrow}. \tag{2.12}$$

In a non-magnetic conductor, $\overline{D}$ corresponds to the diffusion coefficient D introduced in connection with the drift-diffusion equation of the spin density (Eq. 2.2). Thus, also the corresponding spin diffusion lengths are equal in this case ($L_s = \lambda_s$).

2.2 Electrical spin injection and detection

The basic theoretical concepts of electrical spin injection and detection within the scope of the standard model of spin injection were introduced by A. Aronov [31], and later expanded and generalized mainly by M. Johnson and R. Silsbee [32, 33], P. van Son [34], T. Valet and A. Fert [35], S. Hershfield and H. Zhao [36], and numerous other authors [37–40]. The following summary of the fundamental concepts of electrical spin injection and detection is based on the comprehensive review articles by J. Fabian et al. [26], I. Žutić et al. [27], and E. Rashba [41]. The notation is adapted from Ref. [26] and Ref. [27]. A typical device configuration allowing electrical spin injection and detection is shown in Fig. 2.2. This so-called non-local spin injection geometry was introduced by M. Johnson and R. Silsbee [42], and, in a very simplified schematic representation, consists of a non-magnetic conduction channel (NM) and two ferromagnetic contacts (FM). By passing a charge current through one of the FM contacts into the channel, a non-equilibrium spin accumulation is generated in the NM conductor (spin injection). As this current is passed to a non-magnetic reference contact (left), no charge current flows between the two ferromagnetic contacts, or in the detection circuit respectively (non-local setup). The injected spin accumulation then dif-

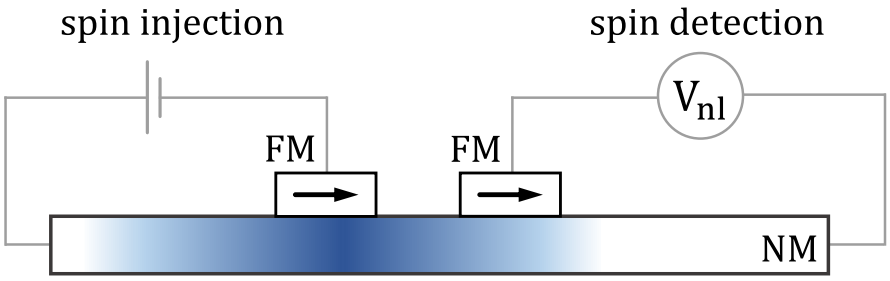

Figure 2.2. Non-local spin injection and detection setup introduced by M. Johnson and R. Silsbee [42]. Spins are injected at the left FM contact and diffuse in each direction in the NM channel (color gradient). The generated spin accumulation underneath the detecting contact (right FM) can be measured as a non-local voltage drop V_{nl}. Adapted from [26].

fusively spreads in the NM, which, for a sufficiently large spin diffusion length, results in a finite non-equilibrium spin distribution underneath the detecting FM, the magnitude of which can be measured as a non-local voltage drop V_{nl}.

Standard model of spin injection

Electrical spin injection from a ferromagnet into a non-magnetic conductor can be described theoretically with the so-called standard model of spin injection, in which spin transport across a FM-NM junction is regarded [26, 27, 33, 34, 36, 39–41]. A schematic structure, consisting of a ferromagnetic and a non-magnetic layer with an infinitesimally narrow contact region C in between, is shown in Fig. 2.3. The spatial extent of the FM, as well as that of the NM, are larger than the corresponding spin diffusion lengths L_{sF} and L_{sN}. The current polarization in the NM, in which case $P_\sigma = 0$ and $\sigma_\uparrow = \sigma_\downarrow$, can be obtained by solving the spin diffusion equation (Eq. 2.11) in combination with Eq. 2.10, and an appropriate

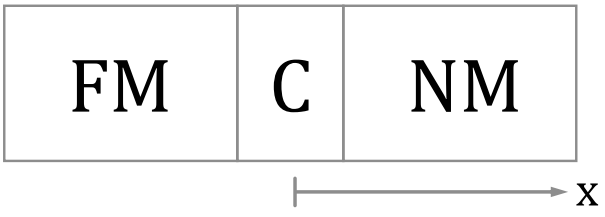

Figure 2.3. Schematic depiction of a FM-C-NM junction, allowing a basic theoretical description of electrical spin injection. Adapted from [26].

boundary condition ($\mu_{sN}(+\infty) = 0$), which yields

$$P_{jN}(0) = -\frac{1}{j}\frac{\mu_{sN}(0)}{R_N}, \tag{2.13}$$

with the effective spin resistance in the NM $R_N = L_{sN}/\sigma_N$. Thus, a larger spin diffusion length L_{sN} leads to a greater spin accumulation $\mu_{sN}(0) = -jP_{jN}(0)R_N$. The current polarization $P_{jF}(0)$ in the FM at the interface ($x = 0$), and that of the contact region P_{jC}, can be derived based on similar considerations, yielding

$$P_{jF}(0) = P_{\sigma F} + \frac{1}{j}\frac{\mu_{sF}(0)}{R_F} \quad \text{and} \quad P_{jC} = P_\Sigma + \frac{1}{j}\frac{\Delta\mu_s(0)}{R_C}, \tag{2.14}$$

with

$$\begin{aligned}
R_F &= \frac{\sigma_F}{4\sigma_{F\uparrow}\sigma_{F\downarrow}}L_{sF} && \text{(effective resistance of FM)}\\
R_C &= \frac{\Sigma_\uparrow + \Sigma_\downarrow}{4\Sigma_\uparrow\Sigma_\downarrow} && \text{(effective contact resistance)}\\
P_\Sigma &= \frac{\Sigma_\uparrow - \Sigma_\downarrow}{\Sigma_\uparrow + \Sigma_\downarrow} && \text{(conductance spin polarization of the contact),}
\end{aligned}$$

and the conductances $\Sigma_\uparrow$ and $\Sigma_\downarrow$. Assuming the continuity of the spin current at the contact, i.e. neglecting spin flip scattering in the contact, so that $P_{jF}(0) = P_{jC}(0) = P_{jN}(0) \equiv P_j$, allows deriving an expression for the spin injection efficiency P_j:

$$P_j = \frac{R_F P_{\sigma F} + R_C P_\Sigma}{R_F + R_N + R_C}, \tag{2.15}$$

which is also referred to as spin injection coefficient [39, 41]. This equation for P_j is one of the main results derived from the standard model of spin injection and can be related to the spin accumulation:

$$\mu_{sN}(0) = -jP_jR_N. \tag{2.16}$$

The configuration in which electrons flow from the FM into the NM ($j < 0$, $\mu_{sN}(0) > 0$) is typically referred to as spin injection, while spin extraction relates to the opposite case ($j > 0$, $\mu_{sN}(0) < 0$). In the following, however, there is no

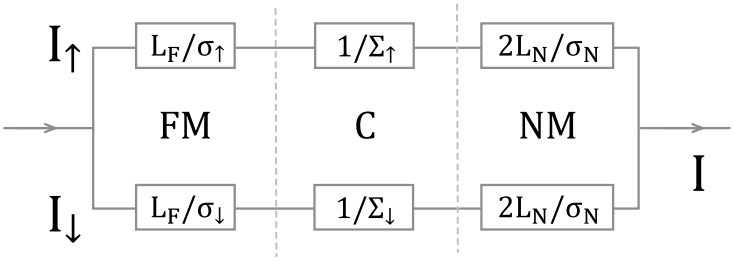

Figure 2.4. Equivalent electrical circuit of a FM-C-NM junction with separate channels for spin-up and spin-down electrons. Adapted from [26].

explicit differentiation, instead the term spin injection is used for both cases. Additionally, it can be remarked that Eq. 2.15 can also be derived more descriptively by regarding the equivalent electrical circuit of the FM-C-NM junction, which consists of two separate channels for spin-up and spin-down electrons in parallel (Fig. 2.4). Each region (FM, C and NM) is characterized by different resistances. The injection efficiency can then be obtained by evaluating the current in each channel: $P_j = (I_\uparrow - I_\downarrow)/I$.

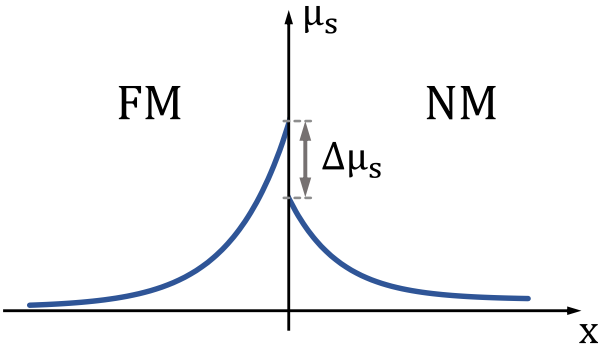

Figure 2.5. Spatial distribution of μ_s in the FM ($x < 0$) and the NM ($x > 0$): μ_s decays exponentially in both regions on the scale of the corresponding spin diffusion lengths, and is discontinuous at the interface ($\Delta\mu_s$). Adapted from [26].

The spatial profile of the quasi-chemical potential μ_s is shown in Fig. 2.5. In the absence of spin-flip scattering in the contact region, the spin current j_s is continuous at the contact ($x = 0$), while there occurs a distinct discontinuity of μ_s ($\Delta\mu_s$), which directly follows from the equation describing P_{jC} (Eq. 2.14):

$$\Delta\mu_s(0) = \mu_{sN}(0) - \mu_{sF}(0) = jR_C(P_j - P_\Sigma). \tag{2.17}$$

Note that for a FM-NM junction without a contact resistance ($R_C = 0$), μ_s is continuous at the interface. Within the FM and NM region, μ_{sF} and μ_{sN} decay

exponentially with the distance from the interface ($x = 0$) on the scale of the corresponding spin diffusion length L_{sF}, or L_{sN} respectively (Eq. 2.11):

$$\mu_{sN/sF}(x) = \mu_{sN/sF}(0) \exp\left(\mp \frac{x}{L_{sN/sF}}\right). \tag{2.18}$$

Spin bottleneck

The presence of a non-equilibrium spin distribution in the FM and the contact leads to a spin diffusion away from the contact. This spin current gives rise to a charge current in the FM and the contact region ($P_\sigma \neq 0$) according to Eq. 2.9 (spin charge coupling), which flows in the opposite direction compared to the charge current flowing due to the externally applied voltage. This, in turn, leads to an additional resistance δR (spin bottleneck [43]), such that the total resistance of the junction adds up to:

$$\tilde{R}_N + \tilde{R}_F + 1/\Sigma + \delta R, \tag{2.19}$$

where $\tilde{R}_F$ and $\tilde{R}_N$ are the actual electrical resistances of the FM and NM region, normalized to the cross-sectional area. In case of an equal contact conductance for both spin species ($\Sigma_\uparrow = \Sigma_\downarrow$), $1/\Sigma$ equals the contact resistance R_C. The non-equilibrium contribution to the junction resistance δR is given by [26, 27, 39, 41]

$$\delta R = \frac{R_N(P_\Sigma^2 R_C + P_{\sigma F}^2 R_F) + R_F R_C (P_{\sigma F} - P_\Sigma)^2}{R_F + R_C + R_N}. \tag{2.20}$$

In case of neglecting spin-flip scattering in the contact, δR is always larger than zero. Thus, a spin accumulation increases the junction resistance, while in the absence of a non-equilibrium spin distribution δR vanishes.

Conductivity mismatch

Considering an ohmic contact ($R_C \ll R_N,\ R_F$) between the ferromagnet and the NM region, the spin injection efficiency (Eq. 2.15) can be approximated by

$$P_j \approx \frac{R_F}{R_F + R_N} P_{\sigma F}. \tag{2.21}$$

For spin injection from a ferromagnetic metal into a metallic NM ($R_F \sim R_N$), $P_j \sim P_{\sigma F}$ can be sufficiently large. On the contrary, spin injection into semiconductors (SC), in which case $R_N \gg R_F$, yields a substantially suppressed injection efficiency $P_j \ll P_{\sigma F}$, which is commonly referred to as conductivity mismatch problem [38]. This conductivity mismatch problem can be resolved by implementing highly spin polarized half metallic ferromagnets, in which either $\sigma_{\uparrow F}$ or $\sigma_{\downarrow F}$ is very small, such that $R_F = L_{sF}\sigma_F/4\sigma_{\uparrow F}\sigma_{\downarrow F}$ is large [27, 41], or, which is the more common approach, by introducing a spin selective tunnel barrier with $R_C \gg R_F, R_N$ [26, 27, 37, 39–41, 44]. Thus, the spin injection efficiency is determined by P_Σ, even if $R_N \gg R_F$, such that

$$P_j = P_\Sigma. \tag{2.22}$$

Sharvin resistance

For spin injection into 1-dimensional NM channels, in which transport is ballistic, while interface scattering is considered to be still diffusive, an additional resistance, the so-called Sharvin resistance R_{sh}, has to be taken into account [27, 45–48]. It becomes relevant for NM channels with a width smaller than the corresponding electron mean free path and is given by

$$R_{sh} = \frac{2\pi h}{e^2 k_F^2 A}, \tag{2.23}$$

where A is the contact area, and k_F denotes the Fermi wave-vector. Taking into account the ballistic Sharvin resistance in the diffusive model modifies the electrical resistance of the channel, such that $\tilde{R} \to \tilde{R} + R_{sh}$ [45].

Electrical spin detection - Silsbee-Johnson spin charge coupling

Due to the coupling between spin and charge in the FM and the contact region ($P_\sigma \neq 0$), as described by Eq. 2.9, a spin accumulation in the NM gives rise to a charge current in the FM in case of a closed electric circuit, while for an open circuit an electromotive force (emf) builds up across the junction [26, 27, 33, 41, 42, 49]. This effect leads to the additional resistance contribution δR described

above (spin bottleneck). For the emf the following expression can be derived:

$$emf = -\frac{R_F P_{\sigma F} + R_C P_\Sigma}{R_F + R_C + R_N}\mu_{sN}(\infty) = -P_j \mu_{sN}(\infty). \tag{2.24}$$

The emf at a FM contact can be measured as a non-local voltage drop, thus providing an experimental access for probing the non-equilibrium spin accumulation in the NM channel. In combination with electrical spin injection, the non-local device geometry presented above (Fig. 2.2) can be realized. There, spins are injected through a FM-C-NM junction into the NM channel, diffuse in all directions, and can be detected as a non-local voltage at another FM-C-NM junction (detector). Following from Eq. 2.15, the observation of a large emf requires R_N to be smaller than R_C and R_F, similar to the requirement for obtaining a large injection efficiency P_j. The detection scheme for measuring the emf related voltage drop at the detecting FM junction was conceptually introduced by R. Silsbee [49] and later experimentally demonstrated by M. Johnson and R. Silsbee [42].

Experimental realization of spin injection

One of the first experiments successfully establishing electrical spin injection into a paramagnetic metal was published in 1985 by M. Johnson and R. Silsbee [42]. They introduced the non-local spin injection and detection scheme described above (Fig. 2.2), thus achieving spin injection into an aluminium channel with a spin injection efficiency of $P_j \approx 5\,\% - 8\,\%$ [42, 50]. Spin injection from a FM metal directly into a semiconductor (SC) 2DEG channel could be demonstrated in 1999 by P. Hammar et al. [51], yet only considerably low injection efficiencies on the order of $1\,\%$ were observed. Only after the conductivity mismatch problem was identified as the major obstacle for spin injection into SC structures, FM-SC structures with a tunnel barrier in between resulted in the observation of more efficient spin injection [9, 17]. In most publications reporting efficient electrical spin injection into SC structures, spin-LED heterostructures were implemented, which rely on the optical detection of the spin accumulation [52–63]. Fewer reports [9–17] present all-electrical FM-SC lateral devices, which allow electrical injection and detection as introduced by M. Johnson and R. Silsbee [42]. Fully SC-based lateral

device geometries could be experimentally realized by M. Ciorga et al. [18]. There, spin-polarized electrons are injected from the ferromagnetic SC (Ga,Mn)As, which is intrinsically p-doped, into an n-GaAs bulk channel. Spin injection is based on electrons tunneling through the depletion zone of a highly doped pn-junction, from the valence band of (Ga,Mn)As into the conduction band of GaAs. Subsequently, a similar spin injection structure could be established which allowed electrical spin injection into a GaAs/(Al,Ga)As 2DEG channel, yielding spin injection efficiencies of about $P_j \approx 75\,\%$ [19]. A similar heterostructure system with an (In,Ga)As QW channel is the basis of the experiments conducted within the scope of this thesis. The corresponding heterostructure layer sequence and the spin injection process are explained in detail in Chapter 3.

2.3 Spin orbit coupling

In a simplified picture, spin orbit coupling (SOC) can be regarded as an effective magnetic field, which can interact with the spin of a moving electron. This gives rise to spin precession, if the spin is not aligned with the SOC related effective magnetic field, which in turn leads to fundamental effects observed in spintronics, like spin relaxation phenomena for instance (Chapter 2.4). One of the most important properties of SOC with regard to spintronic applications is the possibility of tuning its strength by an external electric field. This allows externally manipulating the spin precession angle for instance, which is the basis for realizing the spin field effect transistor (spinFET) proposed by S. Datta and B. Das [8] (Chapter 2.5). In the following, the general concept of spin orbit coupling (SOC) is introduced, especially focusing on 2D semiconductor systems. There, depending on the origin of SOC two contributions are distinguished: a contribution arising from a bulk inversion asymmetry (BIA), and one that is due to a structural inversion asymmetry (SIA). Moreover, typical values of the SOC strength in (In,Ga)As and InAs heterostructures are summarized, and the effect of quasi-1-dimensional confinement on SOC is discussed. The following overview of spin orbit interaction in semiconductors is primarily based on the comprehensive review articles by J. Fabian et al. [26] and S. Ganichev et al. [64], while additional remarks and brief

summaries can be found in Refs. [65–67].

General aspects

An electron moving in an external electric field $\vec{E}$ with velocity $\vec{v}$ experiences an effective magnetic field

$$\vec{B}_{eff} = \frac{1}{c^2}\left(\vec{E} \times \vec{v}\right) = \frac{\hbar}{mc^2}\left(\vec{E} \times \vec{k}\right), \tag{2.25}$$

which can interact with its spin. This interaction between the spin and the effective magnetic field is commonly referred to as spin orbit coupling (SOC), or spin orbit interaction (SOI). In the most general form, the corresponding SOC contribution to the Hamiltonian is given by

$$H_{SO} = \frac{\hbar}{4m_0^2c^2}\,\vec{p}\cdot\left(\vec{\sigma} \times \vec{\nabla}V\right), \tag{2.26}$$

with $\vec{\sigma} = (\vec{\sigma}_x, \vec{\sigma}_y, \vec{\sigma}_z)$ being the vector containing the Pauli matrices, $\vec{p}$ is the kinetic momentum operator, and V the crystal potential, the gradient of which corresponds to the electric field $\vec{E} = -\vec{\nabla}V$. Depending on the origin of the electric field, two contributions to the SOC are generally distinguished in the solid state. One contribution arises from the absence of an inversion symmetry of the bulk crystal itself, which is the case for zinc-blende or wurtzite semiconductors for instance, and is commonly referred to as bulk inversion asymmetry (BIA), or Dresselhaus contribution [68]. The other one is due to the absence of an inversion symmetry of the confining potential in QW structures, the so-called structural inversion asymmetry (SIA), or Rashba contribution [69]. As a consequence of SOC, the energy bands for spin-up and spin-down split. Unlike Zeeman splitting in a magnetic field, however, which leads to a shift of the energy dispersion by a certain energy difference, the SOC related splitting results in a shift of the energy bands by a certain wave-vector.

Bulk inversion asymmetry in 2D systems (Dresselhaus)

Of particular interest, especially with regard to the heterostructure analyzed within the scope of this thesis, are 2-dimensional (001)-grown III-V zinc-blende systems with a confining potential along the growth direction (z-direction). Taking into account only bulk inversion asymmetry (BIA), the corresponding Hamiltonian is given by [65]:

$$\begin{aligned} H_D &= H_{D1} + H_{D3} \\ &= \underbrace{\beta_1 \left(k_x \vec{\sigma}_x - k_y \vec{\sigma}_y\right)}_{\text{linear}} + \underbrace{\gamma \left(k_x k_y^2 \vec{\sigma}_x - k_x^2 k_y \vec{\sigma}_y\right)}_{\text{cubic}}, \end{aligned} \tag{2.27}$$

for $x \parallel [100]$, $y \parallel [010]$, and $z \parallel [001]$. Note that it contains both a linear-in-k and a cubic contribution. The linear Dresselhaus parameter β_1 in the Hamiltonian is defined as [26, 70, 71]

$$\beta_1 = -\gamma \langle k_z^2 \rangle \propto -\gamma \left(\frac{\pi}{d}\right)^2, \tag{2.28}$$

with the bulk Dresselhaus parameter γ, and the expectation value of the squared wave-number in z-direction $\langle k_z^2 \rangle$, which is determined by the strength of the confinement of the electron wave-function in the quantum well (QW). In the limit of an infinite QW, β_1 can be approximated based on the QW thickness d. The Dresselhaus Hamiltonian can be conveniently rewritten by defining the angle θ between k-vector and x-axis ([100]), such that $k_x = k_F \cos(\theta)$ and $k_y = k_F \sin(\theta)$, which results in:

$$H_D = \beta \left(k_x \vec{\sigma}_x - k_y \vec{\sigma}_y\right) + \beta_3 k \left(\cos(3\theta)\vec{\sigma}_x + \sin(3\theta)\vec{\sigma}_y\right). \tag{2.29}$$

There, the cubic Dresselhaus parameter β_3 is introduced, which is given by

$$\beta_3 = -\gamma \frac{k_F^2}{4} = \frac{-\gamma \pi n_s}{2}. \tag{2.30}$$

Substituting the Fermi wave-vector $k_F = \sqrt{2\pi n_s}$ allows expressing β_3 in terms of the charge carrier density n_s. Usually, this cubic contribution is especially important for semiconductors with a narrow band-gap, or for highly doped quantum

wells (QWs), but it is also found to be the dominating contribution in wide QWs. Additionally, the parameter β is defined as

$$\beta = \beta_1 - \beta_3. \tag{2.31}$$

It is typically referred to as Dresselhaus parameter and should not be confused with the linear Dresselhaus parameter β_1. Comparing the Dresselhaus Hamiltonian to the Zeeman Hamiltonian $H_{SOC} = g\mu_B \left(\vec{\sigma} \cdot \vec{B}_{eff}(\vec{k})\right)$, allows defining an effective magnetic field $\vec{B}_{eff}$. For the Dresselhaus SOC this effective magnetic field contains linear and cubic contributions, and is given by [65]

$$\begin{aligned} \vec{B}_D &= \vec{B}_{D1} + \vec{B}_{D3} \\ &= \frac{2k}{g\mu_B} \begin{pmatrix} \beta\cos(\theta) \\ -\beta\sin(\theta) \end{pmatrix} + \frac{2k}{g\mu_B} \begin{pmatrix} \beta_3\cos(3\theta) \\ \beta_3\sin(3\theta) \end{pmatrix}, \end{aligned} \tag{2.32}$$

where μ_B is the Bohr magneton and g denotes the effective gyromagnetic factor (g-factor).

Structural inversion asymmetry in 2D systems (Rashba)

The so-called structural inversion asymmetry (SIA) or Rashba contribution to SOC was originally introduced by F. Ohkawa and Y. Uemura [72], who derived the spin splitting in 2D zinc-blende SC structures. The model was subsequently expanded and generalized by F. Vasko [73], and by Y. Bychkov and E. Rashba [69]. SIA originates from the absence of an inversion symmetry due to an asymmetric confining potential in QW structures. This contribution can be influenced by an asymmetric doping distribution or non-symmetric interfaces, for instance. A detailed discussion of the tunability of the Rashba SOC strength can be found in Chapter 2.5. The corresponding SIA Hamiltonian can be written as:

$$H_R = \alpha \left(\vec{\sigma}_x k_y - \vec{\sigma}_y k_x\right) = \alpha \left(\vec{\sigma} \times \vec{k}\right) \cdot \hat{z}, \tag{2.33}$$

with the Rasbha parameter α determining the strength of the Rashba SOC. The corresponding effective magnetic field is given by [65]

$$\vec{B}_R = \frac{2\alpha}{g\mu_B}\begin{pmatrix} k_y \\ -k_x \end{pmatrix} = \frac{2k}{g\mu_B}\begin{pmatrix} \alpha\sin(\theta) \\ -\alpha\cos(\theta) \end{pmatrix}. \tag{2.34}$$

There, θ is defined as the angle between the k-vector direction and the x-axis ([100]). Note that the direction of the Rashba spin orbit field (SO-field) is always oriented perpendicular to the k-vector, independent of the crystallographic orientation.

Interplay between Rashba and Dresselhaus SOC

In 2D heterostructures, typically both contributions have to be considered. Their interplay can be expressed as the sum of the Rashba (Eq. 2.33) and Dresselhaus Hamiltonian (Eq. 2.27):

$$H_{SO} = H_R + H_D. \tag{2.35}$$

Similarly, the total effective magnetic field is given by sum of the individual effective field contributions $\vec{B}_D$ (Eq. 2.32) and $\vec{B}_R$ (Eq. 2.34). For $x \parallel [100]$ and $y \parallel [010]$ this total SO-field is given by

$$\begin{aligned} \vec{B}_{SO} &= \vec{B}_R + \vec{B}_D \\ &= \frac{2k}{g\mu_B}\begin{pmatrix} \alpha\sin(\theta) + \beta\cos(\theta) + \beta_3\cos(3\theta) \\ -\alpha\cos(\theta) - \beta\sin(\theta) + \beta_3\sin(3\theta) \end{pmatrix}. \end{aligned} \tag{2.36}$$

For regarding the total SO-field along the [110] and [$\bar{1}$10] direction, it is most convenient to rotate the coordinate system, such that $x \parallel [110]$ and $y \parallel [\bar{1}10]$, which results in:

$$\vec{B}_{SO} = \frac{2k}{g\mu_B}\begin{pmatrix} (\alpha-\beta)\sin(\tilde{\theta}) - \beta_3\sin(3\tilde{\theta}) \\ -(\alpha+\beta)\cos(\tilde{\theta}) + \beta_3\cos(3\tilde{\theta}) \end{pmatrix}. \tag{2.37}$$

The angle $\tilde{\theta}$ is now the angle between the new x-axis ([110]) and the k-vector direction. The SO-fields for the main k-vector directions can then be easily calculated.

For $x \parallel [100]$ and $y \parallel [010]$ it thus follows:

$$\begin{aligned} B_{k\parallel[100]} &= \frac{2k}{g\mu_B}\begin{pmatrix}\beta+\beta_3\\-\alpha\end{pmatrix} \\ B_{k\parallel[010]} &= \frac{2k}{g\mu_B}\begin{pmatrix}\alpha\\-\beta-\beta_3\end{pmatrix}, \end{aligned} \tag{2.38}$$

while for $x \parallel [1\bar{1}0]$ and $y \parallel [110]$ the SO-fields are given by:

$$\begin{aligned} B_{k\parallel[110]} &= \frac{2k}{g\mu_B}\begin{pmatrix}-\alpha-\beta+\beta_3\\0\end{pmatrix} \\ B_{k\parallel[1\bar{1}0]} &= \frac{2k}{g\mu_B}\begin{pmatrix}0\\\alpha-\beta+\beta_3\end{pmatrix}. \end{aligned} \tag{2.39}$$

In Fig. 2.6 the individual SO-fields for the main k-vector orientations are shown. Note that the signs of the SO parameters are defined such that $\alpha > 0$, $\beta = \beta_1 - \beta_3 > 0$, $\beta_1 > 0$, and $\beta_3 > 0$, while $g < 0$. From this representation it is apparent that the effective Rashba field is always perpendicular to the k-vector direction, independent of the crystallographic orientation. The orientation of the

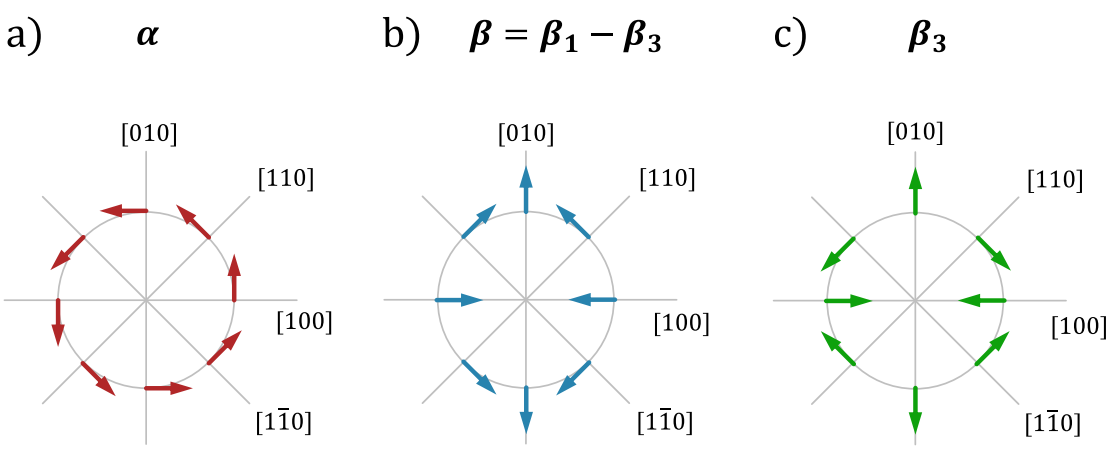

Figure 2.6. Orientation of the individual SO-fields for the main k-vector directions for Rashba SOC α (**a**), Dresselhaus contribution $\beta = \beta_1 - \beta_3$ (**b**), and cubic Dresselhaus parameter β_3 (**c**). In this representation $\alpha > 0$, $\beta = \beta_1 - \beta_3 > 0$, $\beta_1 > 0$, $\beta_3 > 0$, and $g < 0$. Adapted from [65].

linear and cubic Dresselhaus fields, on the other hand, strongly depends on the direction of the k-vector. This gives rise to an anisotropy of the total SO-field, the magnitude of which depends on the relative strength of the individual parameters. In the Dyakonov-Perel spin relaxation regime this leads to a dependence of the spin relaxation rates on the spin orientation, for instance (Chapter 2.4). Notably, the total SO-fields for $k \parallel [110]$ and $k \parallel [1\bar{1}0]$ are oriented perpendicular to the direction of the k-vector.

SOC strength in (In,Ga)As based QWs

The SOC parameters and the relative strengths of SIA and BIA depend strongly on the specific heterostructure, thus it is not possible to find generally valid values for α and β in literature. Especially the value of the Rashba parameter exhibits a significant dependence on the symmetry of the QW and can be tuned over a large range by means of an external gate electric field [22, 23, 74–76]. Thus, the following values have to be considered as rough approximations of the order of magnitude of the corresponding values. For (In,Ga)As structures with a low indium content of 10 %, similar to the heterostructure under investigation in this thesis, the values for α and β can be expected to lie in the low 10^{-13} eV m range [77, 78]. Consequently, both SIA and BIA have to be taken into account. More reports can be found on structures with higher indium contents above 50 %, and InAs QW heterostructures. With increasing indium content, the Rashba contribution typically dominates over the Dresselhaus related SOC. There, values for α lie in the 10^{-12} eV m range for $In_{0.53}Ga_{0.47}As$ QWs [79–81], as well as for InAs QWs [82–84].

SOC in quasi-1D systems

The SOC related properties of a quasi-1-dimensional channel can be examined by introducing an additional in-plane confining potential $V(x)$. This leads to a coupling between the quantum wire subbands [85–89], the relevance of which can be estimated by the parameter s:

$$s \approx \frac{w}{L_{SO}}, \tag{2.40}$$

where w denotes the width of the wire and $L_{SO} = \hbar^2 / (2\, SOC\, m^*)$ is the spin precession length with the SOC strength SOC [8, 90]. In case of a weak SOC ($w \ll L_{SO}$) the subband coupling contribution is small and the energy dispersion is still parabolic. Similar to the 2-dimensional case, the presence of SOC leads to a spin splitting of the energy bands in k-direction. For large SOC strengths ($w \gtrsim L_{SO}$), on the other hand, the energy dispersion becomes strongly non-parabolic, which requires taking into account changes of the SOC strengths due to the coupling between neighboring subbands. This can result in crossings of energy bands even at low energies, thus implying non-trivial alterations of spin precession and spin transport patterns [85–89]. In case of the (In,Ga)As QW structures examined within this thesis, the SOC strength can be assumed to lie in the low 10^{-13}eV m range and $m^* \approx 0.0625\, m_0$, so that the spin precession length $L_{SO} \approx 6\,\mu\text{m}$ largely exceeds the width of the narrowest channel ($w = 400\,\text{nm}$), i.e. the coupling parameter s is small ($s \ll 1$). Thus, effects of spatial confinement on SOC can be neglected in this case.

2.4 Spin relaxation

2.4.1 Spin relaxation mechanisms in semiconductors

In general, spin relaxation describes the decay of the non-equilibrium spin polarization. For conduction electrons in semiconductors four major spin relaxation mechanisms can be identified: Elliott-Yafet, Dyakonov-Perel (DP), and Bir-Aronov-Pikus mechanism, as well as spin relaxation due to hyperfine interaction with nuclear spins. The fundamental concepts and theoretical consideration are comprehensively presented by J. Fabian et al. [26, 91], I. Žutić et al. [27], and M. Wu et al. [92], while an additional brief summary is provided by M. Dyakonov [93]. The suppression of spin relaxation in narrow conductive channels approaching the quasi-1-dimensional limit is discussed in Chapter 2.4.2.

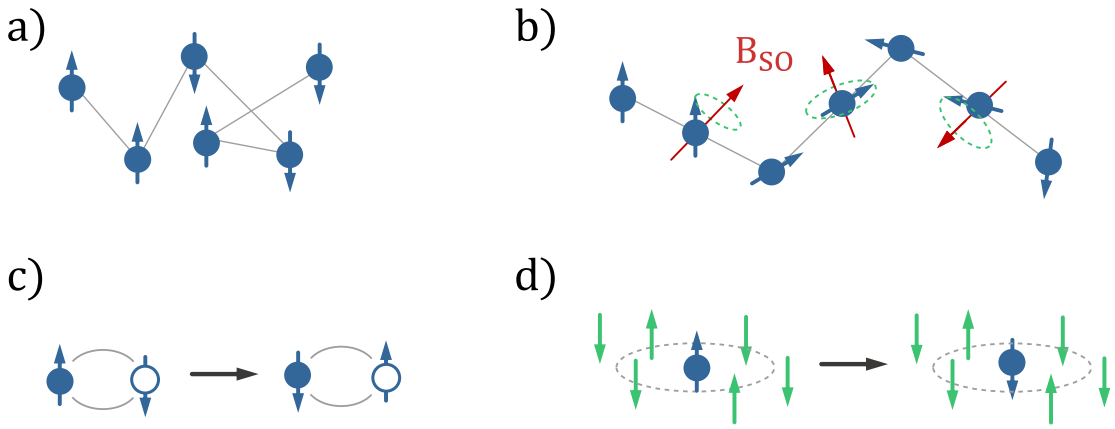

Figure 2.7. Simplified illustration of the basic spin relaxation mechanisms in semiconductors. In case of the Elliott-Yafet mechanism (**a**), spin flip events at momentum scattering sites lead to spin relaxation, while for the Dyakonov-Perel mechanism (**b**) spin relaxation is due to spin precession around the k-vector dependent SO-field. Bir-Aronov-Pikus spin relaxation (**c**) is a result of the electron-hole exchange coupling. Spin relaxation can also be due to localized electrons interacting with the spin of the lattice nuclei (**d**). Adapted from [26, 91].

Elliott-Yafet

In the presence of SOC the Bloch states are no longer spin eigenstates, instead the eigenstates consist of a mixture of spin-up and spin-down states. In combination with momentum scattering, this coupling between spin-up and spin-down states gives rise to spin relaxation. This contribution to spin relaxation was introduced by R. Elliott [94]. Momentum scattering events are typically induced by impurities, which are dominating at low temperatures, and phonons, which are relevant at higher temperatures. An additional momentum scattering related contribution to spin relaxation occurs, if the impurity, which gives rise to the momentum scattering event, induces a SOC potential. This gives rise to a certain spin flip probability at each scattering site, which ultimately leads to spin relaxation (Fig. 2.7a). Spin flip scattering can also be introduced by phonons, which modulate the SOC potential of the lattice-ions. This phonon induced effect was first taken into account by A. Overhauser [95] and later applied to band-structure systems by Y. Yafet [96]. Typically, the Elliott-Yafet spin relaxation is particularly relevant for small band gap semiconductors with large SOC strengths, like

InSb [27].

Bir-Aronov-Pikus

Bir-Aronov-Pikus spin relaxation [97] is based on the electron-hole exchange interaction, such that a spin-up electron, for instance, can exchange its spin with a spin-down hole (Fig. 2.7c). Due to the strong SOC induced spin mixing in the valence band, spin relaxation for holes is fast, so that the electron spin polarization is lost to quickly decaying holes. This mechanism is found to be the most relevant in p-doped semiconductors.

Dyakonov-Perel

SOC can be regarded as an effective k-vector dependent magnetic field $\vec{B}_{eff}(\vec{k})$, which gives rise to spin precession with the Larmor frequency

$$\vec{\Omega}(\vec{k}) = \frac{ge}{2m^*}\,\vec{B}_{eff}(\vec{k}). \tag{2.41}$$

Strength and orientation of $\vec{B}_{eff}(\vec{k})$ vary with the direction of the electron's momentum vector $\vec{k}$, which, in the diffusive transport regime, randomly changes due to momentum scattering events. This, in turn, leads to a random variation of both the precession axis, as well as the precession frequency, which results in a randomization of the initial spin orientation. This spin relaxation process is referred to as Dyakonov-Perel (DP) mechanism [93], and is schematically illustrated in Fig. 2.7b. Within the DP regime, two limiting cases are generally distinguished [27, 92, 93]. If the spin undergoes many rotations in between two momentum scattering events, such that the product of averaged precession frequency $\langle\vec{\Omega}\rangle$ and momentum relaxation time τ_p is large ($\langle\vec{\Omega}\rangle\tau_p \gtrsim 1$), the spin relaxation time τ_s is proportional to the momentum relaxation time τ_p ($\tau_s \propto \tau_p$). In the other limiting case, which is the usual definition of the DP regime, the precession angle in between two scattering events is small ($\langle\vec{\Omega}\rangle\tau_p \ll 1$), i.e. the collision rate $1/\tau_p$ is large compared to $\langle\vec{\Omega}\rangle$. In this regime the spin orientation dependent spin relaxation times $\tau_{s,i}$ ($i = x, y, z$)

are given by [26, 27, 92]

$$\frac{1}{\tau_{s,i}} = \gamma_l^{-1} \left(\overline{\Omega^2} - \overline{\Omega_i^2} \right) \tau_p, \tag{2.42}$$

where the average is taken over all directions of $\vec{k}$, and $\vec{\Omega}_i$ corresponds to the precession frequency, which is due to the SO-field oriented parallel to the considered spin orientation. The parameter γ_l is defined as $\gamma_l = \tau_p/\tilde{\tau}_l$, with the effective momentum scattering time $\tilde{\tau}_l$, where l is the order of $\vec{k}$ in $\vec{\Omega}(\vec{k})$. For linear-in-k SOC terms ($l = 1$) τ_l is equal to the momentum scattering time τ_p, such that $\gamma_1 = 1$, while in general $\gamma_l > 1$ for $l > 1$ [27]. Regarding the Dresselhaus related cubic SOC terms, the parameter γ_3 becomes important. Its value depends on the dominating scattering mechanism. Considering DP spin relaxation in bulk III-V semiconductors, $\gamma_3 \approx 6$ for impurity dominated scattering for instance [27]. Setting $\gamma_l = 1$ can be considered a lower bound for the spin relaxation time. The equation for $\tau_{s,i}$ (Eq. 2.42) implies that an increased momentum scattering leads to a longer spin lifetime, which is referred to as motional narrowing. Additionally, according to this equation, the spin relaxation rates $1/\tau_{s,i}$ are linked to the SO-field. For a QW grown along the z-direction [001], with $x \parallel [1\bar{1}0]$, and $y \parallel [110]$, the corresponding spin relaxation rates can thus be expressed as a function of the SOC parameters [98–100]:

$$\begin{aligned}
\frac{1}{\tau_x} &= \frac{4Dm^{*2}}{\hbar^4} \left[\frac{\tau_1}{\tau_p} \left(\alpha - (\beta_1 - \beta_3) \right)^2 + \frac{\tau_3}{\tau_p} \beta_3^2 \right] \\
\frac{1}{\tau_y} &= \frac{4Dm^{*2}}{\hbar^4} \left[\frac{\tau_1}{\tau_p} \left(\alpha + (\beta_1 - \beta_3) \right)^2 + \frac{\tau_3}{\tau_p} \beta_3^2 \right] \\
\frac{1}{\tau_z} &= \frac{8Dm^{*2}}{\hbar^4} \left[\frac{\tau_1}{\tau_p} \alpha^2 + \frac{\tau_1}{\tau_p} \left(\beta_1 - \beta_3 \right)^2 + \frac{\tau_3}{\tau_p} \beta_3^2 \right].
\end{aligned} \tag{2.43}$$

If either BIA ($\beta \equiv \beta_1 - \beta_3$) or SIA ($\alpha$) dominates, in-plane spin relaxation is isotropic, with

$$\frac{1}{\tau_x} = \frac{1}{\tau_y} = \frac{1}{2\,\tau_z}. \tag{2.44}$$

In case of Dresselhaus and Rashba contribution being similar in strength, on the other hand, the spin relaxation of spins oriented in-plane can become strongly anisotropic. In this case, τ_x can get significantly larger compared to τ_y, or vice

versa. This is especially relevant for asymmetric (In,Ga)As QW structures with low indium contents, in which case both SOC contributions are found to be of a similar order of magnitude [77, 78]. An additional remark concerns the importance of the cubic Dresselhaus coefficient β_3, or the parameter $\gamma_3^{-1} = \tau_3/\tau_p$ respectively. If the corresponding term in Eq. 2.43, i.e. $(\tau_3/\tau_p)\,\beta_3^2$, becomes dominating, the isotropy of spin relaxation is restored. The spin relaxation anisotropy can be quantified by introducing the parameter k, which is defined as the ratio of τ_x to τ_y:

$$k \equiv \frac{\tau_x}{\tau_y} = \frac{\left(\alpha + (\beta_1 - \beta_3)\right)^2 + \frac{\tau_3}{\tau_1}\beta_3^2}{\left(\alpha - (\beta_1 - \beta_3)\right)^2 + \frac{\tau_3}{\tau_1}\beta_3^2}, \tag{2.45}$$

where $\tau_1 = \tau_p$. In the DP regime the spin relaxation anisotropy k is thus determined by the SOC components.

Hyperfine interaction

The interaction between electron spin and the disordered effective magnetic field, which originates from the spin of the lattice nuclei, results in an additional contribution to spin relaxation. It is relevant for localized electrons, for example in quantum dots, while for higher-dimensional systems the effect on spin relaxation is typically negligible, as the spatially extended electron states experience only the vanishing average effective magnetic field of the nuclei.

2.4.2 Suppression of spin relaxation in the quasi-1D limit

The main source of spin relaxation in III-V semiconductor heterostructures is the DP mechanism. In general, momentum scattering events result in a randomization of the electron's direction of motion. In the presence of a $\vec{k}$ dependent effective spin orbit field (SO-field), which induces spin precession, this leads to a randomization of the spin orientation, thus giving rise to spin relaxation. The DP spin relaxation in 2D structures can be strongly suppressed by introducing a lateral confinement, such that the electron's motion is restricted to a narrow transport channel [101–105]. As the motion perpendicular to the channel orientation is limited, there is only a single precession axis in the 1-dimensional limit.

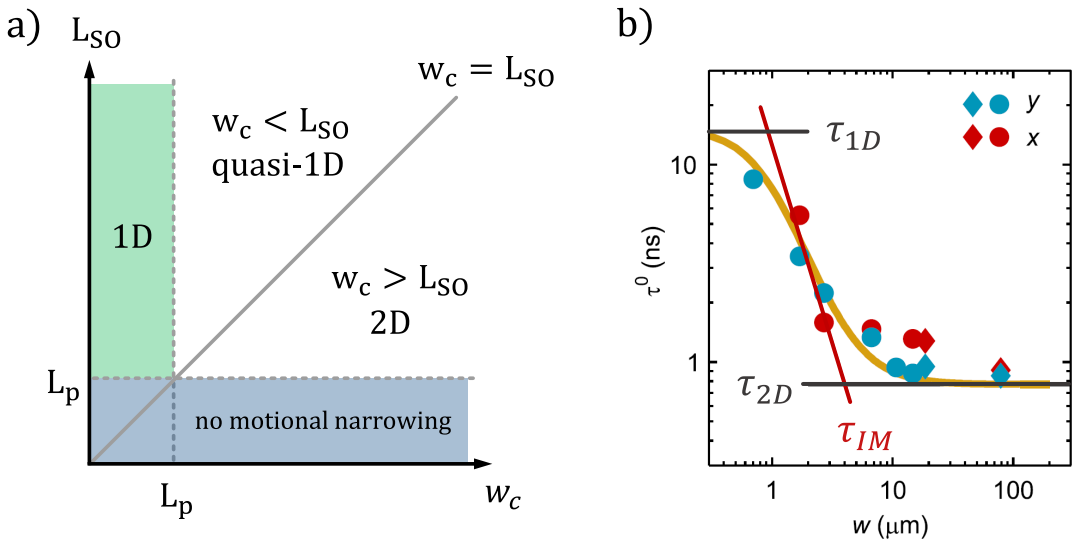

Figure 2.8. (**a**) Categorization of different spin relaxation regimes, characterized by the channel width w_c and the spin precession length L_{SO}. Adapted from [101]. (**b**) Experimentally determined spin relaxation time in dependence of the channel width by P. Altmann et al. [102], showing the $1/w_c^2$ dependence of $\tau_s \equiv \tau^0$ in the intermediate regime between 2D and 1D spin transport (τ_{IM}). Adapted from [102].

Thus, spin relaxation due to randomly changing precession angles and frequencies is suppressed. The effect of confinement on the spin transport characteristics can be categorized by regarding the ratio of channel width w_c and spin precession length $L_{SO} = 2m^* SOC/\hbar^2$, as sketched in Fig. 2.8a. For a mean free path L_p larger than the spin precession length ($L_p \geq L_{SO}$) the accumulated precession angle between two momentum scattering events is large, which gives rise to a fast decay of the initial spin polarization (no motional narrowing). In this case, the spin relaxation time τ_s is determined by the momentum relaxation time τ_p, such that $\tau_s \propto \tau_p$. In the regime of motional narrowing, on the other hand, the precession angle in between two subsequent scattering events is small, and $L_p < L_{SO}$. In this case, as described in the previous section, the DP spin relaxation time in the 2D case ($w_c > L_{SO}$) is inversely proportional to the momentum scattering time ($\tau_s \propto 1/\tau_p$). Within the motional narrowing regime spin transport is quasi-1-dimensional for a channel width w_c smaller than L_{SO}, yet larger than the mean free path L_p ($L_p < w_c < L_{SO}$). The 1-dimensional limit is reached for a channel

width smaller than the mean free path ($w_c < L_p$). In this case, the linear-in-k contributions of the SOC are suppressed, yet the cubic Dresselhaus term yields a finite value for the spin relaxation time, which, for out-of-plane oriented spins, is then given by

$$\frac{1}{\tau_{1D}} = \frac{6Dm^{*2}}{\hbar^4}\,\beta_3^2, \tag{2.46}$$

with the cubic Dresselhaus parameter $\beta_3 = -\gamma\pi n_s/2$. In the intermediate regime between the 2-dimensional case and the 1D limit, the spin relaxation time is found to be inversely proportional to the squared channel width w_c:

$$\tau_{IM} \propto \frac{1}{w_c^2}. \tag{2.47}$$

The increase of the spin relaxation time with decreasing channel width is experimentally confirmed by a number of reports for out-of-plane oriented spins in optical [102, 106, 107], and weak antilocalization measurements [90, 108]. In Fig. 2.8b the experimental results of P. Altmann et al. [102] visualize the increase of τ_s with decreasing channel width w_c in the regime between the 2D case and the 1-dimensional limit. In this intermediate regime, the spin relaxation time is expected to satisfy Eq. 2.47. Within this thesis, the dependence of spin relaxation on the channel width is investigated experimentally for an (In,Ga)As QW structure (Chapter 4.1).

2.5 Gate induced spin precession (spinFET)

The main focus of this thesis is the experimental realization of spin injection devices which allow tuning the SOC strength by an external gate voltage V_g, thus giving rise to spin precession related phenomena. In the following, a brief summary of the gate tunability of the Rashba parameter, the most common spin field effect transistor (spinFET) proposal introduced by S. Datta and B. Das [8], as well as experimental works on this topic are presented. It is important to keep in mind, however, that the Rashba parameter α is not the only gate tunable parameter in the experimentally investigated (In,Ga)As 2DEG structures. Instead, applying a gate voltage can also affect the charge carrier density n_s, which gives rise to a gate

dependence of the cubic Dresselhaus contribution $\beta_3 \propto n_s$. This is discussed in detail in the experimental part of this thesis (Chapter 4.3).

Gate tunability of Rashba SOC

The strength of the SIA in heterostructure systems consists of several main contributions and can be qualitatively described as [74]:

$$\alpha \propto \underbrace{a\langle E_A \rangle}_{\text{SOC from QW}} + \underbrace{b\left(\langle E_{B,u} \rangle + \langle E_{B,l} \rangle\right)}_{\text{barrier leakage}} - \underbrace{c\left(|\Psi_u|^2 - |\Psi_l|^2\right)}_{\text{interface term}}, \tag{2.48}$$

where $\langle E_A \rangle$ is the average electric field in the QW, $\langle E_{B,u} \rangle$ and $\langle E_{B,l} \rangle$ are the corresponding electric field values in the upper and lower barrier of the QW, while $|\Psi_u|^2$ and $|\Psi_l|^2$ refer to the electron probabilities at the upper and lower barrier of the QW. The first term describes a linear dependence of α on the average electric field $\langle E_A \rangle$ in the quantum well [8, 71, 74, 75, 79, 109–113]. The electric field in the QW additionally affects the charge carrier density n_s, which, in turn, self-consistently influences $E \propto n_s$ [75, 114]. Thus, α is typically, yet not necessarily, found to be a linear function of n_s [71, 111–113, 115, 116], which is also confirmed by experimental works [71, 111, 115]. An additional contribution arises from the electron wave-function penetrating the barrier of the potential well (barrier leakage), which leads to an increase of the spin splitting [71, 74, 75]. The third considered contribution originates from an abrupt potential change at the heterojunction interfaces [71, 74]. Taking into account different electron probabilities at both sides of the QW adds an additional term to the Rashba parameter, which in general also increases the magnitude of α.

Applying an external electric field allows tuning α by directly affecting the electric field in the QW and/or the corresponding charge carrier density n_s, or by altering the potential profile of the QW, which gives rise to a shift of the electron probability function [23, 71, 74, 76, 79, 104, 115]. Thus, the term describing the penetration of the wave-function into the barrier, as well as the interface contribution can be functions of the gate voltage. A further modification of the Rashba parameter is found to be due to electron-electron interactions, which additionally

increase α [116, 117]. As the strength of the Coulomb interaction increases for decreasing electron density n_s, electron-electron interaction can also be gate dependent. Hence, also the corresponding contribution of α can be a function of V_g. It has to be emphasized that α is not the only SOC contribution that is tunable by a gate voltage, however. Instead, the total SOC also contains the linear and cubic Dresselhaus contributions β_1 and β_3. The latter is dependent on the charge carrier density n_s ($\beta_3 \propto \gamma n_s$). Hence, in systems in which n_s changes with V_g, also β_3 is a function of V_g.

SpinFET functionality

A well-known concept of a spin field effect transistor (spinFET) was introduced by S. Datta and B. Das [8], who proposed a gated device in which unidirectional, ballistic spin transport takes place between an injecting and a detecting spin polarized contact (Fig. 2.9a). Applying a gate voltage allows tuning the Rashba SOC contribution α, which gives rise to a gate dependent spin precession frequency. Thus, depending on the gate voltage, the angle at which the spins arrive at the detector changes, which gives rise to an oscillating voltage signal V_{nl} (Fig. 2.9b). Note that in the original spinFET proposal a local device setup is considered, i.e. the charge current is passed directly between the two spin polarized contacts. However, the concept can be directly transferred to the non-local device configuration, as shown in Fig. 2.9a.

Taking into account only the Rashba contribution to SOC implies that the effective SO-field is always perpendicular to the k-vector. This SO-field gives rise to spin precession, if the injected spin has a component which is perpendicular to this field, i.e. parallel to the orientation of the channel. The strength of the Rashba SO-field is determined by the Rashba parameter $\alpha(V_g)$ [22, 23, 76]:

$$B_R = \frac{2k_F}{g\mu_B}\,\alpha(V_g), \tag{2.49}$$

and is thus tunable by an external gate voltage V_g. Note that in this simplified case, only the Rashba contribution is taken into account. In general, however, the effective SO-field also contains the linear and cubic Dresselhaus parameter,

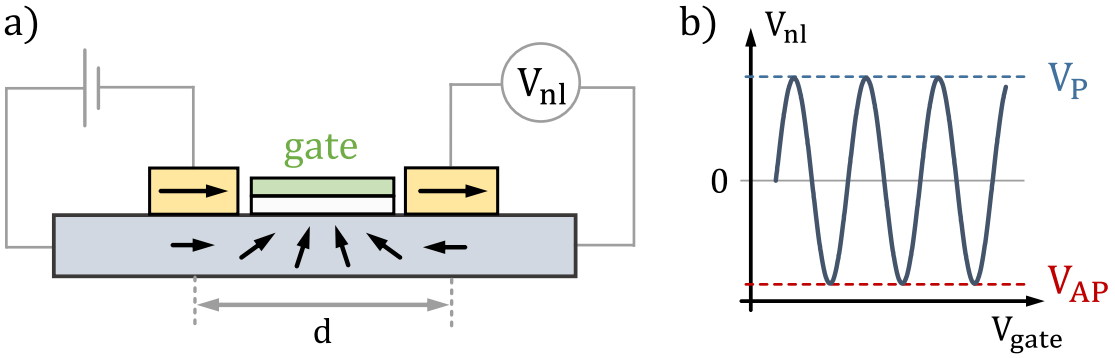

Figure 2.9. (**a**) Spin transistor concept similar to the one introduced by S. Datta and B. Das [8]. (**b**) Gate dependent oscillatory non-local spin signal V_{nl}. Adapted from [23].

according to Eq. 2.36 in Chapter 2.3. The gate tunability of the SO-field gives rise to a gate dependent spin precession angle Θ:

$$\Theta = \frac{2m^* d}{\hbar^2}\alpha(V_g), \tag{2.50}$$

where d is the distance between injecting and detecting contact. Thus, depending on the applied gate voltage, the precession angle of the spins arriving at the position of the detector can be manipulated. Consequently, the orientation of the spins underneath the detector relative to the magnetization of the detecting contact changes as a function of V_g, which gives rise to an oscillating voltage signal:

$$V_{det} = A\cos\left(\frac{2m^* d}{\hbar^2}\,\alpha(V_g)\right) = A\cos\left(\Theta\right). \tag{2.51}$$

This signal oscillates between the level at which the orientation of the detected spin is parallel (P) to the magnetization of the detector, and the antiparallel level (AP), as shown in Fig. 2.9b. The amplitude A of the oscillation corresponds to the spin accumulation in the channel and is thus given by [118]

$$A = \frac{P_{inj}P_{det}I_{inj}R_s\lambda_s}{2w_c}, \tag{2.52}$$

with the injecting and detecting efficiency P_{inj} and P_{det}, the injection current I_{inj},

sheet resistance R_s of the channel, and the channel width w_c. There, spin transport is assumed to be ballistic, which can be experimentally realized by choosing an injector-detector distance smaller than the corresponding mean free path [22–25, 113]. Alternatively, the channel width can be reduced (lateral confinement), such that the mean free path increases [117, 119, 120].

In case of a 2D channel, scattering events at lattice imperfections lead to random changes of the electron wave-vector. Depending on the direction of motion, the strength of the effective magnetic field a spin experiences differs. Thus, depending on the path an electron takes, the precession angle at the detector varies for different electrons, resulting in spin relaxation (Dyakonov-Perel mechanism, Chapter 2.4.1). In this context, A. Bournel et al. [104] derived from Monte-Carlo transport simulations that oscillating spin precession signals are also observable in 2D channels, yet significantly suppressed due to spin relaxation (Fig. 2.10). Decreasing the width of the channel consequently leads to the 2D signal approaching the oscillating signal of the 1D case. Other theoretical publications also confirm SOC related conductance oscillations in 2D systems [105, 121, 122].

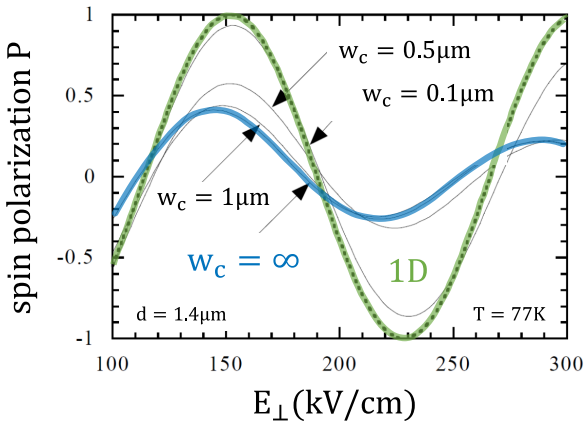

Figure 2.10. Simulated spin signal in dependence of an external electric field for different channel widths w_c, in a device similar to the spinFET setup shown in Fig. 2.9. Oscillations are observable not only in the ballistic 1-dimensional case (green, dashed line), but also for 2D channels (solid lines). Adapted from [104].

A. Zainuddin et al. [123] extended the 1-dimensional spin precession equation (Eq. 2.51) to the 2-dimensional case, whereby spin transport is still assumed to be ballistic. One of the major differences is the dependence of the oscillation amplitude on the precession frequency, so that the amplitude becomes gate dependent ($A \rightarrow A(V_g)$). Additional differences compared to the 1-dimensional case are due

to the spatial extent of the injecting and detecting contact along the channel, for instance. A finite extent of the contacts gives rise to a variation of the electron's path length depending on the injection and detection point, thus resulting in a spread of precession angles for different electrons. This gives rise to an additional phase shift of the oscillatory signal, but also reduces the oscillation amplitude. Additionally, oscillation frequency and amplitude can be affected due to a variation of the SOC strength underneath the contacts. This can be caused by the metallic contacts screening the effect of the gate underneath, or by affecting the SOC strength due to the local magnetic field of the ferromagnetic contact material.

Experimental demonstration of gate-induced spin precession

The tunability of the SOC strength by a gate voltage has been confirmed in numerous reports for various heterosturcture systems [20, 22, 23, 71, 74–76, 79, 111, 115], while the experimental demonstration of gate induced spin precession is more challenging. A collaboration of several research groups successfully established gate control of spin precession in InAs QW structures in a number of connected publications [20–25]. In one of the earlier reports [23] a device is presented in which spins are injected electrically into an InAs 2DEG channel via a $Ni_{81}Fe_{19}$ ferromagnetic electrode. The non-local voltage is measured at the FM detector, while a gate electrode allows modulating the Rashba SOC contribution. The distance between injector and detector is chosen smaller than, or comparable to the corresponding mean free path, which justifies claims of operating in a quasi-ballistic transport regime. Analyzing the beating pattern in the Shubnikov–de Haas oscillations allowed confirming the gate tunability of α for a constant electron density n_s [71, 74, 124, 125]. The corresponding gate dependent values of α and n_s are shown in Fig. 2.11b. It has to be remarked that for the spin precession measurements an external magnetic field of about 0.5 T is necessary in order to overcome the shape anisotropy of the FM, and magnetize the contacts along the orientation of the channel. Thus, also the orientation of the injected spins is set perpendicular to the effective SO-field and spin precession is induced. The gate dependent non-local voltage signals are presented in Fig. 2.11a for two different injector-detector distances, which both show an oscillating behav-

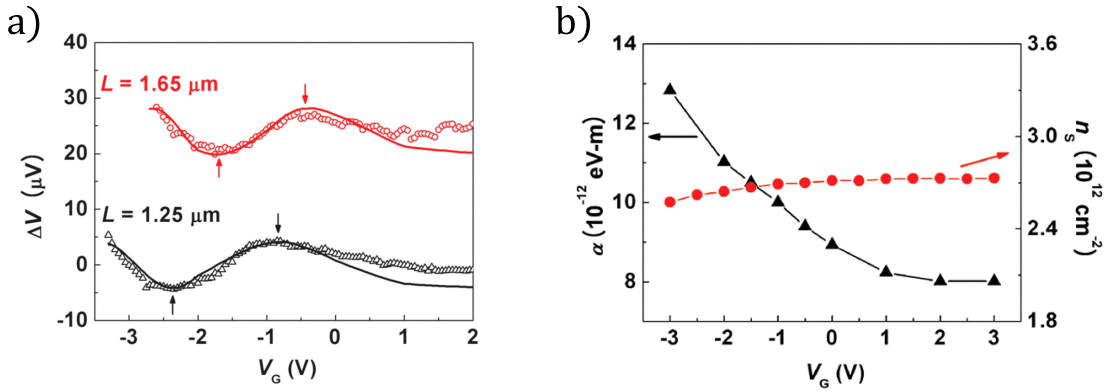

Figure 2.11. (**a**) Experimentally observed gate dependent spin signal oscillations by H. Koo et al. [23]. The device geometry is similar to the one shown in Fig. 2.9a. (**b**) The corresponding gate dependence of α and n_s, which confirms the tunability of α, while n_s hardly depends on V_g. From [23].

ior. The signal is modeled by a simple cosine function with a SOC related period and a phenomenological phase shift (Eq. 2.51), which only roughly resembles the measurement, however. In subsequent publications involving contributing authors of Ref. [23], spin precession measurements were performed on similar InAs QW structures, confirming previous results [20–22]. Later, special ferromagnetic material combinations were implemented, which allowed a stable magnetization of the contacts perpendicular to the orientation of the channel, thus enabling spin precession experiments without having to apply an external magnetic field [24, 25]. Even basic logic operations could be realized [25].

2.6 Spin diffusion equation with spin orbit coupling

In the following, an extended version of the spin diffusion equation (Eq. 2.2 in Chapter 2.1) is presented, which additionally takes into account SOC. This extended model is provided by J. Fabian [126], and is solved numerically in order to obtain the spatial profile of the spin signal in the presence of SOC. For that purpose the software tool COMSOL is implemented, which solves the system of partial differential equations (PDE) numerically for a specific device geometry, based on a finite element approach. Compared to other software environments,

the advantage of COMSOL lies in the convenient implementation of a least-squares optimizer, which allows fitting the obtained solution of the PDE to experimental data.

Expanded diffusion equation with SOC

The spatial and temporal evolution of the diffusively spreading spin density $s = (n_\uparrow - n_\downarrow)$ in the presence of an external magnetic field $\vec{B}$ can be derived from a random walk approach, which results in the spin drift-diffusion equation [26]:

$$\frac{\partial \vec{s}}{\partial t} = D\,\Delta\vec{s} + \vec{\omega}_0 \times \vec{s} - \frac{\vec{s}}{\tau_s}, \tag{2.53}$$

with the diffusion constant D, spin relaxation time τ_s, and Larmor frequency $\vec{\omega}_0 = \gamma\vec{B}$, where γ denotes the gyromagnetic ratio. In order to introduce SOC to the spin diffusion equation, the random walk derivation has to be expanded, i.e. spin precession due to SOC has to be additionally taken into account [126]. As shown in Fig. 2.12a, electrons at position (x, y) can move there either from $(x \pm a, y)$ or $(x, y \pm a)$. Orientation and magnitude of the effective SO-field depend on the direction of the electron motion, such that the electron spin is exposed to different precession angles and frequencies. Note that in case of an external magnetic

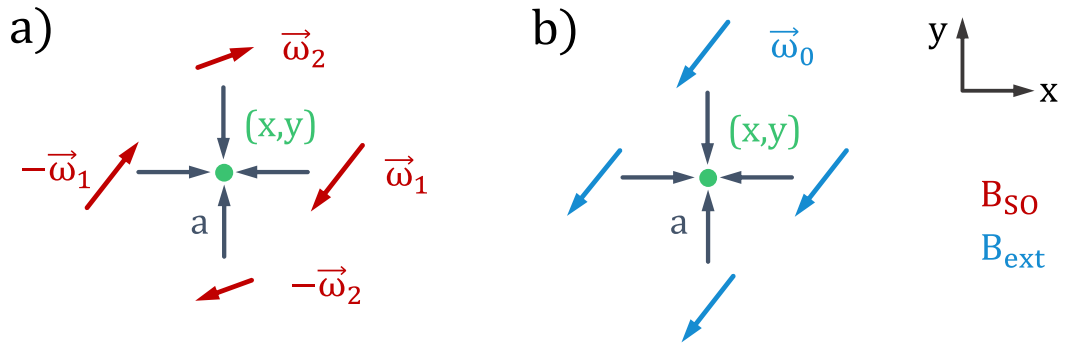

Figure 2.12. Illustration of the random walk approach: electrons at position (x, y) can move there either from $(x \pm a, y)$ or $(x, y \pm a)$. In the presence of a SO-field spin precession is induced, whereby precession angle and frequency $(\vec{\omega}_{1/2})$ depend on the k-vector direction (**a**). For an actual external magnetic field $\vec{B}_{ext}$, $\vec{\omega}$ does not depend on $\vec{k}$ (**b**). Adapted from [126].

field, precession frequency and precession angle do not depend on the direction of motion (Fig. 2.12b). Taking into account the direction-of-motion dependent spin precession frequencies $\vec{\omega}_1$ and $\vec{\omega}_2$ in the random walk approach yields an expanded form of the spin diffusion equation, which includes SOC [126]:

$$\frac{\partial \vec{s}}{\partial t} = D\,\Delta\vec{s} - \underbrace{\left(\frac{a}{2}\vec{\omega}_1 \times \frac{\partial \vec{s}}{\partial x} + \frac{a}{2}\vec{\omega}_2 \times \frac{\partial \vec{s}}{\partial y}\right)}_{\text{SOC}} + \vec{\omega}_0 \times \vec{s} - \frac{\vec{s}}{\tau_s}. \tag{2.54}$$

Based on the relations of the effective SO-field in Chapter 2.3 (Eq. 2.37), the precession frequencies for $x \parallel [1\bar{1}0]$ and $y \parallel [110]$ are given by

$$\begin{aligned} \vec{\omega}_1 &= \frac{\alpha - \beta + \beta_3}{\hbar}\, k_F \hat{y} \\ \vec{\omega}_2 &= \frac{-\alpha - \beta + \beta_3}{\hbar}\, k_F \hat{x}, \end{aligned} \tag{2.55}$$

while the step length a of the random walk is related to the mean free path L_p:

$$a = \sqrt{2}\, L_p. \tag{2.56}$$

Implementation in COMSOL

Implementation of the expanded spin diffusion equation (Eq. 2.54) requires introducing SOC and an external magnetic field $\vec{B}_{ext} = (B_x, B_y, B_z)^T$ to the partial differential equation module in the COMSOL model, which has the following general form:

$$e_a \frac{\partial^2 \boldsymbol{u}}{\partial t^2} + d_a \frac{\partial \boldsymbol{u}}{\partial t} + \nabla \cdot (-\tilde{c}\nabla \boldsymbol{u} - \tilde{\alpha}\boldsymbol{u} + \gamma) + \tilde{\beta} \cdot \nabla \boldsymbol{u} + \tilde{a}\boldsymbol{u} = f, \tag{2.57}$$

with the vector of the spin components $\boldsymbol{u} = (s_x, s_y, s_z)^T$, which corresponds to $\vec{s}$, and the vector containing the partial derivatives $\nabla = (\partial_x, \partial_y)$. Comparison to Eq. 2.54 allows reducing this equation to:

$$d_a \frac{\partial \boldsymbol{u}}{\partial t} = \nabla \cdot (\tilde{c}\nabla \boldsymbol{u}) - \tilde{\beta} \cdot \nabla \boldsymbol{u} - \tilde{a}\boldsymbol{u}, \tag{2.58}$$

with $d_a = I_3$ being the 3×3 unit matrix. The matrix $\tilde{c}$ contains the diffusion constant D, whereby diffusion is assumed to be isotropic:

$$\tilde{c} = \begin{pmatrix} D & 0 & 0 \\ 0 & D & 0 \\ 0 & 0 & D \end{pmatrix}, \tag{2.59}$$

while the SOC is introduced to the model via $\tilde{\beta}$:

$$\tilde{\beta} = -\begin{pmatrix} \begin{pmatrix} 0 \\ 0 \end{pmatrix} & \begin{pmatrix} 0 \\ 0 \end{pmatrix} & \begin{pmatrix} -\frac{a}{2}\omega_1 \\ 0 \end{pmatrix} \\ \begin{pmatrix} 0 \\ 0 \end{pmatrix} & \begin{pmatrix} 0 \\ 0 \end{pmatrix} & \begin{pmatrix} 0 \\ -\frac{a}{2}\omega_2 \end{pmatrix} \\ \begin{pmatrix} \frac{a}{2}\omega_1 \\ 0 \end{pmatrix} & \begin{pmatrix} 0 \\ \frac{a}{2}\omega_2 \end{pmatrix} & \begin{pmatrix} 0 \\ 0 \end{pmatrix} \end{pmatrix}. \tag{2.60}$$

There, for $x \parallel [1\bar{1}0]$ and $y \parallel [110]$, the components can be expressed in terms of the SOC parameters α, $\beta \equiv \beta_1 - \beta_3$, and β_3:

$$\begin{aligned} \frac{a}{2}\omega_1 &= \frac{\sqrt{2}k_F L_p}{2\hbar}(\alpha - \beta + \beta_3) \\ \frac{a}{2}\omega_2 &= \frac{\sqrt{2}k_F L_p}{2\hbar}(-\alpha - \beta + \beta_3), \end{aligned} \tag{2.61}$$

where L_p is the mean free path, and k_F refers to the Fermi wave-vector. It is important to remark that only the SOC terms along the channel direction are relevant for the result of the simulation, i.e. for a channel oriented along the y-direction only the contributions containing w_2 have to be taken into account, for instance. The matrix $\tilde{a}$ is defined as

$$\tilde{a} = \begin{pmatrix} \frac{1}{\tau_x} & 0 & \frac{ge}{2m_e}B_y \\ 0 & \frac{1}{\tau_y} = \frac{k}{\tau_x} & -\frac{ge}{2m_e}B_x \\ -\frac{ge}{2m_e}B_y & \frac{ge}{2m_e}B_x & \frac{1}{\tau_z} = \frac{1+k}{\tau_x} \end{pmatrix}. \tag{2.62}$$

It contains the spin relaxation τ_x and introduces an external magnetic field in the x-y-plane $\vec{B}_{ext} = (B_x, B_y, 0)^T$. An additional anisotropy of the spin relaxation rate is introduced by the parameter k, such that, depending of the spin orientation, the spin relaxation rates differ. As a reference, the spin relaxation time τ_x for spins oriented perpendicular to the channel (x-direction) is used, so that τ_y is related to τ_x via k ($\tau_y = \tau_x/k$). The relaxation time τ_z is determined by τ_x and τ_y:

$$\frac{1}{\tau_z} = \frac{1}{\tau_x} + \frac{1}{\tau_y} = \frac{1+k}{\tau_x}. \tag{2.63}$$

It has to be remarked that in the COMSOL model a compact operator notation is defined, such that

$$\nabla \cdot (\tilde{c}\nabla \boldsymbol{u}) = \frac{\partial}{\partial x}\left(\tilde{c}\frac{\partial \boldsymbol{u}}{\partial x}\right) + \frac{\partial}{\partial y}\left(\tilde{c}\frac{\partial \boldsymbol{u}}{\partial y}\right) \tag{2.64}$$

$$= D\Delta\vec{u}, \tag{2.65}$$

and

$$\tilde{\beta} \cdot \nabla \boldsymbol{u} = \tilde{\beta}_x \frac{\partial \boldsymbol{u}}{\partial x} + \tilde{\beta}_y \frac{\partial \boldsymbol{u}}{\partial y} \tag{2.66}$$

$$= \begin{pmatrix} \frac{a}{2}\omega_1 \frac{\partial s_z}{\partial x} \\ \frac{a}{2}\omega_2 \frac{\partial s_z}{\partial y} \\ -\frac{a}{2}\omega_1 \frac{\partial s_x}{\partial x} - \frac{a}{2}\omega_2 \frac{\partial s_y}{\partial y} \end{pmatrix} \tag{2.67}$$

$$= \frac{a}{2}\vec{\omega}_1 \times \frac{\partial \vec{s}}{\partial x} + \frac{a}{2}\vec{\omega}_2 \times \frac{\partial \vec{s}}{\partial y}, \tag{2.68}$$

with $\tilde{\beta}_x$ and $\tilde{\beta}_y$ being the matrices consisting of the x and y component of the matrix $\tilde{\beta}$. In the model, a simplified device geometry is investigated. It consists of a single transport channel along the y-direction with a width of $w_c = 1\,\mu\text{m}$ (Fig. 2.13a). The injecting contact (blue) is spatially extended along the x-direction, while the spins are detected at single points, which does not imply any restrictions concerning the obtained spin signal, yet it is more convenient for the practical implementation in the model. Introducing a spatial extent of the

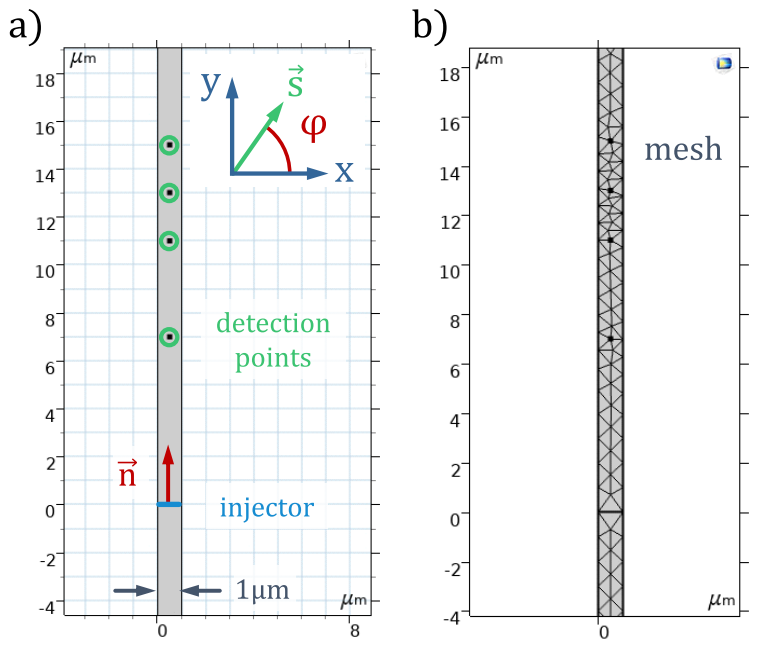

Figure 2.13. (**a**) Device geometry in COMSOL, consisting of a spatially extended injector (blue), and multiple detection points (green). The angle φ determines the orientation of the injected spin $\vec{s}$ (inset). Injected spin and $\vec{B_{ext}}$ are parallel in the model. (**b**) Automatically generated mesh for FEM.

detectors would require integrating the spin signal over the width of the channel, which only rescales the detected signal, compared to a detection point. Moreover, the spatial extent of the channel in y-direction (100 µm) is much larger than the channel width w_c, and the injector-detector distances, and also compared to the spin diffusion length. Thus, effects originating from the boundaries at the far end of the channel can be neglected. Setting a constant flux of spins through the injector is realized by implementing the following boundary condition in the model:

$$-\boldsymbol{n} \cdot (-\tilde{c}\nabla \boldsymbol{u}) = g, \tag{2.69}$$

where $\boldsymbol{n} = (0,1)^T$ is the normal vector on the injection line (Fig. 2.13a), so that the equation can be written as

$$D\frac{\partial \boldsymbol{u}}{\partial y} = g. \tag{2.70}$$

The vector g is given by

$$g = \begin{pmatrix} f\cos(\varphi) \\ f\sin(\varphi) \\ 0 \end{pmatrix}, \tag{2.71}$$

and determines orientation φ and magnitude f of the injected spin density. There, φ refers to the angle between the x-axis and the orientation of the injected spin (Fig. 2.13a). In the model, the orientation of the injected spin is parallel to direction of the external magnetic field $\vec{B}_{ext}$. The parameter f quantifies the spin flux through the injector and can be related to physical quantities by comparison to the definition of the spin current [26]:

$$j_s = j\,P_j = eD\frac{\partial s}{\partial y}. \tag{2.72}$$

Thus, the parameter f in the model is determined by the charge current j through the injector, and the injection efficiency P_j:

$$f = \frac{j\,P_j}{e}, \tag{2.73}$$

while the orientation of the spin can be set arbitrarily in the model. At the detection points, the projection of the spin along the orientation of the external magnetic field is regarded:

$$s_{det} = s_x\cos(\varphi) + s_y\sin(\varphi). \tag{2.74}$$

The finite element method (FEM) itself is based on reducing a set of partial differential equations to a discrete set of algebraic equations, which can be solved numerically [127]. The geometry V, in which the PDEs are defined, is divided into a finite number of elements V^e (mesh), such that $V = \sum V^e$. COMSOL implements triangular elements, as show in Fig. 2.13b. In each subdomain the solution of the PDE, or system of PDEs respectively, is calculated separately. A global solution in V is then obtained by assembling the solutions of the subdomains, whereby the continuity of the solution at the element boundaries has to be taken into account. A more detailed description of the finite element method can be found in Ref. [127], for example. It has to be remarked that the spatial dependence of the spin density can also be calculated with other numeric solvers, like *Maple* for instance. The major advantage of the COMSOL software is the convenient implementation of a least-square solver, which allows fitting the so-

lution of the PDEs to the corresponding experimentally obtained data, which is discussed in detail below.

Limitations of the model

For specific input parameter constellations, which include large spin relaxation times τ_s and/or large SOC strengths for instance, the extended diffusion equation cannot be solved numerically. This shortcoming is illustrated in Fig. 2.14 for an exemplary set of parameters. There, magnetic field sweeps with $\vec{B}_{ext}$ oriented along the direction of the channel are calculated for several combinations of SOC strength and spin relaxation time τ_x. For small values of SOC and τ_x, a peak-like/dip-like magnetic field dependence is obtained (Fig. 2.14a), while for parameter combinations containing larger values the numeric solver does not yield a solution (Fig. 2.14b). In Fig. 2.14c the parameter combinations yielding a solution are marked in green, while the set of parameters for which the expanded diffusion equation cannot be solved are highlighted in red. The lack of finding a solution for certain parameter constellations could be related to non-converging terms occurring during the solving process, i.e. fractions with largely differing values in the numerator and the denominator, for instance. It is important to remark that this issue is not related to COMSOL itself, and it also does not depend on the geometry or the resolution of the mesh. Instead, non-converging solutions are also obtained when solving the expanded diffusion equation numerically with software tools like *Maple*.

Another remark concerns the purely diffusive character of the model, so that ballistic effects, which can occur for narrower transport channels, cannot be taken into account in the model. In particular, the obtained solution does not depend on the channel width in the model, such that identical results are obtained even for a purely 1-dimensional geometry, in which case the channel is only a line. However, in the investigated devices, which are presented in the experimental part of this thesis, spin transport takes place in an intermediate regime, approaching the 1-dimensional limit, which is discussed in detail in Chapter 4.1. This imposes limitations concerning the quantitative analysis of the experimental data.

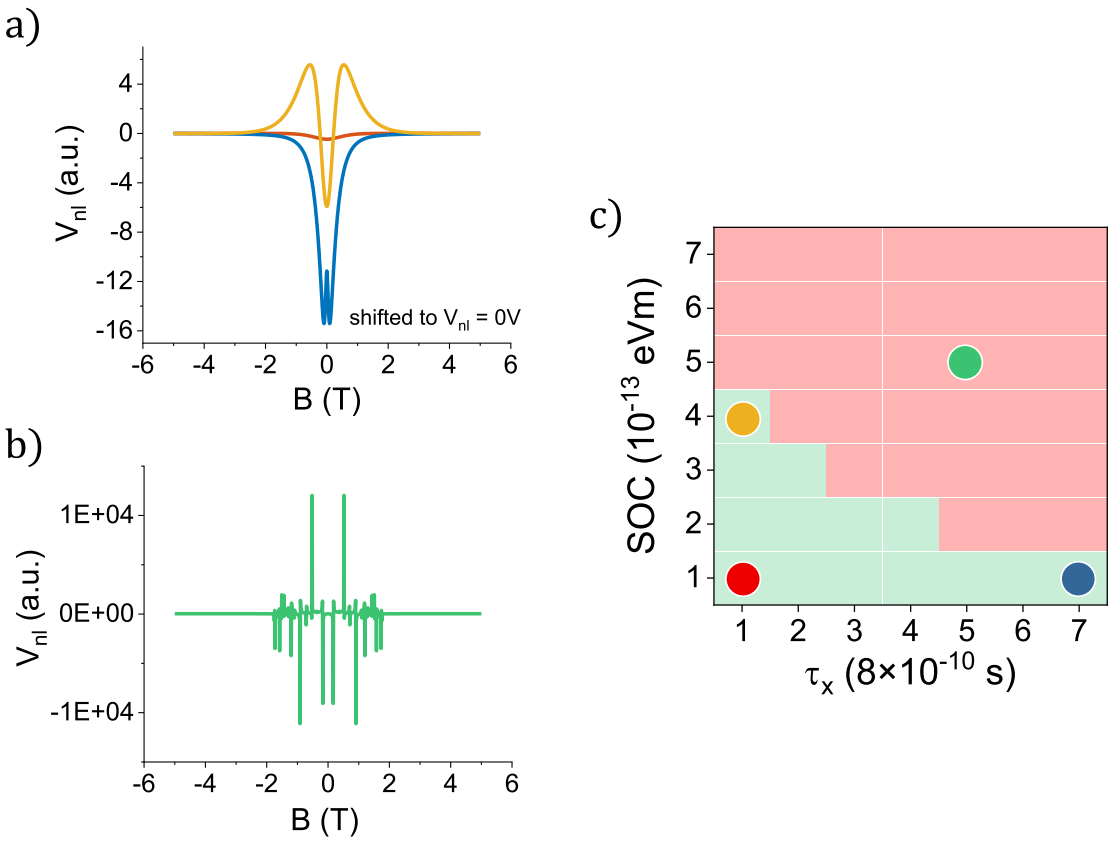

Figure 2.14. (**a**,**b**) Calculated spin signal for an external magnetic field orientation along the channel, for different SOC strengths and spin relaxation times τ_x, but fixed $\mu_e = 3.7\,\mathrm{m^2/V\,s}$, $n_s = 7 \times 10^{15}\,\mathrm{m^{-2}}$, and $k = 3$. For large SOC strength and/or τ_x, or τ_y respectively, the system of PDE cannot be solved numerically (b). (**c**) Visualization of this limitation of the model: a solution for the exemplary set of parameters can be obtained only for a limited range of SOC strengths and spin relaxation times (green), while other combinations do not yield a solution (red). The parameter combinations which yield the spin signals shown in (a) and (b), are marked by the dots in the corresponding color.

3 Methods

In the following, the experimental realization of electrical spin injection and detection is presented. The spin injection devices are based on an Esaki-diode structure with (Ga,Mn)As as a ferromagnet, which is described in Chapter 3.1. The layer sequence of the corresponding heterostructure system and the geometry of a standard spin injection device are presented subsequently, focusing on the fabricational methods, as well as process optimization. The measurements presented in the experimental part of this thesis (Chapter 4) are based on magnetic field dependent non-local measurements, which are described in Chapter 3.4, with special focus on the non-local spin valve (SV) setup.

3.1 Spin injection through an Esaki-diode structure

Overcoming the conductivity mismatch problem can be achieved by introducing a tunnel barrier between the ferromagnet (FM) and the non-magnetic conductor (Chapter 2.2). Such a junction can be conveniently realized by a fully-SC Zener-Easki-diode [128] structure with (Ga,Mn)As [129] as a ferromagnet [18, 57, 63, 130]. Before discussing spin injection through such an Esaki-diode structure, basic properties of (Ga,Mn)As are summarized first. (Ga,Mn)As belongs to the group of diluted ferromagnetic semiconductors (DFS), which combine the properties of SCs and ferromagnets [5, 131–133]. The ferromagnetism is introduced by the magnetic moment of the Mn atoms, which partially replace Ga atoms in the GaAs crystal. (Ga,Mn)As is intrinsically p-doped, whereby antiferromagnetic order is mediated by holes for Mn concentrations between 2 % and 10 %. The magnetic anisotropy of (Ga,Mn)As strongly depends on a variety of parameters, like temperature, strain, external fields, or doping density [134, 135]. For (Ga,Mn)As

films grown on a (001) GaAs substrate with low Mn concentrations of 3 % to 6 %, compressive strain leads to a reduction of the cubic symmetry with the cubic easy axes along ⟨100⟩, resulting in a biaxial anisotropy with in-plane easy axes along [100] and [010] [5, 134, 136, 137]. The magnetic anisotropy can be additionally tailored by lithographically defined narrow stripes, which induce anisotropic strain relaxation, leading to a magnetically hard axis perpendicular to the stripe and an easy one along the stripe [5, 138–141].

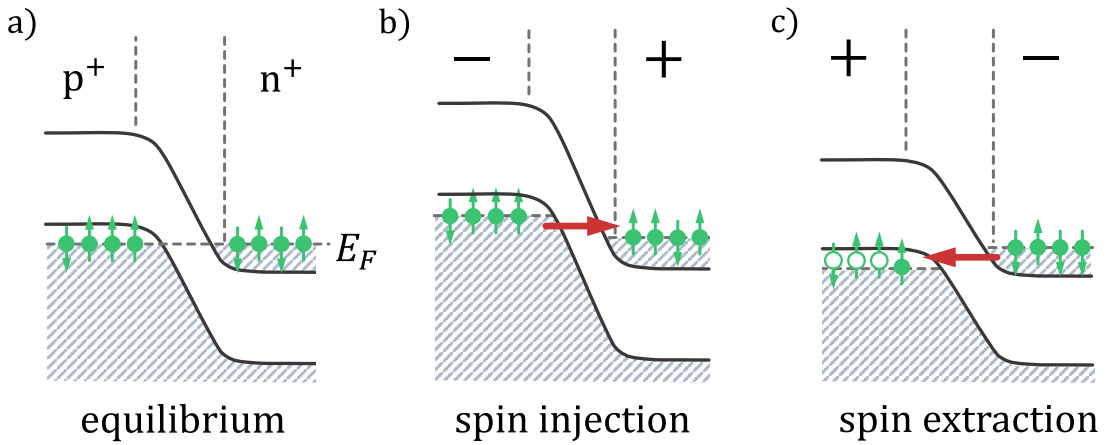

Figure 3.1. (**a**) Highly doped p-(Ga,Mn)As/n-GaAs Esaki-diode junction in equilibrium. (**b**) Spin injection under reverse bias. Spin polarized electrons can tunnel from the valence band of the (Ga,Mn)As layer into the conduction band of the GaAs heterostructure. (**c**) Spin extraction under forward bias. Adapted from [5].

The spin injection process through a highly doped p-(Ga,Mn)As/n-GaAs Esaki-diode structure is schematically depicted in Fig. 3.1. Due to the high doping concentrations on both sides of the junction, the valence band (VB) edge in the (Ga,Mn)As layer is energetically higher than the conduction band (CB) edge on the GaAs side. Thus, in equilibrium the Fermi energy E_F lies within the CB of the GaAs layer, while in the (Ga,Mn)As it lies below the VB edge (Fig. 3.1a). By applying a reverse bias across the junction (Fig. 3.1b), spin polarized electrons can tunnel from the valence band of the (Ga,Mn)As layer into the conduction band of the GaAs, thus generating a non-equilibrium spin accumulation in the GaAs

structure (spin injection). Similarly, a forward bias leads to a non-equilibrium spin distribution in the GaAs layer due to spin extraction (Fig 3.1c). First all-electrical spin injection experiments by M. Ciorga et al. [18] showed spin injection efficiencies of $P \sim 50\,\%$ and later up to about $P \sim 80\,\%$ [142] into bulk n-GaAs.

3.2 Heterostructure layout and sample preparation

The MBE-grown fully-SC heterostructure system, which is the basis of the spin injection experiments conducted within the scope of this thesis, is sketched in Fig. 3.2. In the following, the layer sequence is described in the order of growth.

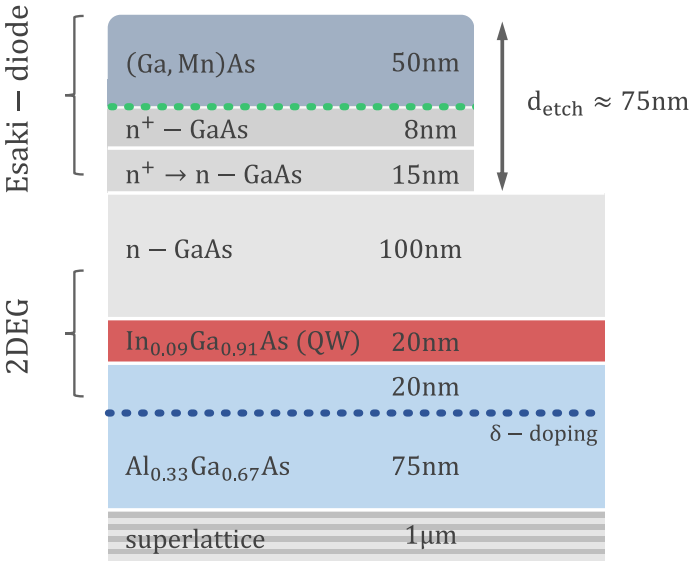

Figure 3.2. Layer sequence of the heterostructure system, which allows electrical spin injection and detection. It basically consists of a p-(Ga,Mn)As/n-GaAs Esaki-diode structure and an (In,Ga)As QW. In between the contacts, the top layers of the structure are removed ($d_{etch} = 75\,\text{nm}$) in order to prevent parallel conduction.

Starting point is a (001) GaAs substrate, followed by a 1 µm GaAs/(Al,Ga)As superlattice, which eliminates the influence of impurities, strain or other crystallographic defects of the substrate. The subsequently grown $Al_{0.33}Ga_{0.67}As$ layer (95 nm) is interrupted by Si δ-doping, which provides free charge carriers, thus allowing the formation of a conductive channel in the quantum well (QW). The QW itself is formed in the $In_{0.09}Ga_{0.91}As$ layer (20 nm), which is followed by 100 nm of lightly Si-doped n-GaAs ($n_{doping} = 7 \times 10^{16}\,\text{cm}^{-3}$). In the following transition layer the doping level of the n-GaAs layer is continuously increased, such that it

matches the doping concentration of the 8 nm thick, highly n^+-doped GaAs layer ($n_{doping} = 5 \times 10^{18}\,\mathrm{cm}^{-3}$) above. On top, (Ga,Mn)As (50 nm) with a Mn content of 5.5 % forms the ferromagnetic layer of the spin injection structure. Based on SQUID measurements, the Curie temperature is found to lie between 60 K and 70 K. The (Ga,Mn)As layer is additionally separated from the n^+-GaAs by 2.2 nm of $Al_{0.33}Ga_{0.67}As$, which prevents diffusion of Mn atoms into lower layers. The top layers of this heterostructure, i.e. the (Ga,Mn)As and the highly doped GaAs layers, form the above mentioned Esaki-diode, which enables electrical spin injection and detection, while spin transport takes place in the $In_{0.09}Ga_{0.91}As$ QW below. Typical values of the corresponding electron mobility μ_e and charge carrier density n_s in the QW are $\mu_e \approx 74\,000\,\mathrm{cm}^2/\mathrm{Vs}$, and $n_s \approx 8.4 \times 10^{11}\,\mathrm{cm}^{-2}$ after external illumination.

The simulated lowest conduction band (CB) of this heterostructure is shown in Fig. 3.3a, along with the corresponding electron density, which result from self-consistent Schrödinger-Poisson calculations. There, between the intrinsically p-doped (Ga,Mn)As and the highly n-doped GaAs layer the CB is strongly bent, thus forming the Esaki-diode structure, which allows efficient spin injection and detection. Note that the peak in the band-structure between the (Ga,Mn)As and the GaAs layer is due to the (Al,Ga)As spacer (2.2 nm). Towards the QW the doping concentration of the GaAs layer is continuously decreased ($n^+ \rightarrow n$), such that the conduction band smoothly bends, until it matches the CB energy of the n-GaAs layer. The QW is formed by the (In,Ga)As layer (20 nm) between the n-GaAs and the (Al,Ga)As. Due to the different band-gaps of the adjacent layers, the QW is slightly asymmetric. Within the (Al,Ga)As a Si δ-doping layer is grown, which provides free charge carries for the population of the 2DEG. This δ-doping gives rise to a dip in the CB. In order to limit conduction between the contacts to the 2DEG channel, thus preventing spin/charge transport in the doped layers above the QW, or within the (Ga,Mn)As, the top layers of the heterostructure have to be removed up to a depth of $d_{etch} \approx 75\,\mathrm{nm}$ (Fig. 3.2). Thus, the (Ga,Mn)As layer, as well as the highly doped GaAs layers are removed, such that the bending of the CB towards the surface is increased (Fig. 3.3b). This gives rise to an increased confinement of the electron wave-function in the QW. In experiment,

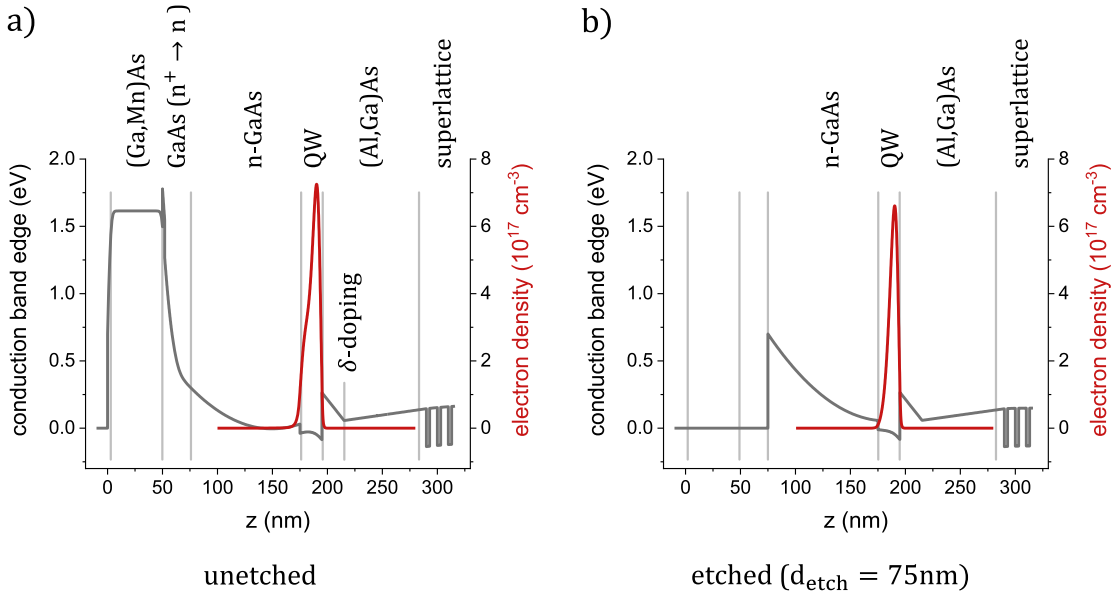

Figure 3.3. Band-structure (black) and electron density (red) for the heterostructure shown in Fig. 3.2, resulting from self-consistent Schrödinger-Poisson simulations. $z = 0$ corresponds to the top of the structure. (**a**) Simulation of the entire heterostructure. (**b**) Simulation without the top-layers ($d_{ecth} = 75\,\mathrm{nm}$), which increases the confinement of the electron wave-function in the QW.

parallel conductance can be identified in magneto-transport measurements as an additional parabolic magnetic field dependent signal on top of the Shubnikov-de Haas (SdH) oscillations in the longitudinal resistance [143]. Additionally, it has to be remarked that the 2DEG channel is typically sparsely populated, i.e. the charge carrier density n_s is low directly after cooling down the sample to cryogenic temperatures. This issue can be resolved by external illumination, which generates additional free charge carriers due to optical excitation of deep donor states (DX centers) in the Si-doped region of the (Al,Ga)As layer (persistent photo effect) [144–146].

3.3 Device geometry and fabrication

Device geometry

In the following, the basic device geometry of standard samples is schematically described. All devices investigated within the scope of this thesis are based on the SC heterostructure presented in Chapter 3.2. A standard spin injection device

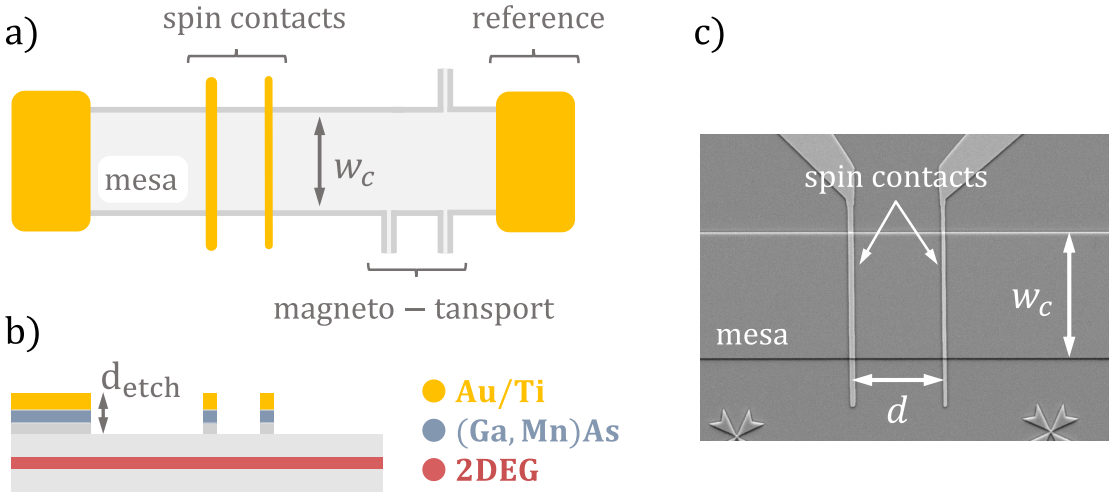

Figure 3.4. (**a**) Schematic sketch of a standard spin injection device (not to scale), consisting of a transport channel (mesa), spin injection and detection contacts (yellow), large reference pads, and probes for magneto-transport measurements. (**b**) Side-view of the device structure shown in (a). The top layers of the heterostructure are removed up to a depth of d_{etch} in order to avoid electrical conduction in the layers above the 2DEG (red). (**c**) SEM image of the spin injection and detection contacts. Scale: $w_c = 20\,\mu m$.

geometry is show in Fig. 3.4. It basically consists of a conducting channel, also referred to as mesa (gray), an injecting and at least one detecting contact (yellow), reference pads (yellow, large), as well as probes for magneto-transport measurements. In between the contacts the top layers of the heterostructure are removed (d_{etch}) in order to ensure that transport takes place *only* in the 2DEG channel (red). It has to be remarked that the reference pads consist of the identical layer sequence as the spin contacts, thus these pads are also ferromagnetic. In order to make sure that the spin injection experiments are not affected, the distance between the reference pads and the spin contacts is required to be sufficiently

large, i.e. much larger than the corresponding spin diffusion length [5, 11, 142, 147]. Thus, the injected spin accumulation is completely dephased when arriving at the reference pads, such that no additional electromotive force builds up at these reference contacts due to spin charge coupling. For the presented sample the distance between spin contact and reference pad is about 300 µm, which is much larger than a typical spin diffusion length of $\lambda_s \approx 5\,\mu m$. A typical channel width of a standard spin injection device is $w_c = 20\,\mu m$, while the width of the spin injection and detection contacts ranges from 300 nm to 800 nm. The varying widths of the spin contacts give rise to differing coercive fields due to the different degrees of lithographically induced lattice relaxation. This is an important requirement for the spin injection experiments described in Chapter 3.4. The optimal etching depth ensuring the formation of an ideally developed 2DEG channel lies between 70 nm and 75 nm.

Fabrication

Fabricating the device structure described above (Fig. 3.4) involves standard semiconductor (SC) fabrication techniques. In the following, the fabrication steps are briefly summarized, without going into technical details. Further information can be found in Refs. [148, 149], for instance. It has to be emphasized, however, that sample fabrication and process optimization has to be considered one of the major challenges of this thesis. The basic fabrication steps are schematically depicted in Fig. 3.5. First, the conductive channel (mesa) is patterned lithographically by electron beam lithography (EBL). There, a negative EBL resist (AR-N 7500.18) is utilized. After developing the resist, the pattern is transferred to the heterostructure by physical ion beam etching (IBE) with argon, which, compared to wet chemical etching approaches, yields a homogeneous, vertical etching profile, and highly reproducible etching rates (Fig. 3.5a). The remaining resist is removed afterwards with acetone. The reference pads and spin contacts are also defined by EBL, yet with multilayer PMMA (positive) as a resist, followed by evaporation of 10 nm of titanium (Ti) and 100 nm of gold (Au) (Fig. 3.5b). There, the Ti layer ensures the adhesion of the subsequently evaporated Au film. Immediately before the evaporation process the sample is immersed into an HCl:H_2O solution, which

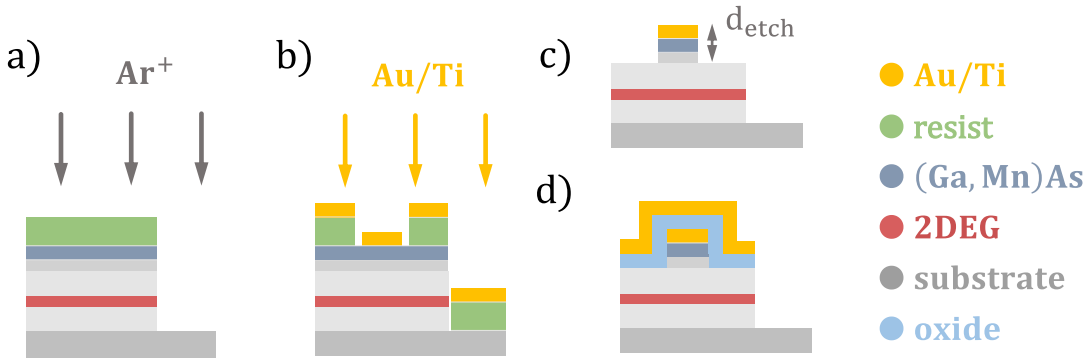

Figure 3.5. (**a**) Physical etching of the mesa channel with argon based ion beam etching. The structure is defined by lithographically patterned resist. (**b**) Evaporation of the Au/Ti spin contacts and reference pads. (**c**) Top-etching step, in which the conductive layers other than the 2DEG channel are removed. (**d**) Additional gate electrode, consisting of an oxide layer and a metal film.

removes native oxides, thus considerably enhancing the contact quality between the metal layer and the semiconductor heterostructure. After lift-off, the parts of the metal film which are on top of the resist are removed along with the resist itself. Subsequently, the top layers of the heterostructure have to be removed in between the contacts in order to avoid electrical conduction in the layers above the 2DEG channel (Fig. 3.5c). For that purpose, wet chemical etching with an acetic acid based solution ($5C_2H_4O_2$:H_2O_2:$5H_2O$) is implemented. There, the gold layer acts as an etching mask. In this step the top 70 nm to 75 nm are removed. Etching too deep leads to a complete depletion of the 2DEG at cryogenic temperatures, which cannot be counteracted by external illumination. Removing not enough material from the top layers, on the other hand, leads to an undesirable parallel conduction channel above the 2DEG, which can be observed in magneto-transport measurements as an additional parabolic magnetic field dependent signature on top of the Shubnikov-de Haas oscillations in the longitudinal resistance. As the etching depth d_{etch} is critical, etching is conducted iteratively in multiple short steps. After each etching step d_{etch} is determined by atomic force microscopy (AFM). For device geometries which require a gate electrode, additional fabrication steps are necessary (Fig. 3.5d). There, EBL patterned multilayer PMMA is used as a mask. Subsequently, an oxide layer is grown, which consists of a 10 nm

PECVD[1]-grown SiO_2 layer at a process temperature of 80 °C, followed by 100 nm of ALD[2]-grown Al_2O_3 at 120 °C. There, the SiO_2 seed layer ensures the homogeneous growth of the Al_2O_3. Without a further lithographic step, 2 nm Ti and 20 nm Au are evaporated, followed by a lift-off process. The thickness of the metal electrode is chosen such, that it forms a homogeneous layer, yet is still transparent enough to allow external illumination, which is required in order to fully populate the 2DEG channel at cryogenic temperatures. Finally, the metallic gate layer has to be electrically connected, which requires an additional EBL pattering step with multilayer PMMA, followed by evaporation of Ti/Au (10 nm/100 nm). After these micro-fabrication steps the spin contacts, reference pads and gate electrode have to be electrically connected to a chip-carrier by conventional wire bonding. There, the large reference pads can be directly bonded, while the spin contacts are electrically accessed via larger pads, which are directly fabricated in the corresponding fabrication step, i.e. in the same step as the spin contacts. A depiction of an exemplary actual sample geometry is shown in Fig. 3.6, where all Au/Ti areas are fabricated in the same step.

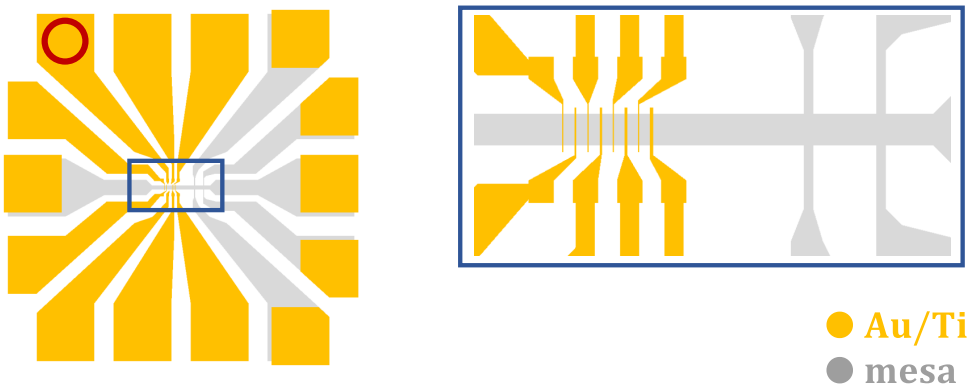

Figure 3.6. An entire device geometry, including the large Au/Ti pads, some of which directly contact the mesa, while others are connected to the spin injection and detection contacts (zoomed in on the right). These pads allow electrical access via wire bonding at the exemplarily marked position (red circle).

[1] plasma enhanced chemical vapor deposition
[2] atomic layer deposition

Fabricational challenges

The fabrication process required extensive optimization in order to eliminate severe shortcomings of previously conducted fabrication routines. One major obstacle arose from wet chemical etching of the mesa structure, which is not reproducible concerning etching depth and profile, and is accompanied by significant underetching of the resist mask. In particular, this can lead to a distinct undercut profile of the mesa sidewall (Fig. 3.7a), such that in the following evaporation step the metal film on top of the mesa is not connected to the part on the substrate. Indeed, this used to be a common problem of previous approaches, resulting in a low stochastic yield of properly functioning spin contacts. Additionally, due to severe underetching of the resist and lacking reproducibility of the etching profile, devices with narrow channels ($\lesssim 4\,\mu m$) could not be realized. Therefore, a dry

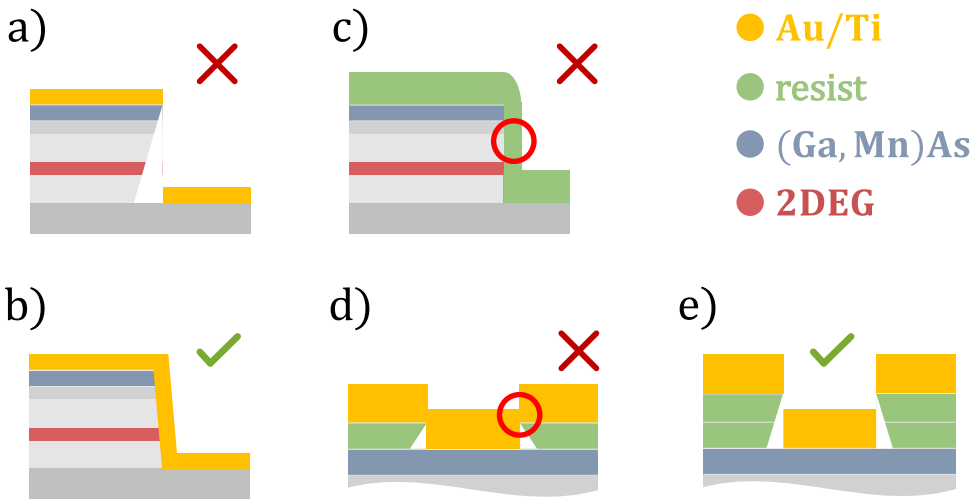

Figure 3.7. Depiction of shortcomings of previous sample fabrication approaches. Wet chemical etching typically leads to an undercut profile of the mesa sidewall, preventing electrical connection of the Au/Ti layer across the mesa edge (**a**). This can be resolved by physical dry etching with IBE, which results in sloped mesa sidewalls (**b**). Especially for low resist thicknesses the resist at the side of the mesa is too thin (**c**). For small resist thicknesses, however, the evaporated metal film can overlap (**d**), which could damage the metal layer during the lift-off process. This can be resolved by implementing resist combinations with a significantly larger thickness (**e**).

etching technique was established, with the aim of a stable process and the possibility of fabricating narrow channels ($w_c \sim 500\,\mathrm{nm}$). Process development and optimization required extensive testing of a variety of resist combinations (CSAR (positive), multilayer PMMA (positive), double layer AR-N 7500.18 (negative)). Double layer AR-N 7500.18 was found to yield the best results in terms of withstanding dry etching processes, while CSAR resist has a better resolution, yet could not be completely removed after etching, even by applying a high-power oxygen plasma. PMMA resist, on the other hand, is strongly attacked during the dry etching process and is therefore not applicable for this type of etching. Also, different dry etching techniques were implemented, including reactive ion etching (RIE) and ion beam etching (IBE) with argon ions. In case of the RIE process a variety of gases, primarily $SiCl_4$ alone, but also $SiCl_4$ in combination with methane for an increased etching rate of the (In,Ga)As layer, or a mixture with argon for an additional physical etching component, were tested. Additionally, the gas flow rate and process power were varied, but also trials with short periodic etching intervals were conducted in order to remove residues of the wafer material in the plasma, thus trying to stabilize the etching rates. However, even after extensive testing no stable process could be established, which can be assumed to be due to the RIE system itself. Ion beam etching with argon ions in combination with the AR-N 7500.18 negative resist, on the other hand, yields a reproducible etching rate and highly anisotropic etching profiles, giving rise to slightly sloped mesa sidewalls, which allows ideal connection of the evaporated metal layer across the mesa edge (Fig. 3.7b).

The spin injection and detection contacts typically used to be patterned with double layer PMMA resist (200k9 % + 950k2 %), yielding a layer thickness of roughly 400 nm. However, at the sides of the mesa for instance, the resist thickness can be assumed to be much thinner (Fig. 3.7c). In areas on the sample, in which the resist is thinner, the evaporated metal layer can overlap (Fig. 3.7d), such that the parts of the metal, which are supposed to stay on the substrate, could be ripped off during the lift-off process. This shortcoming could be resolved by introducing a triple layer PMMA resist ($2 \times$ 200k9 % + 950k2 %) with a thickness of about 800 nm, which additionally involved adjusting EBL dose and development time.

The increased thickness of the resist prevents an overlap of the metal layers, thus significantly facilitating the lift-off process (Fig. 3.7e).
Concerning the top-etching step, different solutions were tested, including phosphoric, citric, and acetic acid. The most reproducible results concerning etching rate and spatial homogeneity could be achieved with an acetic acid based solution ($5C_2H_4O_2$:H_2O_2:$5H_2O$).

3.4 Experimental methods

Non-local device geometry

The non-local device geometry, which allows electrical injection and detection of spins, was first introduced and experimentally realized by M. Johnson and R. Silsbee [42]. This measurement setup is the basis of the experiments conducted within the scope of this thesis (Chapter 4). The non-local setup is schematically sketched in Fig. 3.8a. It consists of a non-magnetic conduction channel (NM), a ferromagnetic injecting contact FM_1, at least one detecting contact FM_2, and reference contacts at the far end of the channel (R_1, R_2). The FM/NM junction consists of the Esaki-diode structure described in Chapter 3.1, while the NM channel is an (In,Ga)As QW. The entire layer sequence of the heterostructure is presented in Chapter 3.2. Spin injection is achieved by passing a charge current I_{inj} through the FM_1/NM interface to the reference contact R_1, which generates a non-equilibrium spin accumulation s in the NM channel underneath the injecting contact FM_1. In this non-local setup no charge current flows between the ferromagnets, and spin transport can be considered purely diffusive in this region. The diffusive spread of the injected spin accumulation s is accompanied by spin relaxation, which gives rise to an exponential decay of $s \propto \exp(-x/\lambda_s)$. A sufficiently large spin diffusion length λ_s in the NM channel, however, can result in a non-equilibrium spin distribution underneath the detecting contact FM_2, the magnitude of which can be measured as a non-local voltage drop V_{nl}. The magnitude of this non-local voltage signal can be determined by regarding the spatial distribution of the quasi-chemical potential μ, which is introduced in Chapter 2.2 (Fig. 3.8b). There, a gradient of $\mu = 1/2\,(\mu_\uparrow + \mu_\downarrow)$ (green) in the injection circuit between

FM_1 and R_1 ($x < 0$), gives rise to a charge current $j = j_\uparrow + j_\downarrow$, which generates a non-equilibrium spin accumulation $\mu_s(0) = 1/2\,(\mu_\uparrow(0) - \mu_\downarrow(0))$ in the NM channel (spin injection). This spin accumulation decays exponentially with the distance

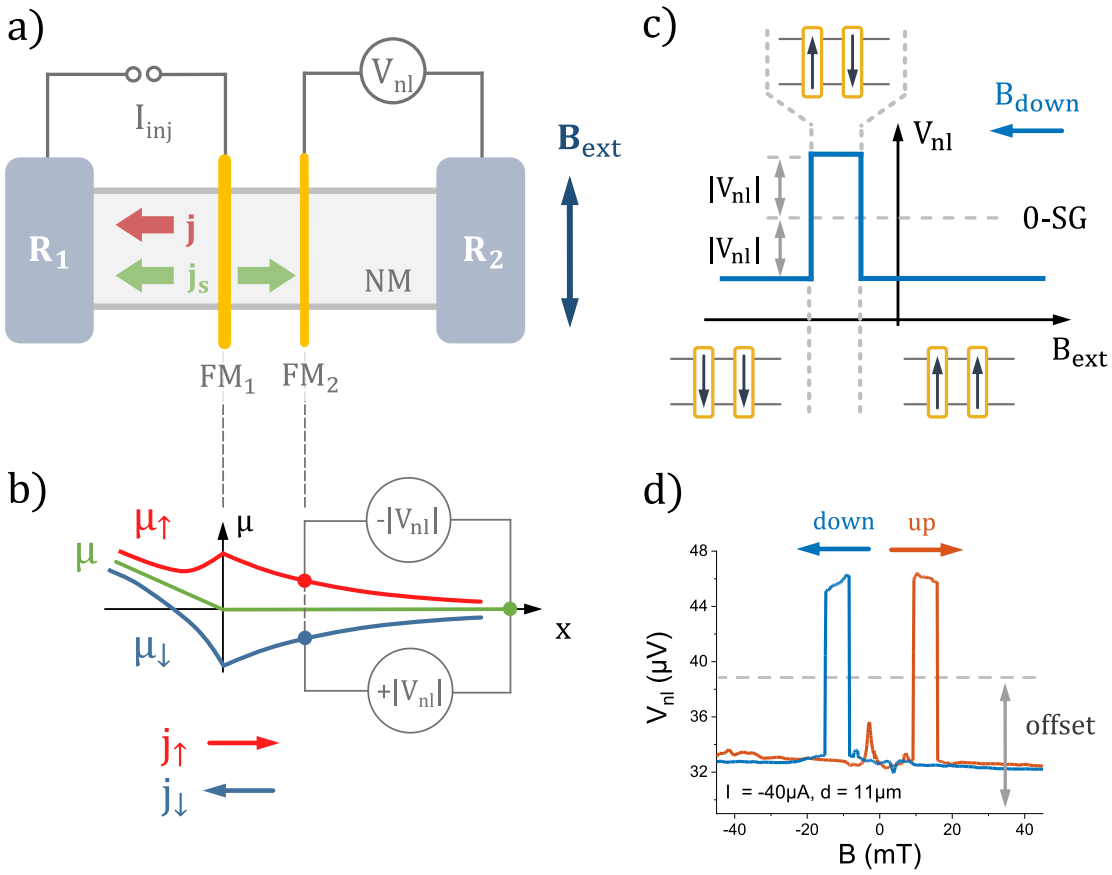

Figure 3.8. (**a**) Device geometry of the non-local spin injection setup. A charge current j is passed from the ferromagnetic spin injection contact FM_1 to the reference contact R_1. The thus injected spins diffuse in each direction (j_s), so that underneath the detecting contact FM_2 a finite spin accumulation is present, which can be measured as a non-local voltage drop V_{nl}. (**b**) Spatial profile of the quasi-chemical potentials for spin-up $\mu_\uparrow$ (red) and spin-down $\mu_\downarrow$ (blue) electrons, along with the total quasi-chemical potential μ (green). The non-local voltage drop at the position of the detector is related to the difference between $\mu_\uparrow$ and $\mu_\downarrow$. (**c**) SV measurement for a magnetic down-sweep. The step-like signal characteristic results from a change of the magnetization orientation of injecting and detecting contact (arrows). (**d**) Experimental non-local SV signal for magnetic up- and down-sweep. Adapted from [5].

from the injector ($x = 0$). In Fig. 3.8b μ_s is shown for majority (red) and minority (blue) spins. The non-local voltage drop V_{nl} at the detector is related to μ_s and given by [5, 19]

$$V_{nl}(d) = \mp P_{det}\mu_s(d) = \pm\frac{P_{inj}P_{det}I_{inj}R_s\lambda_s}{2w_c}\exp\left(-\frac{d}{\lambda_s}\right), \tag{3.1}$$

with the injection current I_{inj}, the injection and detection efficiencies P_{inj} and P_{det}, the sheet resistance R_s of the channel, the spin diffusion length λ_s, and the channel width w_c.

Non-local SV measurement

A common method of probing a non-equilibrium spin accumulation relies on the so-called non-local spin valve (SV) effect. Spin valve measurements can be conducted with non-local devices, as shown in Fig. 3.8a, by additionally applying an external in-plane magnetic field $\vec{B}_{ext}$, which is oriented parallel to the easy magnetic axis of the injecting/detecting contact. The non-local voltage drop V_{nl} is then measured as a function of B_{ext}. A typical non-local SV signal is schematically sketched in Fig. 3.8c. For large magnetic fields the magnetization of both ferromagnetic spin contacts is aligned parallel to $\vec{B}_{ext}$. This configuration does not change until the magnetic field direction is reversed and one of the contacts, either the injecting or the detecting one, eventually switches its magnetization by 180°. In this situation the magnetization of the contacts is antiparallel relative to each other. Thus, also the spin orientation underneath the detector is antiparallel relative to its magnetization direction, and V_{nl} changes sign. At larger reversed magnetic fields, also the other contacts switches, so that again the parallel configuration is established, which again gives rise to a change of sign of V_{nl}. The change from P to the AP level and back to P yields the typical rectangular SV signal shown in Fig. 3.8c. The height of the SV signal ΔV_{nl} is related to the non-local voltage drop (Eq. 3.1):

$$\Delta V_{nl}(d) = 2|V_{nl}(d)| = \frac{P_{inj}P_{det}I_{inj}R_s\lambda_s}{w_c}\exp\left(-\frac{d}{\lambda_s}\right), \tag{3.2}$$

with the injector-detector distance d. It has to be remarked that the clear formation of the AP configuration requires different coercive fields of injecting and detecting contact. This can be realized by different widths of the contacts, thus inducing different degrees of lattice strain relaxation. Additionally, experimentally obtained spin valve signals are typically shifted by an offset voltage (Fig. 3.8d). This can be related to inhomogeneities of the FM/NM junction, like a non-uniform tunnel barrier thickness along the spin contacts, or pinholes, which give rise to a spatially varying injection and detection distribution along the contacts [150]. Also thermoelectric contributions, like Seebeck voltages resulting from Peltier or Joule heating, can lead to a significant voltage offset [151]. As the quantitative evaluation of the SV signal relies on the difference between the P and the AP level (ΔV_{nl}), however, the offset contribution cancels out. This offset voltage can be corrected by defining the 0-spin-signal (0-SG), for which no spin dependent voltage drops at the detector. It can be determined as sketched in Fig. 3.8c from SV measurements and basically lies in the middle between the parallel and the antiparallel level of the SV signal. Extracting the SV signal height ΔV_{nl} from experiment for various injector-detector distances d, allows determining important spin related quantities, like the spin diffusion length λ_s, or the injection/detection efficiency $P_{inj/det}$.

4 Experimental results

The experimental part of this thesis is divided into three main topics. Their order sketches the conceptual approach towards the aim of this thesis, which is the realization of devices that allow the manipulation of the spin signal by means of an external gate voltage. In the first experimental part (Chapter 4.1), a device geometry is introduced, which allows realizing transport channels with widths down to $w_c = 400\,\mathrm{nm}$, while still achieving large spin injection efficiencies. There, the expected suppression of spin relaxation upon decreasing the channel width is experimentally confirmed by investigating the channel width dependence of the spin diffusion length. In these narrow transport channels the motion of spins is restricted mainly to one principle axis. Therefore, the SO-field for $\vec{k}$ along the direction of the channel can be considered to be the main source of spin precession, which facilitates the qualitative interpretation of the measured spin signals. Signatures of this effective magnetic field can be observed in non-local spin transport measurements, which are presented in Chapter 4.2. In combination with qualitative finite element simulations, it is thus possible to relate magnetic field dependent characteristics of the non-local spin signal to SOC. Additionally, crystallographic orientation dependent investigations show a distinct anisotropy of the SO-field strength. In the subsequent chapter (Chapter 4.3), devices with an additional gate electrode are investigated. There, the gate dependence of charge transport properties is examined first, followed by a detailed analysis of the influence of the electric field on spin related quantities, like the spin diffusion length, and the spin injection efficiency. Subsequently, the tunability of the SOC related signal features is confirmed. There, it is possible to extract gate dependent spin signal oscillations from non-local SV measurements, which can be related to spin precession due to a change of SOC strength. In previous publications similar spin

precession signatures could only be observed in InAs QW structures in the ballistic transport limit, i.e. for small injector-detector distances [20–25]. In the presented devices, on the other hand, an $In_{0.09}Ga_{0.91}As$ QW structure provides the conducting channel, in which a relatively low SOC strength on the order of $10^{-13}\,\mathrm{eV\,m}$ is expected. Additionally, in these devices spin transport is not ballistic, instead it takes place in an intermediate regime, which is still diffusive, yet approaches the quasi-1D limit. Despite the low SOC strength and the diffusion dominated spin transport, gate induced spin precession oscillations can be observed, which is indeed a remarkable finding and has to be considered the central result of this thesis.

4.1 Spin transport in narrow channels

As discussed in Chapter 2.4.2, Dyakonov-Perel spin relaxation can be strongly suppressed by introducing lateral confinement, which can be realized by decreasing the width of the transport channel, thus approaching the 1-dimensional limit. In contrast to reports which confirm the increase of the spin relaxation time τ_s for out-of-plane spins in narrow transport channels [90, 102, 106–108], in this chapter an all-semiconductor electrical spin injection and detection device is investigated in which spins are injected in-plane.

4.1.1 Device geometry and measurement setup

In the following, two different device geometries are examined, both based on the heterostructure presented in Chapter 3.2. The standard spin valve (SV) device geometry shown in Fig 4.1a, is described in detail in Chapter 3.4. It basically consists of a 2DEG transport channel ($In_{0.09}Ga_{0.91}As$ QW), which is in this case oriented along the [010] crystallographic direction, and two ferromagnetic (Ga,Mn)As contacts allowing electrical spin injection and detection. Note that injecting and detecting contacts are oriented along one of the magnetic easy axes of the (Ga,Mn)As layer, i.e. along $\langle 100 \rangle$. In the following, the distance between these contacts is denoted d (center-center), while w_c refers to the width of the

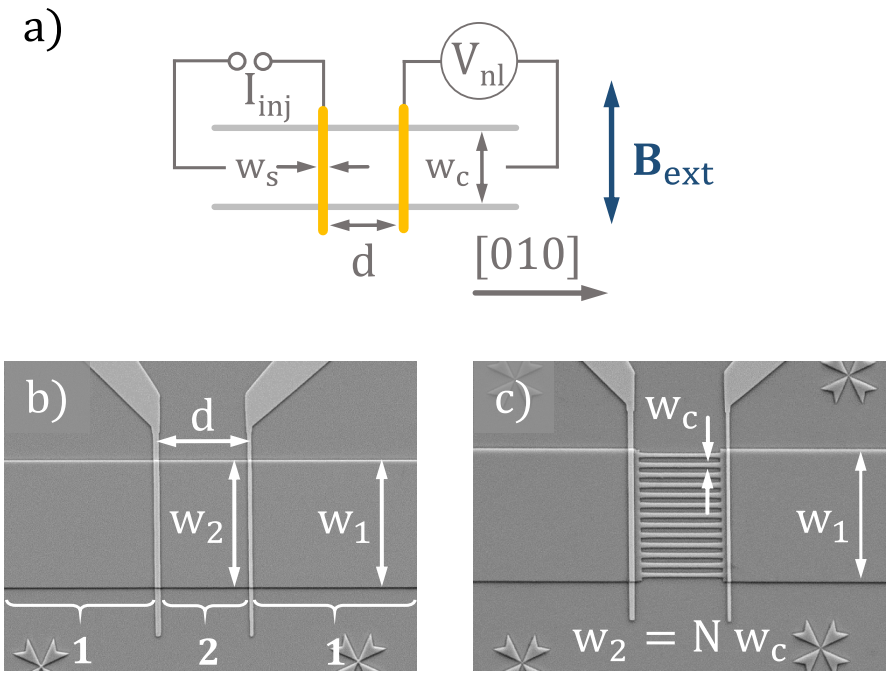

Figure 4.1. (**a**) Standard SV geometry and non-local measurement setup. (**b**) SEM image of a standard SV device, which is divided into region *1* and region *2* (between the contacts). The corresponding widths of region *1* and *2* are denoted w_1 and w_2. The spin contacts are 300 nm and 500 nm in width (w_s). (**c**) SEM image of a device geometry with an array of N narrow channels between injecting and detecting contact (region *2*). The width of a single channel is w_c, while the effective width of region *2* is given by the sum of the narrow channels $w_2 = N w_c$. Scale: $w_1 = 20\,\mu m$, $w_c = 1\,\mu m$.

channel (Fig. 4.1a). Spin transport is probed by means of non-local SV measurements, which are described in Chapter 3.4. For the standard device geometry the investigation of the suppression of Dyakonov-Perel (DP) spin relaxation due to a reduced channel width, is experimentally limited mainly by the aspect ratio of the injecting and detecting contact (contact width w_s/channel width w_c). For disadvantageous aspect ratios, i.e. $w_c \lesssim w_s$, the effect of lithographically induced lattice relaxation is reduced, thus no dominating magnetically easy axis along the contact is formed. In this case, no clear AP signal level can be observed in SV experiments, which is already noticeable for channel widths below about 4 µm (aspect ratio $\gtrsim 0.125$). Thus, for the realization of devices with narrow channel

widths below about 4 µm, it is necessary to introduce a new sample design, which is shown in Fig. 4.1c. In this array geometry the contacts lie on the wide part of the channel ($w_1 = 20\,\mu m$), while the diffusive path between the contacts consists of an array of narrow channels. In the following, the part of the channel between injecting and detecting contact is labeled as region *2* with an effective width w_2, while region *1* denotes the remaining sections of the channel, i.e. the part between a spin contact and the closest reference pad (Fig. 4.1b). In case of the array geometry with N narrow channels, each with a width w_c, the effective width of region *2* is given by $w_2 = N \cdot w_c$. The width of region *1* is labeled w_1, which in case of the standard geometry is equal to that of region *2* ($w_1 = w_2 = w_c$). With the array geometry it is possible to realize spin transport in channels with considerable lateral confinement, approaching the ballistic 1-dimensional limit, yet, at the same time, the advantageous aspect ratio of the contacts allows ideal magnetic switching characteristics, in particular regarding the formation of the AP magnetization configuration in SV experiments. Another main advantage of this device setup is the larger injection efficiency P_{inj} in the array geometry, compared to a standard sample with only one narrow channel. This is related to the voltage drop V_{int} at the spin injection contact, which is inversely proportional to the channel width w_c for a given injection current. A smaller channel width results in a larger voltage drop V_{int} at the interface, which in turn yields a smaller spin injection efficiency P_{inj} in (Ga,Mn)As/GaAs Esaki-diode structures [18, 63, 152]. The array geometry therefore allows combining the advantages of narrow spin transport channels, i.e. the partial suppression of spin relaxation, with the larger spin injection efficiency of device geometries with wider channels.

4.1.2 Experimental results

In Fig. 4.2 non-local spin signals are exemplarily shown for a standard device with a channel width of 20 µm (a), and a sample with an array of 400 nm wide channel segments between injecting and detecting contact (b). Different injector-detector distances d are investigated, while all measurements are conducted at a cryogenic temperature of 1.4 K. The most notable feature is the almost textbook-like magnetic switching characteristic of the signal and the clear formation of the

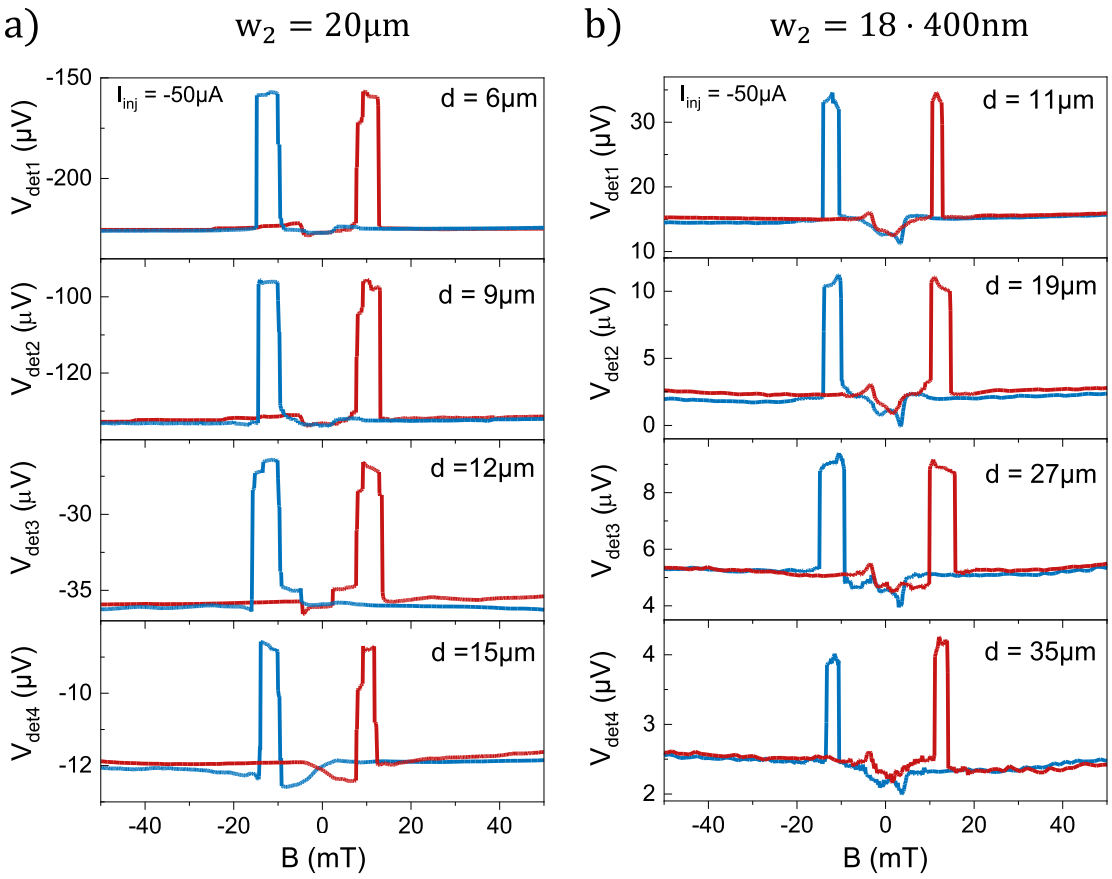

Figure 4.2. Exemplary distance dependence of non-local SV signals for a standard device with a 20 µm wide channel (**a**), and a device with an array of 400 nm wide channels ($N = 18$) between injector and detector (**b**). Both measurements were conducted at a temperature of 1.4 K with an injection current $I_{inj} = -50$ µA (DC).

AP configuration. Such clearly defined SV signals could not be achieved in the standard geometry with channel widths below about 1 µm. The decaying behavior of the spin signal height with distance already provides qualitative information about the spin diffusion length λ_s. It is obvious from a qualitative point of view that the decay of the SV signal with distance d is significantly decreased for the sample with an array of 400 nm wide stripes between the contacts, compared to the 20 µm wide standard sample. This becomes most apparent when regarding the signal of the array sample in a distance of $d = 35$ µm from the injector,

which is still clearly visible ($\Delta V_{nl} \approx 1.8\,\mu V$). This is remarkable, as for the standard device geometry no spin signal can be observed for such a large injector-detector distance. The significant increase of the spin diffusion length for the narrow channel geometry is quantitatively analyzed in the following.

4.1.3 Evaluation and discussion

From the distance dependence of the non-local SV signal height (Fig. 4.2) the spin diffusion length λ_s can be extracted, which quantifies the decay of the injected spin accumulation. For the standard geometry, the magnitude of the non-local SV signal ΔV_{nl} is related to the non-local voltage drop at the detector, thus it is expected to decay exponentially with the distance d from the injecting contact:

$$\Delta V_{nl}(d) = \frac{P_{inj} P_{det} I_{inj} R_s \lambda_s}{w_2} \exp\left(-\frac{d}{\lambda_s}\right), \tag{4.1}$$

with the injection current I_{inj}, the width of the channel w_2 in region *2* (Fig. 4.1b), the sheet resistance R_s of the channel, and the spin injection and detection efficiencies P_{inj} and P_{det}. For small injection currents, P_{inj} and P_{det} can be assumed to be equal [5], such that $P \equiv P_{inj} = P_{det}$. For the following discussion, the

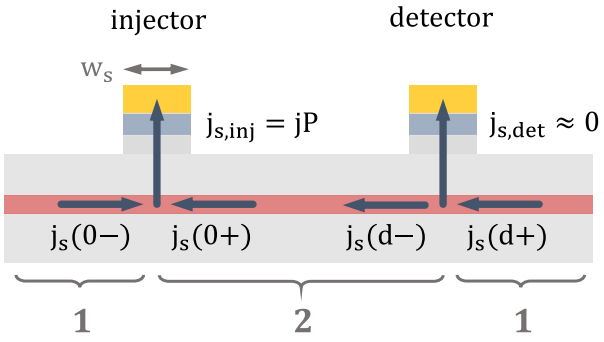

Figure 4.3. Splitting of the injected spin current $j_{s,inj}$ $(x = 0)$ into two, not necessarily equal, components $j_s(0-)$ and $j_s(0+)$. As there is no current through the detector $j_{s,det} \approx 0$ $(x = d)$, $j_s(d-) \approx j_s(d+)$. Adapted from [118].

channel section between the contacts is labeled as region *2*, while the part of the channel between the spin injection/detection contact and the closest reference contact is referred to as region *1*, as shown in Fig. 4.1b and Fig. 4.3. In case of region *1* and *2* having the same width, which corresponds to the standard spin injection geometry, Eq. 4.1 describes the exponentially decaying distance depen-

dence of the non-local SV signal. In the array geometry, however, the effective channel width of region *2* ($w_2 = Nw_c$) is smaller than the width of region *1* (w_1), giving rise to a larger channel resistance of region *2* compared to region *1*. This in turn leads to unequal values of the spin resistances $r_N \propto \rho_N \lambda_s$ in these two regions, where ρ_N denotes the resistivity of the channel. As a result, the injected spin current $j_{s,inj}$ splits into two unequal components $j_s(0-)$ and $j_s(0+)$, as indicated in Fig. 4.3, which leads to a modification of Eq. 4.1. The basic idea of the derivation is sketched in the following, while a detailed description can be found in the supplemental material of Ref. [118]. As illustrated in Fig. 4.3, passing a charge current I_{inj} through the injecting FM contact into the channel leads to the generation of a spin accumulation in the NM. The accompanied splitting of the spin quasi-chemical potential is given by $\mu_s = 1/2\,(\mu_\uparrow - \mu_\downarrow)$. Assuming spin injection in the tunneling regime and limiting the discussion to one dimension, i.e. the thickness of the channel is much smaller compared to the spin diffusion length λ_s, the spatial distribution of this spin accumulation μ_s is given by the spin diffusion equation:

$$\nabla^2 \mu_s(x) = \frac{\mu_s}{\lambda_s}. \tag{4.2}$$

The differing channel resistivities of region *1* and *2* ($\rho_{N,1}$ and $\rho_{N,2}$) give rise to different spin diffusion lengths λ_s in each section (λ_1 and λ_2). Solving the spin diffusion equation with appropriate boundary conditions yields an expression for $\mu_s(x)$, which depends on $\mu_s(0)$ (injected spin accumulation) and $\mu_s(d)$ (spin accumulation at the detector). In order to obtain expressions for $\mu_s(0)$ and $\mu_s(d)$, the continuity of the spin currents $j_s(x)$ at the contacts is implemented, where $j_s(x) = \lambda_s / r_N \nabla \mu_s(x)$. There, the injected spin current density splits into two unequal components, $j_s(0-)$ and $j_s(0+)$, while at the detector no charge current flows through the contact, such that $j_{s,det} \approx 0$ and $j_s(d-) \approx j_s(d+)$ (Fig. 4.3). Continuity therefore implies:

$$\begin{aligned} j_{s,inj} &= j_s(0+) + j_s(0-) && \text{(injector)} \\ j_s(d-) &\approx j_s(d+) && \text{(detector).} \end{aligned} \tag{4.3}$$

This yields a set of two equations, which allows calculating $\mu_s(0)$ and $\mu_s(d)$. In the tunneling regime the latter can be related to the non-local voltage signal at the detector:

$$V_{nl}^{s}(d) = -P\mu_s(d), \tag{4.4}$$

where P is the spin detection efficiency, which is assumed to be equal to the injection efficiency. Additionally, the spin current density j_s can be related to the injection current I_{inj}, and the spin resistance r_N to the sheet resistance R_s of the channel:

$$\begin{aligned} j_s &= \frac{I_{inj}}{w_1 w_s} \\ r_N &= R_{s,1/2}\lambda_{1/2} w_s, \end{aligned} \tag{4.5}$$

with the effective widths of region *1* and *2* ($w_{1/2}$), the spin diffusion lengths in the corresponding region $\lambda_{1/2}$, and the spatial extent of the injecting spin contact along the channel direction w_s. Ultimately, the following expression for the non-local voltage at the position of the detector for the array geometry is obtained:

$$V_{nl}^{s}(d) = \pm \frac{2P^2 I_{inj} R_{s,2}\lambda_2}{w_2} \frac{1}{(1+A)^2 \exp\left(\frac{d}{\lambda_2}\right) + (1-A)^2 \exp\left(-\frac{d}{\lambda_2}\right)}, \tag{4.6}$$

with

$$A = \frac{R_{s,2}\lambda_2 w_1}{R_{s,1}\lambda_1 w_2}.$$

A more detailed derivation of this formula can be found in the supplemental material of Ref. [118]. In case of the standard geometry, the sheet resistances ($R_{s,1} = R_{s,2}$), the spin diffusion lengths ($\lambda_1 = \lambda_2$), and the effective widths of the channel sections ($w_1 = w_2$) are equal for both regions, which allows simplifying Eq. 4.6, resulting in the previously discussed expression (Eq. 4.1).
Assuming the ratio of the effective spin resistances in region *2* and region *1* to be larger than 1 ($A = R_{s,2}\lambda_2 w_1 / R_{s,1}\lambda_1 w_2 \gtrsim 1$), and $d/\lambda_2 \gtrsim 1$, allows reducing Eq. 4.6 to a simple exponential decay, which is determined by the spin diffusion

length λ_2 of region *2*:

$$V_{nl}^{s}(d) \approx \pm\frac{2P^2 I_{inj} R_{s,2}\lambda_2}{w_2}\,\frac{1}{\left[1+R_{s,2}\lambda_2 w_1/R_{s,1}\lambda_1 w_2\right]^2}\exp\left(-\frac{d}{\lambda_2}\right). \tag{4.7}$$

Spin diffusion length

The approximation for the non-local spin signal $V_{nl}^{s}(d)$ (Eq. 4.7) can be implemented for the evaluation of the experimentally obtained SV signals, as the spin resistance of the array section of the channel (region *2*) is larger compared to region *1*, and the smallest used injector-detector distance is on the order of the longest measured spin diffusion length λ_2. This allows extracting λ_2 directly from the distance dependence of the SV signal height by linearly fitting the semi-logarithmically plotted distance dependence of $\Delta V_{nl}(d) = 2|V_{nl}^{s}(d)|$, which is exemplarily shown in Fig. 4.4a. For the standard sample with a 20 µm wide channel, a spin diffusion length of around 4 µm can thus be extracted, while for the array geometry with 400 nm wide transport channels, λ_s is significantly larger with values around 9.2 µm. This corresponds to a major increase by a factor of 2.3. The change of λ_s in dependence of the channel width w_c is shown in Fig. 4.4b. For channel widths larger than $w_c \geq 7.5\,\mu\text{m}$, λ_s is nearly constant at a value of about $\lambda_s \approx 4\,\mu\text{m}$. By decreasing the channel width, especially for $w_c \lesssim 1\,\mu\text{m}$, the spin diffusion length increases significantly up to 9.2 µm for $w_c = 400\,\text{nm}$. This large increase of λ_s can be explained by the suppression of the DP spin relaxation mechanism for narrow channels, as described in Chapter 2.4.2. Depending on the channel width w_c in comparison to the spin orbit length L_{SO} and/or the mean free path L_p, three regimes of spin relaxation can be defined. For wide channels, i.e. for channels wider than the spin orbit length ($w_c > L_{SO}$), spin relaxation is dominated by the DP mechanism. The corresponding spin relaxation rate is given by (Chapter 2.4.1, Eq. 2.43)

$$\frac{1}{\tau_{2D}} = \frac{4Dm^{*2}}{\hbar^4}\left[\frac{\tau_1}{\tau_p}\alpha^2 + \frac{\tau_1}{\tau_p}\left(\beta_1-\beta_3\right)^2 + \frac{\tau_3}{\tau_p}\beta_3^2\right], \tag{4.8}$$

for spins oriented along [100]. In the quasi-1D limit, on the other hand, where w_c is smaller than the corresponding mean free path L_p, spin relaxation is strongly

suppressed and only due to the cubic Dresselhaus contribution β_3, such that

$$\frac{1}{\tau_{1D}} \propto \beta_3^2. \tag{4.9}$$

In the intermediate regime between the 2-dimensional case and the quasi-1D limit, the spin relaxation time is found to be inversely proportional to the squared channel width ($\tau_s \propto 1/w_c^2$). Thus, the spin diffusion length is expected to scale with $1/w_c$ ($\lambda_s \propto \sqrt{\tau_s}$):

$$\tau_{IM} \propto \frac{1}{w_c^2}. \tag{4.10}$$

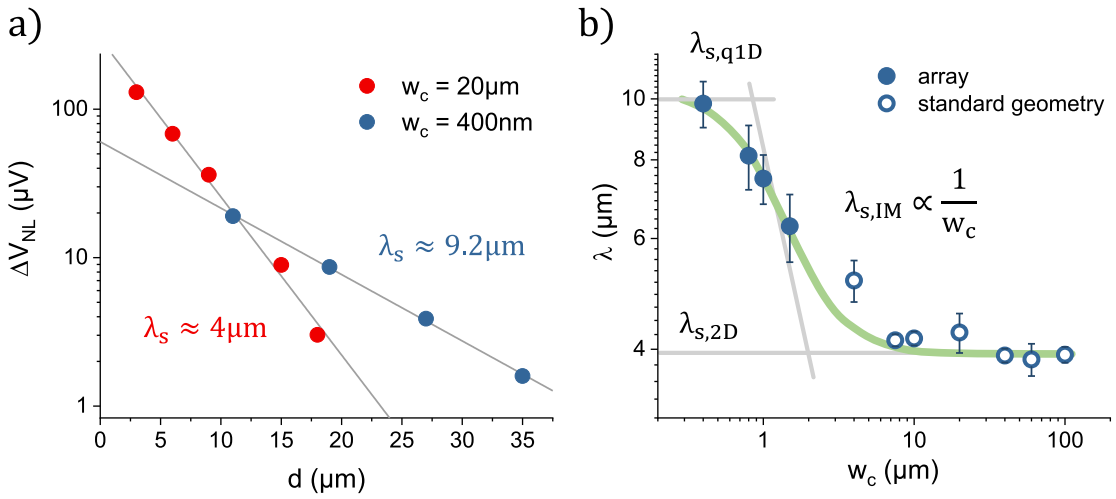

Figure 4.4. (**a**) Semi-logarithmically plotted distance dependence of the nonlocal SV signal height for a standard device with a channel width of 20 µm (red), and a device with an array of narrow channels (w_c = 400 nm) (blue). The spin diffusion length λ_s is obtained from the slope of the linear fit. (**b**) Double-logarithmically plotted channel width dependence of λ_s (determined as shown in (a), averaged over various injection currents). λ_s clearly increases with decreasing w_c, whereby three regions are distinguished: 2D limit with DP spin relaxation dominating ($\lambda_{s,2D}$); quasi-1D limit in which linear-in-k contributions of SOC are suppressed, so that DP spin relaxation is only due to the cubic Dresselhaus term ($\lambda_{s,q1D}$); intermediate regime in which $\lambda_{s,IM}$ is expected to be inversely proportional to w_c.

Note that the spin diffusion length λ_s is linked to the spin relaxation time τ_s via the diffusion constant D:

$$\lambda_s = \sqrt{D\tau_s}. \tag{4.11}$$

In Fig. 4.4b the 2D limit for large channel widths $w_c \gtrsim 7.5\,\mu\text{m}$ can be clearly identified. In this regime λ_s hardly depends on the channel width. For decreasing w_c the spin diffusion length significantly increases and slowly begins saturating for the smallest width of 400 nm, thus entering the quasi-1D limit. The width dependence of λ_s is phenomenologically highlighted in Fig. 4.4b by the green line. Due to the smooth transition between the three regimes, the $1/w_c$ dependence in the intermediate regime is not clearly distinguishable. As a tendency, the increase of λ_s is slower than expected from theory ($\propto 1/w_c$), which could be related to a decrease of the momentum relaxation time τ_p for decreasing channel widths, which was already observed by A. Holleitner et al. [107]. This counteracts the enhancement of τ_s, thus suppressing the increase of $\lambda_s \propto \sqrt{\tau_p \tau_s}$. The decrease of $\tau_p = \mu_e e/m^*$ [153] for narrower channels can be confirmed by experimentally determining the channel width dependence of the electron mobility μ_e from magneto-transport measurements (Fig. 4.5). There, a decreased value of τ_p for smaller channel widths gives rise to a lower mobility, which can be measured as an increased sheet resistance R_s

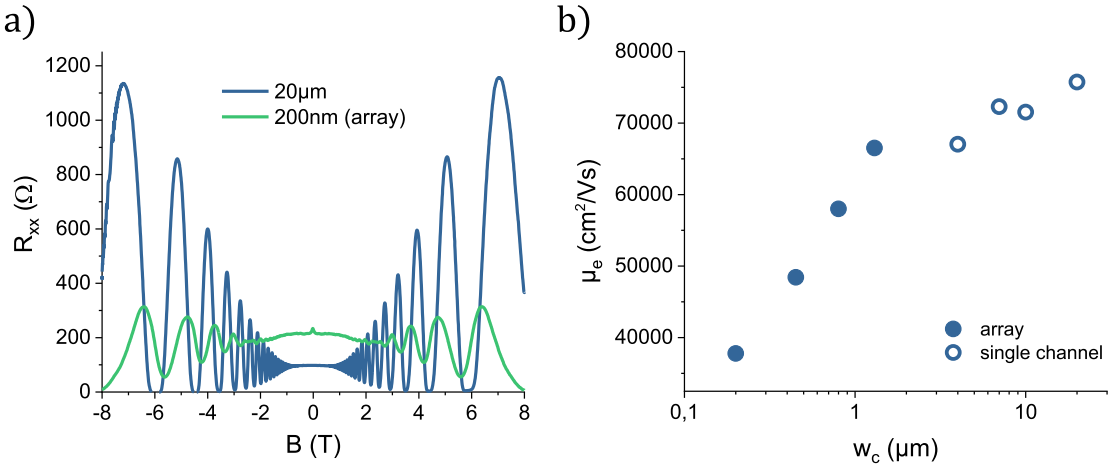

Figure 4.5. (**a**) Exemplary magneto-transport measurements for channel widths of 20 µm (blue) and 200 nm (green). (**b**) Extracted electron mobility μ_e in dependence of the channel width.

for narrower channels ($\mu_e = 1/(en_sR_s)$ [153]). The channel resistivity for narrow channels can increase due to diffuse boundary scattering at a non-smooth confining potential (boundary roughness), for instance, which is especially relevant for ion beam etched channels [153, 154]. These size effects become important for channel widths smaller than, or similar to the corresponding mean free path L_p. In experiment, L_p lies around 1 µm for channel widths larger than 1 µm, while for the narrowest channel ($w_c = 200\,\text{nm}$) $L_p \approx 0.5\,\mu\text{m}$ (Tab. I). Thus, size effects are expected to be relevant for $w_c \lesssim 1\,\mu\text{m}$, which is reflected in the width dependence of μ_e (Fig. 4.5b). The parameter values extracted from the magneto-transport measurements in dependence of the channel width, are summarized in Tab. I. It is important to note that the mean free path is on the order of the channel width for the narrow channels, so that transport is neither fully diffusive nor ballistic, but rather takes place in a crossover regime. Additionally, it has to be remarked that the magneto-transport devices are fabricated separately. Due to fabricational variations the channel widths can therefore slightly vary, such that, depending on EBL dose or development time for instance, the channels can be slightly wider/narrower than intended. Thus, the channels widths of the magneto-transport devices slightly differ from the samples which spin transport is investigated on. Interpolation allows relating charge and spin transport measurements.

w_c (µm)	N	R_s (Ω)	n_s (10^{11} cm^2)	μ_e (cm^2/V s)	L_p (µm)	D_c (m^2/s)	*sample geometry*
0.2	16	216	7.7	37790	0.47	0.11	array
0.45	15	142	9.1	48430	0.76	0.17	array
0.8	13	121	8.9	58004	0.90	0.19	array
1.3	10	108	8.7	66514	1.0	0.22	array
4	1	119	7.8	67033	0.98	0.20	single
7	1	111	7.8	72297	1.1	0.21	single
10	1	111	7.8	71527	1.0	0.21	single
20	1	98	8.4	75733	1.1	0.24	single

Table I. Summary of the values derived from magento-transport measurements in dependence of the channel width w_c. N: number of channels in region *2*; R_s: sheet resistance; n_s: charge carrier density; μ_e: electron mobility; L_p: mean free path; D_c: charge diffusion constant; sample geometry: either standard geometry with a unifrom channel width, or array geometry.

Spin relaxation time

In order to obtain the channel width dependence of the spin relaxation time $\tau_s(w_c) = \lambda_s^2(w_c)/D$ from $\lambda_s(w_c)$ (Fig. 4.4b), the diffusion constant D has to be determined. In particular, D is the *spin* diffusion constant in this case, which is denoted D_s in the following. Often, D_s is not distinguished from the charge diffusion constant D_c, which is determined by the electron mobility μ_e and the charge carrier density n_s:

$$D_c = \frac{\pi\hbar^2\mu_e n_s}{m^* e} \geq D_s. \tag{4.12}$$

However, D_s and D_c are not necessarily equal. Instead, D_s is in general smaller compared to D_c in 2DEG structures, due to electron-electron interactions, which do not conserve the spin current, thus implying an additional damping of spin diffusion (Coulomb drag) [102, 155–157]. Yet, D_s is not accessible experimentally in the investigated devices, as no Hanle signal is observable, which would allow

the direct experimental determination of τ_s [5]. Thus, τ_s has to be approximated on the basis of the charge diffusion constant D_c:

$$\tau_s(w_c) = \frac{\lambda_s^2(w_c)}{D_c} \leq \frac{\lambda_s^2(w_c)}{D_s}. \tag{4.13}$$

As $D_s \leq D_c$, the thus evaluated values of τ_s have to be regarded as a lower limit. The charge diffusion constant D_c is calculated based on Eq. 4.12 with the experimentally obtained values of μ_e and n_s (Tab. I). As n_s hardly changes as a function of the channel width, averaging about $n_s \approx 8.3 \times 10^{11}\mathrm{cm}^{-2}$, D_c consequently follows a similar trend as the width dependence of the electron mobility μ_e (Fig. 4.5b). The values of the spin relaxation time τ_s calculated from Eq. 4.13 are plotted in Fig. 4.6a. For devices with narrow channels, τ_s is found to be larger by nearly an order of magnitude, compared to wider channel widths. Similar to the width dependence of λ_s (Fig. 4.4b), the increase of τ_s with decreasing channel width is slower compared to the expected w_c^{-2} dependence. The decrease in momentum relaxation time τ_p for narrower channels, which is discussed above, is

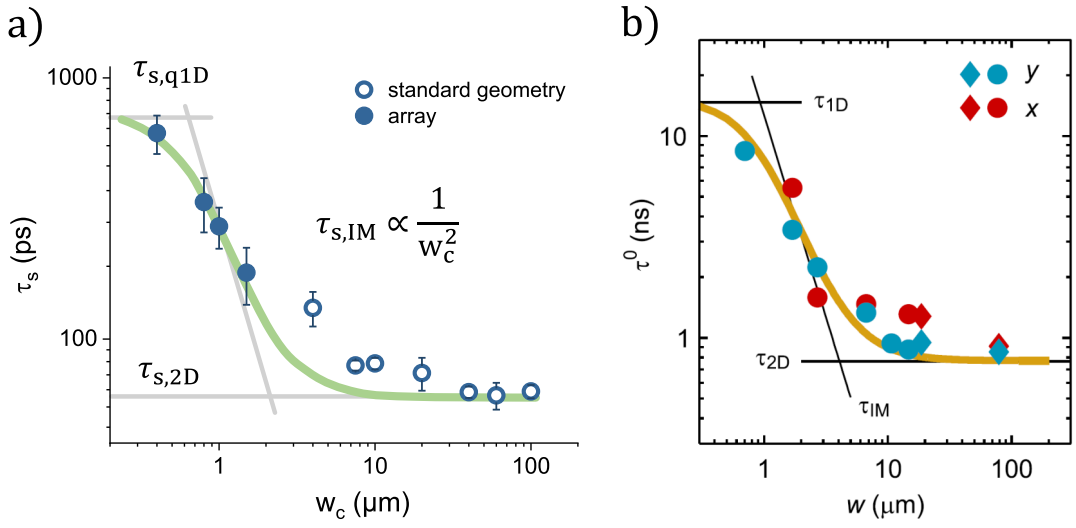

Figure 4.6. (**a**) Extracted channel width dependence of the spin relaxation time $\tau_s = \lambda_s^2/D_c$. (**b**) τ_s as a function of w_c for out-of-plane oriented spins, experimentally determined by P. Altmann et al. [102] for different channel orientations ($x \parallel [1\bar{1}0]$, $y \parallel [110]$).

already taken into account via the charge diffusion constant, however. Thus, the slower increase of τ_s compared to theory is presumably due to an overlap of the 1D and 2D regime. The channel width dependence of τ_s resembles the results of the optical spin injection experiments conducted by P. Altmann et al. [102], shown in Fig. 4.6b. In this case, however, the injected spins are oriented out-of-plane, yet τ_s is also found to increase by an order of magnitude for narrow channels ($w_c \lesssim 1\,\mu\text{m}$), while the increase of τ_s in the intermediate regime between 2-dimensional spin transport and the quasi-1-dimensional case is also slower compared to theory ($\propto 1/w_c^2$).

Spin injection efficiency

Before evaluating the spin injection efficiency, the channel width dependence of the non-local spin valve signal magnitude ΔV_{nl} is discussed for a given injector-detector distance d. In case of the standard geometry with a uniform channel width ($w_1 = w_2 = w_c$) the signal height is given by Eq. 4.1:

$$\Delta V_{nl}(d) = \frac{P^2 I_{inj} R_s \lambda_s}{w_c} \exp\left(-\frac{d}{\lambda_s}\right), \tag{4.14}$$

while in case of a geometry with an array of N narrow channels between injecting and detecting contact with an individual width w_c ($w_2 = N w_c$), the signal height is described according to Eq. 4.7:

$$\Delta V_{nl}^s(d) \approx \frac{4P^2 I_{inj} R_{s,2} \lambda_2}{w_2} \frac{1}{\left[1 + R_{s,2}\lambda_2 w_1 / R_{s,1}\lambda_1 w_2\right]^2} \exp\left(-\frac{d}{\lambda_2}\right). \tag{4.15}$$

In Fig. 4.7a the SV signal height ΔV_{nl} is plotted as a function of the effective channel width of region *2*, i.e. the part of the channel between injecting and detecting contact. For exemplary visualization, an injection current of $I_{inj} = -20\,\mu\text{A}$ (DC), and an injector-detector distance of $d = 12\,\mu\text{m}$ are regarded. For the standard geometry with a uniform channel width ($w_1 = w_2 = w_c$) the signal height (gray squares) clearly follows a $1/w_c$ dependence, as expected from Eq. 4.14 for the standard geometry (gray line). There, the injection efficiency is assumed to be $P = 0.48$, while $R_s = 100\,\Omega$ and $\lambda_s = 4.25\,\mu\text{m}$ are obtained experimentally. Ac-

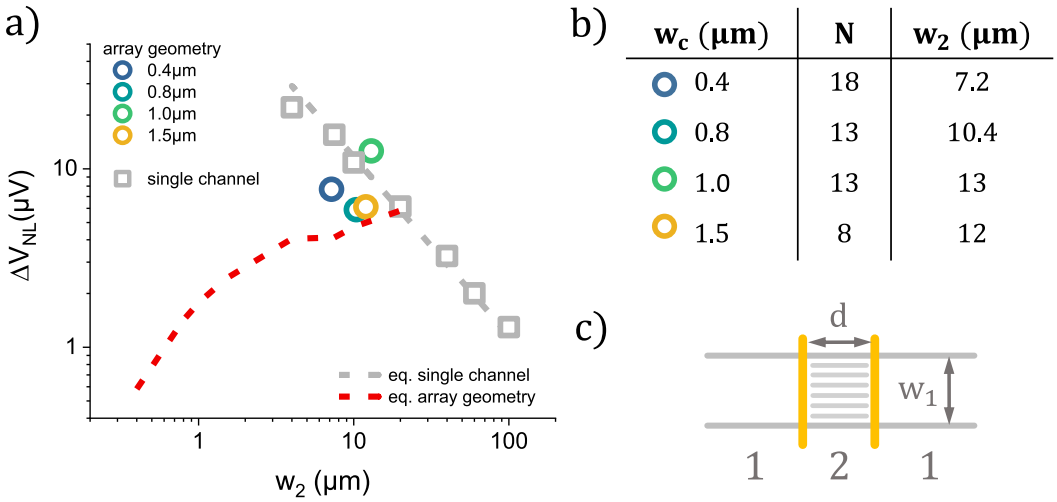

w_c (µm)	N	w_2 (µm)
0.4	18	7.2
0.8	13	10.4
1.0	13	13
1.5	8	12

Figure 4.7. (**a**) SV signal height ΔV_{nl} in dependence of the effective channel width $w_2 = Nw_c$. Symbols: experimental data for standard geometry (gray squares) and array device (circles). The signal height of the standard geometry can be described according to Eq. 4.14 (gray line). For the array geometry Eq. 4.15 yields a decreasing signal height for narrower channel widths w_2 (red line). (**b**) Number of channels N and corresponding effective channel width w_2 for the array samples. (**c**) Sketch of the device geometry, which is divided into region *1* and region *2*.

cording to Eq. 4.14 the SV signal height thus increases for narrower channels in the standard geometry. In the array geometry, on the other hand, a decrease of the effective channel width w_2 leads to a decrease of the signal height, due to an increasing value of w_1/w_2 (Eq. 4.15). Fig. 4.7a shows this decrease of ΔV_{nl} (red), based on Eq. 4.15 for a generic injection efficiency $P = 0.48$, and experimentally determined values for $R_s = R_s(w_c)$, and $\lambda_s = \lambda_s(w_c)$ (Tab. I and Fig. 4.4). Thus, with only one narrow channel between injector and detector the array geometry is in general inferior to the standard device setup in terms of the SV signal height. It is therefore preferable to implement a large number N of narrow channels, such that $w_2 = Nw_c$ is close to w_1. This allows achieving larger spin signals, close to that of the standard geometry, while at the same time spin relaxation can be significantly suppressed due to the spatial confinement perpendicular to the channel in region *2*. In Fig. 4.7a the experimental values of the signal height for the array geometry with multiple narrow channels between injector and detector are shown

as circles. The obtained signal heights lie indeed close to that of the standard geometry. The corresponding number of channels N and the effective widths w_2 are summarized in Fig. 4.7b.

The spin injection efficiency P for the array geometry (Fig. 4.7c) can be determined by rearranging Eq. 4.15:

$$P^2 = \Delta V_{nl}^s(d) \frac{w_2 R_c}{4 V_{int} R_{s,2} \lambda_2} \left[1 + R_{s,2}\lambda_2 w_1 / R_{s,1}\lambda_1 w_2\right]^2 \exp\left(\frac{d}{\lambda_2}\right). \tag{4.16}$$

There, the injection current I_{inj} is replaced by $I_{inj} = V_{int}/R_c$, where R_c is the contact resistance and V_{int} is the voltage drop at the interface of the injecting contact. For the standard geometry ($w_1 = w_2 \equiv w_c$), in which case $R_{s,1} = R_{s,2} \equiv R_s$, and $\lambda_1 = \lambda_2 \equiv \lambda_s$, Eq. 4.16 simplifies:

$$P^2 = \Delta V_{nl}^s(d) \frac{w_c R_c}{V_{int} R_s \lambda_2} \exp\left(\frac{d}{\lambda_s}\right). \tag{4.17}$$

There, the values of the sheet resistances of region *1* and *2* (R_{s1} and R_{s2}) can be derived from transport measurements (Tab. I), the injection current $I_{inj} = V_{int}/R_c$ and the dimensions of the device are known, and the corresponding spin diffusion lengths can be extracted from the distance dependence of the magnitude of the spin signal (Fig. 4.4b). In Fig. 4.8 the calculated spin injection efficiency P for an exemplary injection current of $I_{inj} = -20\,\mu\text{A}$ and an injector-detector separation of $d = 12\,\mu\text{m}$ is plotted as a function of the voltage drop at the injector V_{int}, for different channel widths. For comparison, the values of P obtained from the injection current dependence for a standard sample with $w_1 = w_2 = 40\,\mu\text{m}$ are additionally shown (gray line). There, another major disadvantage of the standard geometry with a single narrow channel becomes apparent. For a narrower channel the contact area of the injecting contact is smaller, which results in a larger voltage drop $|V_{int}|$ at the injector for a given current. This, in turn, leads to a reduction of the injection efficiency, which is found to decrease with increasing V_{int} in (Ga,Mn)As/GaAs Esaki-diode structures [18, 63, 152]. In the array geometry, on the other hand, the channel width w_c in region *2* can be reduced, while the

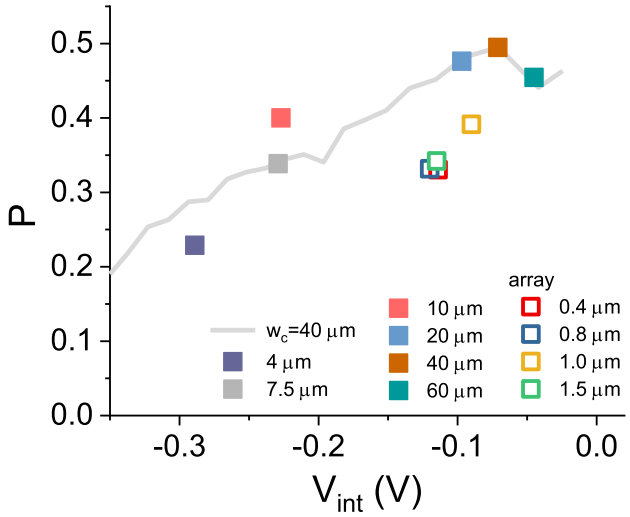

Figure 4.8. Spin injection/detection efficiency P in dependence of the interfacial voltage drop at the injector V_{int} for different channel widths. Filled squares: standard geometry; unfilled squares: array geometry; line: $P(V_{int})$ from injection current dependence of a standard sample with $w_1 = w_2 = 40\,\mu\text{m}$ for comparison.

contact area is still large enough to achieve a small interfacial voltage drop V_{int}, as the spin contacts lie on the wide part of the channel, i.e. in region *1* (Fig. 4.7c). Thus, the voltage drop at the interface is roughly the same as in case of the 20 µm wide standard sample (unfilled squares). The obtained injection efficiencies are slightly lower than for the standard device with $w_1 = w_2 = 20\,\mu\text{m}$, yet still larger compared to the standard device with a narrow 4 µm wide channel. Thus, in the array geometry larger injection efficiencies can be achieved compared to a standard sample with a single narrow channel of width w_c. At the same time, spin transport between the injecting and detecting contact approaches the quasi-1-dimensional limit in the narrow channel segments (region *2*), thus giving rise to a significant suppression of DP spin relaxation.

For the previous discussion, spin injection is assumed to take place in tunneling regime, i.e. the spin resistance of the channel $R^*_{ch} = R_s\lambda_s/w_c$ is assumed to be much smaller than the spin resistance of the tunnel contact $R^*_c = R_c/(1-P^2)$. A typical value of R^*_{ch} for a standard device with a channel width of 20 µm is $R^*_{ch} \approx 20\,\Omega$ ($R_s \approx 100\,\Omega$, $\lambda_s \approx 4\,\mu\text{m}$), while for a device with an array of 400 nm wide channels $R^*_{ch} \approx 190\,\Omega$ ($R_s \approx 150\,\Omega$, $\lambda_s \approx 9\,\mu\text{m}$, $w_2 = 18{\cdot}0.4\,\mu\text{m}$). Both values are significantly smaller than the spin resistance of the contact $R^*_c \approx 9.3\,\text{k}\Omega$ for an injection efficiency of $P \approx 0.5$. Thus, the tunneling condition is fulfilled in the devices under investigation. An additional remark concerns the effect of lateral

confinement in the array geometry. There, albeit spin transport in the presented devices can be considered to take place in a crossover between the 2D and the quasi-1D regime, the effect of the Sharvin resistance R_{sh} (Chapter 2.2) has to be discussed, which yields an additional contribution to the channel resistance in the ballistic limit (Chapter 2.2):

$$R_{sh} = \frac{2\pi h}{e^2 k_F^2 A}, \tag{4.18}$$

where A is the contact area, and k_F denotes the Fermi wave-vector. For the narrowest investigated channel width ($w_c = 400\,\text{nm}$), a Sharvin resistance of $R_{sh} \approx 390\,\Omega$ is obtained for a single channel of the array, with $n_s \approx 8.3 \times 10^{11}\text{cm}^{-2}$, and $A = 400\,\text{nm} \cdot 20\,\text{nm}$. For $N = 18$ channels in parallel, R_{sh} is consequently around $22\,\Omega$. This total contribution of the Sharvin resistance is much smaller than the contact resistance $R_c^* \approx 9\,\text{k}\Omega \gg R_{sh}$, so that the condition for efficient spin injection is not compromised. This is true, independent of the channel width, as both R_c^* and R_{sh} scale with $1/w_c$. Compared to the channel resistance $R_{ch}^* \approx 190\,\Omega$, R_{sh} is only slightly smaller. Taking into account R_{sh} modifies the channel resistance $R_{ch}^* = R_s\lambda_s/w_c$, such that $R_{ch}^* \rightarrow R_{ch}^* + R_{sh}$, which consequently enters the evaluation of the injection efficiency. Note that in the calculated values shown in Fig. 4.8 the Sharvin resistance is already taken into account. Neglecting R_{sh} yields values of P which are about 20 % larger, yet follow the similar trend.

4.1.4 Conclusion

In this chapter the effect of narrowing the channel width on spin transport properties was investigated. In particular, for narrower channels the Dyakonov-Perel spin relaxation mechanism is expected to be strongly suppressed by introducing a lateral confinement, as discussed in Chapter 2.4.2. One of the main issues regarding devices with narrower channels, however, is the disadvantageous aspect ratio of the injecting and detecting contacts. There, for narrower channels the spatial extent of the contact along the channel becomes comparable to the channel width, such that no clearly defined magnetically easy axis along the contact is formed. Thus, in non-local SV measurements the AP magnetization level is typically not resolved, such that the magnitude of the spin signal cannot be determined. There-

fore, a new device geometry was introduced in this chapter, which consists of an array of narrow channel segments between the injecting and the detecting contact, while the contacts themselves lie on the wide part of the channel. With this array geometry it is possible to realize spin transport in channels with considerable lateral confinement, approaching the ballistic 1-dimensional limit, yet, at the same time, the advantageous aspect ratio of the contacts allows ideal magnetic switching characteristics. A detailed investigation of this device geometry confirmed a significant increase of the spin diffusion length λ_s for narrow transport channels. There, in the 2-dimensional limit $\lambda_{2D} \approx 4\,\mu\text{m}$, while for the narrowest channel ($w_c = 400\,\text{nm}$) the spin diffusion length is considerably larger $\lambda_{400\,\text{nm}} \approx 9.2\,\mu\text{m}$. Regarding the width dependence of λ_s, the suppression of DP spin relaxation due to lateral confinement could be confirmed. An additional crucial advantage of the array geometry is the larger spin injection efficiency compared to a standard sample with only one narrow channel, which is related to the lower voltage drop V_{int} at the injecting contact for a given current [18, 63, 152]. This could also be confirmed experimentally.

4.2 Signatures of spin orbit coupling in spin transport measurements

In the previous chapter, it could be shown that an array of narrow channels between injecting and detecting contact results in a significant increase of the spin diffusion length λ_s. At the same time, large spin injection efficiencies and sharp magnetic switching of the contacts along their symmetry axis could be achieved. In the following chapter, SOC related effects are investigated. Due to the considerable lateral confinement in these narrow channel segments, spin transport can be regarded as being restricted to one principle axis. Therefore, the SO-field for $\vec{k}$ along the direction of the channel can be considered to be the main source of spin precession, which facilitates the qualitative interpretation of the measured spin signals. In this chapter, the SOC related signal characteristics are identified in non-local spin transport measurements and qualitatively modeled

with the extended spin diffusion equation presented in Chapter 2.6. Additionally, a distinct anisotropy of the SOC strength with regard to the crystallographic orientation is observed.

4.2.1 Device geometry and measurement setup

Sample design and measurement setup, which are based on the heterostructure system described in Chapter 3.2, are schematically sketched in Fig. 4.9. The device structure itself consists of a 20 µm wide conductive channel and two ferromagnetic (Ga,Mn)As contacts, allowing electrical injection and detection of spins. In between these contacts an array of 1 µm wide channels imposes a spatial confinement, such that spin transport between injector and detector approaches the quasi-1-dimensional limit, resulting in a partial suppression of spin relaxation (Chapter 4.1). At the same time, spin transport is restricted mainly to one axis, such that the SO-field for $\vec{k}$ along the direction of the channel can be considered to be the main source of spin precession. In order to probe the spin accumulation in a given distance d from the injecting contact, non-local spin injection experiments are conducted at a cryogenic temperature of 1.4 K (Fig. 4.9). For spin injection, a current of $I_{inj} = 4\,\mu A$ (AC) is passed through one of the ferromagnetic contacts to a reference contact, while the other contact allows the detection of the spin accumulation by measuring the non-local voltage drop V_{nl}. The spin transport between the two spin contacts is therefore not affected by drift, as the charge current only flows between the injector and the left reference contact. More details on this non-local SV setup can be found in Chapter 3.4. In addition to standard

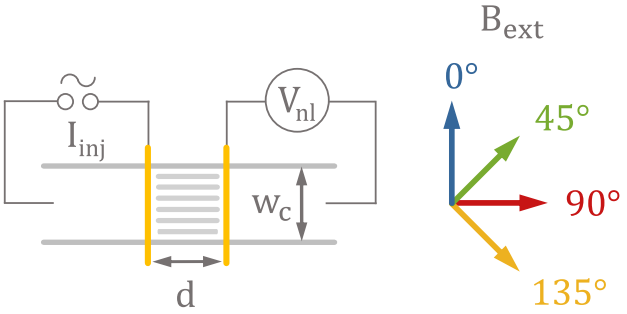

Figure 4.9. Device geometry for non-local SV measurements (array geometry) for different orientations of the external magnetic field B_{ext} (notation, i.e. angle and color, is kept consistent regarding subsequent measurements).

spin valve (SV) experiments, where the magnetic field is oriented parallel to the spin contacts (0°, Fig. 4.9), magnetic field sweeps are also performed along the main crystallographic directions, as indicated in Fig. 4.9 (45°, 90°, and 135°). In these configurations already small magnetic fields on the order of 100 mT are sufficiently large to magnetize the ferromagnetic contacts parallel to the external field, thus setting the orientation of the injected spins. The notation describing the external magnetic field direction relative to the channel orientation is based on the angles shown in Fig. 4.9 and is consistently used in the following chapters. There, 0° refers to the external magnetic field being swept parallel to the contact (standard SV measurement), while in case of 90° the magnetic field points along the channel.

4.2.2 Experimental results and discussion

In the following, channels oriented along [110] and [1$\bar{1}$0] are investigated, as along these directions the largest and smallest SOC is expected, in case of Rashba and Dresselhaus contribution being similar in strength. Additionally, the effective SO-field is oriented perpendicular to the k-vector direction in these cases (Chapter 2.3). Although spin transport is not strictly 1-dimensional in the presented devices, the discussion of SOC related effects is limited to the k-vector direction along the channel orientation, due to the strong lateral confinement in these narrow channels. Fig. 4.10a and Fig. 4.10b exemplarily show the spin signal for these two crystallographic directions for an injector-detector distance of $d = 7\,\mu\text{m}$. For each orientation, magnetic field sweeps are performed along different directions, which are specified in Fig. 4.10c. It is important to remark that the presented data is background and offset corrected. Detailed information on this phenomenological signal correction approach can be found in the appendix (App. A.1). Additionally, the 0° and 90° signals are symmetrized with respect to $\vec{B} = 0\,\text{T}$, which is justified, as in these configurations the absolute angle between the SO-field $\vec{B}_{SO}$ and the external magnetic field $\vec{B}_{ext}$ does not change upon reversing the direction of $\vec{B}_{ext}$, as illustrated in Fig. 4.10d. In particular, for the 0° signal no spin precession is expected, as $\vec{B}_{SO}$ is parallel to $\vec{B}_{ext}$. Additionally keep in mind that the orientation of the injected spin is parallel to $\vec{B}_{ext}$.

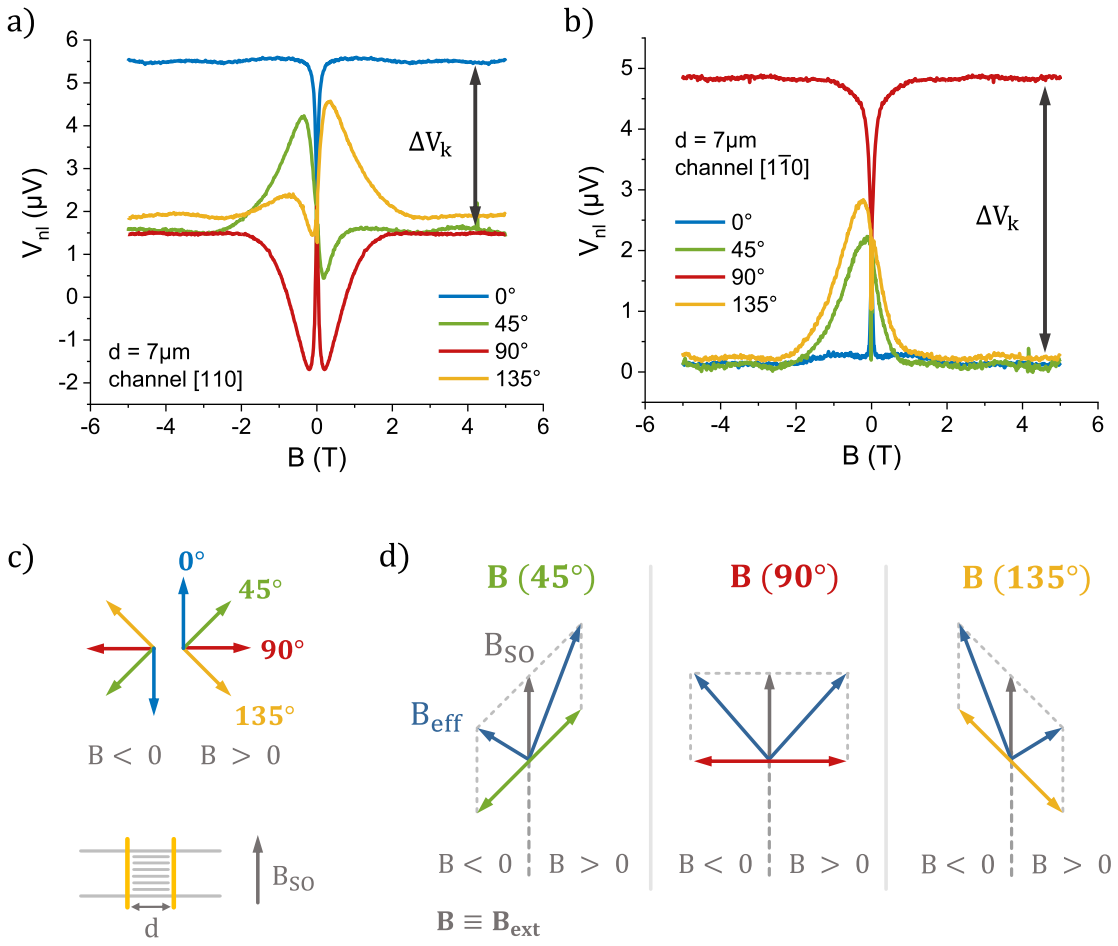

Figure 4.10. (**a**) Background and offset corrected non-local spin signal for a channel oriented along [110], for different orientations of the external magnetic field $\vec{B}_{ext}$, which are specified in (c). Injection current $I_{inj} = 4\,\mu A$ (AC), injector-detector distance $d = 7\,\mu m$, and measurement temperature $T = 1.4\,K$. (**b**) Similar measurement as in (a), but for a channel along [1$\bar{1}$0]. (**c**) Definition of the external magnetic field orientations, which correspond to the orientation of the injected spin. For channels along [110] and [1$\bar{1}$0] the SO-field $\vec{B}_{SO}$ is oriented perpendicular to the orientation of the channel. (**d**) Visualization of the effective magnetic field $\vec{B}_{eff}$, resulting from the sum of external field and SO-field ($\vec{B}_{eff} = \vec{B}_{ext} + \vec{B}_{SO}$), for the 45°, 135°, and 90° configuration.

As expected, the spin signal for a channel orientation along [110] (Fig. 4.10a) does not show a magnetic field dependence when $\vec{B}_{ext}$ is swept parallel to the contact (0°, blue), as the SO-field is parallel to the external field in this case. Therefore,

also the orientation of the injected spins is parallel to $\vec{B}_{SO}$, so that no spin precession occurs in this configuration. In case of the external magnetic field being oriented perpendicular to the contact (90°, red), i.e. parallel to the channel, a distinct dip-feature can be observed. This feature could be related to SOC induced spin precession, as the orientation of the injected spins does not align with the direction of the effective magnetic field $\vec{B}_{eff} = \vec{B}_{ext} + \vec{B}_{SO}$ (Fig. 4.10d). It is important to point out, that the observed dip-like spin signal characteristic of the 90° signal changes sign. As the signal shown in Fig. 4.10a is already shifted to 0-spin-signal, negative values indicate a spin component which arrives AP at the detector, relative to the magnetization of the detecting contact. This can only be the case if the spins precess in between the contacts, due to the presence of a SO-field. That this magnetic field dependence of the spin signal is indeed related to SOC, is further discussed in Chapter 4.2.3. Another striking characteristic is the large difference in signal magnitude at high magnetic fields between the 0° and the 90° signal, which is labeled ΔV_k in Fig 4.10a. It is shown in the following qualitative analysis (Chapter 4.2.3), that this is a result of the spin relaxation anisotropy k. As discussed in Chapter 2.4.1, the spin relaxation times can depend on the spin orientation in the DP spin relaxation regime. The spin relaxation anisotropy $k = \tau_x/\tau_y$ is then defined as the ratio of the spin relaxation time τ_x for spins oriented along $[1\bar{1}0]$, to the relaxation time τ_y for spins along [110]. Moreover, also for spins injected at an angle of 45° and 135° relative to the channel orientation spin precession is expected, as the injected spin has a component which is perpendicular to the effective magnetic field $\vec{B}_{eff}$ (Fig. 4.10d). In these configurations an asymmetric signal with respect to $B_{ext} = 0$ is obtained, which can be understood by regarding the angle between the effective magnetic field $\vec{B}_{eff}$ and the orientation of the injected spin, which corresponds to the direction of the external magnetic field $\vec{B}_{ext}$ (Fig. 4.10d). There, direction and magnitude of $\vec{B}_{eff}$ change upon reversing the sign of $\vec{B}_{ext}$, which leads to a different spin precession frequency and precession axis for $B_{ext} < 0$ and $B_{ext} > 0$, thus giving rise to the asymmetry. Moreover, the 45° signal is mirror-symmetric to the 135° signal at $B_{ext} = 0$. There, the relative orientation and magnitude of B_{eff} is the same for the 45° signal for $B_{ext} < 0$, and the 135° signal for $B_{ext} > 0$ (Fig. 4.10d). Similarly,

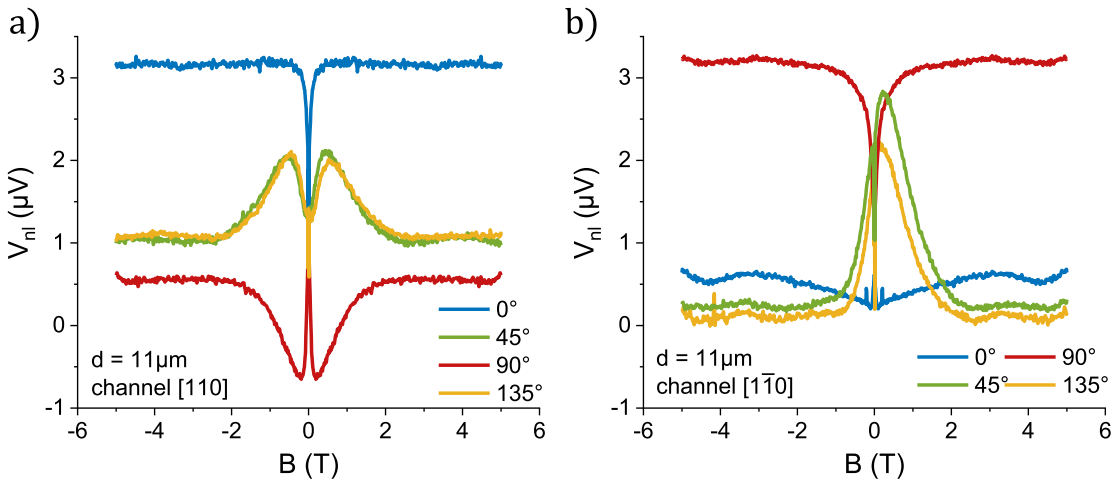

Figure 4.11. Background and offset corrected non-local spin signal for various directions of the external magnetic field (Fig. 4.10), and an injector-detector distance of $d = 11\,\mu m$. Channel orientations along [110] (**a**), and along [1$\bar{1}$0] (**b**) are investigated.

the 45° signal for $B_{ext} > 0$ corresponds to the 135° signal for $B_{ext} < 0$. This gives rise to the mirror-symmetry at $B_{ext} = 0\,T$ between the 45° signal and the 135° signal.

An entirely different signal constellation is obtained for spins moving along the [1$\bar{1}$0] direction (Fig. 4.10b). In this case, neither the 0° nor the 90° signal exhibit a relevant magnetic field dependence. One explanation could be, that the SOC strength is much weaker in this direction compared to the [110] orientation, such that no measurable spin precession is induced, even for spins oriented perpendicular to the SO-field. Furthermore, the 45° and 135° signals do not show the clear asymmetry observed in case of the channel being oriented along the [110] direction. Moreover, contrary to the [110] direction, the magnitude of the 0° signal at high magnetic fields is smaller than that of the 90° signal, while the magnitude of the absolute difference is similar. These observations are analyzed in more detail in Chapter 4.2.3.

Similar measurements are also conducted for another set of devices with a larger injector-detector distance d. In Fig. 4.11 the non-local spin signal is shown for

$d = 11\,\mu m$ and channels oriented along [110] (a) and [1$\bar{1}$0] (b), which can be compared to the previously presented measurements for $d = 7\,\mu m$ (Fig. 4.10). Most features are similar, including the magnetic field independence of the 0° signal, and the dip-shape of the 90° signal for a channel along [110], while the 90° curve for a channel orientation along [1$\bar{1}$0] does not depend on the magnetic field. The magnitude of the signal, on the other side, is in general smaller for the larger distance d, due to spin relaxation. The obvious deviation of the 45° and 135°, which are almost symmetric with respect to $B = 0\,T$ for $d = 11\,\mu m$, is also discussed in more detail in Chapter 4.2.3.

4.2.3 Qualitative analysis

Summary of the extended spin diffusion model

In the following, the most relevant features of the measurements presented in the previous chapter are discussed qualitatively, based on the expanded diffusion model, which is introduced in Chapter 2.6. There, the diffusion equation, which contains SOC, is given by:

$$d_a \frac{\partial \boldsymbol{u}}{\partial t} = \nabla \cdot (\tilde{c} \nabla \boldsymbol{u}) - \tilde{\beta} \cdot \nabla \boldsymbol{u} - \tilde{a} \boldsymbol{u}, \tag{4.19}$$

with the 3×3 unit matrix $d_a = I_3$. The matrix $\tilde{c}$ contains the diffusion constant D (isotropic diffusion):

$$\tilde{c} = \begin{pmatrix} D & 0 & 0 \\ 0 & D & 0 \\ 0 & 0 & D \end{pmatrix}, \tag{4.20}$$

while the SOC is introduced to the model by $\tilde{\beta}$, which is given by ($x \parallel [1\bar{1}0]$, $y \parallel [110]$):

$$\tilde{\beta} = -\frac{\sqrt{2}k_F L_p}{2\hbar} \begin{pmatrix} \begin{pmatrix} 0 \\ 0 \end{pmatrix} & \begin{pmatrix} 0 \\ 0 \end{pmatrix} & \begin{pmatrix} -(\alpha - \beta + \beta_3) \\ 0 \end{pmatrix} \\ \begin{pmatrix} 0 \\ 0 \end{pmatrix} & \begin{pmatrix} 0 \\ 0 \end{pmatrix} & \begin{pmatrix} 0 \\ -(-\alpha - \beta + \beta_3) \end{pmatrix} \\ \begin{pmatrix} (\alpha - \beta + \beta_3) \\ 0 \end{pmatrix} & \begin{pmatrix} 0 \\ (-\alpha - \beta + \beta_3) \end{pmatrix} & \begin{pmatrix} 0 \\ 0 \end{pmatrix} \end{pmatrix}, \tag{4.21}$$

where L_p is the mean free path, and k_F refers to the Fermi wave-vector. It is important to remark, that only the SOC terms along the channel direction are relevant for the result of the simulation, i.e. for a channel oriented along the y-direction only the contributions containing $(-\alpha - \beta + \beta_3)$ have to be taken into account, for instance. The matrix $\tilde{a}$ contains spin relaxation and introduces an external magnetic field $\vec{B}_{ext} = (B_x, B_y, 0)^T$ in the x-y-plane:

$$\tilde{a} = \begin{pmatrix} \frac{1}{\tau_x} & 0 & \frac{ge}{2m_e} B_y \\ 0 & \frac{1}{\tau_y} = \frac{k}{\tau_x} & -\frac{ge}{2m_e} B_x \\ -\frac{ge}{2m_e} B_y & \frac{ge}{2m_e} B_x & \frac{1}{\tau_z} = \frac{1+k}{\tau_x} \end{pmatrix}. \tag{4.22}$$

An additional anisotropy in the spin relaxation rate is introduced by the parameter $k = \tau_x/\tau_y$, such that, depending of the spin orientation, the spin relaxation rates differ. As discussed in Chapter 2.4.1, k is related to the SOC parameters in a DP dominated spin relaxation regime, and is in this case defined as the ratio of τ_x and τ_y ($x \parallel [1\bar{1}0]$, $y \parallel [110]$):

$$k \equiv \frac{\tau_x}{\tau_y} = \frac{\left(\alpha + (\beta_1 - \beta_3)\right)^2 + \frac{\tau_3}{\tau_1}\beta_3^2}{\left(\alpha - (\beta_1 - \beta_3)\right)^2 + \frac{\tau_3}{\tau_1}\beta_3^2}. \tag{4.23}$$

According to this expression, k not only depends on the linear Rashba (α) and Dresselhaus ($\beta = \beta_1 - \beta_3$) contributions, but also on the cubic Dresselhaus parameter β_3. The importance of the latter is determined not only by its absolute strength, but also by the factor τ_3/τ_1, which contains the effective momentum scattering times $\tau_1 = \tau_p$, and $\tau_3 < \tau_p$. There, τ_1 is equal to the momentum scattering time τ_p, while τ_3 depends on the electron scattering mechanisms in the regarded structure. Considering DP spin relaxation in bulk III-V semiconductors, $\tau_3 \approx \tau_p/6$ for impurity dominated scattering [27]. The spin relaxation time τ_z for spins oriented out-of-plane (z-direction) is then determined by the in-plane spin relaxation times τ_x and τ_y:

$$\frac{1}{\tau_z} = \frac{1}{\tau_x} + \frac{1}{\tau_y} = \frac{1+k}{\tau_x}. \tag{4.24}$$

Qualitative analysis of the extended spin diffusion model

For the simulations presented in the following, the effect of varying SOC strengths and a finite spin relaxation anisotropy $k \neq 1$ on the spin signal is investigated in detail. The simplified device geometry consists of a single channel with a width of $w_c = 1\,\mu\text{m}$. In the model, the SOC term (Eq. 4.21) is sensitive only to the total SOC strength for spins moving along the channel direction. For a channel oriented along [110] the only relevant SOC contributions in Eq. 4.21 are therefore the components of the tensor, which contain $(-\alpha - \beta + \beta_3)$, while for $[1\bar{1}0]$ only the terms containing $(\alpha - \beta + \beta_3)$ have to be taken into account. Thus, from the simulation only the total SOC strength is obtained, while it is not directly possible to distinguish between α, β, or β_3. The spin relaxation anisotropy k is regarded as an independent parameter, although it could be directly connected to SOC related quantities by Eq. 4.23. However, it is more convenient and intuitive for the qualitative analysis to vary k independently. Similar to the non-local spin injection experiments described in Chapter 4.2.1, an external in-plane magnetic field $\vec{B}_{ext}$ is applied in the simulation, which is introduced in Eq. 4.22. The injected spins are oriented parallel to $\vec{B}_{ext}$. The orientation of $\vec{B}_{ext}$ is either parallel to the channel (90° signal), or perpendicular thereto (0° signal). Note that for the considered channel orientations along [110] and $[1\bar{1}0]$, the SO-field is perpen-

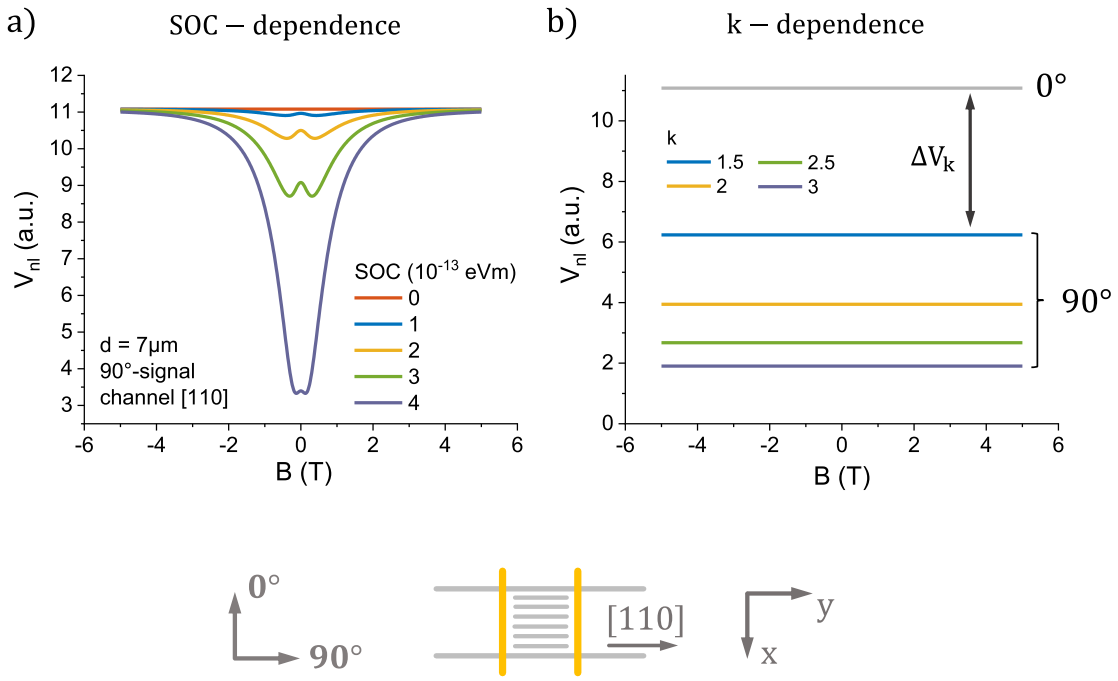

Figure 4.12. (**a**) Simulated magnetic field dependence of the 90° spin signal for different values of SOC, but with isotropic spin relaxation $k = 1$. The channel is oriented along [110], and $d = 7\,\mu\text{m}$. The dip-feature observed in experiment (Fig. 4.10a) occurs only in the presence of a finite SOC. The 0° signals coincide with the 90° curve for $SOC = 0\,\text{eV m}$, and are independent of SOC strength. (**b**) Influence of the spin relaxation anisotropy k on 0° and 90° signal, without SOC. Note that for $k = 1$ (no anisotropy), 0° and 90° signal coincide. ($\mu_e = 6.2\,\text{m}^2/\text{V s}$ (exp.), $n_s = 8.7 \times 10^{15}\,\text{m}^{-2}$ (exp.), $\tau_s = 86\,\text{ps}$ (assumed)).

dicular to the channel. Thus, in the 90° configuration the injected spins, which are oriented parallel to $\vec{B}_{ext}$, are perpendicular to the SO-field, which gives rise to spin precession.

In Fig. 4.12a the effect of SOC on the simulated magnetic field sweep is investigated in case of isotropic spin relaxation, i.e. $k = 1$. There, a distinct dip-feature becomes increasingly pronounced with increasing SOC strength, while there is no external magnetic field dependence in the absence of SOC. As orientation and magnitude of the effective magnetic field B_{eff}, which consists of external magnetic field and SO-field, is the only changing quantity in the regarded configuration, the dip-like signal characteristic can be related to spin precession. For the simulated

0° signal, on the other hand, in which case injected spin, external magnetic field, and SO-field are all oriented perpendicular to the channel direction, no magnetic field dependence is observable. The resulting signal is equal to the 90° signal in the absence of SOC (Fig. 4.12a).

According to Eq. 4.22, a finite spin relaxation anisotropy $k \neq 1$ introduces different spin relaxation times, depending on the orientation of the spin. In Fig. 4.12b simulated spin signals (0° and 90°) for various values of k are shown in the absence of SOC. Without SOC the effective total magnetic field only consists of B_{ext}, which is parallel to the injected spin. Thus, no spin precession is induced, and the non-local spin signal is independent of the external magnetic field. For isotropic spin relaxation ($k = 1$), i.e. $\tau_x = \tau_y = 2\tau_z$, 0° and 90° signal are identical, while introducing a finite spin relaxation anisotropy results in a shift of the non-local voltage level. In Fig. 4.12b this voltage shift, relative to the level obtained for $k = 1$, is labeled ΔV_k. There, for the 90° signal an increasing value of k results in a larger ΔV_k, while the signal level in the 0° configuration does not change. According to Eq. 4.22, an increase in k leads to a decreasing spin relaxation time τ_y for spins oriented along the channel (y-direction), which in turn results in a smaller spin signal for the same injector-detector distance. For spins oriented along the x-direction, on the other hand, the corresponding spin relaxation time τ_x does not change as a function of k, such that the 0° signal is not affected. This difference between τ_x and τ_y gives rise to the difference ΔV_k between the 0° and the 90° signal.

In the experimentally investigated structure, a finite SOC strength can be expected (Chapter 4.1.3), which, according to Eq. 4.23, also gives rise to a finite spin relaxation anisotropy k. Thus, both SOC and a finite value of k have to be taken into account in the simulations. In Fig. 4.13a magnetic field sweeps for various values of k and a fixed SOC strength are shown. There, the voltage level difference ΔV_k is found to increase for increasing k, but also the shape (width and amplitude) of the 90° signal is affected. The SOC strength dependence of the simulated spin signal for a fixed value of k (Fig. 4.13b), on the other hand, shows that ΔV_k is independent of SOC. However, the shape of the 90° signal changes as a function of SOC. As a tendency, the dip-like magnetic field characteristic of the

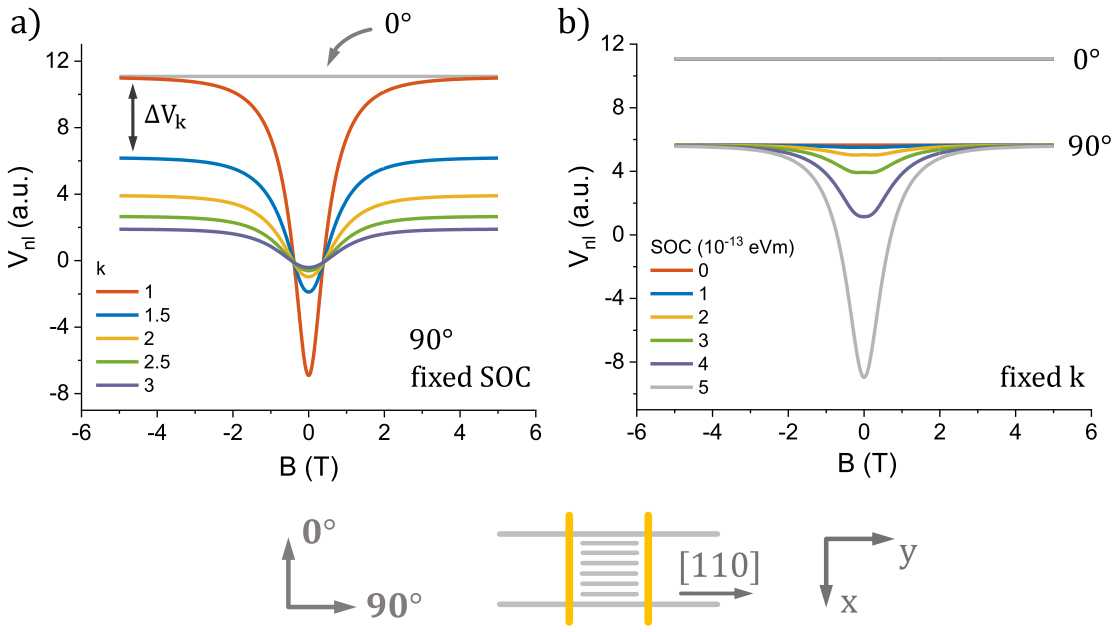

Figure 4.13. Simulated 0° and 90° spin signal. (**a**) Dependence of the spin signal on the spin relaxation anisotropy k, for a fixed SOC strength of 4.45×10^{-13} eV m. (**b**) SOC strength dependence for a fixed spin relaxation anisotropy $k = 1.6$. ($\mu_e = 6.2\,\mathrm{m^2/V\,s}$ (exp.), $n_s = 8.7 \times 10^{15}\,\mathrm{m^{-2}}$ (exp.), $\tau_s = 86\,\mathrm{ps}$ (assumed))

90° configuration, which originates from SOC, increases in amplitude and width for an increased SOC strength. From these qualitative simulations, it becomes apparent that amplitude and width of the dip-shaped spin signal strongly vary as a function of SOC *and* spin relaxation anisotropy k. The interplay between SOC strength and k thus limits the possibilities of a quantitative analysis, as discussed below in Chapter 4.2.4.

Qualitative comparison to experiment for channel ∥ [110]

A parameter range, in which the simulated spin signals qualitatively reproduce the angle dependence of the measured signal, can be approached manually. Fig. 4.14a and Fig. 4.14b show a comparison between experimental data and simulated spin signal, with a manually adjusted finite SOC strength and spin relaxation anisotropy k. The modeled 0° signal exhibits no magnetic field dependence (Fig. 4.14b), while a distinct dip-feature is observable for spins injected perpen-

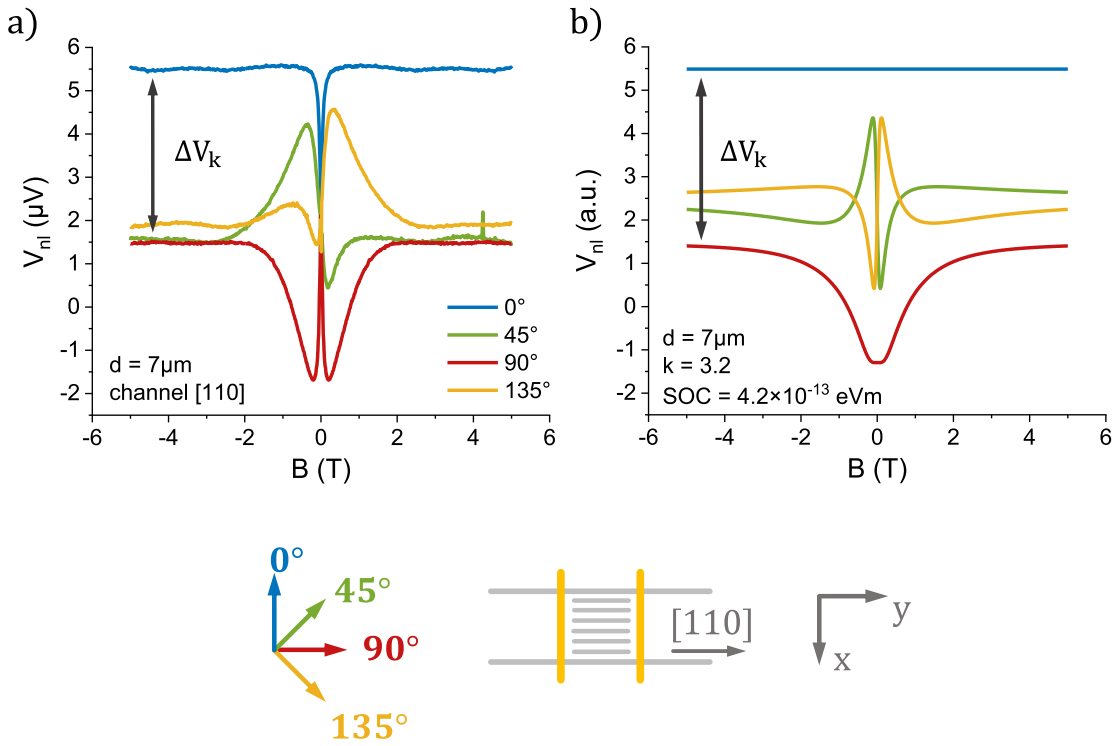

Figure 4.14. (**a**) Non-local spin signal for channel oriented along [110] for different orientations of the external magnetic field. (**b**) Simulated spin signal, which qualitatively reproduces the experiment (a) by adjusting SOC strength and k in the model. ($k = 3.2$, $SOC = 4.2 \times 10^{-13}$eV m, $\tau_x = 265$ ps, $g = -0.3$)

dicular to the contact orientation (90°), which results from a finite SOC. An important characteristic of the 90° signal is the change of sign, which indicates that a spin component arrives at the detector antiparallel to the magnetization of the detecting contact. As injecting and detecting contact are magnetized parallel by the external magnetic field, also the injected spin is oriented parallel to the magnetization of the detector. Thus, an antiparallel spin component at the detector can only be due to spin precession, causing the injected spin to precess by an angle between $\pi/2$ and $3/2\,\pi$, or integer multiples thereof. Another important characteristic of the signal is the voltage difference ΔV_k between the 0° and 90° signal at large magnetic fields. This can be reproduced by introducing a spin relaxation anisotropy k, which is basically a result of the presence of a finite SOC according to Eq. 4.23. For a magnetic field angle of 45° and 135° relative to the

orientation of the contacts, the simulated signals are asymmetric with respect to $B_{ext} = 0\,\mathrm{T}$, with the 45° signal being mirror-symmetric at $B_{ext} = 0\,\mathrm{T}$ to the 135° signal. The symmetry properties of the signal can be understood by regarding the direction of the effective magnetic field B_{eff}, as discussed above (Fig. 4.10d).
The simulated spin signal (Fig. 4.14b) agrees well with the experimentally obtained data (Fig. 4.14a), with all key features of the signal being qualitatively reproduced. This requires introducing a finite SOC strength, which also gives rise to an anisotropy of spin relaxation k. The dip-feature of the 90° signal can be attributed to the presence of SOC, while the non-local voltage difference ΔV_k is a result of the spin relaxation anisotropy k. Thus, a signature of SOC can be observed experimentally in the 90° signal, which is a central finding, especially, as SOC related spin precession is typically linked to ballistic spin transport. For the presented devices, however, spin transport is dominated by diffusion, which is apparent from the exponential decay of the spin signal with increasing injector-detector distance, but is also supported by the qualitative agreement with the purely diffusive model.
Additional remarks concern the features of the experimental non-local signals for $|B_{ext}| \lesssim 100\,\mathrm{mT}$. There, for large magnetic fields ($|B_{ext}| \gtrsim 100\,\mathrm{mT}$), injecting and detecting contact are magnetized parallel to B_{ext}, while in the low magnetic field range their magnetization can rotate, preferably towards one of the magnetically easy axes. Thus, for small external magnetic fields the magnetization of the contacts, especially their relative orientation, is not determined, such that an interpretation of the signal is not possible in this range. Additionally, it has to be remarked that the scale of the simulated curves is phenomenologically set in order to roughly match the experimental data. The main limitation of determining the scaling factor in the model is the lacking knowledge on the spin relaxation time τ_x, which cannot be accessed experimentally in the presented structure and can only be estimated on the basis of the spin diffusion length λ_s. This, however, requires assuming the spin diffusion constant D_s to be equal to the charge diffusion constant D_c, which is not necessarily the case. Instead, D_s is in general smaller compared to D_c in 2DEG structures, due to electron-electron interactions, which do not conserve the spin current, thus implying an additional damping of

spin diffusion (Coulomb drag) [102, 155–157]. Furthermore, a minor inconsistency between experiment and simulation are the voltage levels at high magnetic fields. Especially for the 45° and 135° configuration these signal levels are closer to the 90° signal in experiment compared to the model. This is most likely related to an inaccurate experimental determination of the 0-spin-signal (0-SG). The 0-SG can be extracted from SV measurements and basically lies in the middle between the parallel and the antiparallel level of the SV signal. Inaccuracies can be due to imperfect magnetic switching of the ferromagnetic contacts, which can inhibit the formation of a clearly distinguishable antiparallel magnetization level, for instance. Also, it has to be kept in mind that the parallel and antiparallel levels of the SV signal typically form along the magnetically easy axes of the ferromagnet, i.e. along [100] or [010]. The thus determined 0-SG is therefore only valid for spins oriented along these directions, yet in experiment this 0-SG is used as a reference for all orientations, as it is not possible to determine the specific 0-SG levels for spins oriented along the [110] or [1$\bar{1}$0] direction. This could lead to a shift of the experimentally obtained spin signals relative to each other, which could explain the discrepancy with regard to the simulation.

Qualitative comparison to experiment for channel ∥ [1$\bar{1}$0]

For the measurements regarded above, the channel is oriented along the [110] direction. By comparison to finite element simulations, the dip-like signal characteristic of the 90° signal could be related to the presence of a finite SOC. For a channel orientation along the [1$\bar{1}$0] direction, on the other hand, the experimental 90° signal shows no magnetic field dependence, apart from irrelevant features in the low field range (Fig. 4.15a). This implies that the SOC which affects spins moving along the [1$\bar{1}$0] direction, is much weaker compared to the previously investigated [110] orientation. This anisotropy can be understood by regarding the absolute values of the total SOC strength for channels along $\vec{k}$ ∥ [110] and

$\vec{k} \parallel [1\bar{1}0]$, which are given by ($x \parallel [1\bar{1}0]$, $y \parallel [110]$):

$$\begin{aligned} SOC_{k\parallel[110]} &= |-\alpha + 2\,\beta_3 - \beta_1| \\ SOC_{k\parallel[1\bar{1}0]} &= |\alpha + 2\,\beta_3 - \beta_1|. \end{aligned} \tag{4.25}$$

There, the linear Dresselhaus parameter β_1 is related to the expectation value of $\langle k_z^2 \rangle$, and the bulk Dresselhaus parameter γ [26, 70, 71]:

$$\beta_1 = -\gamma \langle k_z^2 \rangle \approx 1.37 \times 10^{-13}\,\mathrm{eV\,m}. \tag{4.26}$$

For (In,Ga)As/GaAs quantum well structures with low In-contents of 10 % and 12 %, which is similar to the heterostructure investigated within the scope of this thesis (9 % In-content), and an identical QW width of 20 nm, a value of $\gamma \approx -7.5\,\mathrm{eV\AA}^3$ is reported by M. Studer et al. [77]. The expectation value of $\langle k_z^2 \rangle$ can be obtained from self-consistently solving the Schrödinger-Poisson equation, which allows determining the electron wave-function for the given heterostructure. Calculating the quantum mechanical average then yields $\langle k_z^2 \rangle \approx 1.83 \times 10^{16}\,\mathrm{m}^{-2}$ for $n_s = 8.3 \times 10^{11}\,\mathrm{cm}^{-2}$. With these values for γ and $\langle k_z^2 \rangle$, $\beta_1 \approx 1.37 \times 10^{-13}\,\mathrm{eV\,m}$. The cubic Dresselhaus parameter β_3, on the other hand, is determined by the charge carrier density n_s [26, 100, 158]:

$$\beta_3 = -\gamma \frac{k_F^2}{4} = \frac{-\gamma \pi n_s}{2} \approx 9.78 \times 10^{-14}\,\mathrm{eV\,m}. \tag{4.27}$$

For n_s the experimentally determined value of $n_s = 8.3 \times 10^{15}\,\mathrm{m}^{-2}$ is taken.
The lacking dip-like characteristic in the 90° signal for a channel along $[1\bar{1}0]$ implies that the SOC strength for $\vec{k} \parallel [1\bar{1}0]$ is much weaker compared to $\vec{k} \parallel [110]$:

$$SOC_{k\parallel[110]} > SOC_{k\parallel[1\bar{1}0]} \tag{4.28}$$

Therefore,

$$\begin{aligned} |-\alpha + 2\,\beta_3 - \beta_1| &> |\alpha + 2\,\beta_3 - \beta_1| \\ |-\alpha + 5.9 \times 10^{-14}\,\mathrm{eV\,m}| &> |\alpha + 5.9 \times 10^{-14}\,\mathrm{eV\,m}|, \end{aligned} \tag{4.29}$$

which strongly suggests that

$$\alpha < 0. \tag{4.30}$$

A further analysis of the experimental data presented in Fig. 4.15a, shows that, unlike in case of the channel directed along [110], the signal level of the 0° signal is lower than that of the 90° signal. Another difference is the symmetry of the spin signal obtained for an external magnetic field orientation of 45° and 135°. In order to model the spin signal for a channel along [1$\bar{1}$0], the model geometry which is introduced in Chapter 2.6 has to be rotated by -90°, and the nomenclature of the external magnetic field direction has to be adjusted accordingly, such that $\vec{B}_{ext}$ is again directed perpendicular to the channel for the 0° signal. The resulting simulations are shown in Fig. 4.15b. Qualitatively reproducing the measurements

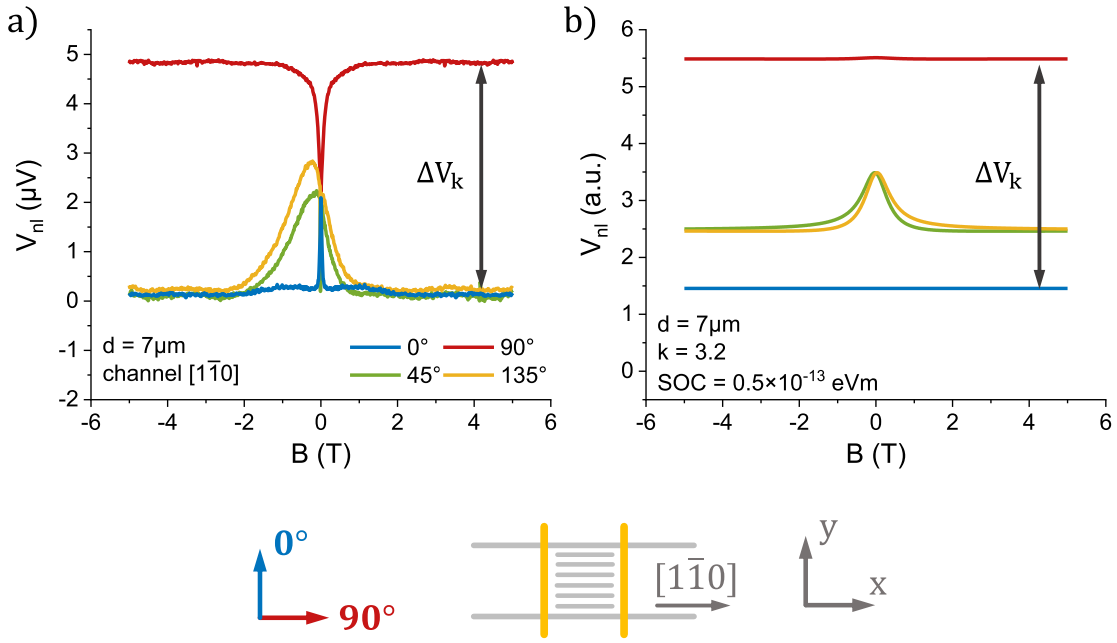

Figure 4.15. (**a**) Experimental non-local spin signals for a channel orientation along [1$\bar{1}$0] and various magnetic field directions. (**b**) Corresponding simulations, qualitatively reproducing the experimental data in (a). ($k = 3.2$, $SOC = 0.5 \times 10^{-13}$eV m, $\tau_x = 265$ ps, $g = -0.3$)

requires setting a small SOC strength, which is around an order of magnitude weaker compared to the [110] direction. The small SOC in the model results in a very weak modulation of the 90° signal and introduces a minor asymmetry of

the 45° and the 135° signal with respect to $B_{ext} = 0\,\mathrm{T}$. Without SOC the 90° signal is independent of the external magnetic field, and the 45° and 135° signals are identical. Comparison to experiment indicates the presence of a small SOC contribution due to the minor asymmetry of the 45° and the 135° signal. For the spin relaxation anisotropy k the same value as for the previously conducted calculations for a channel orientation along [110] is taken. This is reasonable, as, according to Eq. 4.23, the spin relaxation anisotropy k is given by the ratio of the spin relaxation times τ_x and τ_y, which does not change for a channel along $[1\bar{1}0]$ compared to the [110] direction. Due to the same value of k, the voltage level difference ΔV_k is identical to the simulations for a channel orientation along [110], which is in good agreement with the experimental findings.

For the channel along $[1\bar{1}0]$ the external magnetic field is oriented along the x-direction for the 90° signal in the model, not along the y-direction as for the previously regarded channel along [110]. Thus, the relaxation of spins oriented along the channel (90°) is now determined by the spin relaxation time τ_x, while for spins perpendicular to the channel (0°) spin relaxation is determined by τ_y. Due to the finite spin relaxation anisotropy $k = \tau_x/\tau_y > 1$, τ_x is now larger than τ_y. Thus, for the same injector-detector distance, the spin signal is larger for spins oriented along the channel (90°) compared the spins oriented perpendicular to the channel direction (0°). This gives rise to the reversal of the signal level magnitudes of the 0° and 90° signal compared to the [110] direction.

Furthermore, also the asymmetry of the 45° and 135° signal arises from the presence of a finite SOC strength. Without SOC the spin signals in these configurations are symmetric with respect to $B_{ext} = 0\,\mathrm{T}$, and the 45° and 135° signals are identical. Introducing a finite SOC leads to an asymmetry of the spin signal, which gets more pronounced for an increased SOC strength, as shown in Fig. 4.16. Note that the 135° signal is mirror-symmetric to the 45° signal at $B_{ext} = 0\,\mathrm{T}$. For a SOC strength of $4 \times 10^{-13}\,\mathrm{eV\,m}$, the signal approaches that of the simulation for a channel along [110] (Fig. 4.14b).

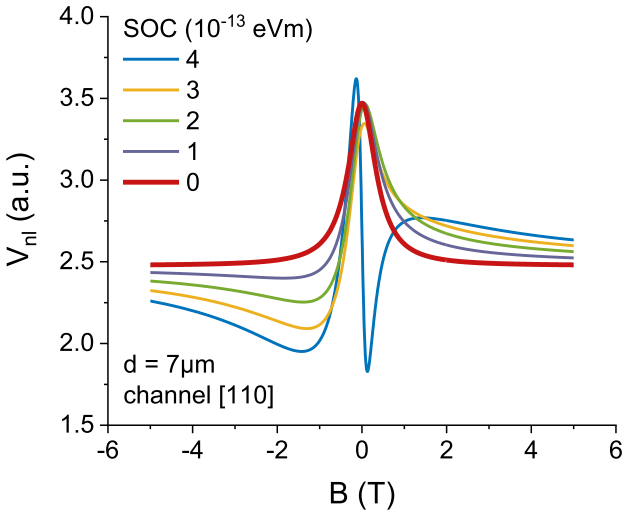

Figure 4.16. Dependence of 45° spin signal on SOC strength. In the absence of SOC the signal is symmetric (red), while a finite SOC strength introduces an asymmetry with respect to $B_{ext} = 0\,\mathrm{T}$. ($k = 3.2$, $\tau_x = 265\,\mathrm{ps}$, $g = -0.3$, $\mu_e = 6.2\,\mathrm{m^2/V\,s}$, $n_s = 8.7 \times 10^{15}\,\mathrm{m^{-2}}$)

4.2.4 Semi-quantitative evaluation

Quantitative evaluation and fitting is subject to restrictions, yet a rough estimation of the order of magnitude of some parameters, like spin relaxation anisotropy k and SOC strength, is possible. As there is a mutual dependence between many of the parameters in the model, however, some prerequisites and assumptions have to be made in order to extract conclusive values. First of all, the spin relaxation time $\tau_x = \lambda_s^2/D_c$ has to be determined by the charge diffusion constant D_c and the spin diffusion length λ_s. There, λ_s is obtained from the SV signal for an external magnetic field orientation parallel to the contact (0°). However, the switching between the parallel and antiparallel level of the SV signal takes place along one of the magnetically easy axes of the contacts, i.e. along [100] or [010]. Thus, the extracted spin diffusion length of $\lambda_s = 7.4\,\mu\mathrm{m}$ is valid for spins oriented along these directions. In the model, however, the x-direction is along $[1\bar{1}0]$, so that the spin diffusion length, which is extracted for [100], or [010] respectively, can only be used as an approximation for the spin relaxation time τ_x. Additionally, the charge diffusion constant D_c, which can be obtained from the experimental values of the charge carrier density n_s and the electron mobility μ_e, is implemented for calculating τ_x, instead of the spin diffusion constant D_s. This approximation has to be used, as there is no direct experimental access to the spin relaxation time in this structure. In general, D_s can be smaller compared to D_c due to electron-

electron interactions [102, 155–157]. Based on these approximations, a value of $\tau_x = 265\,\mathrm{ps}$ is obtained.

The fitting routine itself is based on two separate steps. First, the scaling factor in the model is determined in such a way that it matches the simulated signal height with the experimental one. For a given τ_x and $D_s = D_c$, a unique value of the scaling factor in the model can be determined from the level of the experimental 0° signal, which is magnetic field independent, and also does neither depend on the SOC strength, nor on the spin relaxation anisotropy k. The dip-like feature of the 90° signal is then fitted with the thus extracted scaling factor. There, SOC strength, and spin relaxation anisotropy k are the main fitting parameters. In order to obtain matching fits, however, it is additionally found to be necessary to allow variations of the electron g-factor, which basically scales the magnetic field axis. The spin relaxation anisotropy k is the only parameter, which introduces a voltage difference ΔV_k between the 0° and 90° signal at large magnetic fields. Therefore, k could be uniquely determined from the fitting routine. The dip-feature of the 90° signal, on the other hand, depends not only on the strength of SOC, but also on k and the g-factor. Although k is assumed to be given by the difference between the 0° and 90° data, it is therefore still not possible to obtain a unique value of the SOC strength.

The main sources of error come from a dependence of the shape of the 90° signal on the background removal procedure (App. A.1), as it affects the obtained values of SOC strength and g-factor. Significant inaccuracies may also arise from the erroneous determination of the 0-spin-signal (0-SG), which potentially gives rise to an additional artificial voltage offset. The 0-SG can only be determined from the SV signal (0°) and is then subtracted from all experimental curves, assuming it is the same for all external magnetic field directions. When this is not the case, there is an artificial shift between the considered curves, which affects the obtained values of the scaling factor and the spin relaxation anisotropy k. As a different value of k not only affects the difference between the 0° and 90° signal (ΔV_k), but also changes the shape of the 90° curve, also different values for the SOC strength and the g-factor are obtained. Thus, it has to be kept in mind that the parameter determination can only be understood as a semi-quantitative

approximation, yielding a rough order of magnitude of the extracted parameters. In Fig. 4.17a and Fig. 4.17b the internal fitting routine of the COMSOL software is applied to the experimental data obtained for two different injector-detector distances d. The magnetic field range for $|B| < 200\,\mathrm{mT}$ is not taken into account in the fitting process. The 0° signal is fitted separately in order to obtain a value for the scaling factor. Subsequently, the 90° data is matched with k, SOC and g-factor as free parameters. As the 0° signal shows no magnetic field dependence, both in experiment and simulation, the fit can be adjusted perfectly by setting the scaling factor (Fig. 4.17). The fit of the 90° signal for a injector-detector distance of $d = 7\,\mu\mathrm{m}$ shows some deviations from the experimental curves, which are most likely related to the limitations of the fitting routine, due to the before mentioned sources of inaccuracies. For a distance of $d = 11\,\mu\mathrm{m}$, on the other hand, a significantly better fitting result is obtained.

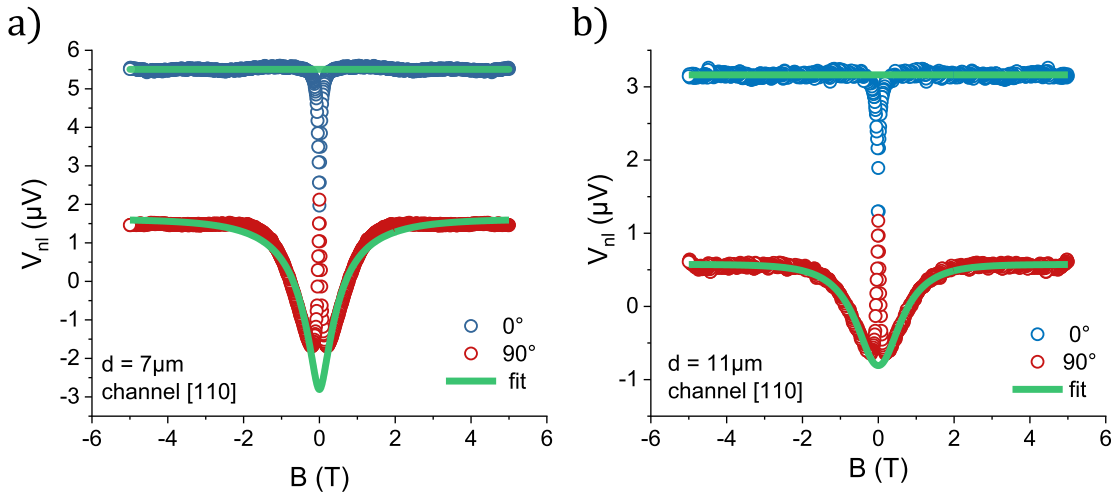

Figure 4.17. Fitted 0° and 90° spin signals for a channel orientation along [110], for two different injector-detector distances of $d = 7\,\mu\mathrm{m}$ (**a**) and $d = 11\,\mu\mathrm{m}$ (**b**). The resulting fitting curves are shown in green.

The extracted parameter values are summarized in Tab. II. There, a value for the spin relaxation anisotropy of around $k \approx 3$ can be estimated, and the strength of the total SOC lies in the lower $10^{-13}\,\mathrm{eV\,m}$ range. For the electron g-factor a value of $g = -0.34$ for $d = 7\,\mu\mathrm{m}$, and $g = -0.26$ for $d = 11\,\mu\mathrm{m}$ is obtained from the fit. These values are in good agreement with the g-factor value of $g = -0.29$, which

was experimentally determined by M. Studer et al. [159] in an $In_{0.1}Ga_{0.9}As/GaAs$ QW structure with a similar indium concentration as the heterostructure under investigation.

d (µm)	scale f'	k	$SOC_{k\parallel[110]}$ (10^{-13} eV m)	g-factor	P_{inj}
7	0.79	2.94	4.20	-0.34	0.41
11	0.78	3.11	3.29	-0.26	0.40

Table II. Summary of the parameter values obtained from the fitting routine, i.e. scaling factor f', spin relaxation anisotropy k, total SOC strength $SOC_{k\parallel[110]}$, and electron g-factor, for a channel orientation along [110]. The value of P_{inj} is calculated separately.

Additionally, from the scaling factor f', which results from the fitting approach, it is possible to obtain a value of the spin injection efficiency P_{inj}. The model simulates the spatial distribution of the spin density accumulation $s = n_\uparrow - n_\downarrow$. In this context, the scaling factor f in the model can be related to P_{inj} by the following expression (Chapter 2.6):

$$f = \frac{j\, P_{inj}}{e}. \tag{4.31}$$

However, in experiment the spin accumulation is measured as a non-local voltage drop V_{nl} at the detector. Thus, the scaling factor obtained from the fitting routine cannot be connected to P_{inj} based on this equation. Instead, an additional factor has to be taken into account, which connects V_{nl} to the spin density s. Generally, the non-local voltage can be expressed in terms of the spin accumulation μ_s:

$$V_{nl} = P_{det}\mu_s \approx P_{inj}\mu_s. \tag{4.32}$$

There, P_{det} is assumed to be equal to the injection efficiency P_{inj}, which is valid for small injection currents [18]. The spin accumulation μ_s itself is related to the

spin density s by the following expression:

$$\mu_s = \frac{s}{e\,DOS}\ , \quad \text{with} \quad DOS = \frac{m^*}{\pi\hbar^2}, \tag{4.33}$$

where DOS is the density of states of the 2-dimensional system. Thus, the non-local voltage drop V_{nl} can be linked to the spin density s:

$$V_{nl} = \frac{P_{inj}}{eg} s, \tag{4.34}$$

which requires taking into account an additional factor of P_{inj}/eg. The scaling factor f', which results from fitting the non-local voltage signal, can therefore be related to P_{inj} by the following formula:

$$f' = \frac{P_{inj}}{eg}\, f = \frac{P_{inj}^2 j}{e^2 g}. \tag{4.35}$$

Rearranging yields:

$$P_{inj} = \sqrt{\frac{f' e^2 g}{j}}. \tag{4.36}$$

For a current density of $j = 4\,\mu\text{A}/20\,\mu\text{m}$, which assumes a 1-dimensional contact with no spatial extension along the channel, similar to the simplified geometry implemented in the simulation, a spin injection efficiency of $P_{inj} \approx 40\,\%$ is obtained for both distances. This value is in excellent agreement with the previously determined injection efficiencies for an array geometry with a channel width of $w_c = 1\,\mu\text{m}$ (Chapter 4.1.3).

4.2.5 Conclusion

In this chapter, the array device geometry introduced in Chapter 4.1 was implemented in order to investigate SOC related phenomena. The transport channels were oriented along [110] and [1$\bar{1}$0], such that the corresponding SO-fields are perpendicular to the channel. Thus, if the injected spin has a component which is perpendicular to this SO-field, spin precession is induced. There, an external

magnetic field allowed setting the orientation of the injected spins, which is considered parallel to B_{ext}. For an orientation of the injected spins which is parallel to the channel direction (90° signal), a distinct dip-feature was observable in the magnetic field sweep for a channel along [110]. This signal characteristic could be attributed to the presence of a finite SOC strength, which could be confirmed qualitatively by simulations based on the extended spin diffusion model presented in Chapter 2.6. A semi-quantitative approach additionally allowed fitting the experimental data. There, the total SOC was found to lie in the low 10^{-13} eV m range. For a channel orientation along $[1\bar{1}0]$, on the other hand, no distinct SOC related features could be observed in the 90° signal, which suggests that the SOC strength along this direction is significantly smaller compared to [110]. This crystallographic orientation dependence of the SO-fields gives rise to a dependence of the spin relaxation time on the spin orientation, which is referred to as spin relaxation anisotropy k. A consequence of a finite k could be observed in experiment as a difference ΔV_k in the signal levels between the 0° and the 90° signal, at high magnetic fields. This could also be confirmed qualitatively by the extended spin diffusion model.

4.3 Gate control of spin precession

In the previous chapter, the presence of a finite SOC strength in the structure under investigation could be confirmed. There, specific spin signal characteristics could be assigned to SOC. In a next step, the gate tunability of the SOC related features is investigated. First, however, basic properties and general aspects regarding gated devices are discussed, before focusing on gated spin transport measurements, and on a qualitative comparison of the experimental data to simulations.

4.3.1 General aspects

In common semiconductor devices, gate electrodes allow modulating the properties of the transport channel, in particular the charge carrier density n_s and the

electron mobility μ_e [143, 160–162]. In most cases, gated structures consist of a thin metal layer which is electrically separated from the channel by an insulating oxide. For industrial applications, SiO_2 is commonly used as an oxide material, in particular for Si-based structures [163–165]. However, in order to reduce leakage currents between the gate electrode and the channel, it is advantageous to implement so-called high-k materials with a dielectric constant k_{diel} larger than that of SiO_2 ($k_{diel} = 3.9$) [163, 164, 166, 167]. Due to the higher dielectric constant, these oxides can be grown thicker while the capacitive coupling remains the same compared to materials with lower values of k_{diel}. In the following experiments aluminium oxide (Al_2O_3) is implemented, the dielectric constant of which lies around $k_{diel} = 8 - 10$ [163, 164, 166]. This oxide can be fabricated in a good quality by atomic layer deposition (ALD). Additionally, the large bandgap of Al_2O_3 (7 eV to 9 eV) compared to other high-k materials effectively prevents charge transfer through the oxide [163, 166, 168]. The effect of an applied gate voltage on the conductive channel can be described in a simplified picture as a parallel plate capacitor, consisting of the gate electrode and a 2DEG with a dielectric layer in between [165]. In this approximation, the relation between the charge carrier density n_s in the 2DEG and the gate voltage V_g can be given by:

$$V_g = V_{th} + \frac{en_s}{C_g}, \tag{4.37}$$

with the total capacitance C_g per unit area of the layers between the gate electrode and the channel, and the threshold voltage V_{th}. The latter defines the gate voltage at which the channel starts becoming conductive, or gets pinched-off respectively. Above V_{th} the charge carrier density changes linearly as a function of the gate voltage. It directly follows from Eq. 4.37 that applying a gate voltage allows tuning the charge carrier density n_s. A change in n_s, in turn, affects the electron mobility μ_e, which therefore also indirectly depends on V_g [143, 160–162, 169–173]. Determining the actual dependence of the electron mobility on carrier density requires distinguishing two cases. For densities below about $n_s = 2 \times 10^{12}\,\mathrm{cm}^{-2}$ the electron mobility increases with increasing n_s, which is ascribed to Coulomb scattering at charged dislocation lines or ionized impurities [160–162, 169]. For

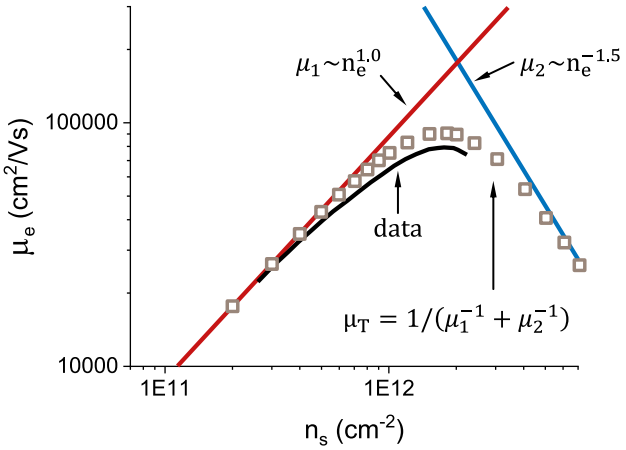

Figure 4.18. Experimental results of M. Manfra et al. [160], showing the dependence of electron mobility μ_e on the electron density n_s. There, two regions for low $n_s \lesssim 2 \times 10^{12}\,\mathrm{cm}^{-2}$ and high $n_s \gtrsim 2 \times 10^{12}\,\mathrm{cm}^{-2}$ are distinguished. Adapted from [160].

higher densities interface roughness and alloy scattering dominate, which leads to a decrease of mobility with increasing n_s [160, 161, 169, 170]. In Fig. 4.18 a typical n_s dependence of the electron mobility is shown, which is based on the experimental results of M. Manfra et al. [160]. In general, an increase of n_s leads to a larger Fermi wave-vector $k_F = \sqrt{2\pi n_s}$ [160, 174]. Considering only Coulomb scattering, which is the dominant scattering mechanism for low carrier concentrations, a larger k_F results in a smaller scattering angle for a given scattering wave-vector. Therefore, the electron mobility increases with increasing n_s. In the low density regime, a power law dependence is found to describe the relation between μ_e and n_s [160–162, 169, 171–173]:

$$\mu_e \propto n_s^a. \tag{4.38}$$

Introducing Coulomb scattering at charged dislocation lines, D. Jena et al. [171] found a theoretical value of $a = 1.5$, while the experimentally observed values range from $a = 0.6$ to $a = 2.1$ [160–162, 169, 172, 173].

A common issue with dielectric layers grown on a SC structure is the presence of so-called trap states, which act as charge traps and limit the performance of the device. These trap states arise from defects at the interface between the dielectric layer and the SC, or within the oxide layer itself [143, 167, 175–184]. Defects in Al_2O_3 can originate from aluminium or oxygen vacancies, or from aluminium or oxygen interstitials [185]. W. Choi et al. [185] derived the defect type from calculating the corresponding energy levels of these states, finding that aluminium

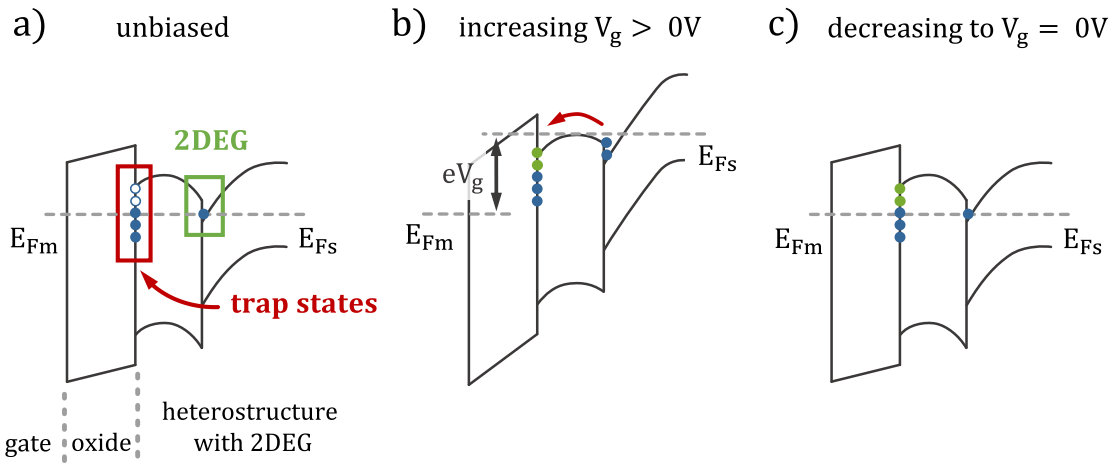

Figure 4.19. Visualization of the filling process of deep trap states, which are located at the interface between oxide and SC structure. (**a**) In the unbiased case the Fermi levels of the metal gate E_{Fm} and the heterostructure E_{Fs} are equal. The trap states are filled up to the Fermi level. (**b**) Applying a positive bias at the gate makes charge transfer from the 2DEG into the trap states possible, thus resulting in the population of more trap states. (**c**) Returning to the unbiased situation only leads to a partial depopulation of the trap states. Adapted from [178].

vacancies and oxygen interstitials act as deep acceptor sates, while aluminium interstitials act as deep donors. Oxygen vacancies, on the other hand, can form either acceptor or donor states, depending on the position of the Fermi level. Additional states within the bandgap can arise from dangling bonds at the interface between the dielectric layer and the SC. In Fig. 4.19 the trapping process is schematically depicted for a general heterostructure system with a 2DEG channel. In equilibrium, the Fermi level of the metal gate E_{Fm} and that of the SC heterostructure E_{Fs} are equal, and only the trap states below the Fermi energy are occupied (Fig. 4.19a). Applying a voltage at the gate electrode leads to a tilt of the bandstructure (Fig. 4.19b). If the applied voltage is large enough, a charge transfer from the 2DEG to the interface between oxide and SC is possible, which results in the population of additional trap states [177, 178, 181]. Subsequently decreasing the voltage at the gate leads to the emission of the trapped charges, especially those which populate energy levels close to the conduction band (shallow traps), while traps which lie deeper within the bandgap (deep traps) remain popu-

lated (Fig. 4.19c). Due to the extremely long emission times of the deep trap states (up to $\sim 10^{20}$ s at room temperature [177]), their population can be considered permanent [177, 178, 181]. Depopulation by applying a large reverse gate voltage or by thermal emission, even at room temperature, is not possible. However, populated deep trap states can be ionized by optical excitation via external illumination [177]. As a result of the additional quasi-permanently trapped charges between the gate electrode and the channel, the capacitive effect of the gate on the 2DEG is screened. A consequence observed in experiment is the irreversible shift of the threshold voltage V_{th} towards higher voltages once the applied gate voltage exceeds a critical value, a phenomenon which is commonly reported for gate-oxide-semiconductor structures [143, 167, 175–185]. Also the linear change of the charge carrier density n_s with gate voltage (Eq. 4.37) is affected, such that n_s can become independent of V_g. There, the additional electrons in the QW for an increased gate voltage can be partially transfered to the deep trap states instead of populating the transport channel, such that n_s in the channel does not increase. Additionally, at even larger gate voltages, the populated trap states can completely screen the capacitive effect of gate electrode, so that n_s does not change with V_g.

4.3.2 Gated charge transport measurements

Magneto-transport measurements are conducted on a separate set of devices, which consist only of a conductive transport channel, reference contacts, and voltage probes, allowing experimental access to the longitudinal voltage V_{xx}. The

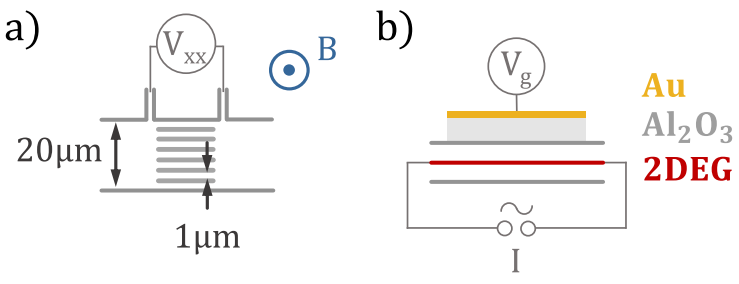

Figure 4.20. Gated magneto-transport measurement setup from the top (**a**) and from the side (**b**). For simplicity, the gate is not show in (a).

device geometry is schematically depicted in Fig. 4.20. The transport channel itself is 20 µm wide, yet between the longitudinal voltage probes the channel is divided into an array of 1 µm wide stripes, similar to the spin injection device geometry (Chapter 4.1.1). For reasons of simplicity, the gate itself is not shown in the top view (Fig. 4.20a), while on the actual sample the entire channel is covered by the gate electrode, separated from the heterostructure by 20 nm of SiO_2 and 100 nm of Al_2O_3 (Fig. 4.20b). On these devices no spin injection or detection contacts are fabricated, however, the same heterostructure system is used. Applying

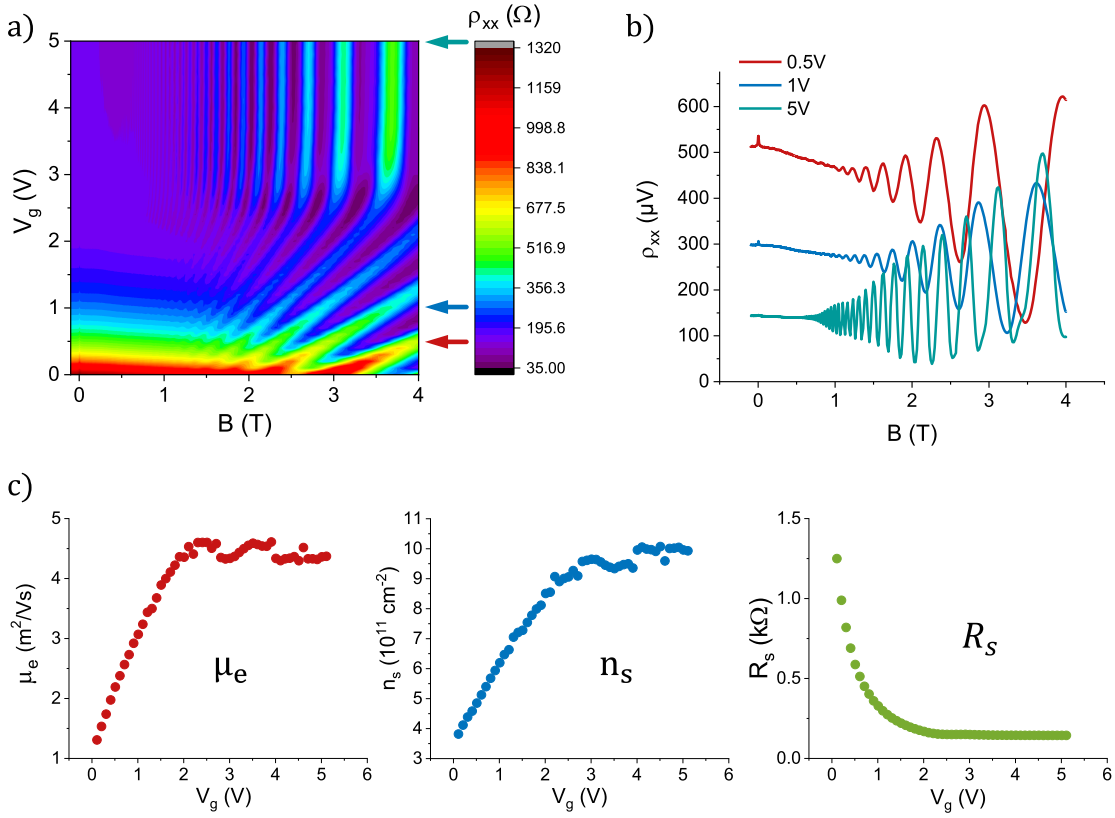

Figure 4.21. (**a**) Longitudinal resistivity ρ_{xx} in dependence of gate voltage V_g and out-of-plane magnetic field B, showing clear Shubnikov-de Haas oscillations. Gate control of the oscillation period, which is related to n_s, is only possible up to a gate voltage of about 3 V. (**b**) Single exemplary magnetic field sweeps (horizontal cut-lines in (a)). (**c**) Gate dependence of electron mobility μ_e, charge carrier density n_s, and sheet resistance $R_s = \rho_{xx}(B = 0\,\mathrm{T})$, extracted from the magneto-transport measurements shown in (a).

a current (AC) across the channel in combination with an external out-of-plane magnetic field, gives rise to Shubnikov-de Haas oscillations in the longitudinal voltage V_{xx} (magneto-transport measurement). From the period of these oscillations the charge carrier density n_s can be extracted [153], so that it is possible to resolve the gate dependence of n_s. In Fig 4.21a the longitudinal resistivity ρ_{xx} obtained from magnetic field sweeps for different gate voltages is summarized in a color-plot, along with exemplary single magnetic field sweeps in Fig 4.21b (horizontal cut-lines). There, clear Shubnikov-de Haas oscillations can be observed, especially for larger gate voltages, i.e. higher charge carrier densities. However, the period of these oscillations, thus also n_s, changes as a function of gate voltage only up to about $V_g \approx 3\,\mathrm{V}$, while the influence of the gate is significantly suppressed for larger voltages. The charge carrier density n_s can be directly obtained from the period of the Shubnikov-de Haas oscillations (Fig. 4.21c). Additionally extracting the sheet resistance $R_s = \rho_{xx}(B = 0\,\mathrm{T})$ from the transport measurements allows calculating the electron mobility $\mu_e = 1/(en_sR_s)$ [153] (Fig. 4.21c). In the gate range below $V_g \approx 3\,\mathrm{V}$, both n_s and μ_e change approximately linearly with V_g. According to Eq. 4.37, the linear change of n_s with gate voltage is expected, while the loss of capacitive coupling for larger gate voltages can most likely be attributed to the population of trap states. There, either the additional charge carriers in the channel for higher V_g directly populate these trap states, such that n_s in the 2DEG does not increase with V_g, or the effect of the gate electrode is capacitively screened for even larger gate voltages, in which case most trap states are populated (Chapter 4.3.1). Similar gate dependent transport characteristics are also reported by M. Trottmann [143] for InAs QW heterostructures.

The linear change of the charge carrier density n_s with a gate voltage is expected from Eq. 4.37. As according to Eq. 4.38 the electron mobility μ_e is related to n_s, the gate dependence of μ_e is a consequence of the dependence of n_s on V_g. In Fig. 4.22 the experimentally determined dependence of μ_e on n_s is shown, which can be compared to the experimental findings of M. Manfra et al. [160] (Fig. 4.18). As the maximum carrier density is below $1 \times 10^{12}\,\mathrm{cm}^{-2}$, the above mentioned power law dependence ($\mu_e \propto n_s^a$) is expected to describe the correlation between μ_e and n_s (Eq. 4.38). Fitting this dependence to the experimental data yields a

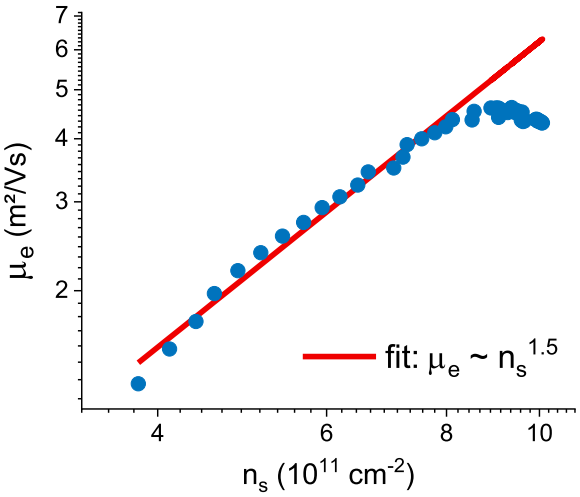

Figure 4.22. Electron mobility μ_e in dependence on charge carrier density n_s. For $n_s \lesssim 2 \times 10^{12}\,\mathrm{cm}^{-2}$ μ_e is expected to be proportional to $n_s^{1.5}$ [171], which is in perfect agreement with the experimental findings.

value of $a = 1.52$, which agrees exceptionally well with theoretical consideration ($a_{theor} = 1.5$ [171]). This suggests that the gate dependent transport properties of the investigated samples are dominated by Coulomb scattering, which affects the mobility as a function of n_s. For larger charge carrier densities ($n_s \gtrsim 8 \times 10^{11}\,\mathrm{cm}^{-2}$) the relation between μ_e and n_s deviates from the $n_s^{1.5}$ dependence, similar to the findings of M. Manfra et al. [160] (Fig. 4.18). The decrease of μ_e with increasing n_s for higher densities is attributed to an increasing importance of interface roughness and alloy scattering [160, 161, 169, 170]. As μ_e is linked to n_s, the gate dependence of μ_e is introduced by the dependence of n_s on the gate voltage. The observed increase of the electron mobility μ_e with increasing gate voltage (Fig. 4.21c) is commonly observed in gated 2DEG structures in this charge carrier density range [143, 160–162, 169–173].

Another effect of the capacitive shielding of the gate electric field due to trapped charges can be observed as a shift of the threshold voltage (V_{th}). There, a constant voltage V_{appl} is applied to the channel and the current through the channel is measured as a function of the applied gate voltage V_g (Fig. 4.23c). At a certain threshold gate voltage V_{th} the channel is fully depleted and the conduction is suppressed accordingly (pinch-off), while for larger gate voltages electrical conduction is possible. The value of the threshold voltage hardly changes and shows no significant hysteretic behavior, when sweeping the gate only in a small voltage range up to about $V_g = 2.5\,\mathrm{V}$ (Fig. 4.23a). Applying large positive voltages to the gate

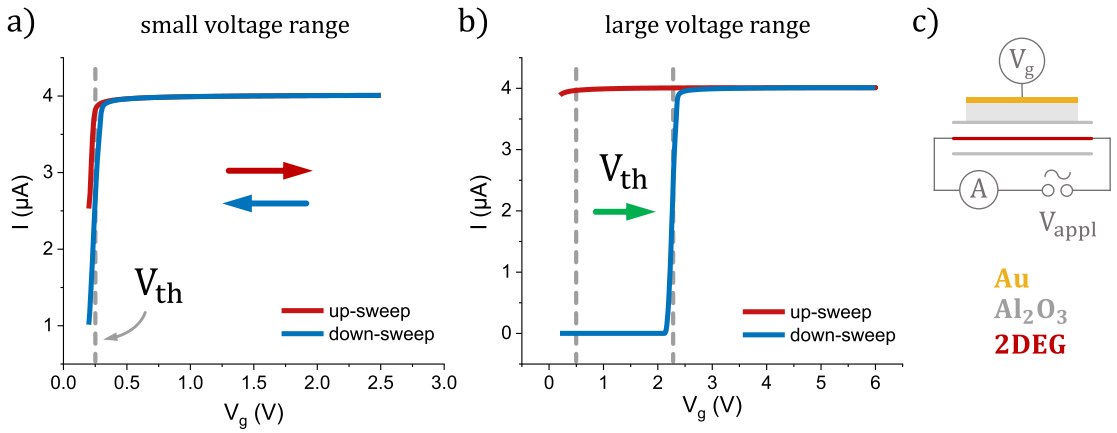

Figure 4.23. Current through the channel as a function of the applied gate voltage. There, a constant voltage $V_{appl} = 4\,\mathrm{V}$ (AC) is applied across the channel with an additional $10\,\mathrm{M\Omega}$ resistance in series, and the current through the channel is measured as a function of V_g (**c**). Sweeping the gate in a small voltage range (**a**) causes no hysteresis, while applying a large gate voltage (**b**) leads to a significant shift of the threshold voltage V_{th} towards higher values, which can only be reversed by external illumination.

leads to a shift of the pinch-off voltage towards a higher gate voltage (Fig. 4.23b). This effect cannot be reversed by applying a large negative bias at the gate. This shift of the threshold voltage is a common phenomenon observed in gated SC structures and is typically attributed to the population of deep trap states [143, 167, 175–185], as described in Chapter 4.3.1. The effect of charge trapping can only be reversed by external illumination, thus inducing optical emission of the trapped charges [177]. In the presented experiments an LED with a wavelength of about 645 nm (1.9 eV) is used for this optical excitation. In order to illuminate the structure underneath the gate electrode, the gate itself is required to be sufficiently transparent, which can be achieved by choosing a small metal layer thickness of 20 nm of gold. This thickness is, on the other hand, large enough to ensure homogeneous evaporative deposition during fabrication.

4.3.3 Gated spin transport measurements

In case of the well-known spinFET device proposed by S. Datta and B. Das [8], a gate electrode allows tuning the strength of the SOC, thus altering the spin precession frequency (Chapter 2.5). In previous publications spin precession signatures could be observed in InAs QW structures in the ballistic transport limit, i.e. for small injector-detector distances below the mean free path [20–25]. The main objective of this thesis is the experimental demonstration of gate induced spin precession in the all-semiconductor (In,Ga)As based 2DEG system described in Chapter 3.2. In the following, the general influence of the gate electric field on spin related properties, like the spin diffusion length, is discussed first, followed by gated spin precession experiments. There, gate dependent spin signal oscillations are presented, the origin of which is discussed and attributed to a gate voltage induced change of the SOC strength. The relative change of SOC with a gate voltage is evaluated and the oscillations are modeled qualitatively.

Device geometry and measurement setup

The device geometry is similar to the one described in Chapter 4.2.1, with an array of 1 µm wide stripes between the injecting and detecting contact, which themselves lie on the 20 µm wide part of the channel (Fig. 4.24). In addition, this structure is covered with an electric gate, consisting of 10 nm SiO_2 as an oxide seed layer, 100 nm of ALD-grown Al_2O_3, and 20 nm of gold on top. The thickness of the gold layer is chosen such that it is sufficiently transparent for external

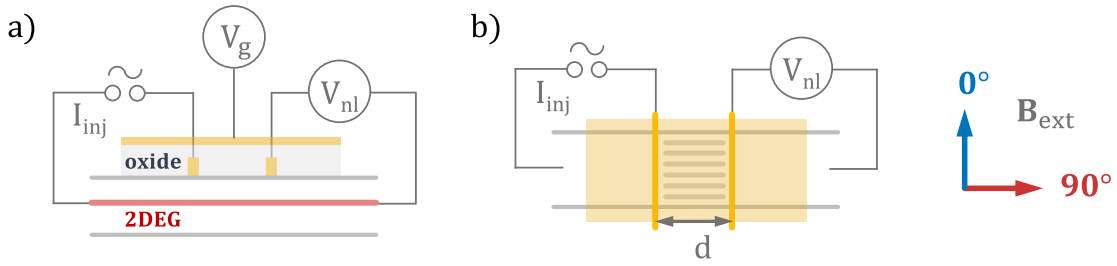

Figure 4.24. Gated device geometry and non-local measurement setup in side-view (**a**) and from the top (**b**). The notation of the external magnetic field orientations is shown on the right.

illumination, while still allowing homogeneous deposition during fabrication. The gate structure covers the entire length of the channel. Separate samples with three different distances d between injector and detector are investigated (7 µm, 11 µm and 15 µm). The following gated measurements are conducted in the non-local configuration (Fig. 4.24), while a gate voltage is applied with respect to ground. The notation concerning the external magnetic field is kept consistent with regard to previous chapters: 0° refers to the magnetic field parallel to the long axis of the contacts, while 90° denotes the orientation parallel to the channel direction. Moreover, the following measurements are conducted at a cryogenic temperature of 1.4 K with an injection current of $I_{inj} = 4\,\mu A$ (AC).

Gate dependence of spin transport properties

First, the effect of the applied gate voltage on basic properties of spin transport is discussed. Therefore, the gate dependence of the standard non-local spin valve signal with an external magnetic field parallel to the long axis of the injection/detection contact (0° signal) is investigated. In Fig. 4.25a the SV signal for an injector-detector distance of $d = 7\,\mu m$ and for an exemplary gate voltage of $V_g = 2\,V$ is shown. The channel is oriented along the [110] crystallographic direction. The spin contacts are consequently parallel to $[1\bar{1}0]$, so that for a large external magnetic field their magnetization is parallel to B_{ext}, i.e. both contacts are magnetized along $[1\bar{1}0]$ in this case. The magnetization configurations of the contacts are schematically shown as arrows in Fig. 4.25a. In the low magnetic field range, the contacts are still magnetized parallel, yet start to rotate towards one of the magnetically easy axes, i.e. towards [100] or [010]. Upon reversing the external magnetic field direction, one of the contacts eventually switches its magnetization by 180°, such that the antiparallel configuration is established. Notably, in the antiparallel configuration both contacts are also magnetized along [100], or [010] respectively. From these non-local SV measurements two important quantities can be extracted. First of all, the signal height $\Delta V_{nl,SV}$ of the standard SV signal can be obtained. In this case, injecting and detecting contact are magnetized along [100] or [010], i.e. at a ±45° angle with respect to the channel orientation. Another important value is the difference between the 0-spin-signal (0-SG) and the spin

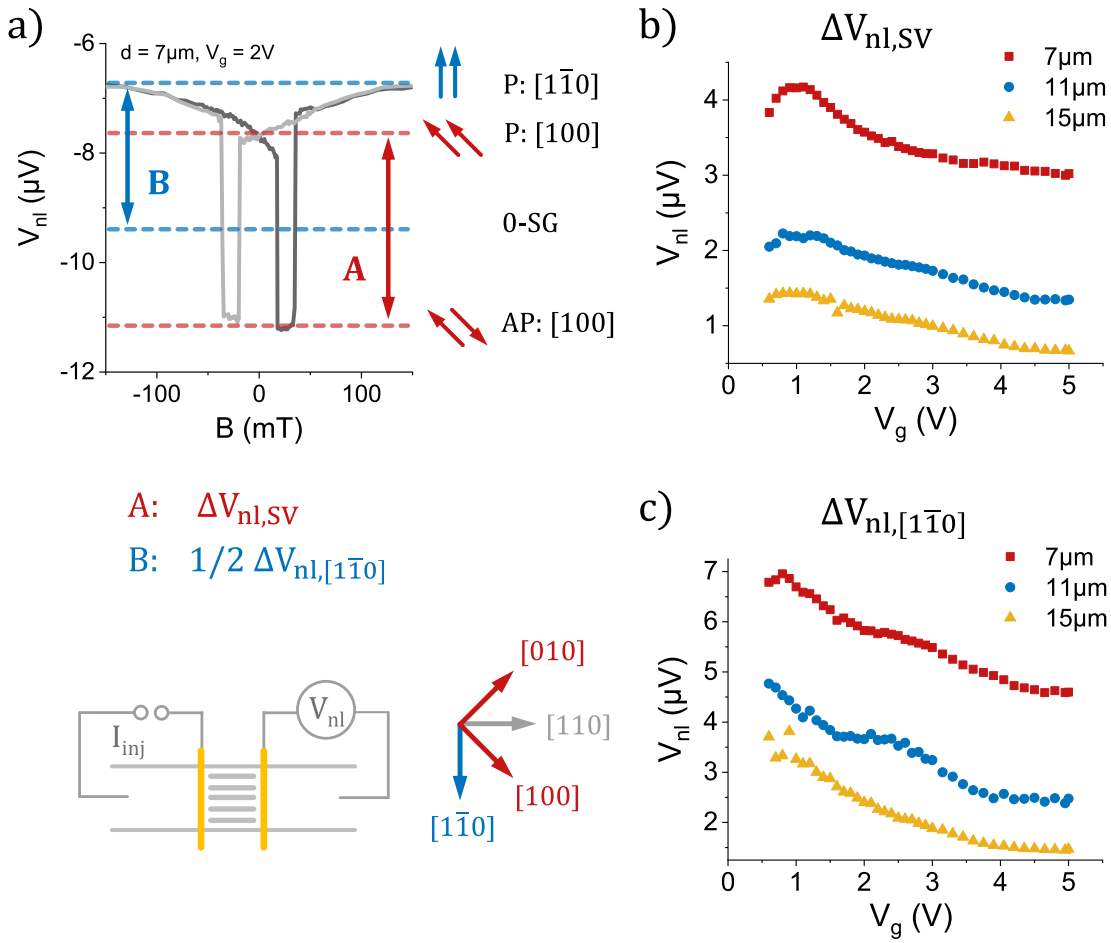

Figure 4.25. (**a**) Exemplary SV signal for $V_g = 2\,\mathrm{V}$ and $d = 7\,\mu\mathrm{m}$. For large magnetic fields the contacts are magnetized parallel to their long axis ([1$\bar{1}$0]), as indicated by the arrows. For smaller fields, the contacts rotate towards one of the magnetically easy axes ([100], or [010]), eventually switching to the antiparallel configuration (AP). From these SV measurements, two quantities can be extracted: the SV signal height $\Delta V_{nl,SV}$ (A), and the non-local voltage drop for spins oriented along [1$\bar{1}$0], $1/2\Delta V_{nl,[1\bar{1}0]}$ (B). (**b**) Gate dependence of SV signal height $\Delta V_{nl,SV}$, i.e. for spins oriented along [100], or [010] respectively. (**c**) Gate dependence of the spin signal $\Delta V_{nl,[1\bar{1}0]}$, in which case the spins are oriented along [1$\bar{1}$0].

signal level for high external magnetic fields. In this case, the contacts are magnetized parallel to their long axis ([1$\bar{1}$0]). This quantity is denoted as $1/2\,\Delta V_{nl,[1\bar{1}0]}$, as indicated in Fig. 4.25a. Notably, the 0-SG corresponds to the middle between the

parallel and antiparallel signal level of the SV signal for the contacts magnetized along [100], or [010] respectively. The signal height $\Delta V_{nl,[1\bar{1}0]}$ can be considered as an equivalent to the SV signal height with contacts oriented along $[1\bar{1}0]$, which is not directly observable in experiment, as the magnetic switching of the contacts is along the [100] or [010] direction instead ($\Delta V_{nl,SV}$). The gate dependence of the spin signal heights for all investigated injector-detector distances is summarized in Fig. 4.25b for $\Delta V_{nl,SV}$, and in Fig. 4.25c for $\Delta V_{nl,[1\bar{1}0]}$. In both cases, the spin signal height clearly decreases with increasing gate voltage. There, the decrease of the signal height for spins oriented along the contact ($\Delta V_{nl,[1\bar{1}0]}$) is significantly larger compared to $\Delta V_{nl,SV}$. In order to explain these observations, the general form of the SV signal height for the array geometry is regarded, which can be approximated by Eq. 4.7:

$$\Delta V_{nl}(d) \approx \frac{4P^2 I_{inj} R_{s,2}\lambda_2}{w_2} \frac{1}{\left[1 + R_{s,2}\lambda_2 w_1 / R_{s,1}\lambda_1 w_2\right]^2} \exp\left(-\frac{d}{\lambda_2}\right), \tag{4.39}$$

which is discussed in detail in Chapter 4.1.3. The spin diffusion length of the channel segment between the contacts is denoted λ_2, while for the other regions of the transport channel it is referred to as λ_1. Note that this equation does not directly depend on the orientation of the injected spin, such that it holds for the spin signal height $\Delta V_{nl,SV}$, as well as for $\Delta V_{nl,[1\bar{1}0]}$. The decreasing trend of these two quantities with increasing gate voltage could be related to a gate dependence of the sheet resistance R_s, the spin diffusion length λ_2, and/or the injection efficiency P. Accordingly, differences between $\Delta V_{nl,SV}$ and $\Delta V_{nl,[1\bar{1}0]}$ could be due to differences in the spin diffusion length, and/or differing injection efficiencies for spins oriented along [100] compared to $[1\bar{1}0]$. The sheet resistance R_s, on the other hand, is an electronic property and therefore does not depend on the spin orientation. Additionally, $R_{s,1}$ and $R_{s,2}$, as well as λ_1 and λ_2, are assumed to exhibit a similar gate dependence, such that the ratio of $R_{s,2}\lambda_2/R_{s,1}\lambda_1$ in Eq. 4.39 is independent of the gate voltage.

In the following, the gate dependent parameters entering Eq. 4.39 are investigated in detail. First of all, based on the charge transport measurements presented in Chapter 4.3.2, the sheet resistance $R_s \equiv R_{s,2}$ is found to decrease with increasing

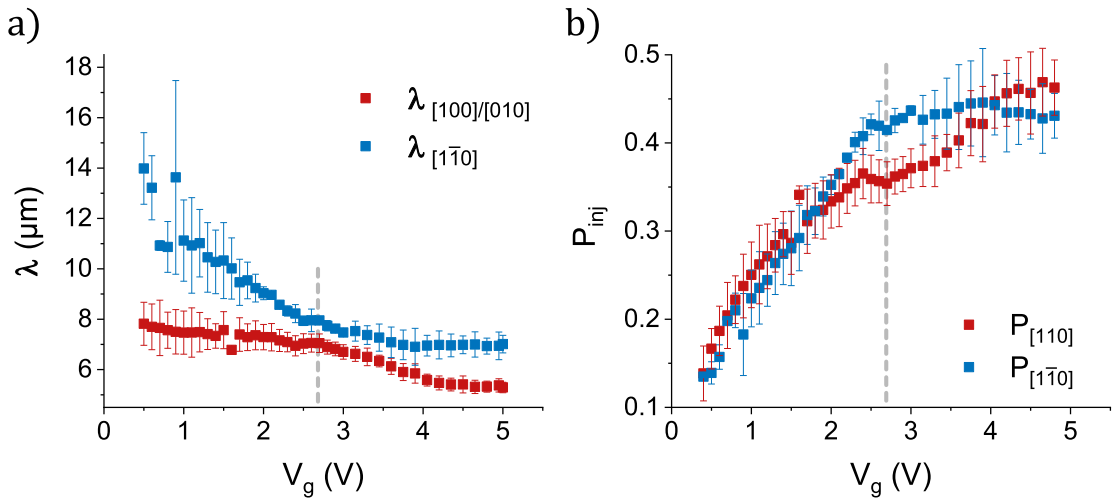

Figure 4.26. (**a**) Gate dependence of spin diffusion length $\lambda_{[100]}$, for spins oriented along [100], or [010] respectively, and $\lambda_{[1\bar{1}0]}$ for spins along [1$\bar{1}$0]. Both values are determined experimentally from distance resolved SV measurements (Fig. 4.25). (**b**) Gate dependence of injection efficiency $P_{inj} \equiv P$, for spins oriented along [100] or [010], and along [1$\bar{1}$0]. Note that the error bars indicate the error of the fit.

gate voltage (Fig. 4.21), which partially contributes to the decreasing trend of ΔV_{nl} with increasing gate voltage (Fig. 4.25). Moreover, the spin diffusion length $\lambda_s \equiv \lambda_2$ can be obtained from the exponential decay of the spin signal with injector-detector distance d. As two different spin signals are investigated, i.e. $\Delta V_{nl,SV}$ and $\Delta V_{nl,[1\bar{1}0]}$, the corresponding spin diffusion lengths $\lambda_{SV} \equiv \lambda_{[100]}$ and $\lambda_{[1\bar{1}0]}$ are also determined separately. In Fig. 4.26a the gate resolved spin diffusion lengths are shown, which both exhibit a clear decreasing trend with increasing gate voltage, with a distinct change of slope at about $V_g \approx 2.7\,\mathrm{V}$, which coincides with the value at which screening effects reduce the influence of the gate on the channel, as already discussed in connection with the charge transport measurements in Chapter 4.3.1. The decrease of λ_s with increasing gate voltage indicates a gate dependent change of the DP spin relaxation rates, which could result from a gate voltage dependence of the SOC strength. In particular, for spins oriented along [1$\bar{1}$0] the DP related spin diffusion length $\lambda_{[1\bar{1}0]}$ can be linked to the SO related

parameters by the following expression:

$$\lambda^2_{[1\bar{1}0]} = \frac{\hbar^4}{2m^{*2}} \left[(\alpha + (\beta_1 - \beta_3))^2 + \gamma_3^{-1}\beta_3^2 \right]^{-1}, \tag{4.40}$$

as discussed in Chapter 2.4.1. For spins oriented along [100] or [010] the corresponding spin diffusion length $\lambda_{[100]}$ is given by:

$$\lambda^2_{[100]} = \frac{\hbar^4}{4m^{*2}} \left[\alpha^2 + (\beta_1 - \beta_3)^2 + \gamma_3^{-1}\beta_3^2 \right]^{-1}. \tag{4.41}$$

Thus, the difference in spin diffusion length between spins oriented along $[1\bar{1}0]$ and [100], or [010] respectively, can be a result of the anisotropy of the SO-fields with respect to the crystallographic orientation.
Another quantity which can contribute to the gate dependence of the spin signal height ΔV_{nl}, is the spin injection efficiency P_{inj}. It can be estimated by rearranging Eq. 4.39:

$$P^2 = \Delta V_{nl}(d) \frac{w_2}{4 I_{inj} R_{s,2} \lambda_2} \left[1 + R_{s,2}\lambda_2 w_1 / R_{s,1}\lambda_1 w_2 \right]^2 \exp\left(\frac{d}{\lambda_2} \right). \tag{4.42}$$

There, the gate dependence of the spin diffusion length $\lambda_s \equiv \lambda_2$ (Fig. 4.26a), as well as the experimentally obtained values of the sheet resistance $R_{s,2}$ (Chapter 4.3.2), and the SV signal height ΔV_{nl} (Fig. 4.25) are implemented. The injection current is $I_{inj} = 4\,\mu\text{A}$, the effective width of channel segment between injecting and detecting contact is $w_2 = (13 \cdot 1\,\mu\text{m})$, and the width of the channel in the remaining regions is $w_1 = 20\,\mu\text{m}$. The ratio of $R_{s,2}\lambda_2 / R_{s,1}\lambda_1$ is regarded to be independent of the gate voltage, as $R_{s,1}$ and $R_{s,2}$, as well as λ_1 and λ_2, are assumed to exhibit a similar gate dependence. Therefore, the corresponding values of the un-gated devices (Chapter 4.1) are taken to calculate this ratio ($R_{s,1} \approx 100\,\Omega$, $R_{s,2} \approx 115\,\Omega$, $\lambda_1 \approx 4\,\mu\text{m}$, and $\lambda_2 \approx 7.5\,\mu\text{m}$). The calculated spin injection efficiencies P_{inj} for spins oriented along $[1\bar{1}0]$, and along [100], or [010] respectively, are shown in Fig. 4.26b. For both orientations P_{inj} shows a clear increasing trend with increasing gate voltage. Also a change of the gate dependence at about $V_g \approx 2.7\,\text{V}$ is observable. This can be related to the changing gate response of the spin diffusion

length, which directly enters Eq. 4.42, and is itself a result of screening effects due to the population of deep trap states (Chapter 4.3.1). The difference between $P_{inj,[100]}$ and $P_{inj,[1\bar{1}0]}$ could be either related to measurement errors, or indicate a minor anisotropy of the injection efficiency with respect to the orientation of the injected spin, which is reported for similar structures [137, 186]. In the intermediate gate voltage region between $V_g = 2\,\mathrm{V}$ and $V_g = 3\,\mathrm{V}$, in which the spin diffusion length λ_s, as well as the charge transport properties (n_s, R_s, and μ_e) are comparable to the un-gated devices presented in Chapter 4.1, the obtained values of the spin injection efficiency P lie in a range between 35 % and 45 %, similar to the value of P for the un-gated samples.

Gate induced spin signal oscillations

For narrow channels along [110] and [1$\bar{1}$0] the SO-field is expected to be oriented perpendicular to the channel direction. Thus, in the standard SV configuration (0°) the orientation of the injected spins aligns with the direction of the effective SO-field, so that no spin precession due to SOC is expected. This measurement setup therefore allows probing basic spin transport properties of the channel, like the spin diffusion length. SOC related effects, on the other hand, are expected to be most pronounced for spins oriented parallel to the channel, i.e. perpendicular to the SO-field. This configuration is established by setting the magnetization of the contacts by applying an external magnetic field perpendicular to the long axis of the contacts (90°, Fig. 4.27). The gate dependent non-local spin signals for magnetic field sweeps along the 0° and 90° direction are shown in Fig. 4.27 for an exemplary injector-detector distance of $d = 7\,\mu\mathrm{m}$ and a crystallographic orientation of the channel along [110]. There, the spin independent background is removed and the voltage offset is corrected (App. A.1). For the 90° signals shown in Fig. 4.27a, a distinct dip-like feature is observable, which, concluding from the simulations presented in Chapter 4.2, can be attributed to the presence of SOC. The orientation of this dip-like signal characteristic changes, depending on the applied gate voltage. This is indeed a remarkable observation, as it hints at a gate tunability of the SOC strength, which is discussed in more detail in the following. The gate resolved 0° signal, on the other hand, does not show a

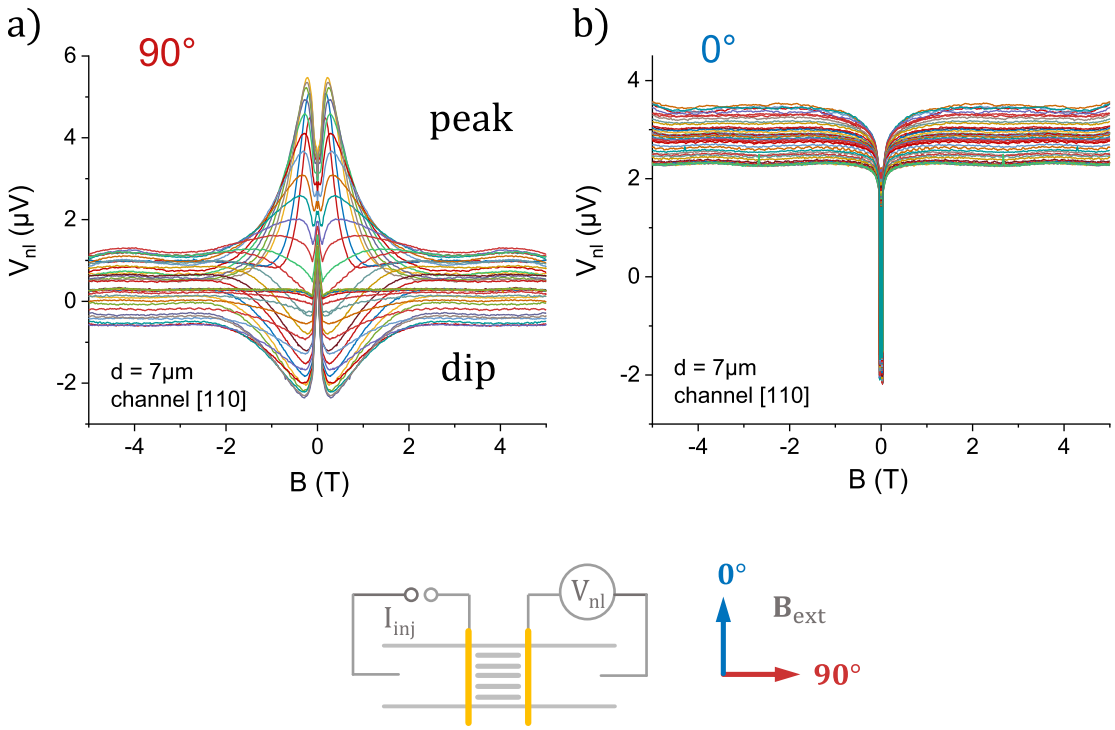

Figure 4.27. (**a**) Gate dependent 90° non-local spin signal for an injector-detector distance of $d = 7\,\mu\text{m}$ and a channel orientation along [110]. The focus is on the dip-like/peak-like magnetic field dependence of the signal, especially its change of orientation, thus the color-coded gate voltage values are not labeled. (**b**) Similar measurements as shown in (a) for a magnetic field orientation along the contact (0°). There, the signals are independent of the external magnetic field, apart from the low magnetic field range (SV signal).

dependence on the magnetic field (Fig. 4.27b), as the injected spins are oriented parallel to the SO-field. For both magnetic field orientations, a spread of the signal level at high magnetic fields can be observed, which is presumably related to the gate dependent change of injection efficiency P, sheet resistance R_s, and spin diffusion length λ_s, according to Eq. 4.39. But also inaccuracies concerning the determination of the 0-SG could add an artificial signal offset. Notably, the features occurring in the low magnetic field range for $|B| \lesssim 100\,\text{mT}$, which are observable for both magnetic field orientations, are not considered relevant for the interpretation of effects associated with spin precession. Instead, for low magnetic fields the magnetization of the contacts starts to rotate towards a magnetically

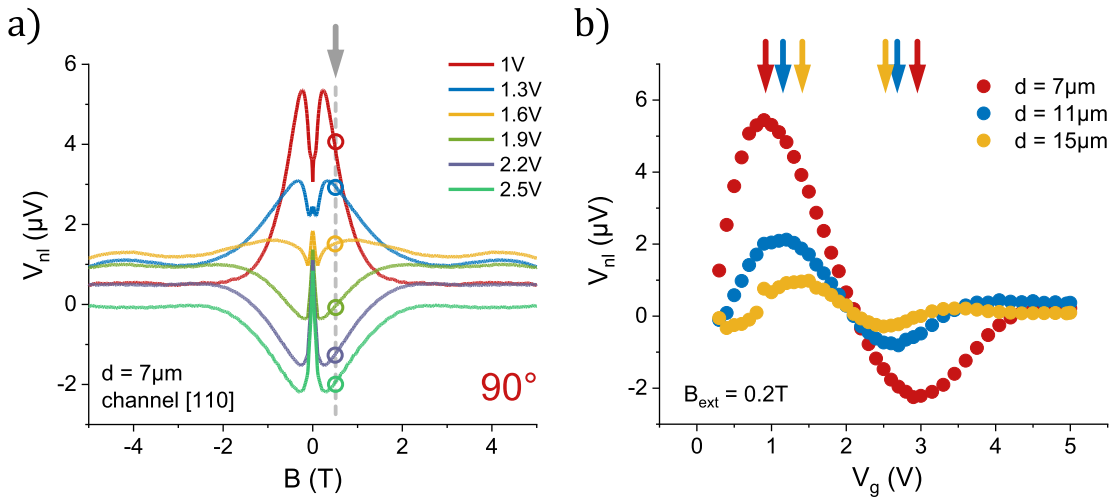

Figure 4.28. (**a**) Gate dependent non-local spin signal for a magnetic field orientation along the channel (90° signal), for selected gate voltage values. (**b**) Gate dependent oscillations of the spin signal for a fixed external magnetic field of $B_{ext} = 200\,\mathrm{mT}$, extracted from the cut-line through the magnetic field sweeps shown in (a). The oscillations can be reproduced for different injector-detector distances d. The arrows highlight the minimum and maximum of the signal, showing a clear decrease of the oscillation period with increasing distance d.

easy axis ([100] or [010]), such that the relative magnetization of the contacts is not determinable, which prevents an interpretation of the spin signal.

The gate induced alteration in the shape of the 90° signal, which changes from a dip-like feature to a peak-like signal characteristic, strongly implies a tunability of SOC. In the following, this signature of spin precession observed in the 90° signal is further analyzed by regarding the spin signal at a fixed external magnetic field value, which corresponds to a cut-line through the magnetic field sweeps at a fixed value of B_{ext}, as indicated in Fig. 4.28a. There, for a sufficiently large magnetic field ($|B_{ext}| \gtrsim 100\,\mathrm{mT}$), the magnetization of injecting and detecting contact, and hence also the orientation of the injected spin, is parallel to $\vec{B}_{ext}$, which, in case of the 90° signal, is parallel to the channel orientation. For an exemplary cut-line along $B_{ext} = 0.2\,\mathrm{T}$, remarkably well-defined gate dependent spin signal oscillations are observable for all three investigated injector-detector distances (Fig. 4.28b). This observation agrees well with the expected behavior. There, the SOC strength is expected to change as a function of the applied gate voltage, which gives rise to

a gate dependent variation of the SOC induced spin precession frequency. Thus, the angle at which the injected spins arrive at the detector depends on V_g, such that the measured spin signal is expected to oscillate between the P and the AP signal level as a function of V_g. Details can be found in Chapter 2.5.

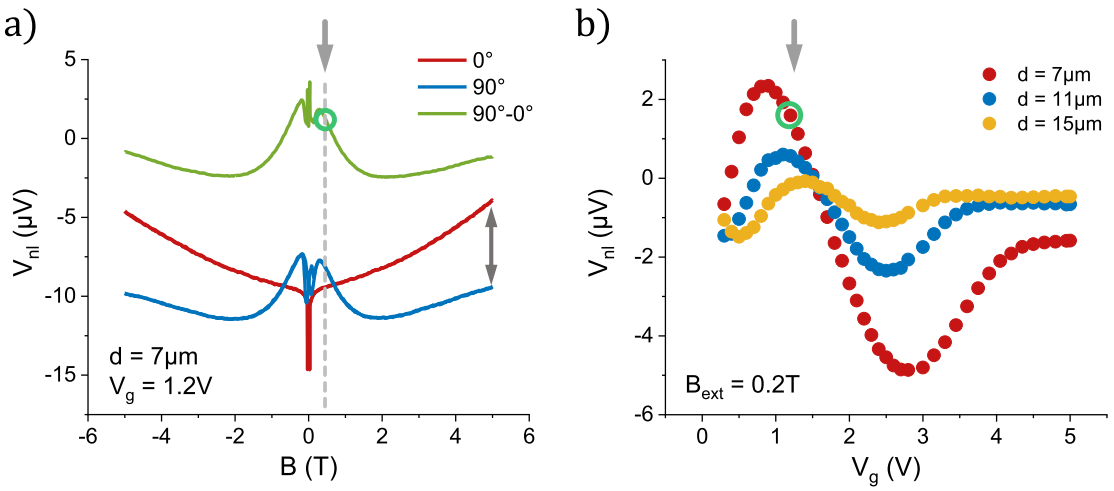

Figure 4.29. (**a**) Unprocessed raw data (0° and 90° signal) for a distance of $d = 7\,\mu\text{m}$ and a gate voltage of $V_g = 1.2\,\text{V}$, along with the difference between these signals ($90° - 0°$), i.e. using the 0° signal as a reference. (**b**) From the spin signal difference (a) at a certain magnetic field ($B_{ext} = 200\,\text{mT}$), gate dependent oscillations can be extracted for different distances d, which can be compared to the oscillatory signal obtained from the background and offset corrected 90° signal shown in Fig. 4.28b.

The gate dependent spin signal oscillations presented in Fig. 4.28b are extracted from background and offset corrected magnetic field sweeps. In order to confirm that these oscillations are not artificial, the unprocessed raw data, i.e. the measured non-local voltage at the detector, can be further analyzed. By regarding the 0° spin signal, in which case no spin precession is expected, as a reference, it is possible to extract similar gate dependent spin signal oscillations from the difference between the 90° and the 0° signal (Fig. 4.29). The thus obtained oscillations exhibit similar characteristics compared to the ones extracted from the magnetic field sweeps, especially concerning relative phase relation for different distances, position of extrema, and oscillation period. This strongly indicates that the os-

cillating spin precession signal is not an artifact. The signal offset, however, is clearly differing compared to the one extracted from the offset and background corrected data, especially for the smallest injector-detector distance of $d = 7\,\mu m$. This could be a result of the dependence of the background signal on the direction of the external magnetic field. When the background is different for the 0° and the 90° signal, signatures of this background remain in the signal difference (90°−0°), which could also give rise to an additional offset contribution in the gate resolved representation (Fig. 4.29b). Therefore, for the following detailed analysis, the spin signal oscillations, which are extracted from the background and offset corrected magnetic field sweeps, are further investigated.

Reproducibility and dependence on crystallographic orientation

In order to additionally confirm the gate dependent spin signal oscillations, another set of samples is investigated. There, the same wafer which is described in Chapter 3.2, is used. Also the same device geometry with an array of 1 µm wide channels between injector and detector, as described above (Fig. 4.24), is utilized. For a channel orientation along [110] similar oscillations are observable, which are shown in Fig. 4.30a for injector-detector distances of $d = 7\,\mu m$ and $d = 11\,\mu m$. This oscillatory gate dependence of the spin signal can be compared to the previously presented experimental data (Fig. 4.28b), clearly showing similar signal characteristics, especially with regard to the oscillation period and the decreasing signal amplitude with increasing gate voltage. Compared to the previously presented measurements, however, the signal oscillations for $d = 11\,\mu m$ are even more pronounced with a full period being observable. This could be a result of a difference in the strength of the capacitive coupling between the gate and the 2DEG channel in both sets of devices, but could also be related to a different absolute value of the SOC strength. The latter is, besides other factors, determined by the shape of the electron wave-function and the asymmetry of the quantum well (Chapter 2.5), which could vary for different samples due to variations in the sample processing, for instance.
For this set of devices, additionally a channel along the $[1\bar{1}0]$ crystallographic direction is investigated. As already qualitatively concluded in Chapter 4.2, the

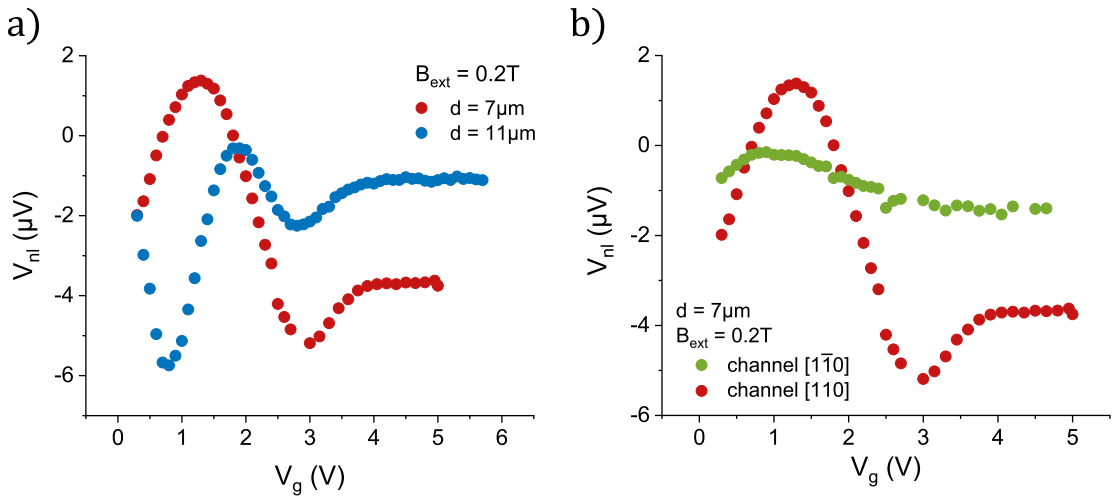

Figure 4.30. (**a**) Reproduction of the gated spin precession measurements discussed above. In particular the observed gate dependent oscillations can be compared to Fig. 4.29b. The signals are directly extracted from the difference between the 0° and 90° signal for an external magnetic field of $B_{ext} = 200\,\mathrm{mT}$. (**b**) Dependence of the oscillatory spin signal pattern on the crystallographic orientation of the transport channel for $d = 7\,\mu\mathrm{m}$. For a channel along [110] spin signal oscillations are observable (red), while for a channel orientation along [1$\bar{1}$0] the extracted signal hardly changes with V_g (green).

SOC strength for $\vec{k}$ along this direction is expected to be significantly smaller compared to $\vec{k} \parallel [110]$. Similar gate dependent non-local measurements with an external magnetic field along the channel confirm that no oscillating spin signal is observable for a channel oriented along [1$\bar{1}$0], as shown in Fig 4.30b. In particular, this indicates that the SO-field for spin transport along $\vec{k} \parallel [1\bar{1}0]$ does not significantly depend on the gate voltage. The SO-field for $\vec{k} \parallel [1\bar{1}0]$ is given by:

$$B_{k\parallel[1\bar{1}0]} \propto |\alpha - (\beta_1 - \beta_3) + \beta_3|, \tag{4.43}$$

and can therefore be independent of V_g, if the gate dependence of β_3 counteracts the gate dependence of α. This can be the case, if α and β_3 have opposite signs. As β_3 is expected to be positive for all gate voltages, this supports the assumption that α is negative. An additional contribution for the absence of oscillations for a channel orientation along [1$\bar{1}$0] could also be that the SO-field for spin transport

along $[1\bar{1}0]$ is significantly weaker compared to [110], such that no measurable spin precession is induced. It has to be noted that the gate dependent oscillations shown in Fig. 4.30 are extracted from the difference between the 90° and 0° spin signal, as the 0-spin-signal for a channel orientation along $[1\bar{1}0]$ cannot be determined without a substantial margin of error, due to inferior magnetic switching characteristics of the SV signals in the investigated devices.

Evaluation of spin signal oscillations with ballistic model

In the following, the gate dependent spin signal oscillations are further investigated based on the ballistic model of spin precession introduced by S. Datta and B. Das [8], which allows a simplified analysis and a rough approximation of the gate dependent contributions to SOC. It has to be kept in mind, however, that spin transport in the investigated devices takes place in an intermediate transport regime, which is dominated by diffusion, yet approaches the 1D limit due to the spatial confinement perpendicular to channel orientation (Chapter 4.1). Subsequently, the spin signal oscillations are investigated in more detail and the purely diffusive model is compared to the ballistic one.
In the spinFET proposal by S. Datta and B. Das [8], which is described in Chapter 2.5, spins are injected parallel to the channel orientation, traveling ballistically to the detecting contact. In the presence of SOC the injected spins precess on their way to the detecting contact with the precession angle Θ:

$$\Theta = \frac{2m^* d}{\hbar^2} SOC(V_g). \tag{4.44}$$

Applying a gate voltage allows tuning the SOC strength, in particular the Rashba and cubic Dresselhaus contributions, which gives rise to a gate dependent spin precession angle $\Theta(V_g)$. Thus, depending on the gate voltage, the angle at which the spins arrive at the detector oscillates between the parallel and the antiparallel configuration. In the ballistic, 1-dimensional limit, i.e. without a wave-vector component perpendicular to the channel, this gate dependent oscillation can be

described by a cosine function with a gate independent amplitude A [8, 23]:

$$V_{det} = A\cos\left(\frac{2m^*d}{\hbar^2}\,SOC(V_g) + \phi\right) = A\cos\left(\Theta + \phi\right). \tag{4.45}$$

The amplitude A corresponds to the signal difference between the parallel and the antiparallel level of the 90° signal, while ϕ is an arbitrary phase shift, which, in the evaluation of H. Koo et al. [23], is adjusted phenomenologically. This phase shift can be related to the finite spatial extent of the injecting and detecting contacts, a variation of the SOC strength underneath the contacts, or by considering an additional Dresselhaus contribution, for instance [123]. In a very basic approximation, a gate dependence of the SOC strength can be assumed to be a linear function of gate voltage, such that

$$SOC(V_g) = \frac{\partial SOC}{\partial V_g}\,V_g + SOC_0. \tag{4.46}$$

There, the gate independent contribution SOC_0 basically gives rise to an additional phase shift of the cosine function. Therefore, the gate independent contributions of SOC cannot be distinguished from an arbitrary phase shift ϕ. In this linear approximation the change of SOC with gate voltage ($\partial SOC/\partial V_g$) can be directly calculated from the period p of the spin signal oscillations:

$$\frac{\partial SOC}{\partial V_g} = \frac{\hbar^2}{2dm^*}\frac{2\pi}{p}. \tag{4.47}$$

In Tab. III the extracted values of the oscillation period and the calculated slopes of the linear gate dependence of SOC are summarized for all investigated distances. As only half a period of the oscillations can be resolved in the gate sweep, these extracted values can be considered only rough estimates, however.

d (µm)	p (V)	$\omega = 2\pi/p$ (1/V)	$\partial SOC/\partial V_g$ (10^{-13} eV m/V)
7	4.14	1.52	1.32
11	3.06	2.05	1.14
15	2.42	2.60	1.06

Table III. Period p and frequency ω extraced from the gate dependent spin signal oscillations shown in Fig. 4.28b, for different injector-detector distances d. Based on p, or ω respectively, the gate dependent change of SOC ($\partial SOC/\partial V_g$) can be calculated according to Eq. 4.47. Averageing over all regarded distances d yields a value of $\partial SOC/\partial V_g = 1.17 \times 10^{-13}$ eV m/V.

In Fig. 4.31 experimentally obtained spin signal oscillations are fitted with the basic ballistic model (Eq. 4.45). The SOC strength is assumed to change linearly as a function of V_g, according to Eq. 4.46. In particular, the gate dependent amplitude of the experimental data cannot be reproduced, which leads to deviations from the expected cosine functionality especially for larger gate voltages. The fitting parameters are summarized in the appendix (App. A.3).

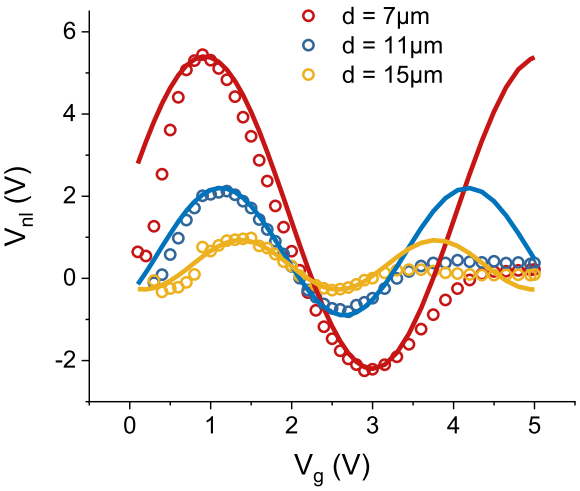

Figure 4.31. Gate dependent spin signal oscillations fitted with the ballistic model, according to Eq. 4.45. The fitting parameters are summarized in the appendix (App. A.3).

As there are no comparable gate induced spin signal oscillations reported in literature for QW structures with low In-contents of 9 %, the average gate tunability of SOC ($\partial SOC/\partial V_g = 1.17 \times 10^{-13}$ eV m/V) can only be compared to the values ob-

tained for high-In ($In_{0.53}Ga_{0.47}As$) and InAs quantum wells, in which $\partial SOC/\partial V_g$ is found to be an order of magnitude larger $\sim 10^{-12}$ eV m/V [23, 76, 79]. However, in these structures also the absolute SOC strength is in general larger, lying in the 10^{-12} eV m range [79–84], which is on a similar order of magnitude as the corresponding gate dependent change $\partial SOC/\partial V_g$. For low In-content heterostructures, similar to the one under investigation, the total SOC strength is found to be in the low 10^{-13} eV m range [77, 78], which is also on a similar order of magnitude compared to the experimentally determined value of $\partial SOC/\partial V_g$. It is important to note, however, that the relative change of SOC with gate voltage also depends on the capacitive coupling, thus in particular on the specific oxide layer thickness of the gated structure itself, which prevents a direct comparison. Additionally, it has to be remarked, that from the evaluation of the oscillation period it is only possible to extract the change of SOC with gate voltage, while there is no direct access to the absolute value of the SOC strength SOC_0. In particular, the additional phase shift ϕ in the cosine function cannot be distinguished from SOC_0. Moreover, it is not possible to draw conclusions on the sign of $\partial SOC/\partial V_g$ at this point.

Another estimation of $\partial SOC/\partial V_g$ in this linear approximation can be obtained from the slope of the distance dependence of the precession frequency ω according to Eq. 4.47:

$$\omega = \frac{2\pi}{p} = \frac{2m^*}{\hbar^2}\frac{\partial SOC}{\partial V_g}\, d. \tag{4.48}$$

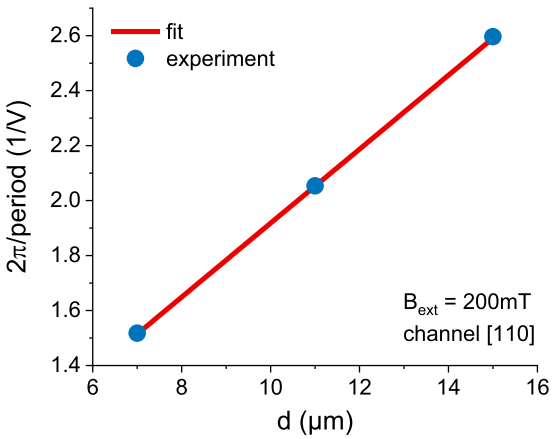

Figure 4.32. Precession frequency $\omega = 2\pi/p$ extracted from the oscillating spin signal (Fig. 4.28b) as a function of the injector-detector distance d for $B_{ext} = 200$ mT (blue). The increase of the precession frequency with distance can be fitted linearly (red) according to Eq. 4.48.

Fig. 4.32 shows the precession frequency ω as a function of the injector-detector distance d for an external magnetic field strength of $B_{ext} = 200\,\mathrm{mT}$, which clearly follows a linear trend. This additionally supports the assumption that the oscillatory spin signal is due to a gate induced change of SOC. From the slope a value of $\partial SOC/\partial V_g \approx 0.82 \times 10^{-13}\,\mathrm{eV\,m/V}$ can be estimated, which is smaller compared to the values directly calculated from the oscillation period (Tab. III), yet is on a similar order of magnitude, such that deviations may be due to an inaccurate extraction of the oscillation period.
Furthermore, it is important to point out, that the values of $\partial SOC/\partial V_g$ contain all gate dependent SOC contributions. In particular, the Rashba contribution α is expected to be a function of gate voltage, but also the cubic Dresselhaus parameter β_3 is found to depend on V_g. The linear Dresselhaus parameter β_1, on the other hand, is independent of V_g. It is related to the expectation value of $\langle k_z^2 \rangle$, and the bulk Dresselhaus parameter γ [26, 70, 71]:

$$\beta_1 = -\gamma \langle k_z^2 \rangle \approx 1.37 \times 10^{-13}\,\mathrm{eV\,m}. \tag{4.49}$$

As discussed above, for γ a value of $\gamma \approx -7.5\,\mathrm{eV\AA}^3$ is implemented [77], while $\langle k_z^2 \rangle \approx 1.83 \times 10^{16}\,\mathrm{m}^{-2}$, which can be calculated from self-consistently solving the Schrödinger-Poisson equation. The cubic Dresselhaus parameter β_3, on the other hand, is determined by the charge carrier density n_s [26, 100, 158]:

$$\beta_3 = -\gamma \frac{k^2}{4} = \frac{-\gamma \pi n_s}{2}. \tag{4.50}$$

As n_s is found to change with the applied gate voltage V_g in experiment (Chapter. 4.3.2), β_3 is therefore gate dependent. In Fig. 4.33 the calculated dependence of β_3 on the gate voltage V_g is shown. As β_3 is proportional to n_s according to Eq. 4.50, its gate voltage dependence directly follows the gate dependence of n_s. In particular, β_3 changes almost linearly with V_g up to about $V_g \approx 2.7\,\mathrm{V}$, while for larger gate voltages β_3 shows hardly any gate dependence. This is assumed to be due to the population of deep trap states at the interface between the oxide and the SC, or within the oxide layer itself, which leads to a capacitive screening of the gate. In the low gate voltage region below about $V_g \lesssim 2.7\,\mathrm{V}$ the

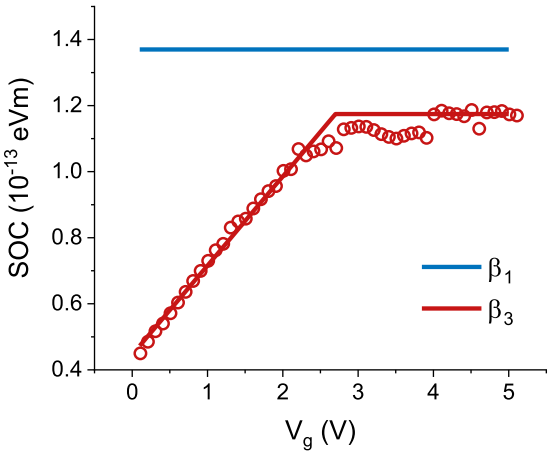

Figure 4.33. Calculated gate dependence of the linear and cubic Dresselhaus parameters, β_1 and β_3, for $\gamma = -7.5\,\mathrm{eV\AA}^3$.

slope of the nearly linearly changing cubic Dresselhaus SOC contribution is about $\partial\beta_3/\partial V_g \approx 2.7 \times 10^{-14}\,\mathrm{eV\,m/V}$. For larger gate voltages $V_g \gtrsim 2.7\,\mathrm{V}$, β_3 is roughly constant at a value of about $\beta_3 \approx 1.15 \times 10^{-13}\,\mathrm{eV\,m}$. The linear Dresselhaus parameter $\beta_1 \approx 1.37 \times 10^{-13}\,\mathrm{eV\,m}$, on the other hand, is independent of V_g.
The total SOC strength for $\vec{k} \parallel [110]$, which is along the channel is this case, is given by:

$$SOC_{k\parallel[110]} = -\alpha - \beta_1 + 2\beta_3, \tag{4.51}$$

for $x \parallel [1\bar{1}0]$, and $y \parallel [110]$. In the linear approximation, the gate dependent change of the total SOC is then given by:

$$\pm\frac{\partial SOC}{\partial V_g} = -\frac{\partial \alpha}{\partial V_g} + 2\frac{\partial \beta_3}{\partial V_g}. \tag{4.52}$$

Rearranging allows estimating the gate tunability of the Rashba contribution:

$$\frac{\partial \alpha}{\partial V_g} = \mp\frac{\partial SOC}{\partial V_g} + 2\,\frac{\partial \beta_3}{\partial V_g}. \tag{4.53}$$

However, as the sign of $\partial SOC/\partial V_g$ cannot be determined based on the analysis of the oscillation period, it is also not possible to determine a unique value of $\partial\alpha/\partial V_g$. Instead, both signs of $\partial\alpha/\partial V_g$ are physically valid. Additionally, according to the gate dependence of β_3, two gate voltage regions have to be distinguished. For small gate voltages below $V_g \leq 2.7\,\mathrm{V}$, β_3 changes approximately linearly with V_g with

$\partial\beta_3/\partial V_g \approx 2.7 \times 10^{-14}\,\mathrm{eV\,m/V}$. In this region, $\partial SOC/\partial V_g$ contains contributions of α and β_3, such that $\partial\alpha/\partial V_g$ differs from $\mp\partial SOC/\partial V_g$. The value for $\partial\alpha/\partial V_g$ in this low gate voltage can be determined from Eq. 4.53:

$$\frac{\partial\alpha}{\partial V_g} = \mp\frac{\partial SOC}{\partial V_g} + 2\,\frac{\partial\beta_3}{\partial V_g} = \begin{cases} +1.71 \times 10^{-13}\,\mathrm{eV\,m/V} \\ -0.63 \times 10^{-13}\,\mathrm{eV\,m/V}, \end{cases} \tag{4.54}$$

where $\partial SOC/\partial V_g = \pm 1.17 \times 10^{-13}\,\mathrm{eV\,m/V}$, which is calculated from the oscillation period. For the value of $\partial SOC/\partial V_g = 0.82 \times 10^{-13}\,\mathrm{eV\,m/V}$, which is obtained from linearly fitting the distance dependence of the oscillation frequency (Fig. 4.32), the obtained values of $\partial\alpha/\partial V_g$ are slightly smaller:

$$\frac{\partial\alpha}{\partial V_g} = \mp\frac{\partial SOC}{\partial V_g} + 2\,\frac{\partial\beta_3}{\partial V_g} = \begin{cases} +1.36 \times 10^{-13}\,\mathrm{eV\,m/V} \\ -0.28 \times 10^{-13}\,\mathrm{eV\,m/V}. \end{cases} \tag{4.55}$$

For $V_g \geq 2.7\,\mathrm{V}$, on the other hand, $\partial\beta_3/\partial V_g = 0$, so that

$$\frac{\partial\alpha}{\partial V_g} = \mp\frac{\partial SOC}{\partial V_g}. \tag{4.56}$$

It has to be kept in mind that the derived values of $\partial\alpha/\partial V_g$ have to be considered as estimates, which only allow approximating the rough order of magnitude.

Gate dependence of spin signal in diffusive model

So far, the gate dependent spin signal oscillations were analyzed based on Eq. 4.45, which is valid in the ballistic, 1-dimensional limit. As spin transport in the samples under investigation takes place in an intermediate regime (Chapter 4.1), the gate dependence of the spin signal is now investigated based on the diffusive spin transport model introduced in Chapter 2.6. As a numerical solving software COMSOL is implemented. Setting up this model requires making assumptions on the gate dependence of various input parameters, however. There, first of all, charge carrier density n_s and electron mobility μ_e are functions of V_g (Fig. 4.34), which can both be determined experimentally from charge transport measurements (Chapter 4.3.2). The gate dependence of n_s and μ_e gives rise to a gate

dependent diffusion constant D. Another contribution that changes with V_g is the spin diffusion length $\lambda_x = \lambda_{[1\bar{1}0]}$ for injected spins oriented along the contact, which can also be extracted experimentally from spin transport measurements (Fig. 4.25). Further gate dependent contributions are spin injection efficiency P_{inj}, and sheet resistance R_s, which additionally affect the gate dependence of the SV signal height (Chapter 2.6). The gate dependence of these quantities is taken into account in the model via a gate dependent flux f through the injecting contact. This factor f can be determined from fitting the 0° signal, in which case the magnetic field is directed along the contact. There, for given values of n_s, μ_e, and $\lambda_x \equiv \lambda_{[1\bar{1}0]}$, this signal level is independent of SOC strength, external magnetic field, and spin relaxation anisotropy k, such that f can be uniquely determined from the 0° signal. In Fig. 4.35 an exemplary fit of the 0° signal is shown, along with the thus extracted gate dependent values of the resulting factor f for all investigated injector-detector distances. The actual simplified parametrization of all these gate dependent input parameters is summarized in the appendix (App. A.2). For the gate dependence of the total SOC strength, on the other hand, an assumed gate voltage dependence is implemented, which is shown in Fig. 4.36a. There, the total SOC is assumed to change linearly in the low gate voltage range ($V_g < 3\,\mathrm{V}$), while for $V_g > 4\,\mathrm{V}$ the SOC strength is expected to be independent of V_g, due to

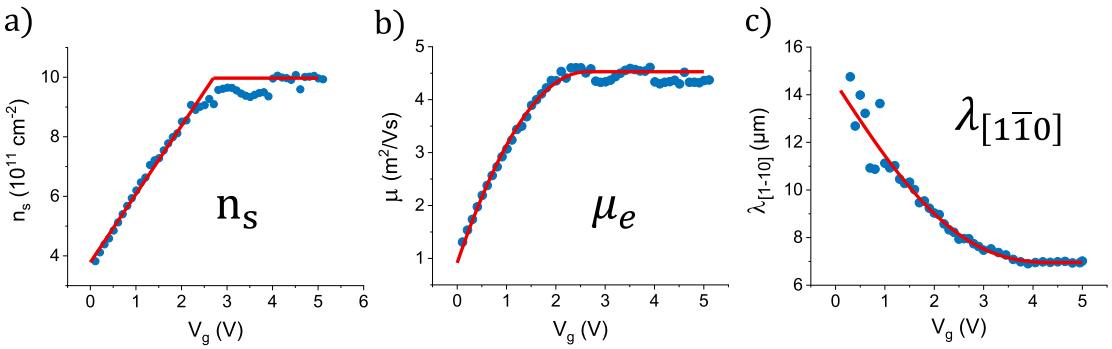

Figure 4.34. Gate dependencies of the input parameters for the purely diffusive model: charge carrier density n_s (**a**), electron mobility μ_e (**b**), and spin diffusion length $\lambda_{[1\bar{1}0]}$ for spins oriented along $[1\bar{1}0]$ (**c**). The red lines indicate the approximate parameterization, which is implemented in the model. Further details on this parametrization can be found in the appendix (App. A.2).

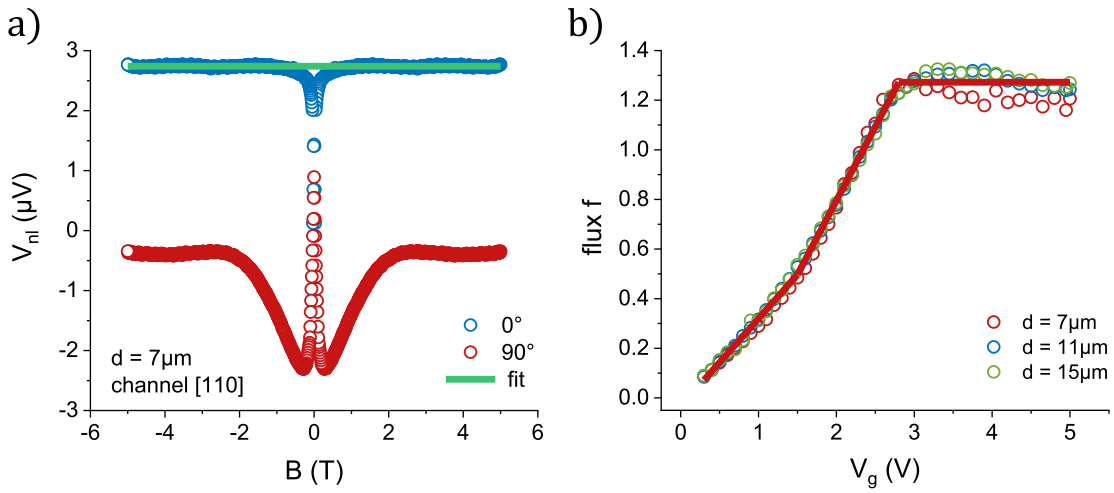

Figure 4.35. (**a**) 0° and 90° signal for an exemplary gate voltage of $V_g = 3\,\mathrm{V}$. The 0° signal is fitted for fixed values of n_s, μ_e, and $\lambda_x \equiv \lambda_{[1\bar{1}0]}$, according to Fig. 4.34. As an only fitting parameter the scaling/flux factor f is used, which is introduced in Chapter 2.6. (**b**) Gate dependence of the scaling/flux factor f, as exemplarily determined in (a).

screening effects, which can be assigned to the population of deep trap states. In between these two gate voltage regions, the slope of the SOC strength is assumed to transition smoothly. The slope of the linear region is assumed to be similar to the one derived from the ballistic spin precession model, in which case a value of $\partial SOC/\partial V_g \approx 1 \times 10^{-13}\,\mathrm{eV\,m/V}$ could be estimated from the period of the gate dependent spin signal oscillations. The intercept of the linearly approximated gate functionality of the SOC strength is set arbitrarily ($SOC_0 = 1.5 \times 10^{-13}\,\mathrm{eV\,m/V}$). Note that, assuming the same gate dependence of the absolute value of SOC, the simulation yields identical results for a positive and a negative sign of SOC.

Fig. 4.36b shows the gate resolved spin signal for similar injector-detector distances d as investigated in experiment. The experimental counterpart is presented above (Fig. 4.28b). For the chosen set of parameters and their assumed gate dependencies, the simulated spin signals show gate dependent oscillations for all three distances, which are similar to experiment, yet less pronounced. Additionally, the oscillation pattern changes sign, indicating an antiparallel spin component at the detector, which can only be due to SOC induced spin precession in the model.

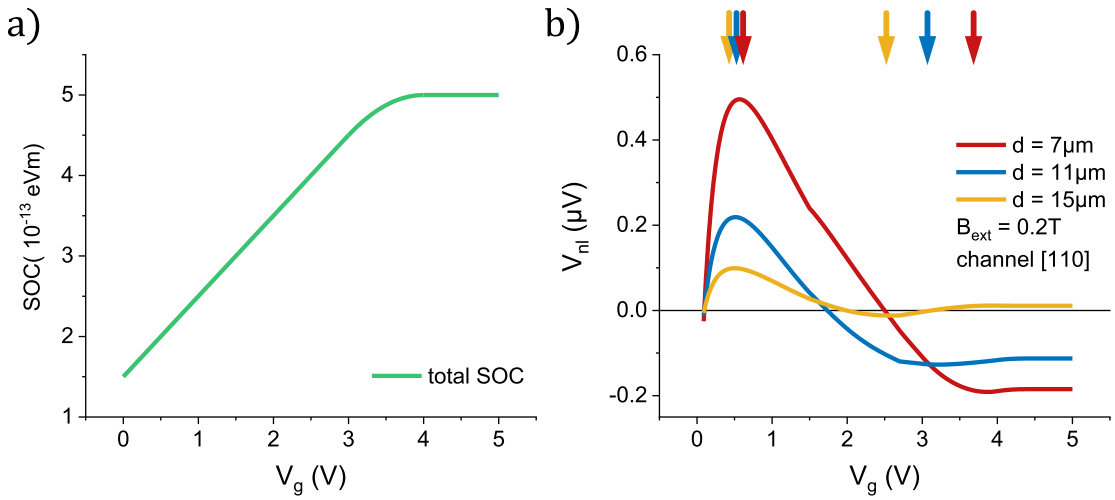

Figure 4.36. (**a**) Assumed gate voltage dependence of the total SOC strength. For small gate voltages, the total SOC is assumed to change linearly with V_g with a slope of $\partial SOC/\partial V_g \approx 1 \times 10^{-13}\,\mathrm{eV\,m/V}$, which is similar to the values previously extracted from the spin signal oscillation period. (**b**) Simulated gate sweeps for a fixed external magnetic field ($B_{ext} = 0.2\,\mathrm{T}$) and different injector-detector distances d, similar to experiment (Fig. 4.28b). The spin signal oscillations can only be conceptually reproduced with the purely diffusive model.

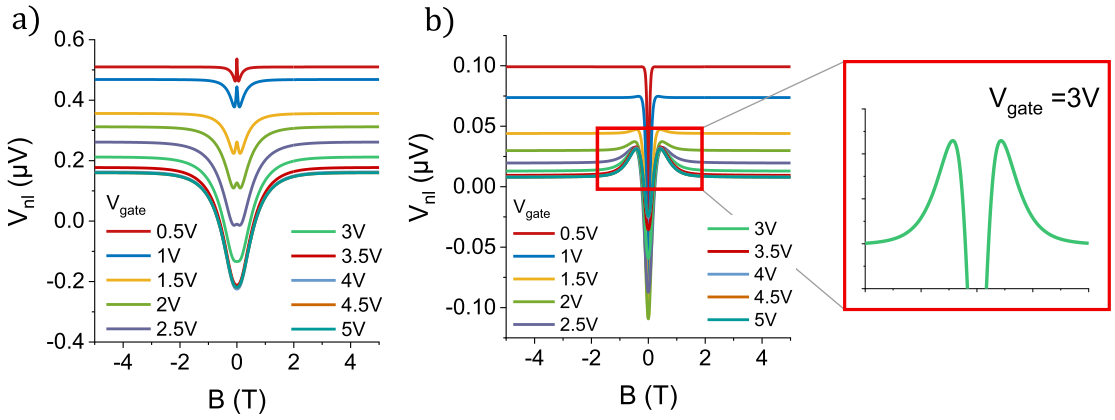

Figure 4.37. (**a**) Simulated gate dependent magnetic field sweeps (90° signal) for an injector-detector distance of $d = 7\,\mu\mathrm{m}$ (**a**), and $d = 15\,\mu\mathrm{m}$ (**b**). Only for larger distances d, the dip-like signal characteristic changes into a peak-like feature (b). However, the experimental data (Fig. 4.28) cannot be properly reproduced with the diffusive model.

Also, the period of these oscillations decreases with increasing injector-detector distance, which also agrees with the experimental findings and the expected behavior for SOC related spin precession. Qualitatively, these oscillations conceptually agree with the experimental findings. Regarding the magnetic field sweep, however, clearly shows the limitations of the diffusive model (Fig. 4.37). Especially for small injector-detector distances (Fig. 4.37a), the reversal of the dip-feature with gate voltage, which is observed in experiment (Fig. 4.28a), cannot be resolved. Only for larger distances d a peak-like feature emerges, which is highlighted in Fig. 4.37b. In summary, the qualitative validity of the diffusive model can be substantiated on a rudimentary level, yet it is not possible to gain quantitative insights, in particular due to the numerous assumptions, which have to be made for the values and gate dependencies of the input parameters.

Gate dependence of spin signal in expanded ballistic model

Compared to the purely diffusive model, the gate induced spin signal oscillations can be modeled more adequately with an extended ballistic model, which is considered by A. Zainuddin et al. [123]. There, the 1-dimensional spin precession equation (Eq. 4.45) is generalized to the 2-dimensional case, whereby spin transport is still assumed to be ballistic. In this model the SV signal height ΔV_x, i.e. the difference between the parallel and the antiparallel signal level ($V_P - V_{AP}$), for spins oriented along the channel (90° signal) can be approximated by [123]:

$$\Delta V_x \simeq \frac{\Delta V_y}{2} + \frac{3\pi \Delta V_y}{2} \frac{1}{\sqrt{2\pi\Theta}} \cos\left(\Theta + \frac{\pi}{4}\right), \tag{4.57}$$

for the simplified case of point contacts. There, ΔV_y is the signal height of the standard SV signal, in which case the spins are oriented along the contact (0° signal). The spin precession angle Θ for $k \parallel [110]$ is given by:

$$\Theta(V_g) = \frac{2m^* d}{\hbar^2} \left(-\alpha + 2\beta_3 - \beta_1\right). \tag{4.58}$$

One of the major differences of Eq. 4.57 compared to the 1-dimensional limit (Eq. 4.45) is that the amplitude of the oscillation depends on the gate dependent

precession angle Θ. The spin signal amplitude $\Delta V_y \equiv \Delta V_{nl,[1\bar{1}0]}$ for spins oriented perpendicular to the channel, i.e. along $[1\bar{1}0]$, can be obtained experimentally (Fig. 4.25c), which exhibits a clearly decreasing trend with increasing V_g. The decreasing oscillation amplitude with increasing gate voltage, which is observed in experiment, can therefore be related to the decreasing spin signal amplitude and a gate dependent change of Θ. Note that an additional offset is added to the oscillatory signal (Eq. 4.57), which is a function of ΔV_y and is therefore also gate dependent. In order to replicate the experimentally observed oscillations, the gate dependent values of $\Delta V_{nl,[1\bar{1}0]}$ are substituted to the expression for ΔV_x (Eq. 4.57) and the Rashba contribution α is varied as a function of V_g. For the linear Dresselhaus SOC term a value of $\beta_1 = 1.37 \times 10^{-13}\,\mathrm{eV\,m/V}$ is assumed, as discussed above, while the cubic contribution β_3 is derived from the gate dependent charge carrier density (Fig. 4.33). Fitting additionally requires introducing a scaling factor SC, and a signal offset OFF, in order to match the experimentally obtained oscillations, such that the fitting function is given by:

$$\Delta V_{[1\bar{1}0]} = \Delta V_x \cdot SC + OFF. \tag{4.59}$$

The precession angle Θ is given by Eq. 4.58, and contains the SOC contributions $\alpha(V_g)$, β_1, and $\beta_3(V_g)$. In the simplest case, the Rashba contribution to SOC is assumed to change linearly with V_g:

$$\alpha = \alpha_0 + \frac{\partial \alpha}{\partial V_g} V_g, \tag{4.60}$$

where α is expected to be negative, based on the considerations presented above.

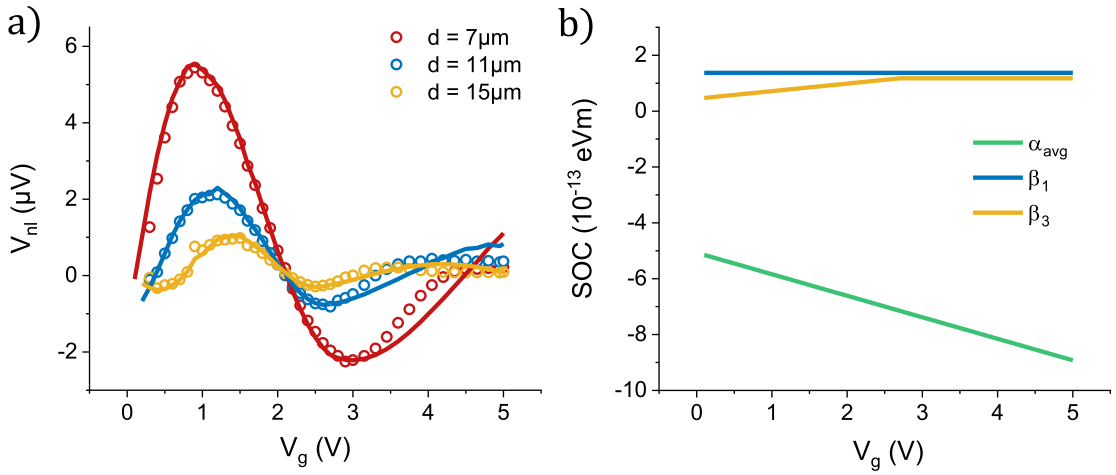

Figure 4.38. (**a**) Gate dependent spin signal oscillations fitted with the expanded ballistic model provided by A. Zainuddin et al. [123]. In particular, the decreasing signal amplitude with increasing gate voltage is reproduced well, only for larger gate voltages the model deviates from the experimental data. (**b**) Individual contributions of the total SOC. The linear Dresselhaus parameter can be determined from self-consistent Schrödinger-Poisson simulations ($\beta_1 = 1.37 \times 10^{-13}\,\mathrm{eV\,m}$), while the cubic Dresselhaus contribution is related to the gate dependent charge carrier density n_s (Fig. 4.33). The gate dependence of the Rashba parameter α is assumed to change linearly with V_g (Eq. 4.60) and is obtained from fitting the spin signal oscillations (a). There, the average over all three regarded distances is shown. The individual values of α_0 and $\partial\alpha/\partial V_g$ are summarized in Tab. IV.

$\boldsymbol{d}$ (µm)	$\boldsymbol{\alpha_0}$ (10^{-13} eV m)	$\boldsymbol{\partial\alpha/\partial V_g}$ (10^{-13} eV m/V)
7	-3.78	-0.90
11	-5.34	-0.72
15	-6.01	-0.68
average	-5.07	-0.77

Table IV. Values of α_0 and $\partial\alpha/\partial V_g$ (Eq. 4.60) obtained from fitting the gate dependent spin signal oscilaltions for differnt injector-detector distances d (Fig. 4.38a).

In Fig. 4.38 the fitted signals for all investigated injector-detector distances are shown, along with the gate dependencies of the individual SOC contributions. The values of α_0 and $\partial\alpha/\partial V_g$, which are obtained from the fit, are summarized in Tab. IV, while the other fitting parameters, like scaling factor and signal offset, can be found in the appendix (App. A.4). As the cosine function, which gives rise to the oscillatory behavior, is identical to the 1-dimensional case (Eq. 4.45), a similar value of $\partial\alpha/\partial V_g = -0.77 \times 10^{-13}\,\mathrm{eV\,m/V}$ (averaged) is obtained from this fit. However, the values of the gate independent contribution α_0 significantly spread, yet no clear functional connection is identifiable. As for each distance a separate device is investigated, it could be possible that fabricational inhomogeneities result in slightly varying gate independent SOC contributions, thus yielding an additional phase shift. Additional contributions resulting in a phase shift could be due to a finite spatial extent of the contacts, a variation of the SOC strength underneath the contacts, or a varying strength of the Dresselhaus SOC [123], which could also be slightly different for separate devices. Due to this spread of the gate independent SOC contributions and the lacking possibility of distinguishing these contributions from an additional phase shift, it is therefore not meaningful to determine α_0 from the fit. However, despite the rather simplified assumption on the gate dependence of α, the experimental data can be described well with the extended ballistic spin precession equation, as shown in Fig. 4.38a. In particular, the decreasing oscillation amplitude with increasing gate voltage is reproduced well. Only for larger gate voltages the fit deviates from the experimental values, which could be due to a change of capacitive coupling (deep trap states). This can either affect the gate response of α ($\partial\alpha/\partial V_g$), or completely screen the gate electrode, such that α becomes independent of V_g.

A significantly better fitting result can be achieved by dividing the gate voltage range into three separate sections: A, B, and C (Fig. 4.39b). In each region, α is assumed to change linearly with V_g, yet the slopes $\partial\alpha/\partial V_g$ may differ in each section. This allows a considerably improved replication of the experimental data, as shown in Fig. 4.39a.

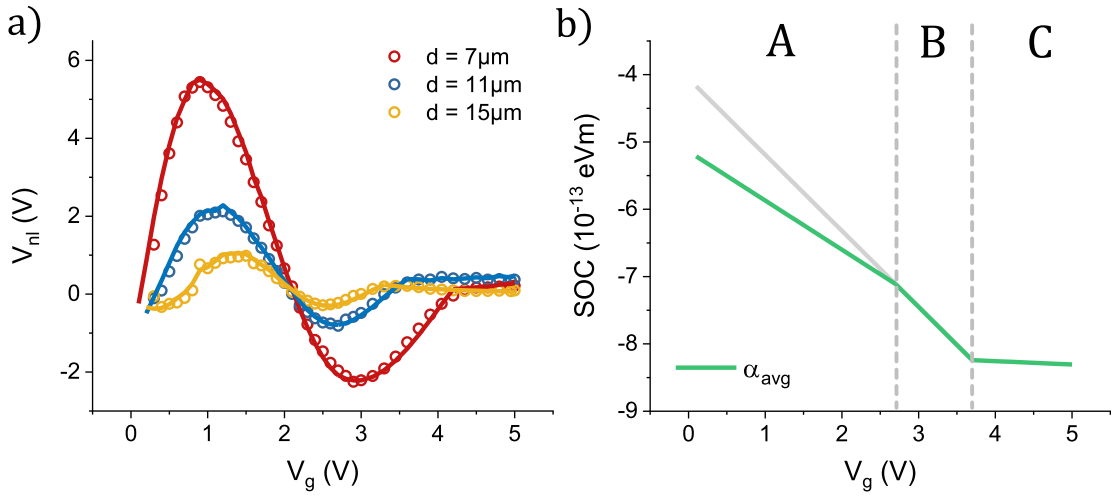

Figure 4.39. (**a**) Fitted spin signal oscillations based on the expanded ballistic model, showing an excellent agreement with the experimental data. (**b**) The gate voltage region is divided into three regions (A, B, and C). In each range, the gate dependence of the Rashba SOC can differ. There, the gate dependence of α is obtained from the fit, and averaged over all injector-detector distances. The slopes $\partial\alpha/\partial V_g$ in each region are summarized in Tab. V.

	A	***B***	***C***
$\partial\boldsymbol{\alpha}/\partial V_g$	-0.73	-1.16	-0.07
$\partial\boldsymbol{\beta_3}/\partial V_g$	0.27	0	0
$\partial\boldsymbol{SOC}/\partial V_g$	1.27	1.16	0.07

Table V. Averaged values of the gate depedence of the SOC parameters for each gate voltage region, in units of 10^{-13} eV m/V. There, the slopes of α are obtained from the fit (averaged over all distances d), $\partial\beta_3/\partial V_g$ is obtained from the gate depdence of the charge carrier density (Fig. 4.33), and $\partial SOC/\partial V_g$ can be determined based on Eq. 4.61.

The average slopes for each gate voltage region are summarized in Tab. V. All fitting parameters can be found in the appendix (App. A.4). Note that the gate

dependent change of the total SOC strength for a channel along [110] is given by:

$$\frac{\partial SOC}{\partial V_g} = -\frac{\partial \alpha}{\partial V_g} + 2\frac{\partial \beta_3}{\partial V_g}, \tag{4.61}$$

in the linear approximation. In the gate voltage region A the values of $\partial\alpha/\partial V_g$ are similar compared to the ones, which are extracted from the oscillation period based on the 1-dimensional model (Eq. 4.45), while in region B, $\partial\alpha/\partial V_g$ is larger. For gate voltages larger than $V_g \gtrsim 4\,\mathrm{V}$ (region C), the effect of the gate electrode is completely screened, presumably due to trapped charges. Thus, neither the total SOC, nor α changes as a function of V_g.

In order to justify the subdivision of the gate voltage range into three separate regions, the total Rashba SOC contribution α_{total} is assumed to contain two contributions. One of which scales linearly with the charge carrier density n_s (α_{ns}), or with the n_s related electric field respectively ($E \propto n_s$ [75, 114]). The other contribution is assumed to be due to the electric field of the gate electrode itself (α_{el}), and does neither have an influence on n_s, nor is affected by a change of n_s. The total Rashba SOC contribution is then given by:

$$\alpha_{total} = \alpha_{ns} + \alpha_{el}. \tag{4.62}$$

The linear relation between α_{ns} and n_s is supported by experimental works [71, 111–113, 115, 116]. The electric field contribution of α_{el}, on the other hand, is expected to depend linearly on the gate electric field. The presence of this n_s independent contribution can be indirectly supported by reports, which show a gate tunability of α for a constant charge carrier density [20, 23, 75]. However, it has to be kept in mind that the differentiation between two Rashba SOC contributions is purely phenomenological at this point, and requires further investigation. The separation of the three gate voltage regions can be discussed by regarding the gate dependence of α_{total} in each gate voltage range. For low gate voltages up to about $V_g = 2.7\,\mathrm{V}$, gate dependent charge transport measurements show that the charge carrier density n_s increases linearly with V_g. Thus, α_{ns} and α_{el} are both expected to change with the applied gate voltage. In the intermediate gate voltage range

(2.7 V − 4 V) the electric field of the gate electrode is not completely screened, yet n_s does not change with V_g, as additional charge carriers populate deep trap states at the interface between the oxide and the semiconductor, instead of the 2DEG channel. Thus, the charge carrier density related contributions α_{ns} does not change with V_g. Despite n_s being independent of V_g in this range, the gate is still assumed to be capacitively coupled to the 2DEG, such that the contribution α_{el} of the Rashba SOC, which directly depends on the gate electric field, is expected to be the only gate dependent contribution of SOC in the intermediate gate voltage region. For $V_g \gtrsim 4\,\mathrm{V}$, on the other hand, α_{total} is nearly gate independent, which can be presumed to be due to a complete capacitive screening of the gate as a result of the population of deep trap states. Thus, the gate has an influence neither on the charge carrier density, nor on SOC. In summary, in region A, the gate dependent contributions of the Rahba SOC consist of α_{ns} and α_{el}, while in region B only α_{el} is gate dependent. In region C, on the other hand, the SOC does not depend on V_g. The total Rasbha SOC contribution is thus given by:

$$\begin{aligned} &\text{region A} \quad && \alpha^{A}_{total} = \alpha_{ns}(V_g) + \alpha_{el}(V_g) \\ &\text{region B} \quad && \alpha^{B}_{total} = \alpha_{ns} + \alpha_{el}(V_g) \\ &\text{region C} \quad && \alpha^{C}_{total} = \alpha_{ns} + \alpha_{el} \approx \text{constant}. \end{aligned} \tag{4.63}$$

There, α_{total} is equal to the Rashba SOC α_{fit}, which is obtained from fitting the gate dependent spin signal oscillations (Fig. 4.39a). Additionally, $\alpha_{el}(V_g)$ is assumed to be equal in region A and region B.

This 3-slope approximation can be further analyzed by conducting self-consistent Schrödinger-Poisson simulations, which allow calculating the n_s dependent contribution of the Rashba SOC α_{ns}. Further technical details can be found in the appendix (App. A.5). From these simulations α_{ns} can be calculated as a function of the charge carrier density n_s. A gate dependent representation can be obtained by matching n_s to V_g, based on the experimentally determined gate dependence of n_s (Chapter 4.3.2). In Fig. 4.40a the calculated values of α_{ns} are shown as a function of V_g. The obtained values are negative, yet the absolute value is decreasing, contrary to the total Rashba SOC α_{fit}, which is obtained from fitting the gate

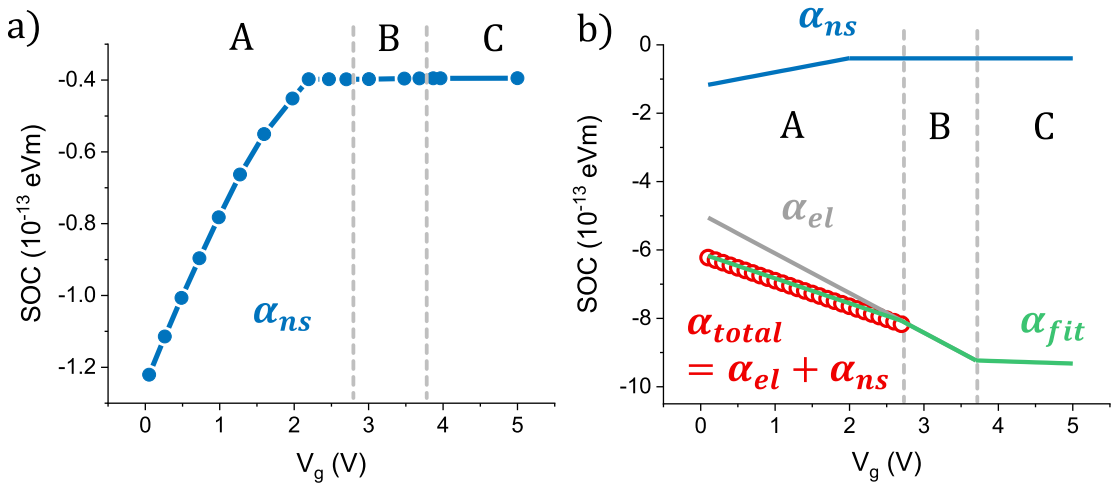

Figure 4.40. (**a**) Charge carrier density dependent contribution of Rashba SOC (α_{ns}), resulting from self-consistent Schrödinger-Poisson simulations. (**b**) From fitting the spin signal oscillations (Fig. 4.39a), the total Rashba SOC strength $\alpha_{total} \equiv \alpha_{fit}$ is obtained (green), which can be phenomenologically divided into an n_s dependent contribution α_{ns} (blue) and an electric field related one α_{el} (gray). The charge carrier density only changes with V_g in region A, such that only in this range both contributions of α have to be taken into account: $\alpha_{total} = \alpha_{el} + \alpha_{ns}$. There, α_{ns} is obtained from simulation (a), while α_{el} is linearly extrapolated from region B.

dependent oscillations (Fig. 4.39). Notably, α_{ns} only changes with V_g in region A, due to the gate dependence of n_s in this range. In gate voltage region B, α_{ns} is gate independent and the only contribution to the gate dependence of the Rashba SOC is α_{el}. As this electric field contribution α_{el} is independent of the charge carrier density n_s, the value of α_{el} in region A is assumed to be equal to that in region B (Fig. 4.40). The total Rashba SOC in region A is thus given by the sum of α_{ns}, which is obtained from the simulation, and α_{el}, which is assumed to be equal to the value of region B. In Fig. 4.40 the values of α_{total} obtained for region A are shown as red dots. There, the calculated value α_{total} perfectly matches the total Rashba SOC α_{fit}, which is obtained from fitting the gate dependent spin signal oscillations. This strongly suggests that the total Rashba SOC indeed contains two contributions α_{ns} and α_{el}.

Finally, the total SOC strength can be calculated, with particular focus on its

dependence on the crystallographic orientation. According to Eq. 2.39 in Chapter 2.3, the total SOC strengths for channels along $\vec{k} \parallel [110]$ and $\vec{k} \parallel [1\bar{1}0]$ are given by ($x \parallel [1\bar{1}0]$, $y \parallel [110]$):

$$\begin{aligned} SOC_{k\parallel[110]} &= |-\alpha + 2\,\beta_3 - \beta_1| \\ SOC_{k\parallel[1\bar{1}0]} &= |\alpha + 2\,\beta_3 - \beta_1|. \end{aligned} \tag{4.64}$$

The value of α is obtained from fitting the spin signal oscillations (Fig. 4.39), while $\beta_1 = 1.37 \times 10^{-13}\,\mathrm{eV\,m}$, and $\beta_3 \propto n_s$ follows the gate dependence of n_s (Chapter 4.3.2). The thus calculated total SOC strength for both channel orientations is plotted in Fig. 4.41. Note that $\alpha < 0$, and $\beta_1, \beta_3 > 0$. In the greater part of the gate voltage range, i.e. for $V_g \gtrsim 0.9\,\mathrm{V}$, the SOC for spins traveling along [110] is larger compared to the $[1\bar{1}0]$ direction. In this gate voltage range $\beta_1 < 2\,\beta_3$, while $\alpha < 0$ for all investigated V_g. Thus, according to Eq. 4.64, $SOC_{k\parallel[110]} > SOC_{k\parallel[1\bar{1}0]}$. Generally, the relation between the SOC strengths does not explain that no spin signal oscillations are observable for a channel orientation along $[1\bar{1}0]$, however. Explaining this requires taking a closer look at the change of the SOC strengths with gate voltage, which, for the linearly approximated SOC parameters, are given by:

$$\begin{aligned} \frac{\partial SOC_{k\parallel[110]}}{\partial V_g} &= -\frac{\partial \alpha}{\partial V_g} + 2\frac{\partial \beta_3}{\partial V_g} \\ \frac{\partial SOC_{k\parallel[1\bar{1}0]}}{\partial V_g} &= \frac{\partial \alpha}{\partial V_g} + 2\frac{\partial \beta_3}{\partial V_g}. \end{aligned} \tag{4.65}$$

As, according to the evaluation of the spin signal oscillations, $\partial\alpha/\partial V_g < 0$, and $\partial\beta_3/\partial V_g \geq 0$ it can be concluded, that

$$\frac{\partial SOC_{k\parallel[110]}}{\partial V_g} \geq \frac{\partial SOC_{k\parallel[1\bar{1}0]}}{\partial V_g}. \tag{4.66}$$

Thus, the change of SOC with gate voltage is larger for a channel orientation along [110] compared to $[1\bar{1}0]$. Therefore, the change of the spin precession angle with gate voltage for $\vec{k} \parallel [110]$ is more pronounced, which gives rise to the observed gate dependent spin signal oscillations. For $\vec{k} \parallel [1\bar{1}0]$, on the other hand, the

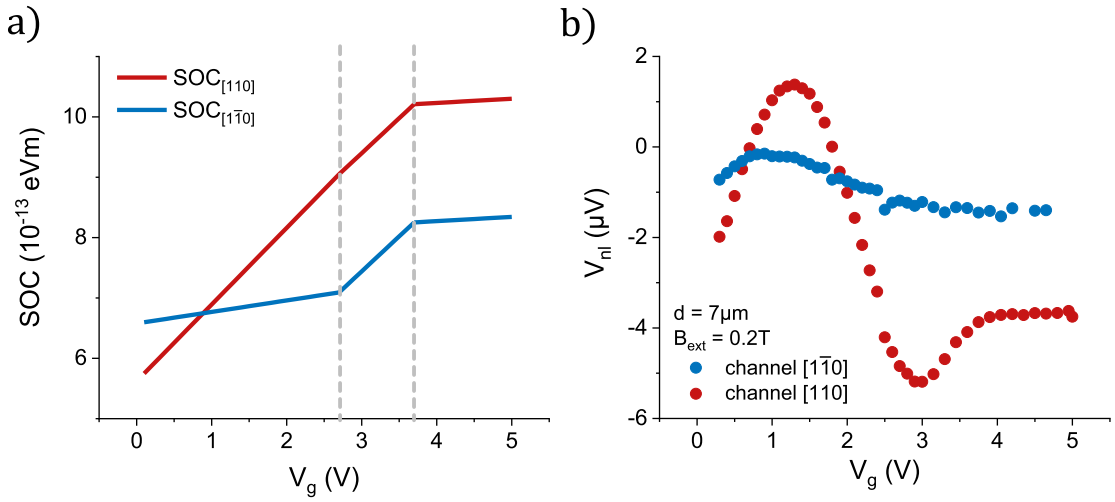

Figure 4.41. (**a**) Calculated total SOC strength for a channel orientation along $\vec{k} \parallel [110]$ (red) and $\vec{k} \parallel [1\bar{1}0]$ (blue). (**b**) Experimentally obtained gate sweeps for $B_{ext} = 0.2\,\mathrm{T}$ for two the different channel orientations shown in (a) (Fig. 4.30b).

change of SOC with V_g is significantly smaller, resulting in a smaller change of the spin precession frequency. Hence, no spin signal oscillations are observable in experiment (Fig. 4.41b). Especially in the low gate voltage range $V_g \lesssim 2.7\,\mathrm{V}$, in which the charge carrier density n_s changes with V_g, $SOC_{k\parallel[1\bar{1}0]}$ is nearly gate independent. In this range, the gate dependence of β_3, which is increasing for larger V_g, counteracts the gate dependent change of α, which is decreasing with V_g, while additionally $\alpha < 0$. In the intermediate gate voltage range ($2.7\,\mathrm{V} \lesssim V_g \lesssim 3.7\,\mathrm{V}$), n_s, and hence also β_3, are gate independent. Therefore, the only gate dependent contribution of the total SOC is α, so that the change of SOC with V_g does not depend on the crystallographic orientation ($\partial SOC_{k\parallel[110]}/\partial V_g = \partial SOC_{k\parallel[1\bar{1}0]}/\partial V_g$). In the experimental spin signal, the intermediate gate voltage range is not clearly distinguishable, however, which might be due to fabricational variations between the different devices. There, the crystallographic orientation dependence is investigated on a separate set of samples, such that minor fabricational variations could result in different gate characteristics. In particular, the gate dependence of n_s, which defines the gate voltage regions considered above, may vary, so that the intermediate gate voltage range could possibly extend towards higher gate voltages. Finally, it has to be emphasized that the gate dependent spin signal oscillations

do not depend on the crystallographic orientation, if β_3 is neglected. The observed anisotropy of the spin signal oscillations is therefore due to the gate dependent cubic Dresselhaus contribution. For the presented case, in which $\partial\alpha/\partial V_g < 0$ and $\partial\beta_3/\partial V_g > 0$, the gate dependence of SOC is enhanced for a channel orientation along $\vec{k} \parallel [110]$, while for $\vec{k} \parallel [1\bar{1}0]$ the increase of β_3 counteracts the decrease of α, thus decreasing the gate dependence of the total SOC.

spinFET-like functionality

The oscillations of the previously presented gate dependent measurements are extracted from magnetic fields sweeps for different gate voltages. This approach yields a detailed understanding of spin precession related phenomena in these devices. For establishing a spinFET-like functionality, however, it is more advantageous to apply a fixed external magnetic field, which aligns the magnetization of the injecting and detecting contact along the channel orientation, and perform gate sweeps. Such gate sweeps with the external magnetic field along the channel (90°), and parallel to the long axis of the injecting/detecting contact (0°) are shown in Fig. 4.42a. From the difference between the 90° and 0° signal gate dependent spin signal oscillations can be extracted (Fig. 4.42b), which shows identical characteristics as the one extracted from the magnetic field sweeps (Fig. 4.30). A possible operation mode of a spinFET-like device can then be established by switching between the gate voltage at which the oscillation pattern shows a minimum, which corresponds to an antiparallel configuration regarding detector magnetization and orientation of the detected spin, and the gate voltage at which a maximum is observable, i.e. the parallel configuration. In case of the measurement shown in Fig. 4.42b, the device can switch between P and AP by changing the gate voltage roughly between 0.9 V and 1.9 V. It is important to point out that the gate operation is possible without hysteretic effects in a small voltage range of roughly 2.5 V. Larger changes of V_g lead to an alteration of the population of deep trap states, which results in a shift of the threshold voltage, as discussed above (Chapter 4.3.2, Fig. 4.23). Thus, for measurements in a larger gate voltage range, as shown in Fig. 4.42, it is necessary to reset the population of these trap states by external illumination after each gate sweep. As the degree of occupation of these states

cannot be directly determined, different measurements can be slightly shifted as to the absolute value of the gate voltage. Matching of the curves is possible by aligning separate measurements with respect to the minimum of the signal trace (Fig. 4.42a).

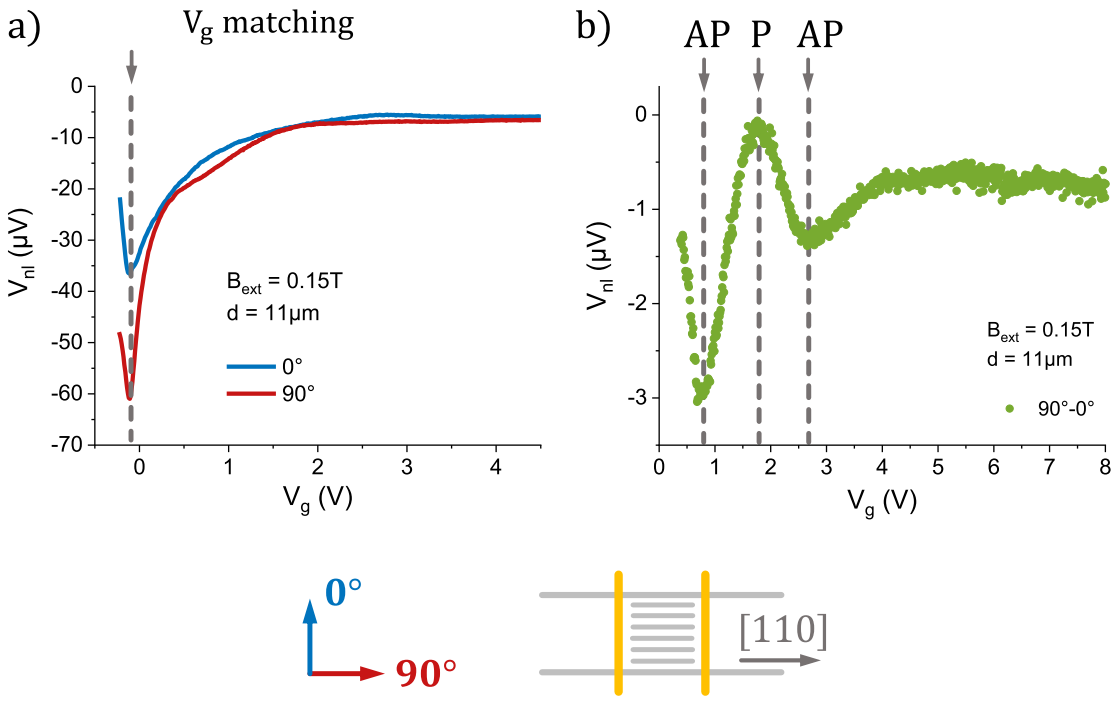

Figure 4.42. (**a**) Gate sweep for a fixed external magnetic field $B_{ext} = 0.15\,\mathrm{T}$, which sets the orientation of the spin contacts either parallel to the channel direction (90°) or perpendicular thereto (0°). As the threshold gate voltage is considerably shifted after sweeping the gate in a large voltage range, both measurements (0° and 90°) are matched by aligning the minima of the curves. (**b**) Signal difference between 90° and 0° curves shown in (a), showing a gate dependent spin precession pattern. At the minimum of the oscillation ($V_g \approx 0.9\,\mathrm{V}$) the spins arrive antiparallel at the position of the detector with respect to its magnetization, while for the gate voltage at which the maximum of the oscillation is observable, the spins are parallel with respect to the detector magnetization ($V_g \approx 1.9\,\mathrm{V}$).

4.3.4 Conclusion

In this chapter the effect of a gate electric field on spin transport properties and SOC related quantities was investigated in detail. The charge transport properties

in dependence of the gate voltage V_g were discussed first, which in particular yielded information on the gate dependence of the electron mobility μ_e, and the charge carrier density n_s. Both quantities are a function of V_g only up to a certain gate voltage, which is attributed to the population of deep trap states at the interface between the oxide and the SC structure, or within the oxide layer itself. In the main part of this chapter the dependence of a gate electric field on the spin transport properties was investigated. First, magnetic field sweeps with B_{ext} oriented perpendicular to the channel (0° signal) were regarded for a channel orientation along [110]. Thus, the gate dependence of the spin diffusion lengths $\lambda_{[100]}$ and $\lambda_{[1\bar{1}0]}$ for spins oriented along [100] and [1$\bar{1}$0] could be extracted. The gate dependent change of the spin diffusion length, the injection efficiency P_{inj}, and the channel resistance R_s gives rise to a gate dependence of the spin signal height. If the external magnetic field is oriented parallel to the channel (90° signal), on the other hand, the injected spins are oriented perpendicular to the SO-field, which gives rise to SOC induced spin precession. For a channel along [110] a distinct dip-like feature in these magnetic field sweeps could be identified as a signature of SOC, which was already discussed in Chapter 4.2. Gate dependent measurements showed a change of the dip-like signal characteristic to a peak-like feature, which implies a tunability of the SOC strength. From these gate resolved 90° signals at a fixed magnetic field gate dependent spin signal oscillations were extracted, which is one of the major results of this thesis. With the purely diffusive model presented in Chapter 2.6, these signal oscillations could not be described adequately, however. Instead, an extended ballistic model introduced by A. Zainuddin et al. [123] allowed fitting the oscillations remarkably well, in particular with regard to the decreasing oscillation amplitude with increasing V_g. There, the Rashba SOC parameter α, which is the main fitting parameter, was divided into a contribution which depends on the charge carrier density n_s, and one that is directly due to the gate electric field. This separation could be confirmed phenomenologically, and was additionally supported by simulations, which allowed deriving the n_s dependent contribution of α. For a channel orientation along [1$\bar{1}$0], on the other hand, no gate dependent spin signal oscillations could be observed, which implied that the change of SOC with V_g is much smaller for $\vec{k} \parallel [1\bar{1}0]$

compared to a channel along [110]. In particular, it could be assumed that the gate dependent change of the cubic Dresselhaus parameter β_3, which follows from the gate dependence of n_s, counteracts the gate voltage dependence of the Rashba contribution α for $\vec{k} \parallel [1\bar{1}0]$. Thus, the gate induced change of the spin precession frequency is smaller compared to the [110] channel orientation, which prevents the observation of gate dependent spin signal oscillations.

5 Conclusion and Outlook

One of the major goals of spintronics remains the realization of semiconductor devices, which allow the manipulation of the spin signal. In this context, the most prominent, but as yet unrealized, device proposal is the spinFET, conceptually introduced by S. Datta and B. Das [8]. Besides efficient electrical spin injection and detection, it requires the SOC strength to be tunable by an external electric field, which gives rise to a modulation of the SOC induced spin precession frequency. Demonstrating the gate control of spin precession in electrical spin injection devices, thus paving the way for the realization of a spinFET device, was one of the main objectives of this thesis.

In the heterostructure system under investigation, efficient electrical spin injection could be achieved through an Esaki-diode structure into an (In,Ga)As QW channel. In order to probe SOC related phenomena, it is advantageous to investigate spin injection devices with a narrow transport channel, such that spin transport is restricted mainly to one principle axis. In this case, the SO-field for $\vec{k}$ along the direction of the channel can be considered to be the main source of spin precession, which significantly facilitates its subsequent control. This required developing a novel device geometry, which allowed realizing narrow transport channels with a width down to $w_c = 400\,\mathrm{nm}$, approaching the 1-dimensional spin transport regime. For narrower transport channels, the Dyakonov-Perel spin relaxation mechanism is expected to be strongly suppressed by introducing a lateral confinement. This could be confirmed by non-local spin injection measurements for various channel widths, which showed a significant increase of the spin diffusion length λ_s for narrower transport channels. There, in the 2-dimensional limit $\lambda_{2D} \approx 4\,\mu\mathrm{m}$, while for the narrowest channel ($w_c = 400\,\mathrm{nm}$) the spin diffusion length was found to be

considerably larger with $\lambda_{400\,\mathrm{nm}} \approx 9.2\,\mu\mathrm{m}$.
With this new device geometry, it was possible to identify SOC related characteristics in non-local spin injection measurements. There, the focus was on transport channels along the [110] and [1$\bar{1}$0] crystallographic orientation, as along these directions the SO-field is perpendicular to the channel orientation. If the injected spin has a component which is perpendicular to this SO-field, spin precession is expected, whereby the orientation of the injected spin can be set by an external magnetic field. For spins injected parallel to the channel orientation, a characteristic signal feature was observable in non-local spin transport measurements for a channel along [110], which could be related to SOC induced spin precession. This was qualitatively confirmed by finite element simulations, based on an extended spin diffusion model. The total SOC strength could be estimated to lie in the low $10^{-13}\,\mathrm{eV\,m}$ range. For a channel orientation along [1$\bar{1}$0], on the other hand, no distinct SOC related features were observable, which suggested that the SOC strength along this direction is significantly weaker compared to the [110] direction. This crystallographic orientation dependence of the SO-fields could also be confirmed qualitatively based on the extended spin diffusion model.
Subsequently, the effect of an external electric field on the spin transport properties was investigated. From standard non-local spin valve (SV) measurements, in which case the external magnetic field is perpendicular to the channel orientation, the gate dependence of the spin diffusion length λ_s could be extracted. In the DP spin relaxation regime, the spin diffusion length can be related to the SOC parameters, such that the gate dependence of λ_s already implied a gate tunability of the SOC strength. Non-local measurements for an external magnetic field orientation parallel to the channel, on the other hand, allowed investigating spin precession related phenomena. There, the SOC related feature in the non-local spin transport measurements was observed to change by applying a gate voltage, consistent with the expected tunability of the SOC strength. From these measurements it was possible to extract gate dependent spin signal oscillations, which are characteristic for the expected spin signal modulation in a spinFET device. Similar spin precession signatures could only be observed before in InAs QW structures with a high SOC strength, in the limit of ballistic spin transport,

i.e. for small injector-detector distances [20–25]. In the presented devices, on the other hand, an $In_{0.09}Ga_{0.91}As$ QW structure provided the conducting channel, in which a relatively low SOC strength on the order of 10^{-13} eV m is expected. Additionally, in these devices spin transport is not ballistic, instead it takes place in an intermediate regime, which is still diffusive, yet approaches the quasi-1D limit. Despite of the low SOC strength and the partially diffusive spin transport, gate induced spin precession oscillations could be observed, which is indeed a remarkable finding and has to be considered as one of the central results of this thesis. Although spin transport takes place in an intermediate regime, it was not possible to adequately model the presented gate induced spin signal oscillations with the purely diffusive model, which is based on the extended spin diffusion equation. Instead, the oscillations could be fitted remarkably well by an extended ballistic model, which is provided by A. Zainuddin et al. [123], with the Rashba SOC contribution α as the main fitting parameter. For a channel orientation along $[1\bar{1}0]$, on the other hand, no gate dependent spin signal oscillations could be observed, which suggested that the gate dependent change of the total SOC is much smaller compared to a channel along [110]. It could be concluded that the gate dependence of the cubic Dresselhaus parameter β_3 counteracts the change of α with V_g for $\vec{k} \parallel [1\bar{1}0]$. The change of the total SOC with gate voltage is therefore smaller compared to a channel along [110], in which case cubic Dresselhaus and Rashba contribution add up.

One of the main obstacles for the realization of spin precession devices, like the spinFET proposal by S. Datta and B. Das [8], is the strict prerequisite for ballistic spin transport. This requires the distance between injecting and detecting contact to be smaller than the corresponding electron's mean free path. In this configuration, it is necessary to work with materials with a large SOC, such that the injected spin can be rotated by an angle larger than π on such a small distance. Within this work, it could be demonstrated that SOC induced spin precession can also be observed in diffusion dominated systems, which considerably relaxes the strict prerequisite of ballistic spin transport. Thus, spin precession devices with larger dimensions can be realized, but also spin precession in systems with

lower SOC strengths can be investigated more intensively in the future, which significantly expands the material choice.

A Appendix

A.1 Signal correction

General spin signal correction

The spin signal presented in Chapter 4.2.2 is phenomenologically background and offset corrected. In the following, this signal correction routine is explained in detail.

The non-local spin injection measurements are conducted in a magnetic field range up to $B_{ext} = 5\,\mathrm{T}$. In this range, however, an additional magneto-resistive background feature occurs (Fig. A.1a), the origin of which is unclear, as a systematic evaluation remains elusive. In Fig. A.1a non-local spin signals for two different external magnetic field orientations (blue: 0°, red: 90°) are shown. Both are significantly affected by a background signal. This background is not considered relevant for the evaluation of the spin signal, so that a phenomenological background removal routine is implemented, which allows extracting the spin related contribution of the signal (Fig. A.1b). In the following, the background removal approach is shortly described. First, magnetic up- and down-sweep are averaged. Subsequently, the result is averaged over opposite angles, which requires mirroring the signal of one of the angles at $B = 0\,\mathrm{T}$, so that the average is taken over the same external magnetic field direction. Removing the background itself is achieved by phenomenologically fitting and subsequently subtracting a 4-th order polynomial function from the averaged signal. There, only the range $|B| > \pm 2\,\mathrm{T}$ is considered to be dominated by the background signal, while at lower fields the magnitude of the spin signal and SOC related phenomena are assumed to prevail. Additional signal corrections concern the spin independent voltage offset. This

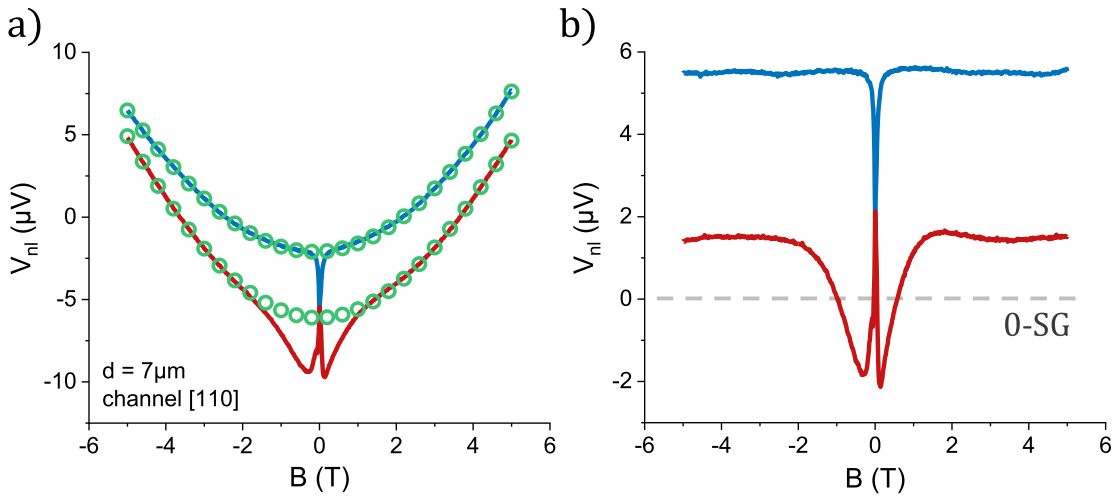

Figure A.1. (**a**) Non-local spin signal for channel along [110]. The external magnetic field is either oriented along the contact (0°, blue) or perpendicular thereto (90°, red). For the regarded large magnetic field range a distinct background signal is observable, which can be fitted by a polynomial function (green). (**b**) Signal shown in (a) with background correction and shifted to 0-spin-signal (0-SG).

offset can be removed by determining the signal level at which no spin dependent voltage drops at the detector, which is referred to as 0-spin-signal (0-SG). This signal level can be determined from standard SV measurements (0°), as described in Chapter 3.4, and basically lies in the middle between the parallel and the antiparallel level of the SV signal.

It has to be kept in mind, however, that the background and offset correction is a phenomenological approach, which implies considerable restrictions concerning the quantitative analysis. This may include artificially introduced changes of the spin signal profile, for instance. Yet all relevant characteristics are clearly distinguishable in the raw data, so that a qualitative discussion of the spin signal is still possible. A considerable source of error can arise from the inaccurate determination of the 0-spin-signal (0-SG). There, depending on whether the magnetization switches from P to AP, or vice versa, slightly different levels of the 0-SG are obtained. Also, imperfect switching characteristics, especially concerning the formation of the AP level, complicate an accurate evaluation. Moreover, it is important to note that the parallel and antiparallel levels of the SV signal

are expected to form along the magnetically easy axes of the ferromagnet, i.e. along [100] or [010] (Fig. A.2). The thus determined 0-SG is therefore only valid for spins oriented along these directions. For the offset correction, however, the obtained 0-SG is assumed to be equal for all orientations, which is not necessarily the case. The thus introduced uncertainty could potentially lead to an artificial shift of the spin signals relative to each other. An additional remark concerns the

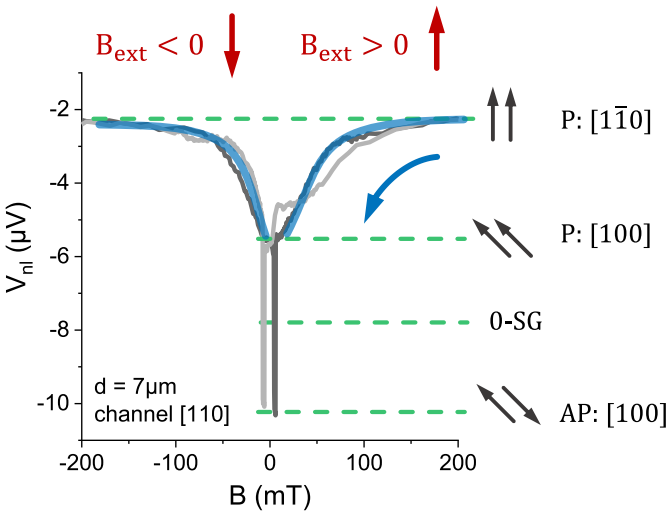

Figure A.2. Non-local SV signal (0°) for a channel along [110]. For large magnetic fields the magnetization of the contacts is parallel to B_{ext} (arrows), while upon reducing B_{ext} the parallel configuration rotates towards one of the easy axes (blue), before switching to the AP configuration.

signal features appearing in the low magnetic field range for $|B| \lesssim 100\,\mathrm{mT}$, which are especially relevant for channels oriented along [110] and [1$\bar{1}$0], in which case the spin injection and detection contacts are oriented along a magnetically hard axis of (Ga,Mn)As. These characteristics of the signal are related to the smooth rotation of the contact magnetization towards one of the magnetically easy axes at low magnetic fields, which is highlighted in Fig. A.2. There, for large magnetic fields the magnetization of the contacts is forced to orient parallel to the external magnetic field, i.e. both contacts are magnetized along [1$\bar{1}$0] (arrows in Fig. A.2). Upon reducing the external magnetic field, the magnetization of the contacts is still parallel, yet starts to rotate continuously towards one of the easy axes ([100] or [010]), before switching to the antiparallel configuration. Notably, the AP configuration is also established along one of the easy axes. For the discussion of the presented measurements, it is important to note that the spin contacts are aligned parallel to the external magnetic field for $|B| \gtrsim 100\,\mathrm{mT}$, while effects occurring

at smaller magnetic field strengths are not considered relevant for the presented investigations.

Spin signal correction for exemplary data

In the following, the spin signal correction is applied to an exemplary data set. For descriptive purposes, the discussion is limited to the signals obtained for an injector-detector distance of $d = 7\,\mu\text{m}$, and a channel orientation along [110]. Additionally, only the external magnetic field directions along the channel (90°) and perpendicular to the channel orientation (0°) are regarded. The sample is physically rotated in the external magnetic field. The corresponding nomenclature for each measurement direction is shown in Fig. A.3a. There, the angle is defined between the *positive* external magnetic field orientation and the channel direction. Note that for each sample orientation the magnetic field is swept from positive to negative values, and vice versa. Thus, the positive magnetic field range of the 0° signal is in principle equal to the negative magnetic field range of the 180° signal, for instance. In Fig. A.3b exemplary non-local spin signals are shown for a magnetic field orientation along the channel (90°, 270°), and B_{ext} parallel to the contact orientation (0°, 180°). For each measurement up- and down-sweeps of the magnetic field are conducted. There, the distinct magnetic field dependent background is clearly observable, as well as the signal offset. In a first step, the magnetic up- and down-sweep are averaged for each sample orientation. Subsequently, the measurements for opposite sample orientations are averaged, which requires mirroring one orientation at $B = 0\,\text{T}$. Thus, up- and down-sweep, as well as opposite angles are combined to one signal. In Fig. A.4a the original curves are shown before averaging, while in Fig. A.4b the corresponding average is presented. Note that the antiparallel signal level in the 0° and 180° signal occurs at difference magnetic field values, such that the AP signal level is not preserved by the averaging process. The background signal is then fitted with a polynomial of 4th order in the range of $|B_{ext}| \geq 2\,\text{T}$, as shown in Fig. A.4b. This polynomial functionality has no physical background, however, and is only chosen phenomenologically. Yet, it is important to note that all features of the raw data are preserved by the background removal routine. In particular the dip-like signal characteristic of the

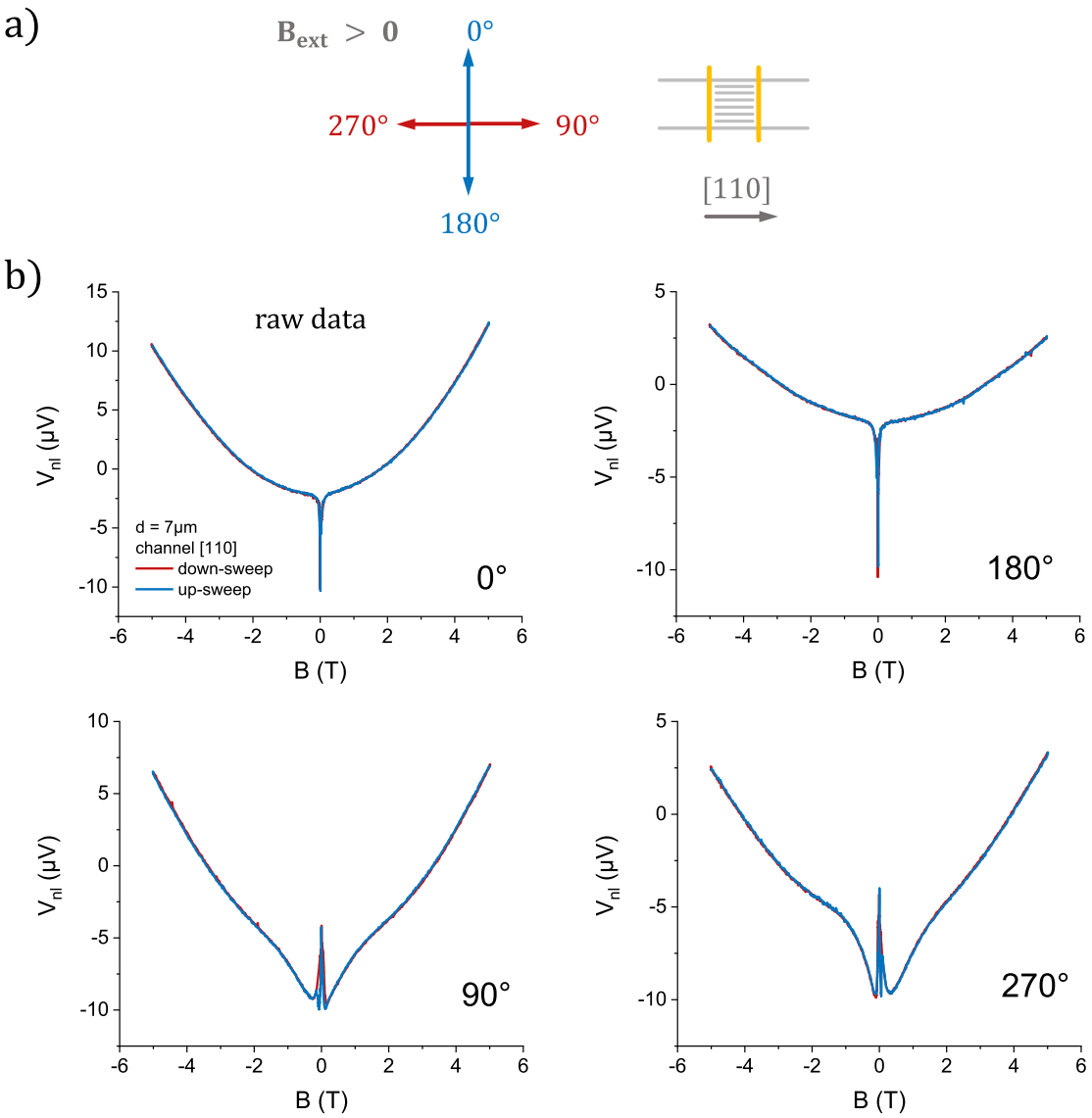

Figure A.3. (**a**) Nomenclature of the magnetic field direction ($B_{ext} > 0$) relative to the orientation of the channel. For sake of clarity only magnetic field orientations along the channel (90°, 270°), and perpendicular thereto (0°, 180°) are shown. (**b**) Raw data for the corresponding magnetic field orientations shown in (a), for a channel orientation along [110] and $d = 7\,\mu m$. For each measurement up- and down-sweeps (blue, red) of the magnetic field are performed.

90° signal is also clearly distinguishable in the original data. This phenomenological 4th order polynomial fit is subsequently subtracted from the averaged data. The thus corrected data is shown in Fig. A.5a. The 0° and 90° signals are then

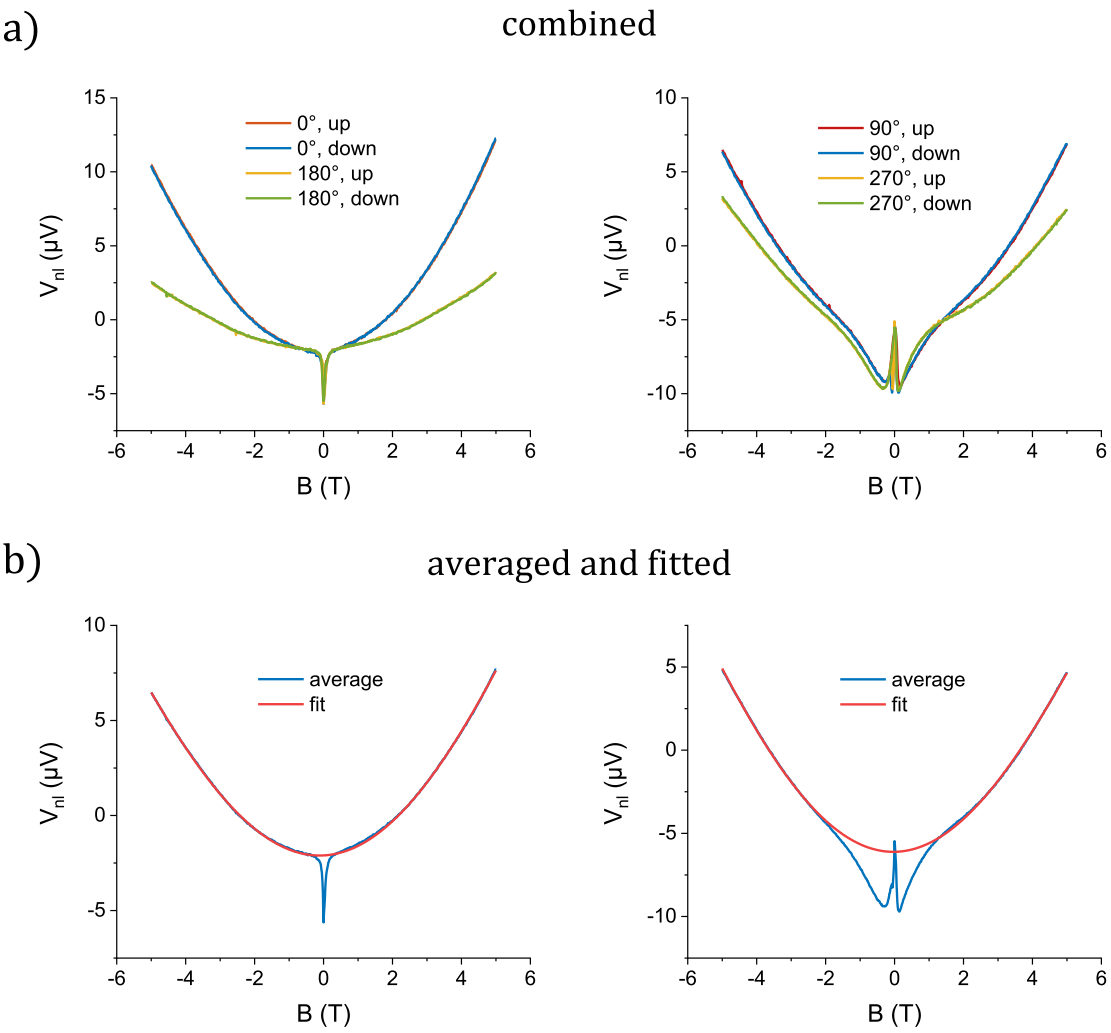

Figure A.4. (**a**) Opposite angels of the data shown in Fig. A.3 combined in one graph. For angles $\leq 180°$, the magnetic field axis is reversed, such that the magnetic field orientations are comparable. (**b**) Measurements shown in (a), averaged over up- and down-sweep, as well as over opposite magnetic field orientations. The background is then fitted by a 4th order polynomial (red).

additionally symmetrized with respect to $B_{ext} = 0\,\mathrm{T}$ (Fig. A.5b), which is valid due to the symmetry of the effective magnetic field ($\vec{B}_{eff} = \vec{B}_{SO} + \vec{B}_{ext}$) upon reversing $\vec{B}_{ext}$, as described in Chapter 4.2. Finally, the curves are shifted, such that the 0-spin-signal (0-SG) corresponds to a non-local voltage of $V_{nl} = 0\,\mathrm{V}$. There, the 0-SG is obtained from the SV signal, and basically lies in the middle between the P and the AP signal level. Note that the switching between P and AP

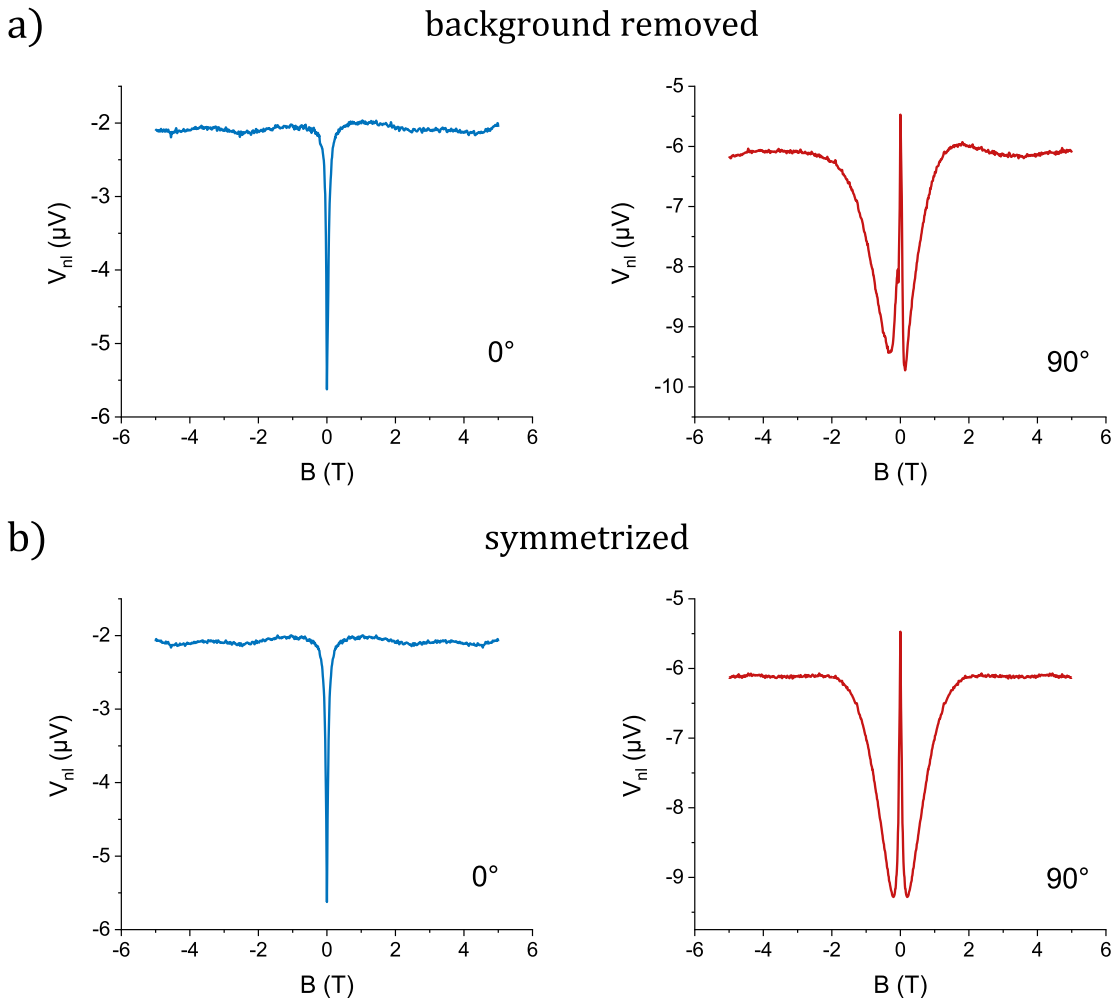

Figure A.5. (**a**) Offset corrected data. There the polynomial fit shown in Fig. A.4 is subtracted from the averaged data. (**b**) The 0° and 90° can additionally be symmetrized with respect to $B_{ext} = 0\,\mathrm{T}$. For these orientations this is valid, as the effective magnetic field is symmetric with regard to a reversal of the external magnetic field (Chapter 4.2).

takes place along one of the magnetically easy axes ([100] or [010]), such that the corresponding 0-SG is strictly speaking only valid for spins oriented along these directions. As there is no experimental access to the 0-SG for spins along the other crystallographic directions, however, this 0-SG for [100]/[010] has to be used as an approximation. In Fig. A.6 the background and offset corrected non-local spin signals are shown.

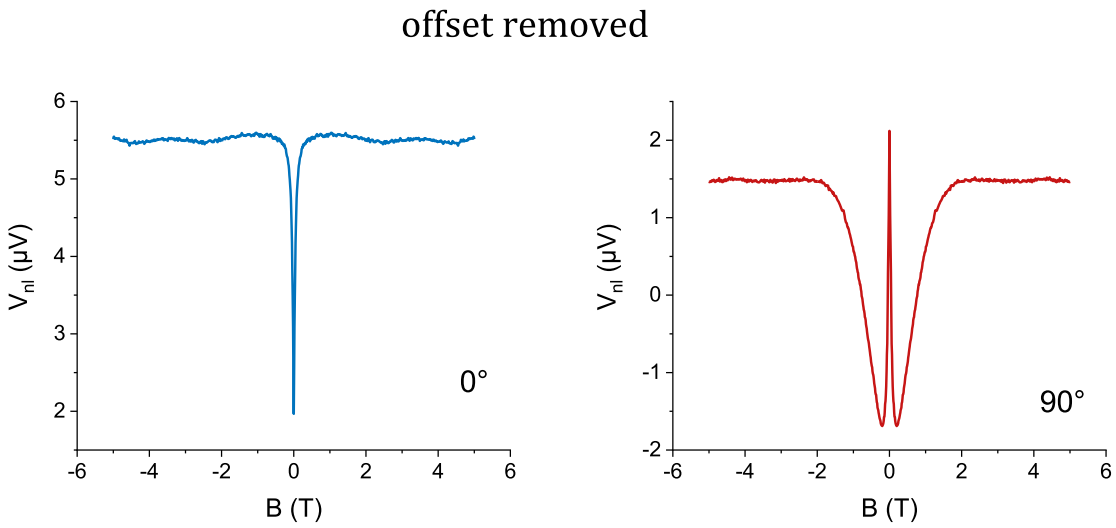

Figure A.6. Finally, the curves shown in Fig. A.5b are additionally shifted relative to the 0-SG (offset correction).

A.2 Parameters for gate dependent diffusive model

Introducing the gate dependence to the diffusive model presented in Chapter 2.6 requires making assumptions on the gate dependence of various input parameters. The gate dependence of charge carrier density n_s, electron mobility μ_e, and spin diffusion length $\lambda_{[1\bar{1}0]}$ can be determined experimentally. Additionally, the scaling factor f in the model, which quantifies the flux through the injecting contact, can be obtained from fitting the 0° signal (Chapter 4.3.3). All these gate dependent input parameters are summarized in Fig. A.7. For implementation in the COMSOL model, however, these quantities have to be parameterized as a function of V_g. In the following the approximate parametrizations are summarized:

- charge carrier density n_s (unit: $10^{11}\,\mathrm{cm}^{-2}$)
  $V_g = 0\,\mathrm{V} \ldots 2.7\,\mathrm{V}$ $\quad n_s = 2.29\,V_g + 3.78$
  $V_g = 2.7\,\mathrm{V} \ldots 5\,\mathrm{V}$ $\quad n_s = 9.97$
- electron mobility μ_e (unit: $10^{-4}\,\mathrm{m}^2/\mathrm{V\,s}$)
  $V_g = 0\,\mathrm{V} \ldots 2.63\,\mathrm{V}$ $\quad \mu_e = 9162.43 + 27453.69\,V_g - 5217.54\,V_g^2$
  $V_g = 2.63\,\mathrm{V} \ldots 5\,\mathrm{V}$ $\quad \mu_e = 45276.42$
- spin diffusion length $\lambda_{[1\bar{1}0]}$ (unit: $10^{-6}\,\mathrm{m}$)

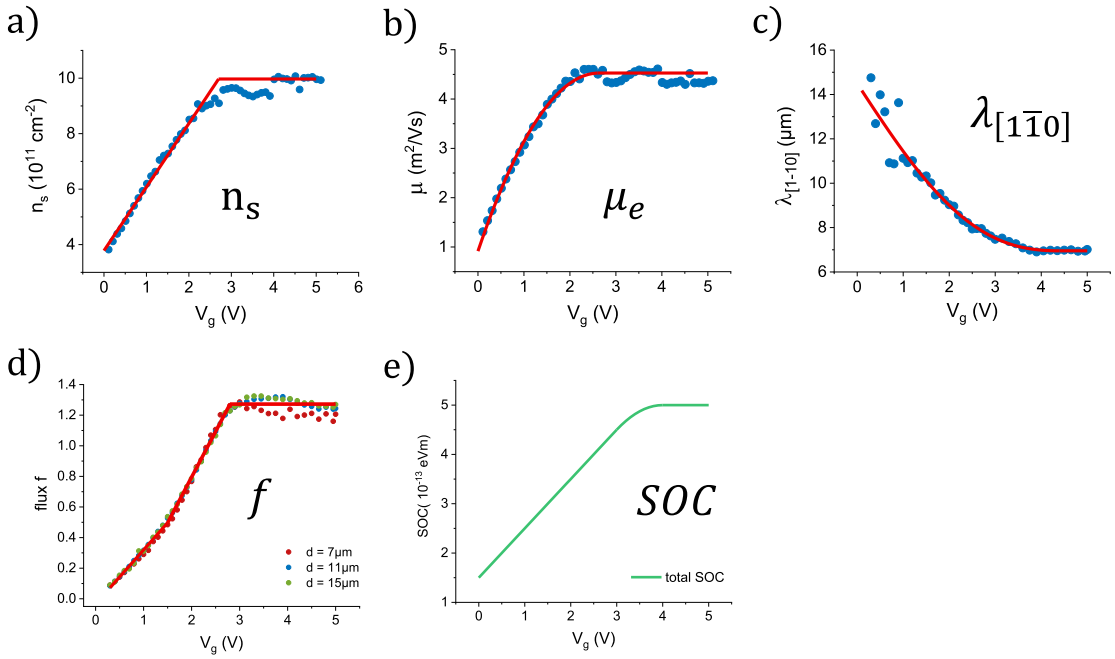

Figure A.7. Gate dependencies of the input parameters for the purely diffusive model: charge carrier density n_s (**a**), electron mobility μ_e (**b**), spin diffusion length $\lambda_{[1\bar{1}0]}$ for spins oriented along $[1\bar{1}0]$ (**c**), and scaling/flux factor f (**d**). The red lines indicate the approximate parameterization, which is implemented in the model. For the SOC strength an assumed gate voltage dependence is implemented (**e**).

$$
\begin{aligned}
V_g = 0\,\mathrm{V} \ldots 4.4\,\mathrm{V} \qquad & \lambda_{[1\bar{1}0]} = 14.5 - 3.17\,V_g - 0.00256\,V_g^2 + 0.131\,V_g^3 \\
& \quad - 0.0110\,V_g^4 - 0.000355\,V_g^5 \\
V_g = 4.4\,\mathrm{V} \ldots 5\,\mathrm{V} \qquad & \lambda_{[1\bar{1}0]} = 6.95
\end{aligned}
$$

- scaling/flux factor f

$$
\begin{aligned}
V_g = 0\,\mathrm{V} \ldots 1.5\,\mathrm{V} \qquad & f = -0.03 + 0.35\,V_g \\
V_g = 1.5\,\mathrm{V} \ldots 2.7\,\mathrm{V} \qquad & f = -0.50 + 0.60\,V_g \\
V_g = 2.7\,\mathrm{V} \ldots 5\,\mathrm{V} \qquad & f = 1.27
\end{aligned}
$$

For the SOC strength, on the other hand, an assumed gate voltage dependence is used, which is parametrized as follows (Fig. A.7e):

- spin orbit coupling strength SOC (unit: $10^{-13}\,\mathrm{eV\,m}$)

$$
\begin{aligned}
V_g = 0\,\mathrm{V} \ldots 3\,\mathrm{V} \qquad & SOC = 1.5 + V_g \\
V_g = 3\,\mathrm{V} \ldots 4\,\mathrm{V} \qquad & SOC = -2.94 + 3.97\,V_g - 0.50\,V_g^2 \\
V_g = 4\,\mathrm{V} \ldots 5\,\mathrm{V} \qquad & SOC = 5
\end{aligned}
$$

A.3 Fitting parameters obtained from simple ballistic model

In the spinFET proposal introduced by S. Datta and B. Das [8], the gate dependent spin signal oscillations are modeled by a simple cosine function:

$$V_{det} = A\cos\left(\frac{2m^*L}{\hbar^2}\,SOC(V_g) + \phi\right) + offset. \tag{A.1}$$

Assuming a linear dependence of the SOC strength on V_g, such that

$$SOC(V_g) = \frac{\partial SOC}{\partial V_g}\,V_g + SOC_0, \tag{A.2}$$

allows modeling the experimentally obtained spin signal oscillations presented in Chapter 4.3.3. The parameters resulting from fitting these oscillations with this simple ballistic spin transport model are summarized in Tab. I.

$\boldsymbol{d}$ (µm)	$\boldsymbol{offset}$ (µV)	$\boldsymbol{A}$ (µV)	$\boldsymbol{SOC_0}$	$\boldsymbol{\partial SOC/\partial V_g}$
7	1.60	3.80	-4.25	-1.32
11	0.65	1.55	-2.20	-1.14
15	0.33	0.60	-1.10	-1.06

Table I. Values of offset voltage, amplitude A, and Rashba SOC in the approxation of a linear gate dependence. The SOC realated quantities are given in units of (10^{-13} eV m), or (10^{-13} eV m/V) respectively.

A.4 Fitting parameters obtained from extended ballistic model

In Chapter 4.3.3 the gate dependent spin signal oscillations are fitted with an extended ballistic model, which is described by A. Zainuddin et al. [123]. There,

the spin signal oscillations can be described according to Eq. 4.57 (Chapter 4.3.3):

$$\Delta V \simeq \frac{\Delta V_{SV}}{2} + \frac{3\pi\Delta V_{SV}}{2}\,\frac{1}{\sqrt{2\pi\Theta}}\,\cos\left(\Theta + \frac{\pi}{4}\right), \tag{A.3}$$

where ΔV_{SV} is the signal height of the standard SV signal, in which case the spins are oriented along the contact, and Θ is the spin precession angle for $k \parallel [110]$, which is given by

$$\Theta(V_g) = \frac{2m^* d}{\hbar^2}\left(-\alpha + 2\beta_3 - \beta_1\right). \tag{A.4}$$

For fitting, additionally a signal offset OFF and a scaling factor SC have to be taken into account, such that

$$\Delta V = \Delta V_x \cdot SC + OFF. \tag{A.5}$$

The Rashba SOC contribution is assumed to change linearly with V_g

$$\alpha = \alpha_0 + \frac{\partial\alpha}{\partial V_g}\,V_g. \tag{A.6}$$

In the simplest case, α can be approximated to change linearly in the entire gate voltage range ($V_g = 0\,\mathrm{V} \ldots 5\,\mathrm{V}$). In Tab. II the corresponding fitting parameters are summarized. In a more advanced fitting approach the gate voltage range is divided into three region (A, B, and C), in which α is adjusted separately. The values, which are obtained from this fit, are summarized in Tab. III.

$\boldsymbol{d}$ (µm)	***offset*** (µV)	***scale***	$\boldsymbol{\alpha_0}$	$\boldsymbol{\partial\alpha/\partial V_g}$
7	-1.6	0.80	-3.78	-0.90
11	-0.8	0.70	-5.43	-0.72
15	-0.4	0.53	-6.01	-0.68

Table II. Values of offset voltage, scale, and Rashba SOC in the approxation of a linear gate dependence of α. The slope of α is assumed to be equal in the entire gate voltage range ($V_g = 0\,\mathrm{V} \ldots 5\,\mathrm{V}$). The SOC realated quantities are given in units of ($10^{-13}\,\mathrm{eV\,m}$), or ($10^{-13}\,\mathrm{eV\,m/V}$) respectively.

d (µm)	$offset$ (µV)	$scale$	α_0	$\partial\alpha/\partial V_g$ (region A)	(region B)	(region C)
7	-1.60	0.80	-3.78	-0.92	-1.09	-0.10
11	-0.82	0.70	-5.53	-0.66	-1.15	-0.10
15	-0.40	0.53	-6.16	-0.60	-1.15	0.05

Table III. Values obatined from fitting the spin signal oscillations, in case of dividing the gate voltage range into three separate regions (A, B, and C). The SOC realated quantities are given in units of (10^{-13} eV m), or (10^{-13} eV m/V) respectively.

A.5 Schrödinger-Poisson simulations

From self-consistent Schrödinger-Poisson simulations, the band profiles of the investigated heterostructure (Chapter 3.2) can be obtained. The structure is shown in Fig. A.8, whereby only the part of the spin injection device, in which spin transport takes place, is relevant. Thus, the Esaki-diode structure is not taken into account. In Fig. A.9 two exemplary simulations are shown. There, a gate dependence is introduced by setting the conduction band energy at the surface of the structure (CB pinning). This mimics the bending of the energy bands when applying a gate voltage. Depending on this CB pinning energy, the charge carrier

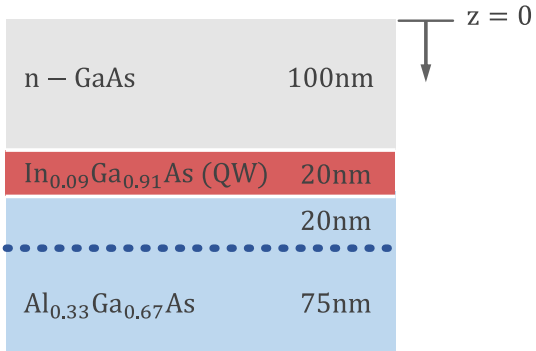

Figure A.8. Schematic layer sequence of the heterostructure system, in which spin transport between injecting and detecting contact takes place. This structure is the basis for the self-consistent Schrödinger-Poisson simulations. The blue dots mark the δ-doping layer.

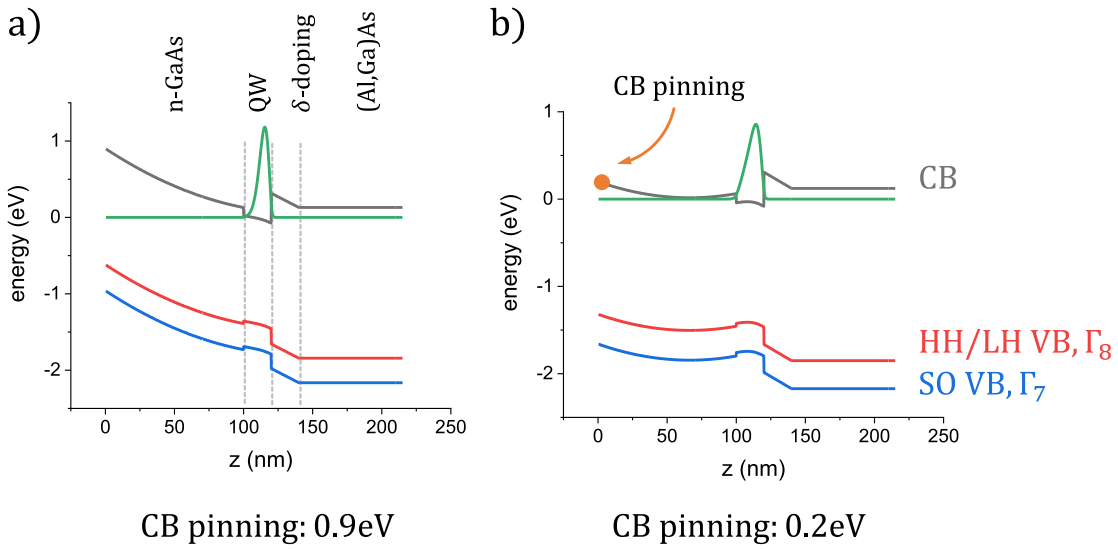

Figure A.9. Simulated energy bands of the heterostructure shown in Fig. A.8: conduction band (gray), heavy/light hole valence band (red, Γ_8), split-off valence band (blue, Γ_7). Additionally, the probability of the electron wave-function (green) is shown. A gate voltage is indirectly simulated by setting the conduction band energy at the surface of the structure (CB pinning). In (**a**) the CB is pinned at 0.9 eV, which corresponds to a gate voltage of about $V_g \approx 0.1$ V. In (**b**) the CB is pinned at 0.2 eV ($V_g \approx 2$ V).

density n_s, which can also be obtained from the simulations, changes. From the experimentally determined gate dependence of n_s (Chapter 4.3.2) it is thus possible to relate the CB pinning energies to gate voltage values. From these band energy calculations a value of the Rashba SOC contribution can be obtained. T. Schäpers et al. [71] present an equation, which, in a simplified case, is given by:

$$\begin{aligned}\alpha = &\frac{\hbar^2 E_p}{6m_0}\vec{e}_z \langle\Psi_z| \left(\frac{1}{(E_{\Gamma_7}^{(A)})^2} - \frac{1}{(E_{\Gamma_8}^{(A)})^2}\right) \varphi'(z)|\Psi_z\rangle \\ &+ \frac{\hbar^2 E_p}{8m_0}\vec{e}_z \sum_n \left[\left(E_{\Gamma_7}^{(B)} - E_{\Gamma_7}^{(A)}\right)\left(\frac{1}{\left(E_{\Gamma_7}^{(A)}\right)^2} + \frac{1}{\left(E_{\Gamma_7}^{(B)}\right)^2}\right)\right. \\ &\left. - \left(E_{\Gamma_8}^{(B)} - E_{\Gamma_8}^{(A)}\right)\left(\frac{1}{\left(E_{\Gamma_8}^{(A)}\right)^2} + \frac{1}{\left(E_{\Gamma_8}^{(B)}\right)^2}\right)\right] s_n |\Psi(z_n)|^2.\end{aligned} \tag{A.7}$$

The first term in Eq. A.7 is related to the electric field $\varphi'(z)$ within the heterostructure. There, Ψ_z is the electron wave-function, and $E_{\Gamma_7}^{(A)}$ and $E_{\Gamma_8}^{(A)}$ are the VB edges within the QW. For the interaction parameter E_p a value of 26.26 eV for $In_{0.09}Ga_{0.91}As$ is taken, which results from linearly interpolating the value of GaAs ($E_p = 28.8$ eV) and that of InAs ($E_p = 21.5$ eV) [187]. The second term in Eq. A.7

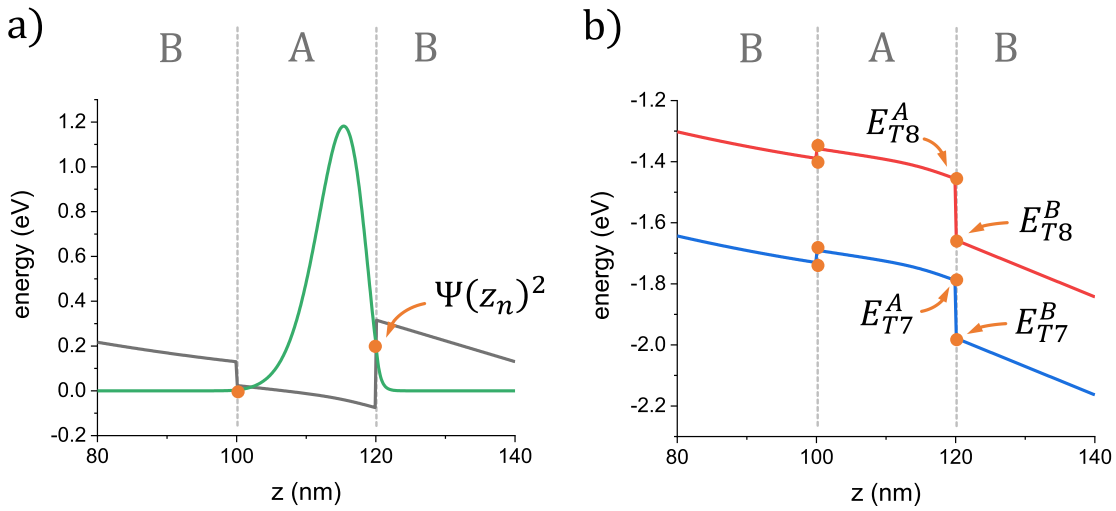

Figure A.10. Band structure shown in Fig. A.9a, zoomed in to the CB (**a**) and the VB (**b**) in the vicinity of the QW. The parameters which are required to calculate the Rashba SOC contribution according to Eq. A.7, are marked by the dots. There, these quantities are labeled only for the right interface, while the designation for the other interface is analogous.

takes into account interface contributions. There, the values of the VB edge at the interface have to be extracted from the simulated band structure, which is exemplarily visualized in Fig. A.10 for the interface, that is closer to the bottom of the heterostructure. The parameter $s_n = -1$ for the left interface, which is closer to surface, and $s_n = +1$ for the other interface. It has to be remarked that contributions to the Rashba SOC, which are due to the electron wave-function leaking into the barrier, are found to be negligible, due to the strong confinement of the wave-function within the QW.

The thus calculated values of α consist of a contribution α_E, which is due to the electric field within the structure, and two contributions, which originate from

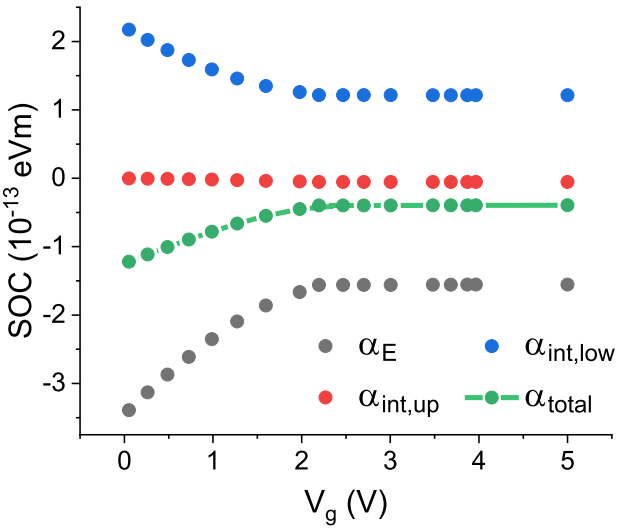

Figure A.11. Individual contributions of the Rashba SOC, which are obtained from the self-consistent Schrödinger-Poisson simulations. There, the total Rasbha SOC (green) consists of a contribution α_E (black), which depends on the electric field within the heterostructure, and the interface contributions of the upper interface $\alpha_{int,up}$ (red), and the lower one $\alpha_{int,low}$ (blue).

the two interfaces of the QW (α_{int}). In Fig. A.11 the individual contributions are plotted as a function of gate voltage V_g. The total Rashba SOC is given by the sum of the individual contributions:

$$\alpha_{total} = \alpha_E + \alpha_{int,up} + \alpha_{int,low}, \tag{A.8}$$

where $\alpha_{int,up}$ is the contribution of the interface, which is closer to the surface of the structure, while $\alpha_{int,low}$ refers to the other interface. Keep in mind however, that these simulations do not directly model a gate electrode. Instead, the conduction band energy at the surface of the structure is adjusted, which gives rise to a bending of the energy bands, and a change of n_s. The change of n_s is then related to a gate voltage by comparison to the measured gate dependence of n_s. Thus, in the discussion in Chapter 4.3.3 the value of α, which is obtained from these simulations, is considered to be only the n_s dependent contribution of the total Rashba SOC.

Bibliography

[1]G. E. Moore, "Cramming more components onto integrated circuits: Reprinted from Electronics, volume 38, number 8, April 19, 1965, pp.114 ff", IEEE Solid-State Circuits Society Newsletter **11**, 33–35 (2006).

[2]D. Burg and J. H. Ausubel, "Moore's Law revisited through Intel chip density", PloS one **16**, e0256245 (2021).

[3]D. Padua, *Encyclopedia of Parallel Computing* (Springer US, Boston, MA, 2011), pp. 1177–1184.

[4]S. E. Thompson and S. Parthasarathy, "Moore's law: the future of Si microelectronics", Materials Today **9**, 20–25 (2006).

[5]M. Ciorga, "Generation and detection of spin currents in ferromagnetic/nonmagnetic semiconductor structures", Habilitationsschrift, Universität Regensburg (2014).

[6]M. N. Baibich, J. M. Broto, A. Fert, F. N. van Dau, F. Petroff, P. Etienne, G. Creuzet, A. Friederich, and J. Chazelas, "Giant Magnetoresistance of (001)Fe/(001)Cr Magnetic Superlattices", Phys. Rev. Lett. **61**, 2472–2475 (1988).

[7]P. Grünberg, R. Schreiber, Y. Pang, U. Walz, M. B. Brodsky, and H. Sowers, "Layered magnetic structures: Evidence for antiferromagnetic coupling of Fe layers across Cr interlayers", Journal of Applied Physics **61**, 3750–3752 (1987).

[8]S. Datta and B. Das, "Electronic analog of the electro-optic modulator", Applied Physics Letters **56**, 665–667 (1990).

[9]P. R. Hammar and M. Johnson, "Spin-dependent current transmission across a ferromagnet-insulator-two-dimensional electron gas junction", Applied Physics Letters **79**, 2591–2593 (2001).

[10]O. M. J. van't Erve, A. T. Hanbicki, M. Holub, C. H. Li, C. Awo-Affouda, P. E. Thompson, and B. T. Jonker, "Electrical injection and detection of spin-polarized carriers in silicon in a lateral transport geometry", Applied Physics Letters **91**, 212109 (2007).

[11]X. Lou, C. Adelmann, S. A. Crooker, E. S. Garlid, J. Zhang, K. S. M. Reddy, S. D. Flexner, C. J. Palmstrøm, and P. A. Crowell, "Electrical detection of spin transport in lateral ferromagnet-semiconductor devices", Nature Physics **3**, 197–202 (2007).

[12]P. Bruski, Y. Manzke, R. Farshchi, O. Brandt, J. Herfort, and M. Ramsteiner, "All-electrical spin injection and detection in the Co_2FeSi/GaAs hybrid system in the local and non-local configuration", Applied Physics Letters **103**, 052406 (2013).

[13]H. C. Koo, H. Yi, J.-B. Ko, J. Chang, S.-H. Han, D. Jung, S.-G. Huh, and J. Eom, "Electrical spin injection and detection in an InAs quantum well", Applied Physics Letters **90**, 022101 (2007).

[14]T. Sasaki, T. Oikawa, T. Suzuki, M. Shiraishi, Y. Suzu, and K. Noguchi, "Evidence of Electrical Spin Injection Into Silicon Using MgO Tunnel Barrier", IEEE Transactions on Magnetics **46**, 1436–1439 (2010).

[15]T. A. Peterson, S. J. Patel, C. C. Geppert, K. D. Christie, A. Rath, D. Pennachio, M. E. Flatté, P. M. Voyles, C. J. Palmstrøm, and P. A. Crowell, "Spin injection and detection up to room temperature in Heusler alloy/n-GaAs spin valves", Physical Review B **94**, 1053 (2016).

[16]N. A. Viglin, V. V. Ustinov, V. M. Tsvelikhovskaya, and T. N. Pavlov, "Electric injection and detection of spin-polarized electrons in lateral spin valves on ferromagnetic metal-semiconductor InSb heterojunctions", JETP Letters **101**, 113–117 (2015).

[17]P. R. Hammar and M. Johnson, "Detection of spin-polarized electrons injected into a two-dimensional electron gas", Physical review letters **88**, 066806 (2002).

[18]M. Ciorga, A. Einwanger, U. Wurstbauer, D. Schuh, W. Wegscheider, and D. Weiss, "Electrical spin injection and detection in lateral all-semiconductor devices", Physical Review B **79**, 565 (2009).

[19]M. Oltscher, M. Ciorga, M. Utz, D. Schuh, D. Bougeard, and D. Weiss, "Electrical spin injection into high mobility 2D systems", Physical review letters **113**, 236602 (2014).

[20]J. Chang, H. Cheol Koo, J. Eom, S. Hee Han, and M. Johnson, "Injection, detection and gate voltage control of spins in the spin field effect transistor", Journal of Applied Physics **109**, 102405 (2011).

[21]W. Y. Choi, H.-j. Kim, J. Chang, S. H. Han, H. C. Koo, and M. Johnson, "Electrical detection of coherent spin precession using the ballistic intrinsic spin Hall effect", Nature nanotechnology **10**, 666–670 (2015).

[22]H. C. Koo, J. H. Kwon, J. Eom, J. Chang, S. H. Han, and M. Johnson, "Gate modulation of spin precession in a semiconductor channel", Journal of Physics D: Applied Physics **44**, 064006 (2011).

[23]H. C. Koo, J. H. Kwon, J. Eom, J. Chang, S. H. Han, and M. Johnson, "Control of Spin Precession in a Spin-Injected Field Effect Transistor", Science (New York, N.Y.) **325**, 1515–1518 (2009).

[24]J. H. Kim, J. Bae, B.-C. Min, H.-j. Kim, J. Chang, and H. C. Koo, "All-electric spin transistor using perpendicular spins", Journal of Magnetism and Magnetic Materials **403**, 77–80 (2016).

[25]Y. H. Park, J. W. Choi, H.-j. Kim, J. Chang, S. H. Han, H.-J. Choi, and H. C. Koo, "Complementary spin transistor using a quantum well channel", Scientific reports **7**, 46671 (2017).

[26]J. Fabian, Matos-Abiague A., Ertler C., Stano P., and Zutic I., "Semiconductor Spintronics", Acta Phys. Slov. **57**, 565–907 (2007).

[27]I. Zutic, J. Fabian, and S. Das Sarma, "Spintronics: Fundamentals and applications", Rev. Mod. Phys. **76**, 323–410 (2004).

[28]N. F. Mott, "Electrons in transition metals", Advances in Physics **13**, 325–422 (1964).

[29]I. A. Campbell, A. Fert, and R. Pomeroy, "Evidence for two current conduction iron", Philosophical Magazine **15**, 977–983 (1967).

[30]A. Fert and I. A. Campbell, "Two-Current Conduction in Nickel", Phys. Rev. Lett. **21**, 1190–1192 (1968).

[31]A. G. Aronov, "Spin injection in metals and polarization of nuclei", JETP Letters (1976).

[32]M. Johnson and R. H. Silsbee, "Thermodynamic analysis of interfacial transport and of the thermomagnetoelectric system", Physical Review B **35**, 4959–4972 (1987).

[33]M. Johnson and R. H. Silsbee, "Coupling of electronic charge and spin at a ferromagnetic-paramagnetic metal interface", Physical Review B **37**, 5312–5325 (1988).

[34]P. C. van Son, H. van Kempen, and P. Wyder, "Boundary Resistance of the Ferromagnetic-Nonferromagnetic Metal Interface", Phys. Rev. Lett. **58**, 2271–2273 (1987).

[35]T. Valet and A. Fert, "Theory of the perpendicular magnetoresistance in magnetic multilayers", Physical Review B **48**, 7099–7113 (1993).

[36]S. Hershfield and H. L. Zhao, "Charge and spin transport through a metallic ferromagnetic-paramagnetic-ferromagnetic junction", Physical Review B **56**, 3296–3305 (1997).

[37]A. Fert and H. Jaffrès, "Conditions for efficient spin injection from a ferromagnetic metal into a semiconductor", Physical Review B **64**, 665 (2001).

[38]G. Schmidt, D. Ferrand, L. W. Molenkamp, A. T. Filip, and B. J. van Wees, "Fundamental obstacle for electrical spin injection from a ferromagnetic metal into a diffusive semiconductor", Physical Review B **62**, R4790–R4793 (2000).

[39]E. I. Rashba, "Theory of electrical spin injection: Tunnel contacts as a solution of the conductivity mismatch problem", Physical Review B **62**, R16267–R16270 (2000).

[40]A. Fert, J.-M. George, H. Jaffres, and R. Mattana, "Semiconductors Between Spin-Polarized Sources and Drains", IEEE Transactions on Electron Devices **54**, 921–932 (2007).

[41]E. I. Rashba, "Diffusion theory of spin injection through resistive contacts", The European Physical Journal B - Condensed Matter **29**, 513–527 (2002).

[42]M. Johnson and R. H. Silsbee, "Interfacial charge-spin coupling: Injection and detection of spin magnetization in metals", Phys. Rev. Lett. **55**, 1790–1793 (1985).

[43]M. Johnson, "Analysis of anomalous multilayer magnetoresistance within the thermomagnetoelectric system", Phys. Rev. Lett. **67**, 3594–3597 (1991).

[44]D. L. Smith and R. N. Silver, "Electrical spin injection into semiconductors", Physical Review B **64**, 665 (2001).

[45]V. Y. Kravchenko and E. I. Rashba, "Spin injection into a ballistic semiconductor microstructure", Physical Review B **67**, 1488 (2003).

[46]G. Wexler, "The size effect and the non-local Boltzmann transport equation in orifice and disk geometry", Proceedings of the Physical Society **89**, 927–941 (1966).

[47]M. J. M. de Jong, "Transition from Sharvin to Drude resistance in high-mobility wires", Physical Review B **49**, 7778–7781 (1994).

[48]B. Nikolic and P. B. Allen, "Electron transport through a circular constriction", Physical Review B **60**, 3963–3969 (1999).

[49]R. H. Silsbee, "Novel Method for the Study of Spin Transport in Conductors", Bulletin of Magnetic Resonance, 284–285 (1980).

[50]M. Johnson and R. H. Silsbee, "Spin-injection experiment", Physical Review B **37**, 5326–5335 (1988).

[51]P. R. Hammar, B. R. Bennett, M. J. Yang, and M. Johnson, "Observation of Spin Injection at a Ferromagnet-Semiconductor Interface", Phys. Rev. Lett. **83**, 203–206 (1999).

[52]Y. Ohno, D. K. Young, B. Beschoten, F. Matsukura, H. Ohno, and D. D. Awschalom, "Electrical spin injection in a ferromagnetic semiconductor heterostructure", Nature **402**, 790–792 (1999).

[53]R. Fiederling, P. Grabs, W. Ossau, G. Schmidt, and L. W. Molenkamp, "Detection of electrical spin injection by light-emitting diodes in top- and side-emission configurations", Applied Physics Letters **82**, 2160–2162 (2003).

[54]A. T. Hanbicki, B. T. Jonker, G. Itskos, G. Kioseoglou, and A. Petrou, "Efficient electrical spin injection from a magnetic metal/tunnel barrier contact into a semiconductor", Applied Physics Letters **80**, 1240–1242 (2002).

[55]V. F. Motsnyi, J. de Boeck, J. Das, W. van Roy, G. Borghs, E. Goovaerts, and V. I. Safarov, "Electrical spin injection in a ferromagnet/tunnel barrier/semiconductor heterostructure", Applied Physics Letters **81**, 265–267 (2002).

[56]H. J. Zhu, M. Ramsteiner, H. Kostial, M. Wassermeier, H. P. Schönherr, and K. H. Ploog, "Room-temperature spin injection from Fe into GaAs", Physical review letters **87**, 016601 (2001).

[57]M. Kohda, Y. Ohno, K. Takamura, F. Matsukura, and H. Ohno, "A Spin Esaki Diode", Japanese Journal of Applied Physics **40**, L1274–L1276 (2001).

[58]X. Jiang, R. Wang, R. M. Shelby, R. M. Macfarlane, S. R. Bank, J. S. Harris, and S. S. P. Parkin, "Highly spin-polarized room-temperature tunnel injector for semiconductor spintronics using MgO(100)", Physical review letters **94**, 056601 (2005).

[59]C. H. Li, G. Kioseoglou, O. M. J. van't Erve, P. E. Thompson, and B. T. Jonker, "Electrical spin injection into Si(001) through a SiO_2 tunnel barrier", Applied Physics Letters **95**, 172102 (2009).

[60]O. M. J. van't Erve, G., Kioseoglou, A. T. Hanbicki, C. H. Li, B. T. Jonker, R. Mallory, M. Yasar, and A. Petrou, "Comparison of Fe/Schottky and Fe/Al_2O_3 tunnel barrier contacts for electrical spin injection into GaAs", Applied Physics Letters **84**, 4334–4336 (2004).

[61]M. Ramsteiner, H. Y. Hao, A. Kawaharazuka, H. J. Zhu, M. Kästner, R. Hey, L. Däweritz, H. T. Grahn, and K. H. Ploog, "Electrical spin injection from ferromagnetic MnAs metal layers into GaAs", Physical Review B **66**, 58 (2002).

[62]G. Kioseoglou, A. T. Hanbicki, J. M. Sullivan, O. M. J. van 't Erve, C. H. Li, S. C. Erwin, R. Mallory, M. Yasar, A. Petrou, and B. T. Jonker, "Electrical spin injection from an n-type ferromagnetic semiconductor into a III-V device heterostructure", Nature materials **3**, 799–803 (2004).

[63]P. van Dorpe, Z. Liu, W. van Roy, V. F. Motsnyi, M. Sawicki, G. Borghs, and J. de Boeck, "Very high spin polarization in GaAs by injection from a (Ga,Mn)As Zener diode", Applied Physics Letters **84**, 3495–3497 (2004).

[64]S. D. Ganichev and L. E. Golub, "Interplay of Rashba/Dresselhaus spin splittings probed by photogalvanic spectroscopy - A review", physica status solidi (b) **251**, 1801–1823 (2014).

[65]M. Kohda and G. Salis, "Physics and application of persistent spin helix state in semiconductor heterostructures", Semiconductor Science and Technology **32**, 073002 (2017).

[66]A. Manchon, H. C. Koo, J. Nitta, S. M. Frolov, and R. A. Duine, "New perspectives for Rashba spin-orbit coupling", Nature materials **14**, 871–882 (2015).

[67]H. C. Koo, S. B. Kim, H. Kim, T.-E. Park, J. W. Choi, K.-W. Kim, G. Go, J. H. Oh, D.-K. Lee, E.-S. Park, I.-S. Hong, and K.-J. Lee, "Rashba Effect in Functional Spintronic Devices", Advanced materials (Deerfield Beach, Fla.) **32**, e2002117 (2020).

[68]G. Dresselhaus, "Spin-Orbit Coupling Effects in Zinc Blende Structures", Phys. Rev. **100**, 580–586 (1955).

[69]Yu. A. Bychkov and E. I. Rashba, "Oscillatory effects and the magnetic susceptibility of carriers in inversion layers", Journal of Physics C: Solid State Physics **17**, 6039–6045 (1984).

[70]M. C. Lüffe, J. Kailasvuori, and T. S. Nunner, "Relaxation mechanisms of the persistent spin helix", Physical Review B **84**, 12 (2011).

[71]T. Schäpers, G. Engels, J. Lange, T. Klocke, M. Hollfelder, and H. Lüth, "Effect of the heterointerface on the spin splitting in modulation doped $In_xGa_{1-x}As$/InP quantum wells for B→0", Journal of Applied Physics **83**, 4324–4333 (1998).

[72]F. J. Ohkawa and Y. Uemura, "Quantized Surface States of a Narrow-Gap Semiconductor", Journal of the Physical Society of Japan **37**, 1325–1333 (1974).

[73]F. T. Vas'ko, "Spin Splitting in the spectrum of two-dimensional electrons due to the surface potential", JETP Letters, 541–544 (1979).

[74]G. Engels, J. Lange, T. Schäpers, and H. Lüth, "Experimental and theoretical approach to spin splitting in modulation-doped $In_xGa_{1-x}As$/InP quantum wells for B→0", Physical Review B **55**, R1958–R1961 (1997).

[75]J. P. Heida, B. J. van Wees, J. J. Kuipers, T. M. Klapwijk, and G. Borghs, "Spin-orbit interaction in a two-dimensional electron gas in a InAs/AlSb quantum well with gate-controlled electron density", Physical Review B **57**, 11911–11914 (1998).

[76]Y. H. Park, H. C. Koo, K. H. Kim, H.-j. Kim, J. Chang, S. H. Han, and H. Kim, "Observation of Spin-Orbit Interaction Parameter Over a Wide Temperature Range Using Potentiometric Measurement", IEEE Transactions on Magnetics **46**, 1562–1564 (2010).

[77]M. Studer, M. P. Walser, S. Baer, H. Rusterholz, S. Schön, D. Schuh, W. Wegscheider, K. Ensslin, and G. Salis, "Role of linear and cubic terms for drift-induced Dresselhaus spin-orbit splitting in a two-dimensional electron gas", Physical Review B **82**, 110 (2010).

[78]L. Meier, G. Salis, I. Shorubalko, E. Gini, S. Schön, and K. Ensslin, "Measurement of Rashba and Dresselhaus spin-orbit magnetic fields", Nature Physics **3**, 650–654 (2007).

[79]J. Nitta, T. Akazaki, H. Takayanagi, and T. Enoki, "Gate Control of Spin-Orbit Interaction in an Inverted $In_{0.53}Ga_{0.47}As/In_{0.52}Al_{0.48}As$ Heterostructure", Phys. Rev. Lett. **78**, 1335–1338 (1997).

[80]T. Koga, J. Nitta, T. Akazaki, and H. Takayanagi, "Rashba spin-orbit coupling probed by the weak antilocalization analysis in InAlAs/InGaAs/InAlAs quantum wells as a function of quantum well asymmetry", Physical review letters **89**, 046801 (2002).

[81]C.-M. Hu, J. Nitta, T. Akazaki, H. Takayanagi, J. Osaka, P. Pfeffer, and W. Zawadzki, "Zero-field spin splitting in an inverted $In_{0.53}Ga_{0.47}As/In_{0.52}Al_{0.48}As$ heterostructure: Band nonparabolicity influence and the subband dependence", Physical Review B **60**, 7736–7739 (1999).

[82]T. Y. Lee, J. Chang, M. C. Hickey, H. C. Koo, H.-j. Kim, S. H. Han, and J. S. Moodera, "Quantum well thickness dependence of Rashba spin-orbit coupling in the InAs/InGaAs heterostructure", Applied Physics Letters **98**, 202504 (2011).

[83]J. H. Kwon, H. C. Koo, J. Chang, S.-H. Han, and J. Eom, "Channel width effect on the spin-orbit interaction parameter in a two-dimensional electron gas", Applied Physics Letters **90**, 112505 (2007).

[84]Y. Ho Park, H.-j. Kim, J. Chang, S. Hee Han, J. Eom, H.-J. Choi, and H. Cheol Koo, "Separation of Rashba and Dresselhaus spin-orbit interactions using crystal direction dependent transport measurements", Applied Physics Letters **103**, 252407 (2013).

[85]M. Governale and U. Zülicke, "Rashba spin splitting in quantum wires", Solid State Communications **131**, 581–589 (2004).

[86]M. Governale and U. Zülicke, "Spin accumulation in quantum wires with strong Rashba spin-orbit coupling", Physical Review B **66**, 1488 (2002).

[87]J. Knobbe and T. Schäpers, "Magnetosubbands of semiconductor quantum wires with Rashba spin-orbit coupling", Physical Review B **71**, R15 (2005).

[88]F. Mireles and G. Kirczenow, "Ballistic spin-polarized transport and Rashba spin precession in semiconductor nanowires", Physical Review B **64**, 665 (2001).

[89]A. V. Moroz and C. H. W. Barnes, "Effect of the spin-orbit interaction on the band structure and conductance of quasi-one-dimensional systems", Physical Review B **60**, 14272–14285 (1999).

[90]T. Schäpers, V. A. Guzenko, M. G. Pala, U. Zülicke, M. Governale, J. Knobbe, and H. Hardtdegen, "Suppression of weak antilocalization in $Ga_x/In_{1-x}As/InP$ narrow quantum wires", Physical Review B **74**, 1247 (2006).

[91]J. Fabian and S. D. Sarma, "Spin relaxation of conduction electrons", Journal of Vacuum Science & Technology B: Microelectronics and Nanometer Structures **17**, 1708 (1999).

[92]M. W. Wu, J. H. Jiang, and M. Q. Weng, "Spin dynamics in semiconductors", Physics Reports **493**, 61–236 (2010).

[93]M. I. D'yakonov and V. Y. Kachorovskii, "Spin relaxation of two-dimensional electrons in noncentrosymmetric semiconductors", Soviet Physics: Semiconductors, 110–116 (1986).

[94]R. J. Elliott, "Theory of the Effect of Spin-Orbit Coupling on Magnetic Resonance in Some Semiconductors", Phys. Rev. **96**, 266–279 (1954).

[95]A. W. Overhauser, "Polarization of Nuclei in Metals", Phys. Rev. **92**, 411–415 (1953).

[96]Y. Yafet, "g factors and spin-lattice relaxation of conduction electrons", in *Solid state physics*, Vol. 14, Solid State Physics (Elsevier, 1963), pp. 1–98.

[97]G. L. Bir, A. G. Aronov, and G. E. Pikus, "Spin relaxation of electrons due to scattering by hole", Sov. Phys.-JETP, 705–712 (1975).

[98]N. S. Averkiev, L. E. Golub, and M. Willander, "Spin relaxation anisotropy in two-dimensional semiconductor systems", Journal of Physics: Condensed Matter **14**, R271–R283 (2002).

[99]J. Kainz, U. Rössler, and R. Winkler, "Anisotropic spin-splitting and spin-relaxation in asymmetric zinc blende semiconductor quantum structures", Physical Review B **68**, 255 (2003).

[100]K. Yoshizumi, A. Sasaki, M. Kohda, and J. Nitta, "Gate-controlled switching between persistent and inverse persistent spin helix states", Applied Physics Letters **108**, 132402 (2016).

[101]A. A. Kiselev and K. W. Kim, "Progressive suppression of spin relaxation in two-dimensional channels of finite width", Physical Review B **61**, 13115–13120 (2000).

[102]P. Altmann, M. Kohda, C. Reichl, W. Wegscheider, and G. Salis, "Transition of a two-dimensional spin mode to a helical state by lateral confinement", Physical Review B **92**, 3023 (2015).

[103]S. Kettemann, "Dimensional Control of Antilocalization and Spin Relaxation in Quantum Wires", Physical Review Letters **98**, 3023 (2007).

[104]A. Bournel, P. Dollfus, P. Bruno, and P. Hesto, "Gate-induced spin precession in an $In_{0.53}Ga_{0.47}As$ two dimensional electron gas", The European Physical Journal Applied Physics **4**, 1–4 (1998).

[105]A. G. Mal'shukov and K. A. Chao, "Waveguide diffusion modes and slowdown of D'yakonov-Perel' spin relaxation in narrow two-dimensional semiconductor channels", Physical Review B **61**, R2413–R2416 (2000).

[106]A. W. Holleitner, V. Sih, R. C. Myers, A. C. Gossard, and D. D. Awschalom, "Dimensionally constrained D'yakonov-Perel' spin relaxation in n-InGaAs channels: transition from 2D to 1D", New Journal of Physics **9**, 342 (2007).

[107]A. W. Holleitner, V. Sih, R. C. Myers, A. C. Gossard, and D. D. Awschalom, "Suppression of spin relaxation in submicron InGaAs wires", Physical review letters **97**, 036805 (2006).

[108]Y. Kunihashi, M. Kohda, and J. Nitta, "Enhancement of Spin Lifetime in Gate-Fitted InGaAs Narrow Wires", Phys. Rev. Lett. **102**, 226601 (2009).

[109]F. G. Pikus and G. E. Pikus, "Conduction-band spin splitting and negative magnetoresistance in A_3B_5 heterostructures", Physical Review B **51**, 16928–16935 (1995).

[110]E. A. de Andrada e Silva, G. C. La Rocca, and F. Bassani, "Spin-split subbands and magneto-oscillations in III-V asymmetric heterostructures", Physical Review B **50**, 8523–8533 (1994).

[111]T. Matsuyama, R. Kürsten, C. Meiner, and U. Merkt, "Rashba spin splitting in inversion layers on p-type bulk InAs", Physical Review B **61**, 15588–15591 (2000).

[112]A. Łusakowski, J. Wróbel, and T. Dietl, "Effect of bulk inversion asymmetry on the Datta-Das transistor", Physical Review B **68**, 665 (2003).

[113]T. Matsuyama, C.-M. Hu, D. Grundler, G. Meier, and U. Merkt, "Ballistic spin transport and spin interference in ferromagnet/InAs(2DES)/ferromagnet devices", Physical Review B **65**, 665 (2002).

[114]E. A. de Andrada e Silva, G. C. La Rocca, and F. Bassani, "Spin-orbit splitting of electronic states in semiconductor asymmetric quantum wells", Physical Review B **55**, 16293–16299 (1997).

[115]T. Koga, J. Nitta, T. Akazaki, and H. Takayanagi, "Rashba spin-orbit coupling probed by the weak antilocalization analysis in InAlAs/InGaAs/InAlAs quantum wells as a function of quantum well asymmetry", Physical review letters **89**, 046801 (2002).

[116]G.-H. Chen and M. E. Raikh, "Exchange-induced enhancement of spin-orbit coupling in two-dimensional electronic systems", Physical Review B **60**, 4826–4833 (1999).

[117]W. Häusler, "Rashba precession in quantum wires with interaction", Physical Review B **63**, 4 (2001).

[118]F. Eberle, D. Schuh, D. Bougeard, D. Weiss, and M. Ciorga, "Diffusive Spin Transport in Narrow Two-Dimensional-Electron-gas Channels", Physical Review Applied **16**, 110 (2021).

[119]A. Bournel, P. Dollfus, S. Galdin, F.-X. Musalem, and P. Hesto, "Modelling of gate-induced spin precession in a striped channel high electron mobility transistor", Solid State Communications **104**, 85–89 (1997).

[120]J. C. Egues, G. Burkard, and D. Loss, "Datta-Das transistor with enhanced spin control", Applied Physics Letters **82**, 2658–2660 (2003).

[121]O. E. Raichev and P. Debray, "Spin injection into ballistic layers and resistance modulation in spin field-effect transistors", Physical Review B **65**, 665 (2002).

[122]M. G. Pala, M. Governale, J. König, and U. Zülicke, "Universal Rashba spin precession of two-dimensional electrons and holes", Europhysics Letters (EPL) **65**, 850–856 (2004).

[123]A. N. M. Zainuddin, S. Hong, L. Siddiqui, S. Srinivasan, and S. Datta, "Voltage-controlled spin precession", Physical Review B **84**, 78 (2011).

[124]B. Das, D. C. Miller, S. Datta, R. Reifenberger, W. P. Hong, P. K. Bhattacharya, J. Singh, and M. Jaffe, "Evidence for spin splitting in $In_xGa_{1-x}As/In_{0.52}Al_{0.48}As$ heterostructures as B→0", Physical Review B **39**, 1411–1414 (1989).

[125]J. Luo, H. Munekata, F. F. Fang, and P. J. Stiles, "Effects of inversion asymmetry on electron energy band structures in GaSb/InAs/GaSb quantum wells", Physical Review B **41**, 7685–7693 (1990).

[126]J. Fabian, "Personal communication",

[127]G. Dhatt, G. Touzot, and E. Lefrançois, *Finite element method*, Numerical methods series (ISTE and Wiley, London and Hoboken N.J., 2012).

[128]L. Esaki, "New Phenomenon in Narrow Germanium p-n Junctions", Phys. Rev. **109**, 603–604 (1958).

[129]H. Ohno, A. Shen, F. Matsukura, A. Oiwa, A. Endo, S. Katsumoto, and Y. Iye, "(Ga,Mn)As: A new diluted magnetic semiconductor based on GaAs", Applied Physics Letters **69**, 363–365 (1996).

[130]E. Johnston-Halperin, D. Lofgreen, R. K. Kawakami, D. K. Young, L. Coldren, A. C. Gossard, and D. D. Awschalom, "Spin-polarized Zener tunneling in (Ga,Mn)As", Physical Review B **65**, 1849 (2002).

[131]A. H. MacDonald, P. Schiffer, and N. Samarth, "Ferromagnetic semiconductors: moving beyond (Ga,Mn)As", Nature materials **4**, 195–202 (2005).

[132]T. Dietl and H. Ohno, "Dilute ferromagnetic semiconductors: Physics and spintronic structures", Reviews of Modern Physics **86**, 187–251 (2014).

[133]T. Dietl, "A ten-year perspective on dilute magnetic semiconductors and oxides", Nature materials **9**, 965–974 (2010).

[134]C. Gould, S. Mark, K. Pappert, R. G. Dengel, J. Wenisch, R. P. Campion, A. W. Rushforth, D. Chiba, Z. Li, X. Liu, W. van Roy, H. Ohno, J. K. Furdyna, B. Gallagher, K. Brunner, G. Schmidt, and L. W. Molenkamp, "An extensive comparison of anisotropies in MBE grown (Ga,Mn)As material", New Journal of Physics **10**, 055007 (2008).

[135]J. Zemen, J. Kučera, K. Olejník, and T. Jungwirth, "Magnetocrystalline anisotropies in (Ga,Mn)As: Systematic theoretical study and comparison with experiment", Physical Review B **80**, 789 (2009).

[136]M. Ciorga, M. Schlapps, A. Einwanger, S. Geißler, J. Sadowski, W. Wegscheider, and D. Weiss, "TAMR effect in (Ga,Mn)As-based tunnel structures", New Journal of Physics **9**, 351 (2007).

[137]M. Ciorga, A. Einwanger, U. Wurstbauer, D. Schuh, W. Wegscheider, and D. Weiss, "In-plane anisotropy of tunneling magnetoresistance and spin polarization in lateral spin injection devices with (Ga,Mn)As/GaAs spin-Esaki diode contacts", Physica E: Low-dimensional Systems and Nanostructures **42**, 2673–2675 (2010).

[138]J. Wenisch, C. Gould, L. Ebel, J. Storz, K. Pappert, M. J. Schmidt, C. Kumpf, G. Schmidt, K. Brunner, and L. W. Molenkamp, "Control of magnetic anisotropy in (Ga,Mn)As by lithography-induced strain relaxation", Physical review letters **99**, 077201 (2007).

[139]J. Wunderlich, A. C. Irvine, J. Zemen, V. Holý, A. W. Rushforth, E. de Ranieri, U. Rana, K. Výborný, J. Sinova, C. T. Foxon, R. P. Campion, D. A. Williams, B. L. Gallagher, and T. Jungwirth, "Local control of magnetocrystalline anisotropy in (Ga,Mn)As microdevices: Demonstration in current-induced switching", Physical Review B **76**, `10.1103/PhysRevB.76.054424` (2007).

[140]F. Hoffmann, G. Woltersdorf, W. Wegscheider, A. Einwanger, D. Weiss, and C. H. Back, "Mapping the magnetic anisotropy in (Ga,Mn)As nanostructures", Physical Review B **80**, `10.1103/PhysRevB.80.054417` (2009).

[141]J. A. Haigh, M. Wang, A. W. Rushforth, E. Ahmad, K. W. Edmonds, R. P. Campion, C. T. Foxon, and B. L. Gallagher, "Manipulation of the magnetic configuration of (Ga,Mn)As nanostructures", Applied Physics Letters **95**, 062502 (2009).

[142]M. Ciorga, M. Utz, D. Schuh, D. Bougeard, and D. Weiss, "Effect of contact geometry on spin-transport signals in nonlocal (Ga,Mn)As/GaAs devices", Physical Review B **88**, 565 (2013).

[143]M. Trottmann, "Characterisation of III-V semiconductor hybrid systems for spinorbitronic functionality", Dissertation (Universität Regensburg), 10.5283/EPUB.43680 (2020).

[144]P. M. Mooney, "Deep donor levels (DX centers) in III-V semiconductors", Journal of Applied Physics **67**, R1–R26 (1990).

[145]P. M. Mooney, "Donor-related levels in GaAs and $Al_xGa_{1-x}As$", Semiconductor Science and Technology **6**, B1–B8 (1991).

[146]P. M. Mooney, "Electrical properties of DX centers in GaAs and AlGaAs", Radiation Effects and Defects in Solids **111-112**, 281–298 (1989).

[147]M. Ciorga, C. Wolf, A. Einwanger, M. Utz, D. Schuh, and D. Weiss, "Local spin valve effect in lateral (Ga,Mn)As/GaAs spin Esaki diode devices", AIP Advances **1**, 022113 (2011).

[148]C. Ashby and A. Baca, "Fabrication of GaAs Devices", The Institution of Electrical Engineering and Technology (2005).

[149]P. L. Reza Ghodssi, "MEMS Materials and Processes Handbook (MEMS Reference Shelf)", Springer (2011).

[150]M. Johnson and R. H. Silsbee, "Calculation of nonlocal baseline resistance in a quasi-one-dimensional wire", Physical Review B **76**, 10.1103/PhysRevB.76.153107 (2007).

[151]F. L. Bakker, A. Slachter, J.-P. Adam, and B. J. van Wees, "Interplay of Peltier and Seebeck effects in nanoscale nonlocal spin valves", Physical review letters **105**, 136601 (2010).

[152]P. van Dorpe, W. van Roy, J. de Boeck, G. Borghs, P. Sankowski, P. Kacman, J. A. Majewski, and T. Dietl, "Voltage-controlled spin injection in a (Ga,Mn)As/(Al,Ga)As Zener diode", Physical Review B **72**, 181 (2005).

[153]C. Beenakker and H. van Houten, "Quantum Transport in Semiconductor Nanostructures", in *Semiconductor Heterostructures and Nanostructures*, Vol. 44, Solid State Physics (Elsevier, 1991), 1–228 (chapter 2).

[154]T. J. Thornton, M. L. Roukes, A. Scherer, and Van de Gaag, B. P., "Boundary scattering in quantum wires", Phys. Rev. Lett. **63**, 2128–2131 (1989).

[155]L. Yang, J. D. Koralek, J. Orenstein, D. R. Tibbetts, J. L. Reno, and M. P. Lilly, "Doppler velocimetry of spin propagation in a two-dimensional electron gas", Nature Physics **8**, 153–157 (2012).

[156]C. P. Weber, N. Gedik, J. E. Moore, J. Orenstein, J. Stephens, and D. D. Awschalom, "Observation of spin Coulomb drag in a two-dimensional electron gas", Nature **437**, 1330–1333 (2005).

[157]I. D'Amico and G. Vignale, "Theory of spin Coulomb drag in spin-polarized transport", Physical Review B **62**, 4853–4857 (2000).

[158]M. P. Walser, C. Reichl, W. Wegscheider, and G. Salis, "Direct mapping of the formation of a persistent spin helix", Nature Physics **8**, 757–762 (2012).

[159]M. Studer, S. Schön, K. Ensslin, and G. Salis, "Spin-orbit interaction and spin relaxation in a two-dimensional electron gas", Physical Review B **79**, 3023 (2009).

[160]M. J. Manfra, K. W. Baldwin, A. M. Sergent, R. J. Molnar, and J. Caissie, "Electron mobility in very low density GaN/AlGaN/GaN heterostructures", Applied Physics Letters **85**, 1722–1724 (2004).

[161]C. Rössler, T. Feil, P. Mensch, T. Ihn, K. Ensslin, D. Schuh, and W. Wegscheider, "Gating of high-mobility two-dimensional electron gases in GaAs/AlGaAs heterostructures", New Journal of Physics **12**, 043007 (2010).

[162]K. Hirakawa and H. Sakaki, "Mobility of the two-dimensional electron gas at selectively doped n-type $Al_xGa_{1-x}As$/GaAs heterojunctions with controlled electron concentrations", Physical Review B **33**, 8291–8303 (1986).

[163]J. Robertson, "High dielectric constant gate oxides for metal oxide Si transistors", Reports on Progress in Physics **69**, 327–396 (2006).

[164]G. D. Wilk, R. M. Wallace, and J. M. Anthony, "High-κ gate dielectrics: Current status and materials properties considerations", Journal of Applied Physics **89**, 5243–5275 (2001).

[165]J. H. Davies, "The Physics of Low-dimensional Semiconductors", in *The Physics of Low-dimensional Semiconductors*, edited by J. H. Davies (Cambridge University Press, 2012), pp. 329–370.

[166]J. Robertson, "Band offsets of wide-band-gap oxides and implications for future electronic devices", Journal of Vacuum Science & Technology B: Microelectronics and Nanometer Structures **18**, 1785 (2000).

[167]G. Bersuker, P. Zeitzoff, J. H. Sim, B. H. Lee, R. Choi, G. Brown, and C. D. Young, "Mobility evaluation in transistors with charge-trapping gate dielectrics", Applied Physics Letters **87**, 042905 (2005).

[168]Y. Hori, C. Mizue, and T. Hashizume, "Process Conditions for Improvement of Electrical Properties of Al_2O_3/n-GaN Structures Prepared by Atomic Layer Deposition", Japanese Journal of Applied Physics **49**, 080201 (2010).

[169]M. J. Manfra, L. N. Pfeiffer, K. W. West, H. L. Stormer, K. W. Baldwin, J. W. P. Hsu, D. V. Lang, and R. J. Molnar, "High-mobility AlGaN/GaN heterostructures grown by molecular-beam epitaxy on GaN templates prepared by hydride vapor phase epitaxy", Applied Physics Letters **77**, 2888–2890 (2000).

[170]I. P. Smorchkova, C. R. Elsass, J. P. Ibbetson, R. Vetury, B. Heying, P. Fini, E. Haus, S. P. DenBaars, J. S. Speck, and U. K. Mishra, "Polarization-induced charge and electron mobility in AlGaN/GaN heterostructures grown by plasma-assisted molecular-beam epitaxy", Journal of Applied Physics **86**, 4520–4526 (1999).

[171]D. Jena, A. C. Gossard, and U. K. Mishra, "Dislocation scattering in a two-dimensional electron gas", Applied Physics Letters **76**, 1707–1709 (2000).

[172]M. Shayegan, V. J. Goldman, M. Santos, T. Sajoto, L. Engel, and D. C. Tsui, "Two-dimensional electron system with extremely low disorder", Applied Physics Letters **53**, 2080–2082 (1988).

[173]L. Pfeiffer, K. W. West, H. L. Stormer, and K. W. Baldwin, "Electron mobilities exceeding $10^7 \mathrm{cm}^2/\mathrm{Vs}$ in modulation-doped GaAs", Applied Physics Letters **55**, 1888–1890 (1989).

[174]H. L. Störmer, A. C. Gossard, and W. Wiegmann, "Observation of intersubband scattering in a 2-dimensional electron system", Solid State Communications **41**, 707–709 (1982).

[175]S. Zafar, A. Callegari, E. Gusev, and M. V. Fischetti, "Charge trapping related threshold voltage instabilities in high permittivity gate dielectric stacks", Journal of Applied Physics **93**, 9298–9303 (2003).

[176]J. Robertson, "High dielectric constant gate oxides for metal oxide Si transistors", Reports on Progress in Physics **69**, 327–396 (2006).

[177]C. Mizue, Y. Hori, M. Miczek, and T. Hashizume, "Capacitance-Voltage Characteristics of Al_2O_3/AlGaN/GaN Structures and State Density Distribution at Al_2O_3/AlGaN Interface", Japanese Journal of Applied Physics **50**, 021001 (2011).

[178]Y. Lu, S. Yang, Q. Jiang, Z. Tang, B. Li, and K. J. Chen, "Characterization of VT-instability in enhancement-mode Al_2O_3-AlGaN/GaN MIS-HEMTs", physica status solidi (c) **10**, 1397–1400 (2013).

[179]S. Zafar, A. Kumar, E. Gusev, and E. Cartier, "Threshold voltage instabilities in high-κ gate dielectric stacks", IEEE Transactions on Device and Materials Reliability **5**, 45–64 (2005).

[180]P. Lagger, C. Ostermaier, G. Pobegen, and D. Pogany, "Towards understanding the origin of threshold voltage instability of AlGaN/GaN MIS-HEMTs", in 2012 International Electron Devices Meeting (2012), pp. 13.1.1–13.1.4.

[181]S. Huang, S. Yang, J. Roberts, and K. J. Chen, "Threshold Voltage Instability in Al_2O_3/GaN/AlGaN/GaN Metal-Insulator-Semiconductor High-Electron Mobility Transistors", Japanese Journal of Applied Physics **50**, 110202 (2011).

[182]E. P. Gusev, D. A. Buchanan, E. Cartier, A. Kumar, D. DiMaria, S. Guha, A. Callegari, S. Zafar, P. C. Jamison, D. A. Neumayer, M. Copel, M. A. Gribelyuk, H. Okorn-Schmidt, C. D'Emic, P. Kozlowski, K. Chan, N. Bojarczuk, L.-A. Ragnarsson, P. Ronsheim, K. Rim, R. J. Fleming, A. Mocuta, and A. Ajmera, "Ultrathin high-κ gate stacks for advanced CMOS devices", in International Electron Devices Meeting. Technical Digest (Cat. No.01CH37224) (2-5 Dec. 2001), pp. 20.1.1–20.1.4.

[183]P. Fiorenza, G. Greco, E. Schilirò, F. Iucolano, R. Lo Nigro, and F. Roccaforte, "Determining oxide trapped charges in Al_2O_3 insulating films on recessed AlGaN/GaN heterostructures by gate capacitance transients measurements", Japanese Journal of Applied Physics **57**, 050307 (2018).

[184]Z. Tang, P. D. Ye, D. Lee, and C. R. Wie, "Electrical measurements of voltage stressed Al_2O_3/GaAs MOSFET", Microelectronics Reliability **47**, 2082–2087 (2007).

[185]M. Choi, A. Janotti, and C. G. van de Walle, "Native point defects and dangling bonds in α-Al_2O_3", Journal of Applied Physics **113**, 044501 (2013).

[186]A. Einwanger, M. Ciorga, U. Wurstbauer, D. Schuh, W. Wegscheider, and D. Weiss, "Tunneling anisotropic spin polarization in lateral (Ga,Mn)As/GaAs spin Esaki diode devices", Applied Physics Letters **95**, 152101 (2009).

[187]I. Vurgaftman, J. R. Meyer, and L. R. Ram-Mohan, "Band parameters for III-V compound semiconductors and their alloys", Journal of Applied Physics **89**, 5815–5875 (2001).

Danksagung

Zuletzt möchte ich mich bei allen Personen bedanken die mich bei der Fertigstellung dieser Arbeit unterstützt haben.

Besonderer Dank gilt dabei **Prof. Dr. Dieter Weiß** für die Möglichkeit an einem überaus interessanten Thema zu forschen, sowie für die ausgezeichnete Betreuung und die perfekten Rahmenbedingungen während meiner Promotion.

Außerdem möchte ich mich bei **apl. Prof. Dr. Mariusz Ciorga** bedanken für die kompetente Betreuung und die Möglichkeit jederzeit Fragen zu stellen, sowohl zu physikalischen, als auch zu laborbezogenen Themen. Zudem möchte ich mich für die zahlreichen inspirierenden physikalischen Diskussionen bedanken, die mir jedes Mal sehr weitergeholfen haben.

Prof. Dr. Dominique Bougeard danke ich besonders für die zahlreichen aufschlussreichen Diskussionen, die wirklich jedes Mal sehr hilfreich waren, sowie natürlich für das Wafermaterial, ohne das diese Arbeit nicht realisierbar gewesen wäre. Dabei möchte ich auch **Dr. Dieter Schuh** für die kompetente Durchführung des MBE-Wachstumsprozesses danken.

Besonderer Dank richtet sich an **Prof. Dr. Jaroslav Fabian** für die zahlreichen Meetings, die jedes Mal sehr interessante Anstöße gaben, aber vor allem auch für die Herleitung der theoretischen Grundlagen für das erweiterte diffusive Spin-Transport-Modell.

Michael Prager und **Lucia Ebnet** danke ich für die tatkräftige Unterstützung bei den Schrödinger-Poisson Simulationen, insbesondere für die Bereitstellung der entsprechenden Vorlagen.

Claudia Moser und **Elke Haushalter** für die Bewältigung bürokratischer Hürden.

Meinen Kollegen für die angenehme Arbeitsatmosphäre und die zahlreichen Kaffeepausen, und die endlosen Diskussionen über Spininjektion.